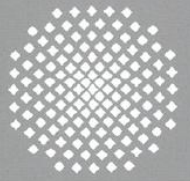
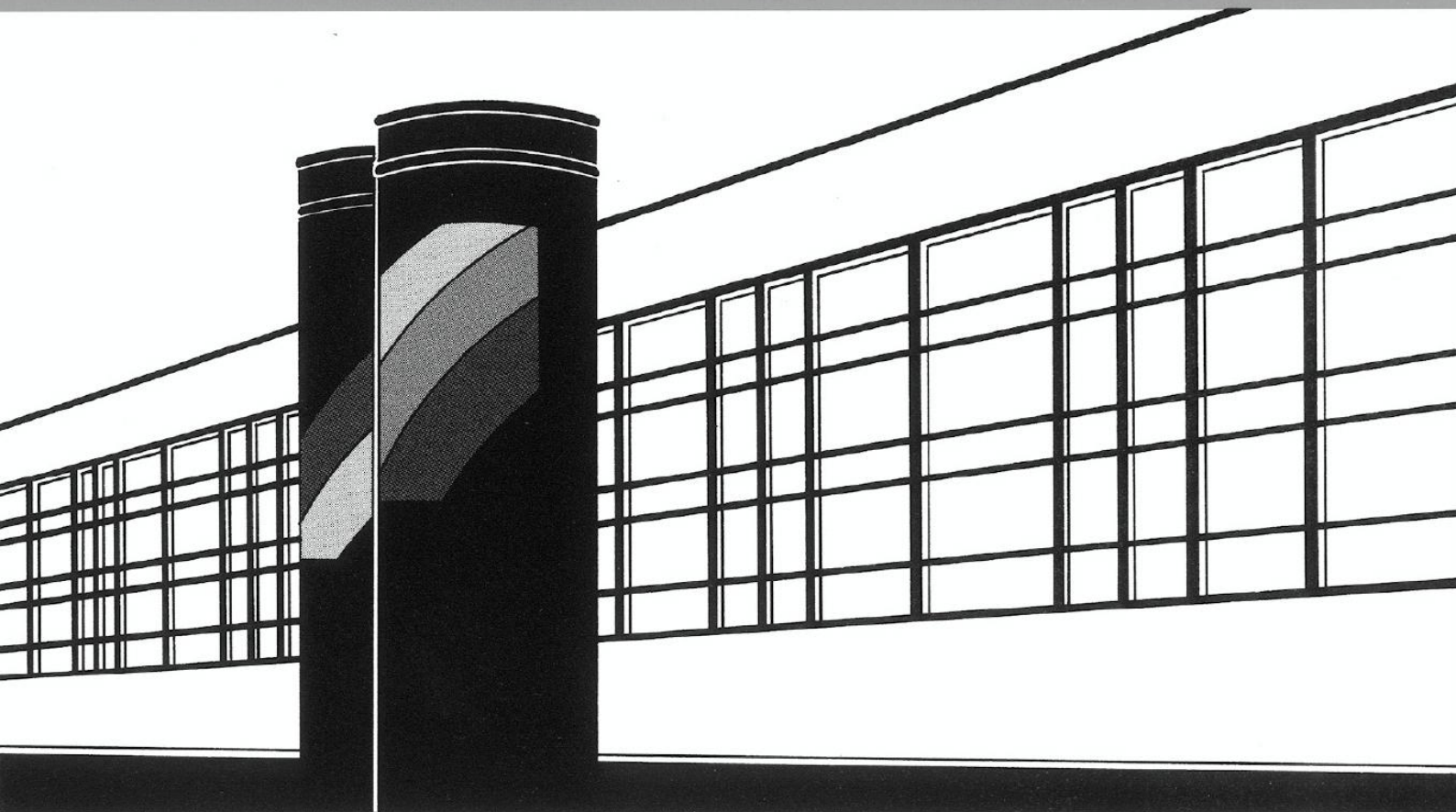


Universität Stuttgart



Institut für Wasser- und Umweltsystemmodellierung

# *Mitteilungen*



Heft 244 Johannes Martin Hommel

Modeling biogeochemical and mass transport processes in the subsurface: Investigation of microbially induced calcite precipitation



Heft 244      Modeling biogeochemical and mass  
transport processes in the  
subsurface: Investigation of  
microbially induced calcite  
precipitation

von  
Dr.-Ing.  
Johannes Martin Hommel

**D93 Modeling biogeochemical and mass transport processes in the subsurface: Investigation of microbially induced calcite precipitation**

**Bibliografische Information der Deutschen Nationalbibliothek**

Die Deutsche Nationalbibliothek verzeichnet diese Publikation in der Deutschen Nationalbibliografie; detaillierte bibliografische Daten sind im Internet über <http://www.d-nb.de> abrufbar

**Hommel, Johannes Martin:**

Modeling biogeochemical and mass transport processes in the subsurface: Investigation of microbially induced calcite precipitation, Universität Stuttgart. - Stuttgart: Institut für Wasser- und Umweltsystemmodellierung, 2016

(Mitteilungen Institut für Wasser- und Umweltsystemmodellierung, Universität Stuttgart: H. 244)

Zugl.: Stuttgart, Univ., Diss., 2016  
ISBN 978-3-942036-48-1

NE: Institut für Wasser- und Umweltsystemmodellierung <Stuttgart>: Mitteilungen

Gegen Vervielfältigung und Übersetzung bestehen keine Einwände, es wird lediglich um Quellenangabe gebeten.

Herausgegeben 2016 vom Eigenverlag des Instituts für Wasser- und Umweltsystemmodellierung

Druck: Document Center S. Kästl, Ostfildern

**Modeling biogeochemical and mass transport processes in the  
subsurface:  
Investigation of microbially induced calcite precipitation**

Von der Fakultät Bau- und Umweltingenieurwissenschaften der Universität Stuttgart  
zur Erlangung der Würde eines Doktors der  
Ingenieurwissenschaften (Dr.-Ing.) genehmigte Abhandlung

Vorgelegt von

**Johannes Martin Hommel**

aus Althengstett-Ottenbronn

Hauptberichter:	apl. Prof. Dr.-Ing. Holger Class
Mitberichter:	Prof. Alfred B. Cunningham
Mitberichter:	Prof. Dr.-Ing. Rainer Helmig

Tag der mündlichen Prüfung: 15.02.2016

Institut für Wasser- und Umweltsystemmodellierung der Universität Stuttgart

2016



## Danksagung

An dieser Stelle möchte ich mich bei allen bedanken, die mich bei meiner Arbeit unterstützt haben. Zuallererst bei der DFG, die diese Arbeit im Rahmen des internationalen Graduiertenkollegs NUPUS finanziert hat.

Besonders bedanken möchte ich mich bei meinem Hauptberichter Holger Class. Durch seine pragmatische und unkomplizierte Art sowie der stets offenen Bürotür hat er mich immer motiviert und unterstützt. Meinem Berichter Rainer Helmig danke ich für seinen grundsätzlichen Optimismus, der sich manchmal auch auf mich übertragen hat. I want to thank my supervisor Alfred B. Cunningham for his research-related support by adding a more application-focused point of view, but also for the many hikes around Bozeman and the support with finding an accommodation during my visits.

Auch bei Maria Costa, Prudence Lawday und Stefanie Siegert möchte ich mich dafür bedanken, dass sie mir unbürokratisch bei der Bewältigung der Unibürokratie geholfen haben. Zusätzlich möchte ich Prudence Lawday für die vielen sprachlichen Anregungen danken.

I want to thank all my publication coauthors for the detailed discussions, recommendations, and the support. Anozie Ebigbo I want to thank for the sophisticated model that he developed which I was able to use as well as for sharing his experience with me. Thanks to Robin Gerlach for sacrificing time during his sabbatical for detailed discussions and for reminding me both of the big picture as well as important details. Ellen Lauchnor and Adrienne Philipps I want to thank for the introduction to laboratory work and to the experimentalist perspective on research as well as for sharing their data treasures. I want to thank all the people from MSU who shared their data with me and helped with experimental investigations. Especially valuable for this thesis was the experimental data of Ellen Lauchnor, Adrienne Philipps, and James Connolly. I was lucky to have Ellen's support with the attachment experiments as well as the possibility to assist James in the planning of his micro-model experiments.

Gleichfalls möchte ich auch allen Kollegen vom LH2 und LS3 danken für die guten Ratschläge und das äußerst angenehme Arbeitsumfeld. Besonders Lena Walter, Alexander Kissinger und Thomas Fetzer sowie Emna Meijri und Beatrix Becker, mit denen ich während meiner Arbeit das Zimmer geteilt habe, möchte ich für die Diskussionen, Anregungen und Tipps danken.

Besonderer Dank gilt selbstverständlich meiner Familie und meiner Freundin Laura, die mich immer unterstützt und während dem Zusammenschreiben motiviert haben.



# Contents

<b>List of Figures</b>	<b>v</b>
<b>List of Tables</b>	<b>xiii</b>
<b>Notation</b>	<b>xix</b>
<b>Abstract</b>	<b>xxiii</b>
<b>Zusammenfassung</b>	<b>xxvii</b>
<b>1. Introduction</b>	<b>1</b>
1.1. Microbes in the subsurface . . . . .	1
1.2. Biogeochemical processes . . . . .	2
1.3. Role of modeling . . . . .	2
1.4. Microbially induced calcite precipitation . . . . .	3
1.5. Objectives of the thesis . . . . .	5
1.6. Structure of the thesis . . . . .	6
<b>2. Fundamentals of modeling flow and transport in porous media</b>	<b>7</b>
2.1. Scale . . . . .	7
2.2. Porous medium properties . . . . .	7
2.2.1. Porosity . . . . .	7
2.2.2. Intrinsic permeability . . . . .	8
2.3. Phases and components . . . . .	8
2.3.1. Mass fraction, mole fraction, molality . . . . .	8
2.4. Fluid properties . . . . .	9
2.4.1. Density . . . . .	9
2.4.2. Viscosity . . . . .	9
2.5. Fluid phase interactions in porous media . . . . .	10
2.5.1. Saturation . . . . .	10
2.5.2. Capillary pressure . . . . .	10
2.5.3. Relative permeability . . . . .	11

2.6.	Transport processes in porous media . . . . .	11
2.6.1.	Advection . . . . .	12
2.6.2.	Diffusion . . . . .	12
2.6.3.	Dispersion . . . . .	13
2.7.	Balance equations . . . . .	13
2.7.1.	Balance equation for component transport in two-phase flow . . . . .	13
2.7.2.	Balance equation for solid phases . . . . .	14
2.8.	Effects of mineral precipitation and biomass growth in porous media . . . . .	14
2.8.1.	Porosity changes due to mineral precipitation and biomass growth . . . . .	14
2.8.2.	Permeability changes due to mineral precipitation and biomass growth . . . . .	15
<b>3.</b>	<b>State of the art prior to this work; experiments</b>	<b>17</b>
3.1.	Model concept . . . . .	18
3.1.1.	Component-specific reactive source and sink terms . . . . .	19
3.1.2.	Supplementary equations . . . . .	25
3.1.3.	Diffusion, dispersion and tortuosity . . . . .	26
3.1.4.	Numerical implementation . . . . .	28
3.2.	Interaction between modeling and experiments . . . . .	28
3.3.	Implementation in DuMu <sup>X</sup> : solution scheme and changes . . . . .	30
<b>4.</b>	<b>Model improvements</b>	<b>33</b>
4.1.	Improvement of the porosity-permeability relation . . . . .	33
4.1.1.	Sandstone core simulations . . . . .	33
4.1.2.	Literature review on porosity-permeability relations . . . . .	37
4.1.3.	Micro-model investigation . . . . .	39
4.1.4.	Conclusions from the micro-model investigation . . . . .	42
4.2.	Improvement of the ureolysis rate equation . . . . .	45
4.2.1.	Processes and recent experiments . . . . .	47
4.2.2.	Model calibration . . . . .	52
4.2.3.	Discussion . . . . .	62
4.2.4.	Summary . . . . .	68
<b>5.</b>	<b>Application of the model to guide experimental investigations</b>	<b>71</b>
5.1.	Investigation of the influence of initial biomass and injection strategy . . . . .	71
5.1.1.	Introduction . . . . .	71
5.1.2.	Results . . . . .	80
5.1.3.	Discussion . . . . .	89
5.2.	Application of the model on the field scale . . . . .	94
5.2.1.	Field site and resulting simulation scenarios . . . . .	94

5.2.2. Investigated injection strategies . . . . .	95
5.2.3. Comparison of model predictions . . . . .	96
5.2.4. Discussion . . . . .	97
5.2.5. Summary and outlook . . . . .	99
<b>6. Perspectives for efficient solution strategies</b>	<b>101</b>
6.1. Options to reduce computational time . . . . .	101
6.1.1. Optimized numerical solution approaches . . . . .	101
6.1.2. Simplification of physics and chemistry . . . . .	104
6.1.3. Other possible ways of reducing computational effort . . . . .	106
6.2. Investigation of selected methods for increasing computational efficiency . . .	107
6.2.1. Optimized numerical solution approaches . . . . .	108
6.2.2. Simplification of physics and chemistry . . . . .	110
6.2.3. Other possibilities for reducing computational effort . . . . .	111
6.3. Preliminary conclusions . . . . .	113
<b>7. Summary</b>	<b>115</b>
<b>Bibliography</b>	<b>121</b>
<b>A. Model improvement: porosity-permeability relation</b>	<b>135</b>
<b>B. Model improvement: ureolysis</b>	<b>137</b>
<b>C. Model application to guide experimental investigations</b>	<b>147</b>
C.1. Grid and boundary conditions used in this study . . . . .	148
C.2. Rates influencing the attached biomass . . . . .	149
C.3. Initial biomass distributions . . . . .	151
C.4. Results . . . . .	155
<b>D. Field scale simulation</b>	<b>163</b>



# List of Figures

1.1. Schematic view of relevant processes during MICP. . . . .	5
4.1. Sketch of the domain, boundary conditions and the grid used for simulation.	34
4.2. Comparison of measured (blue stars) and simulated (red lines) permeability over time. The dashed line represents the permeability as calculated in the original model described in <i>Ebigbo et al. (2012)</i> , whereas the solid one shows the permeability after fitting $\phi_{crit}$ in Equation (3.31) to the experimental data.	35
4.3. Sketch of the micro-model experiment setup. . . . .	39
4.4. Depth-averaged microscopy images of the first half of the micro-model's porous region. Flow is from left to right. The left shows the clean porous medium before inoculation, the right shows the final biofilm developed within the porous medium after 13.6 h. . . . .	41
4.5. Permeability and porosity measured in the first, biomass-only micro-model experiment. And the permeability predictions based on the measured porosity using different relations. . . . .	42
4.6. More sophisticated porosity-permeability relations improve the permeability predictions slightly. The additional shape coefficient $S = e^{-80\phi_f}$ is determined by fitting to results of micro-model experiments. . . . .	43
4.7. Overview of steps taken in the course of model revision. . . . .	46
4.8. Values obtained for the biofilm density $\rho_f$ for each experiment through parameter estimation using iTOUGH2. Multiple experiments (C4, D2, and BR) are combined in the data set M to fit averaged parameters values. . . . .	55
4.9. Values obtained for the attachment coefficient to biofilm $c_{a,1}$ through parameter estimation using iTOUGH2. Multiple experiments (C4, D2, and BR) are combined in the data set M to fit averaged parameters values. . . . .	56
4.10. Values obtained for the attachment coefficient to arbitrary surfaces $c_{a,2}$ through parameter estimation using iTOUGH2. Multiple experiments (C4, D2, and BR) are combined in the data set M to fit averaged parameters values. . . . .	56

4.11. Values obtained for the urease content of biofilm $k_{ub}$ through parameter estimation using iTOUGH2. Multiple experiments (C4, D2, and BR) are combined in the data set M to fit averaged parameters values. For C4, $k_{ub}$ was not included in the set of fitting parameters for the inverse modeling. . . . .	57
4.12. Simulation results for selected parameter sets in comparison with measured $Ca^{2+}$ concentrations for column experiment D2 at 0.2 m distance from the injection point. A total of 7 measurement series were conducted after the end of $Ca^{2+}$ -rich injection pulses (c). For a better temporal resolution, (a) shows a zoom of the second measurement series and (b) one of the last (seventh). The parameter values corresponding to each parameter set are given in Table 4.4. . . . .	59
4.13. Simulation results for selected parameter sets in comparison with measured $NH_4^+$ concentrations for column experiment D2 at 0.2 m distance from the injection point. A total of 7 measurement series were conducted after the end of $Ca^{2+}$ -rich injection pulses (c). For a better temporal resolution, (a) shows a zoom of the second measurement series and (b) one of the last (seventh). The parameter values corresponding to each parameter set are given in Table 4.4. . . . .	60
4.14. Simulation results for selected parameter sets in comparison with measured final volume fractions of calcite for column experiment D2. The error bars on the experimental values represent the standard deviation of triplicate measurements. The parameter values corresponding to each set of parameters are given in Table 4.4. . . . .	60
5.1. Measured cells for two attachment-experiment replicates with inoculation and 8 hour no-flow period. The total number of attached cells measured in those experiments was used to estimate the initial amount of biomass for the numerical study. . . . .	73
5.2. Comparison of the attachment rate to the other rates influencing the biomass distribution as predicted by the model for the first 80 h of experiment D2 by <i>Hommel et al.</i> (2015b). During the initial cell injection (first 0.5 h, labeled ‘inoculation’) and the following batch period (next 8.0 h, labeled ‘batch’), the attachment rate is high. During the following injections and batch periods the attachment rate is significantly lower. The subsequent time periods are labeled according to the main purpose of the injection: ‘growth’ for calcium-free medium injection and ‘ $Ca^{2+}$ ’ for calcium-rich medium injection. A figure comparing the rates for the entire duration of the simulation is included in Figure C.1. . . .	75

5.3.	Initial distributions of attached biomass investigated in the numerical study. Subfigure (a) on the left visualizes the very high initial biomass for the <i>influent spike</i> in the influent region, while subfigure (b) on the right focuses on the other initial biomass distributions over the total length of the column. . . . .	78
5.4.	Comparison of experimental calcite measurements and the resulting calcite volume fractions using the various initial biomass distributions as defined in Section 5.1.1 and shown in Figure 5.3. The results for the pulsed injection strategy are shown on the left (a) and those for the continuous injection strategy on the right (b). . . . .	81
5.5.	Comparison of the resulting biomass volume fractions using the various initial biomass distributions as defined in Section 5.1.1 and shown in Figure 5.3. The results for the pulsed injection strategy are shown on the left (a) and those for the continuous injection strategy on the right (b). . . . .	82
5.6.	Comparison of the resulting shape coefficients $\sigma$ as given in Table 5.3 for the pulsed and continuous injections at various injection rates (Table 5.1) using the <i>homogeneous</i> (a), the <i>first-order</i> (b), and the <i>inverse first-order</i> (c) initial biomass distribution. The shape coefficients $\sigma$ of the other initial biomass distributions for all the injection strategies are shown in Figure C.15. . . . .	85
5.7.	Comparison of the resulting calcite volume fractions for the various injection strategies (see Table 5.1) using the <i>homogeneous</i> (a) and the <i>first-order</i> (b) initial biomass distribution. . . . .	85
5.8.	Comparison of the resulting biomass volume fractions for the various injection strategies (see Table 5.1) using the <i>homogeneous</i> (a) and the <i>first-order</i> (b) initial biomass distribution. . . . .	86
5.9.	Comparison of the resulting calcite volume fractions for various initial amounts of biomass (high: initial biomass distribution multiplied by 5; intermediate: initial biomass distribution as specified in Section 5.1.1; low: initial biomass distribution divided by 5). The final calcite distribution resulting from the varied initial amount of biomass for the <i>first-order</i> distribution of biomass when using the pulsed injection strategy is shown on the left (a); the results for for the <i>homogeneous</i> initial biomass using the pulsed injection strategy in the middle (b) and for the <i>homogeneous</i> initial biomass distribution using the continuous injection strategy on the right (c). . . . .	88

5.10. Comparison of the resulting biomass volume fraction for various initial amounts of biomass (high: initial biomass distribution multiplied by 5; intermediate: initial biomass distribution as specified in Section 5.1.1; low: initial biomass distribution divided by 5). The final biomass distribution resulting from the varied initial amount of biomass for the <i>first-order</i> distribution of biomass when using the pulsed injection strategy is shown on the left (a); the results for the <i>homogeneous</i> initial biomass using the pulsed injection strategy is shown in the middle (b) and for the <i>homogeneous</i> initial biomass distribution using the continuous injection strategy on the right (c). . . . .	88
5.11. Comparison of the resulting $\text{Ca}^{2+}$ precipitation efficiency $\epsilon$ as given in Table 5.2 for the pulsed and continuous injections at various injection rates (Table 5.1) using the <i>homogeneous</i> (a) and the <i>first-order</i> (b) initial biomass distribution. The $\text{Ca}^{2+}$ precipitation efficiencies of the other initial biomass distributions for all the injection strategies are shown in Figure C.14. . . . .	90
5.12. Comparison of the resulting $\text{Ca}^{2+}$ precipitation efficiency $\epsilon$ for the <i>homogeneous</i> initial biomass distribution for both pulsed and continuous injections when (a) varying the injection rate (see Table 5.1) for the medium initial amount of biomass or (b) varying the initial amount of biomass at medium injection rate. $\epsilon$ of the other initial biomass distributions for all the injection strategies are shown in Figure C.14. . . . .	91
5.13. Comparison of the resulting shape coefficients $\sigma$ for the <i>homogeneous</i> initial biomass distribution for both pulsed and continuous injections when (a) varying the injection rate (see Table 5.1) for the medium initial amount of biomass or (b) varying the initial amount of biomass at medium injection rate. $\sigma$ of the other initial biomass distributions for all the injection strategies are shown in Figure C.15. . . . .	92
5.14. Sketch of the grid for the small and the large scenario and the initial pressure as well as the boundary conditions used ( <i>Shigorina, 2014</i> ). . . . .	94
5.15. Predicted porosity along the fracture layer for the simulations done by <i>Shigorina (2014)</i> and using the parameter set from <i>Hommel et al. (2015b)</i> . Note that in <i>Shigorina (2014)</i> , the injections were erroneously assumed to enter the $22.5^\circ$ simulation domain completely, leading to an 8-fold increased injection rate and total mass of injected components. . . . .	96

5.16. Predicted permeability along the fracture layer for the simulations done by <i>Shigorina</i> (2014) and using the parameter set from <i>Hommel et al.</i> (2015b). The fracture was estimated to extend until 4 m for the large scenario and until 1.6 m for the small scenario. The initial formation permeability is $K_0 = 1.0856 \cdot 10^{-14} \text{ m}^2$ while the initial fracture-layer permeability is $K_{\text{frac}} = 1.645 \cdot 10^{-12} \text{ m}^2$ . Note that in <i>Shigorina</i> (2014), the injections were erroneously assumed to enter the 22.5° simulation domain completely, leading to an 8-fold increased injection rate and total mass of injected components. . . . .	97
6.1. Results of the sequential model for the BR experiment ( <i>Hommel et al.</i> , 2015b) comparing the predicted calcite precipitation with the globally implicit reference simulation. . . . .	108
6.2. Comparison of the results for the sequential model with unlimited macro-time steps to the results with limited time steps and the globally implicit reference simulation. . . . .	109
6.3. Results of the model simplification using the initial biofilm, simple chemistry, and the full complexity model for calcite for the BR experiment ( <i>Hommel et al.</i> , 2015b). . . . .	110
A.1. Grid convergence study for the high pressure core simulation. . . . .	136
B.1. Results of a grid convergence study comparing different grid resolutions. . . .	138
B.2. Comparison of the column C4 experiment results for calcite with predictions of the <i>Ebigbo et al.</i> (2012) model and the revised model. The fit to the data is approximately similar for both models. . . . .	138
B.3. Comparison of the column D1 experiment results for calcite with predictions of the <i>Ebigbo et al.</i> (2012) model and the revised model. The model and parameters determined in this study for D2 provide a better fit to the D1 results than the model and parameters proposed by <i>Ebigbo et al.</i> (2012). . . . .	139
B.4. Comparison of the bicycle rim experiment results for calcite with predictions of the <i>Ebigbo et al.</i> (2012) model and the revised model. The <i>Ebigbo et al.</i> (2012) model overpredicts the amount of calcite precipitated, while the revised model with parameters determined for D2 underestimates it. . . . .	139
B.5. Comparison of experimentally measured pH of column experiment D2 to predictions of the revised model. Outgasing of $\text{CO}_2$ probably increased the measured pH, as the pH measurements were not conducted in-situ, but in samples extracted from the column and exposed to atmospheric conditions prior to pH measurement. . . . .	139

C.1. Comparison of the attachment rate to the other rates influencing the biomass distribution as predicted by the model for column experiment D2 ( <i>Hommel et al.</i> , 2015b). . . . .	150
C.2. Comparison of the reference calcite (a) and biomass (b) distribution (including initial inoculation and attachment according to ( <i>Hommel et al.</i> , 2015b)) with the final calcite (a) and biomass (b) distributions obtained assuming the various initial biomass distributions investigated in this study (Table C.1) for the pulsed injection strategy. . . . .	150
C.3. Comparison of the resulting calcite (a) and biomass (b) distributions for the various initial biomass distributions (Table C.1) and the fast pulsed injection strategy. . . . .	156
C.4. Comparison of the resulting calcite (a) and biomass (b) distributions for the various initial biomass distributions (Table C.1) and the pulsed injection strategy. . . . .	156
C.5. Comparison of the resulting calcite (a) and biomass (b) distributions for the various initial biomass distributions (Table C.1) and the slow pulsed injection strategy. . . . .	156
C.6. Comparison of the resulting calcite (a) and biomass (b) distributions for the various initial biomass distributions (Table C.1) and the fast continuous injection strategy. . . . .	157
C.7. Comparison of the resulting calcite (a) and biomass (b) distributions for the various initial biomass distributions (Table C.1) and the continuous injection strategy. . . . .	157
C.8. Comparison of the resulting calcite (a) and biomass (b) distributions for the various initial biomass distributions (Table C.1) and the slow continuous injection strategy. . . . .	157
C.9. Comparison of the resulting calcite (a) and biomass (b) distributions for the homogeneous initial biomass distribution (Table C.1) and the various injection strategies investigated in this study. . . . .	158
C.10. Comparison of the resulting calcite (a) and biomass (b) distributions for the first-order initial biomass distribution (Table C.1) and the various injection strategies investigated in this study. . . . .	159
C.11. Comparison of the resulting calcite (a) and biomass (b) distributions for the inverse first-order initial biomass distribution (Table C.1) and the various injection strategies investigated in this study. . . . .	159
C.12. Comparison of the resulting calcite (a) and biomass (b) distributions for the “influent spike” initial biomass distribution (Table C.1) and the various injection strategies investigated in this study. . . . .	160

C.13. Comparison of the resulting calcite (a) and biomass (b) distributions for the random initial biomass distribution (Table C.1) and the various injection strategies investigated in this study. . . . .	160
C.14. $\text{Ca}^{2+}$ precipitation efficiencies for all injection strategies and initial biomass distributions. The subfigures compare the precipitation efficiencies for the various injection strategies for one initial biomass distribution: (a) homogeneous, (b) first order, (c) influent spike, (d) inverse first-order, (e) random. Additionally, subfigure (f) compares the effect of varying initial amount of biomass on the $\text{Ca}^{2+}$ precipitation efficiency for the pulsed injection strategy and the homogeneous initial biomass distribution. . . . .	161
C.15. Shape coefficients $\sigma$ for all injection strategies and initial biomass distributions. The subfigures compare $\sigma$ for the various injection strategies for one initial biomass distribution: (a) homogeneous, (b) first order, (c) influent spike, (d) inverse first-order, (e) random. Additionally, subfigure (f) compares the effect of varying initial amount of biomass on $\sigma$ for the pulsed injection strategy and the homogeneous initial biomass distribution. . . . .	161
C.16. Oxygen mass fractions for homogeneous initial biomass distributions over time at $z = 0.10625\text{m}$ distance from the injection for different initial amounts of biomass and injection rates. . . . .	162
C.17. Oxygen mass fractions for homogeneous initial biomass distributions over time at $z = 0.5075\text{m}$ distance from the injection for different initial amounts of biomass and injection rates. . . . .	162
D.1. Biofilm distribution for the simulations done by <i>Shigorina</i> (2014) and using the parameter set from <i>Hommel et al.</i> (2015b). Note that in <i>Shigorina</i> (2014), the injections were erroneously assumed to enter the $22.5^\circ$ simulation domain completely, leading to an 8-fold increased injection rate and total mass of injected components. . . . .	165
D.2. Precipitated calcite for the simulations done by <i>Shigorina</i> (2014) and using the parameter set from <i>Hommel et al.</i> (2015b). Note that in <i>Shigorina</i> (2014), the injections were erroneously assumed to enter the $22.5^\circ$ simulation domain completely, leading to an 8-fold increased injection rate and total mass of injected components. . . . .	165



# List of Tables

4.1.	Differences between experiments used for validation of the model (sand columns C1 and C2, <i>Ebigbo et al. (2012)</i> ) and the experimental setup (high-pressure sandstone core (HP) <i>Phillips (2013)</i> ) considered in this investigation. . . . .	34
4.2.	Comparison of simulated and measured volume fractions of calcite, average volume fraction of biofilm, average porosity and mean permeability at the end of the experiment. The experimental volume fraction of biofilm is calculated as $\phi_f = \phi_0 - \phi - \phi_c$ , using Equation (3.32). . . . .	36
4.3.	Porosity-permeability relations proposed to account for the permeability reduction caused by changes in porosity related to mineral precipitation and dissolution (top), biomass accumulation only (middle), and combined biofilm growth and mineral precipitation (bottom). . . . .	40
4.4.	Selected parameter sets obtained by inverse modeling of column experiment D2 data, used for the plots in Figures 4.12, 4.13, and 4.14. . . . .	53
4.5.	Parameter and data sensitivities for the parameter sets given in Table 4.4 and direct correlations for the fitted parameters of the “best fit” as given by iTOUGH2. . . . .	54
4.6.	Comparison of revised, refitted, and other parameter values used to the values given in <i>Ebigbo et al. (2012)</i> . . . . .	65
4.7.	Focal points to improve the conceptual understanding of MICP by targeted experiments and numerical investigations as identified in this study. . . . .	68
5.1.	Injection strategies investigated in this study. The reference values $Q_{\text{ref}}$ and $t_{\text{ref}}$ are based on the experiment D2 from <i>Hommel et al. (2015b)</i> . The time $t_{\text{ref}}$ is the duration of the experiment D2 without the initial inoculation and the first batch period (Figure 5.2). Also, the time of the batch periods is not reduced; only the time of the injection periods is adapted to conserve the total amount of injected components. . . . .	79

5.2. Impact of the initial biomass distribution, representing different attachment mechanisms, on the precipitation efficiency $\epsilon$ of $\text{Ca}^{2+}$ (sum of precipitated $\text{Ca}^{2+}$ normalized by the amount of injected $\text{Ca}^{2+}$ ) as predicted by the numerical model for the various injection strategies. . . . .	83
5.3. Impact of the initial biomass distribution, representing different attachment mechanisms, on the shape coefficient $\sigma$ of the calcite distribution, quantified as the ratio of the influent region calcite (at $z = 0.10625$ m) to the effluent region calcite (at $z = 0.5075$ m). . . . .	83
5.4. Impact of the initial amount of biomass on the precipitation efficiency of $\text{Ca}^{2+}$ $\epsilon$ (sum of precipitated $\text{Ca}^{2+}$ normalized by the amount of injected $\text{Ca}^{2+}$ ) and the shape coefficient $\sigma$ of the distribution of calcite quantified as the ratio of the influent region calcite (at $z = 0.10625$ m) to the effluent region calcite (at $z = 0.5075$ m) as predicted by the numerical model for the pulsed and continuous injection strategy and <i>first-order</i> and <i>homogeneous</i> initial biomass distribution. . . . .	87
5.5. Main characteristic parameters of the injection strategies investigated for the field application. The complete injection strategies are given in the Appendix, Tables D.2-D.4. . . . .	95
5.6. Computational and simulation time for the investigated injection strategies and scenarios. Additionally, the number of $\text{Ca}^{2+}$ -rich injections until the assumed plugging and the mass of $\text{Ca}^{2+}$ injected until plugging are given, together with the precipitation efficiency defined in Section 5.1.2, Equation (5.2): $\text{Ca}_{\text{precipitated}}^{2+}/\text{Ca}_{\text{injected}}^{2+}$ . The mass of $\text{Ca}^{2+}$ injected here is not the total mass of $\text{Ca}^{2+}$ planned to be injected (see Table D.1), but the mass of $\text{Ca}^{2+}$ injected until the model predicts plugging and the simulation is terminated*. The top part gives the values for the simulations done by <i>Shigorina</i> (2014), the bottom part the values for simulations using the parameter set “best fit” from <i>Hommel et al.</i> (2015b) and the corrected injection rate. The field test was terminated after 24 $\text{Ca}^{2+}$ -rich injections, 74.3 hours after starting the first injection. . . . .	98
6.1. Numerical parameters for various combinations of the coupling error $CE$ for the time-step management of the coupling between transport and reaction calculations and convergence criteria of the Newton solver $N$ of the transport subproblem. For comparison, the computational time (CT) of the GIA model with $N = 1 \cdot 10^{-6}$ is 32110 s, see Table 6.2. . . . .	109

6.2.	Numerical parameters and the error compared with the reference solution of the different models (FC, IB, and SC). CT is the computational time, NLIT is the number of non-linear (Newton) iterations needed, LIT is the number of linear iterations needed, and $E$ is the error defined in Equation (6.7). $E_{FC,8}$ is the error defined in Equation (6.7) using the FC model with a strict Newton convergence criterion ( $N = 1 \cdot 10^{-8}$ ) but unlimited time-step size and non-refined grid as a reference solution. For comparison, the estimated error for neglecting the effect of a heterogeneous permeability distribution in the porous medium is $E_{\text{comp}} = 0.0033$ . . . . .	111
6.3.	Numerical parameters and the error compared with the reference solution of the different models (FC, IB, and SC) for different convergence criteria of the Newton solver (Eq. (6.8)). The values for $N = 1 \cdot 10^{-6}$ are already given in Table 6.2. $E_{FC,8}$ is the error defined in Equation (6.7) using the FC model with a strict Newton convergence criterion ( $N = 1 \cdot 10^{-8}$ ) but unlimited time-step size and non-refined grid as a reference solution. For comparison, the estimated error for neglecting the effect of a heterogeneous permeability distribution in the porous medium is $E_{\text{comp}} = 0.0033$ . . . . .	112
A.1.	Porosity and corrected, porous-medium-only pressure difference $\Delta p_{\text{corr}}$ measured in the micro model experiment as well as the permeability calculated from the pressure difference. The injection rate is 1 ml/h, the cross sectional area 605291 $\mu\text{m}^2$ , the viscosity 0.72 Pas (at 37°C), the porous medium length 9729 $\mu\text{m}$ . For each porosity measurement, the permeability is calculated using the averaged $\Delta p_{\text{corr}}$ of the duration of taking the microscopy image. The tubing and non-porous region pressure difference is assumed to be constant and estimated to be 17.2 Pa. . . . .	136
B.1.	Experimental parameters of the experiments used in inverse modeling. Values of column C4 are taken from <i>Ebigbo et al.</i> (2012). The given concentrations are in the units of g/l, except for <i>S. pasteurii</i> . . . . .	140
B.2.	Injected fluid composition for the experiments used in inverse modeling. The given concentrations are in the units of g/l, except for <i>S. pasteurii</i> . . . . .	140

B.3.	Measured final volume fractions of calcite at given distance (Columns) or radius (Bicycle Rim) used as observations in inverse modeling. Values of C4 are taken from <i>Ebigbo et al. (2012)</i> . The values given here are the averages of triplicate measurements at each measurement location. For column D1 and D2, interpolated values are tabulated at locations that match the nearest grid point. These values were obtained through linear interpolation between the two surrounding measurements. The distance between measurement location and the nearest grid node was never greater than 1 cm. The experimental data presented here is also used in the Figures 4.14, B.2, B.3, and B.4. . . . .	141
B.4.	Measured concentrations of ammonium [mol/l] for column experiment D1 used as observations in inverse modeling. . . . .	142
B.5.	Measured concentrations of calcium [mol/l] for column experiment D1 used as observations in inverse modeling. . . . .	143
B.6.	Measured concentrations of ammonium [mol/l] for column experiment D2 used as observations in inverse modeling. The measurements at 20 cm distance from the inlet are used in Figure 4.13. . . . .	144
B.7.	Measured concentrations of calcium [mol/l] for column experiment D2 used as observations in inverse modeling. The measurements at 20 cm distance from the inlet are used in Figure 4.12. . . . .	145
B.8.	Sum of squared residuals and normalized squared residuals of model predictions for the data sets $\text{NH}_4^+$ , $\text{Ca}^{2+}$ , and $\text{CaCO}_3$ . The squared residuals are summed over the 7 measurement pulses with each 6 measurements at the 5 locations for data sets $\text{NH}_4^+$ (total of 419 measurements; See Table B.6) and $\text{Ca}^{2+}$ (total of 418 measurements; See Table B.7) and the 8 measurements along the column length for $\text{CaCO}_3$ (See Table B.3). The values presented here are for the selected parameter sets from Table 2 using the revised model and the parameters and equations as given in <i>Ebigbo et al. (2012)</i> . . . . .	146
C.1.	Values of the initial biomass volume fraction $\phi_{f,0}$ for all distributions investigated as well as the random numbers between 0 and 2 used to generate the random initial biomass distribution. . . . .	153
C.2.	Impact of the initial biomass distribution, representing different attachment mechanisms, on the shape of the distribution of calcite measured by the shape coefficient $\sigma_{5\text{ cm}}$ quantified as the ratio of the influent region calcite (at $z = 0.05$ m) to the effluent region calcite (at $z = 0.5075$ m). Thus high values indicate that the calcite distribution decreases with distance from the influent, while values close to 1 indicate evenly distributed calcite and values smaller than 1 indicate that the calcite is increasing with distance. . . . .	158

D.1. Comparison of the preliminarily estimated parameters as used in <i>Shigorina</i> (2014) to the final parameters determined by <i>Hommel et al.</i> (2015b). All model parameters, which are not given here, are identical to the parameters in <i>Hommel et al.</i> (2015b), see Table 4.6. The scenario setup parameters deviating from those given in Table 4.6 are given in the second part of the table. . . . .	164
D.2. Injection scheme for the <i>simple</i> injection strategy. The injection rate is constant for all injections $Q = 1.0515 \cdot 10^{-5} \text{m}^3/\text{s}$ . . . . .	164
D.3. Injection scheme for the <i>ideal</i> injection strategy. . . . .	166
D.4. Injection scheme for the <i>real</i> injection strategy. . . . .	168



# Notation

The following table shows the most significant symbols and their definitions used in this thesis. Local notations are explained in the text where they are used.

Symbol	Definition	Dimension
<b>Greek letters:</b>		
$\alpha_l$	longitudinal dispersivity	[-]
$\alpha_t$	transverse dispersivity	[-]
$\gamma^\kappa$	activity coefficient of component $\kappa$	[-]
$\epsilon$	precipitation efficiency	[-]
$\lambda$	Brooks-Corey parameter, pore size distribution	[-]
$\mu$	dynamic fluid viscosity	[kg/ms]
$\mu_\alpha$	dynamic fluid viscosity of phase $\alpha$	[kg/ms]
$\mu_g$	specific growth rate of biomass	[1/s]
$\rho$	mass density	[kg/m <sup>3</sup> ]
$\rho_\alpha$	mass density of phase $\alpha$	[kg/m <sup>3</sup> ]
$\rho_\lambda$	mass density of solid phase $\lambda$	[kg/m <sup>3</sup> ]
$\rho_{\text{mol}}$	molar density	[mol/m <sup>3</sup> ]
$\rho_{\text{mol},\alpha}$	molar density of phase $\alpha$	[mol/m <sup>3</sup> ]
$\rho_{\text{mol},\lambda}$	molar density of solid phase $\lambda$	[mol/m <sup>3</sup> ]
$\sigma$	calcite precipitation shape coefficient	[-]
$\phi$	porosity	[-]
$\phi_0$	initial porosity	[-]
$\phi_\lambda$	solid phase volume fraction	[-]
$\phi_{\text{crit}}$	critical porosity, at which $\mathbf{K} = 0$	[-]
$\tau_\alpha$	tortuosity of phase $\alpha$	[-]
$\Omega$	calcite saturation index	[-]

Symbol	Definition	Dimension
<b>Latin letters:</b>		
$A_{cw}$	surface area of calcite	$[\text{m}^2/\text{m}^3]$
$A_{sw}$	interfacial area between solids and the water phase	$[\text{m}^2/\text{m}^3]$
$A_{sw,0}$	initial interfacial area between solids and the water phase	$[\text{m}^2/\text{m}^3]$
$a_c$	specific surface area of calcite	$[\text{m}^2/\text{m}^3]$
$b_0$	decay coefficient for biomass	$[1/\text{s}]$
$C_\alpha^\kappa$	mass concentration of component $\kappa$ in phase $\alpha$	$[\text{kg}/\text{m}^3]$
$c_{a,1}$	attachment coefficient for preferential attachment to biomass	$[1/\text{s}]$
$c_{a,2}$	attachment coefficient for attachment to arbitrary surfaces	$[1/\text{s}]$
$c_d$	detachment coefficient	$[1/\text{s}]$
$D_\alpha^\kappa$	molecular diffusion coefficient of component $\kappa$ in phase $\alpha$	$[\text{m}^2/\text{s}]$
$D_{pm,\alpha}^\kappa$	effective porous medium diffusion coefficient of component $\kappa$ in phase $\alpha$	$[\text{m}^2/\text{s}]$
$\mathbf{D}_{pm,\alpha}^\kappa$	porous medium dispersion tensor of component $\kappa$ in phase $\alpha$	$[\text{m}^2/\text{s}]$
$F$	oxygen consumed per substrate consumed	$[-]$
$\mathbf{g}$	gravitational acceleration vector	$[\text{m}/\text{s}^2]$
$K$	intrinsic permeability	$[\text{m}^2]$
$\mathbf{K}$	intrinsic permeability tensor	$[\text{m}^2]$
$K_0$	initial intrinsic permeability	$[\text{m}^2]$
$K_{eu,1}$	constant for urease inactivation due to low pH	$[\text{mol}/\text{kg}_{\text{H}_2\text{O}}]$
$K_{eu,2}$	constant for urease inactivation due to high pH	$[\text{mol}/\text{kg}_{\text{H}_2\text{O}}]$
$K_{\text{NH}_4^+}$	constant for the inhibition of ureolysis due to $\text{NH}_4^+$	$[\text{mol}/\text{kg}_{\text{H}_2\text{O}}]$
$K_{\text{O}_2}$	Monod kinetics half-saturation constant for oxygen	$[\text{kg}/\text{m}^3]$
$K_{\text{pH}}$	constant for the decay of suspended biomass due to non-optimal pH	$[\text{mol}^2/\text{kg}_{\text{H}_2\text{O}}^2]$
$K_s$	Monod kinetics half-saturation constant for substrate	$[\text{kg}/\text{m}^3]$
$K_{sp}$	solubility product of calcite	$[\text{mol}^2/\text{kg}_{\text{H}_2\text{O}}^2]$
$K_u$	half-saturation constant for urea for the ureolysis rate	$[\text{mol}/\text{kg}_{\text{H}_2\text{O}}]$
$K_{u,\text{old}}$	previous half-saturation constant for urea for the ureolysis rate	$[\text{mol}/\text{kg}_{\text{H}_2\text{O}}]$
$k_\mu$	specific growth rate for biomass	$[1/\text{s}]$
$k_{\mu,\text{old}}$	previous specific growth rate for biomass	$[1/\text{s}]$
$k_a$	attachment rate constant for biomass	$[1/\text{s}]$
$k_b^b$	decay rate constant for suspended biomass	$[1/\text{s}]$
$k_b^f$	precipitation rate constant for biofilm	$[1/\text{s}]$
$k_d$	detachment rate constant for biomass	$[1/\text{s}]$

Symbol	Definition	Dimension
$k_{\text{diss},1}$	dissolution rate constant for calcite	$[\text{kg}_{\text{H}_2\text{O}}/\text{m}^2\text{s}]$
$k_{\text{diss},2}$	dissolution rate constant for calcite	$[\text{mol}/\text{m}^2\text{s}]$
$k_{\text{prec}}$	precipitation rate constant for calcite	$[\text{mol}/\text{m}^2\text{s}]$
$k_{\text{r},\alpha}$	relative permeability for phase $\alpha$	$[-]$
$k_{\text{ub}}$	enzyme content of biomass	$[\text{kg}/\text{kg}]$
$k_{\text{ub,old}}$	previous enzyme content of biomass	$[\text{kg}/\text{kg}]$
$k_{\text{urease}}$	urease enzyme activity	$[\text{mol}/\text{kg}\text{s}]$
$k_{\text{urease,old}}$	previous urease enzyme activity	$[\text{mol}/\text{kg}\text{s}]$
$M^\kappa$	molar mass of component $\kappa$	$[\text{kg}/\text{mol}]$
$M^\lambda$	molar mass of solid phase $\lambda$	$[\text{kg}/\text{mol}]$
$m$	molality	$[\text{mol}/\text{kg}_{\text{H}_2\text{O}}]$
$m^\kappa$	molality of component $\kappa$	$[\text{mol}/\text{kg}_{\text{H}_2\text{O}}]$
$n_\alpha^\kappa$	number of moles of component $\kappa$ in phase $\alpha$	$[-]$
$\mathbf{n}$	normal vector	$[-]$
$n_{\text{diss}}$	exponent for the dissolution rate of calcite	$[-]$
$n_{\text{prec}}$	exponent for the precipitation rate of calcite	$[-]$
$n_{\text{ub}}$	exponent for the non-linear relation of $Z_{\text{ub}}$ to biomass	$[-]$
$p_\alpha$	pressure of phase $\alpha$	$[\text{Pa}]$
$p_c$	capillary pressure	$[\text{Pa}]$
$p_d$	Brooks-Corey parameter, entry pressure	$[\text{Pa}]$
$q^\kappa$	source or sink term for component $\kappa$	$[\text{mol}/\text{m}^3\text{s}]$
$q^\lambda$	source or sink term for solid phase $\lambda$	$[\text{mol}/\text{m}^3\text{s}]$
$r_a$	attachment rate of biomass	$[\text{kg}/\text{m}^3\text{s}]$
$r_b^b$	decay rate of suspended biomass	$[\text{kg}/\text{m}^3\text{s}]$
$r_b^f$	decay rate of biofilm	$[\text{kg}/\text{m}^3\text{s}]$
$r_d$	detachment rate of biomass	$[\text{kg}/\text{m}^3\text{s}]$
$r_{\text{diss}}$	dissolution rate of calcite	$[\text{mol}/\text{m}^3\text{s}]$
$r_g^b$	growth rate of suspended biomass	$[\text{kg}/\text{m}^3\text{s}]$
$r_g^f$	growth rate of biofilm	$[\text{kg}/\text{m}^3\text{s}]$
$r_{\text{prec}}$	precipitation rate of calcite	$[\text{mol}/\text{m}^3\text{s}]$
$r_{\text{urea}}$	ureolysis rate	$[\text{mol}/\text{m}^3\text{s}]$
$r_{\text{urea,old}}$	previous ureolysis rate	$[\text{mol}/\text{m}^3\text{s}]$
$S_\alpha$	saturation of phase $\alpha$	$[-]$
$S_e$	effective saturation	$[-]$
$T$	temperature	$[\text{K } (^\circ\text{C})]$
$t$	time	$[\text{s}]$

Symbol	Definition	Dimension
$\mathbf{v}$	Darcy velocity	[m/s]
$\mathbf{v}_\alpha$	Darcy velocity of phase $\alpha$	[m/s]
$\mathbf{v}_{e,\alpha}$	effective velocity of phase $\alpha$	[m/s]
$X_\alpha^\kappa$	mass fraction of component $\kappa$ in phase $\alpha$	[-]
$x_\alpha^\kappa$	mole fraction of component $\kappa$ in phase $\alpha$	[-]
$X_{\text{sal}}$	mass fraction of the salinity	[-]
$Y$	yield of biomass per mass of substrate consumed	[-]
$z^\kappa$	charge of component $\kappa$	[-]
$Z_{\text{ub}}$	urease concentration	[kg/m <sup>3</sup> ]

### Superscripts

### Subscripts

$\kappa$	component	$\alpha$	fluid phase
b	suspended biomass	$\lambda$	solid phase
Ca, Ca <sup>2+</sup>	calcium	c	calcite
Cl, Cl <sup>-</sup>	chloride	f	biofilm
C <sub>tot</sub>	total inorganic carbon	n	non-wetting fluid phase
CO <sub>3</sub> <sup>2-</sup>	carbonate	w	wetting fluid phase
H <sup>+</sup>	hydrogen cation		
HCO <sub>3</sub> <sup>-</sup>	bicarbonate		
Na, Na <sup>+</sup>	sodium		
N <sub>tot</sub>	total ammonia and ammonium		
NH <sub>4</sub> <sup>+</sup>	ammonium		
O <sub>2</sub>	oxygen		
OH <sup>-</sup>	hydroxide ion		
s	substrate		
u	urea		
w	water		

# Abstract

Microorganisms influencing geochemical processes are ubiquitous in the subsurface. The processes and interactions of microbial activity and geochemical processes are called biogeochemistry. Biogeochemical processes are at the focus of research because of their impact on environmental and technical systems. For engineering applications, it is crucial to be able to understand the behavior of a system and to predict its response to an engineering measure. The complex nature of biogeochemical processes often requires the use of numerical models to analyze the individual interactions of the sub-processes involved and to predict the response of the biogeochemical system to a change in the system conditions. In this thesis, the biogeochemical process of interest is microbially induced calcite precipitation (MICP) used as a leakage mitigation technology.

MICP reduces the porosity and the permeability of a porous medium by the accumulation of biomass and, more importantly, by the precipitation of calcite. It can be used to create subsurface barriers for flow, for example in damaged cap rock in the vicinity of injection or extraction wells in gas storage reservoirs in order to increase storage security or in a groundwater aquifer to confine a contamination plume. For such applications, it is important to be able to predict the amount of reactants such as calcium, urea, and biomass to be injected as well as the resulting reduction of porosity and permeability. The purpose of this thesis is to provide the necessary numerical model to answer such application-relevant questions. This is done by improving a numerical model for MICP developed previously, applying the model to support the design of laboratory experiments and a field application showing the capabilities of the model and the benefits of using it. Further, this thesis identifies possible measures for improving its computational efficiency, facilitating the practical use of the model to guide decision-making in the field.

The model improvement focuses on the driving force of MICP, the microbially catalyzed ureolysis that induces the precipitation of calcite, and the resulting reduction of the permeability. The model's permeability predictions are compared to experimental measurements and the porosity-permeability relation is calibrated. The porosity-permeability relation is able to predict the reduction of permeability satisfactorily well for reductions due to calcite precipitation, but the initial reduction of permeability due to the inoculation of the porous medium is

not matched. An improved porosity-permeability relation is developed using porosity and permeability measurements of a micro-model experiment. This improved porosity-permeability relation leads to more realistic model predictions of the permeability reduction. The description of ureolysis in the model is improved by implementing a species-specific rate equation for ureolysis which is based on the kinetics of living cells of the bacterium *Sporosarcina pasteurii*, commonly used for MICP. This improved the model since the rate equation implemented previously was based on the kinetics of pure enzyme extracted from jack beans *Canavalia ensiformis*. The updated model is recalibrated by inverse modeling to measurements of several experiments, including two new column experiments with spatially and temporally resolved measurements of calcium and ammonium, which the previous model did not match. The improved model is able to match the results of both the new and the old column experiments.

The improved model is applied to a field-scale test of MICP and to the investigation of the influence of the initial amount and distribution of biomass on the resulting MICP for column experiments. Additionally, the influence is compared with the effect of various injection strategies. The results of this investigation show that, for all injection strategies, the effect of the injection strategy on the amount of precipitated calcite is much stronger than the effect of the initial amount and distribution of biomass, except for very extreme distributions. Only for one of the continuous injection strategies is the distribution of the calcite precipitates dependent on the initial distribution of biomass. For all other injection strategies, the resulting calcite distributions are similar for all initial biomass distributions, again with the exception of very extreme initial biomass distributions, which have no biomass at some locations. Due to the limitations of the study, attachment is neglected, such locations without initial biomass stay free of biomass throughout the simulation and only little calcite precipitates at such locations. The model is further applied to predict the outcome of a field-scale application of MICP. Two hypothetical injection strategies are modeled before the field test and after the field test, the actual injection strategy used in the field is modeled as well. One of the challenges in modeling field applications of MICP is the scarcity of data. Important parameters such as porosity and permeability or geometry information are in general only available as uncertain estimates. Despite these uncertainties, modeling is a useful tool during the planning and the evaluation of a field application of MICP.

Another aspect of the thesis is concerned with the computational efficiency of the model. Especially for 3D field-scale simulations, the computational time quickly becomes prohibitively long. This restricts the use of the model to only few simulations of selected representative scenarios. For a practical use of the model to guide decision-making in the field, the computational time has to be reduced. Various methods are available for reducing the computational effort, mainly sophisticated numerical solution schemes, model simplifications and other measures that reduce

the necessary calculations. Model simplifications are an engineering approach balancing the error introduced by a simplification with the error introduced by other model assumptions or incomplete knowledge and with the possible reduction of computational time. In contrast to optimized solution schemes, the applicability of such simplified models is dependent on the setup and therefore has to be evaluated for each application separately. The exemplary simplifications investigated are an initial biofilm model, neglecting the transport and attachment of suspended biomass, and a simple chemistry model, neglecting complex chemical calculations. Other ways of reducing the computational time investigated are increased time-step sizes. Both with the simple chemistry model and with increased time-step sizes, the computational time can be decreased significantly. For the setup investigated, reductions of up to an order of magnitude are achieved, but further alternatives to reduce the computational time remain to be tested.



# Zusammenfassung

Mikroorganismen sind im Untergrund allgegenwärtig und beeinflussen geochemische Prozesse. Diese Interaktion von mikrobieller Aktivität und geochemischen Prozessen wird als Biogeochemie bezeichnet. Wegen ihres großen Einflusses in natürlichen und technischen Systemen sind biogeochemische Prozesse Gegenstand intensiver Forschung. Das Verhalten eines Systems zu verstehen und die korrekte Vorhersage der Auswirkungen einer technischen Maßnahme auf das System sind grundlegend für technische Anwendungen. Die Komplexität biogeochemischer Prozesse erfordert oft die Nutzung numerischer Modelle, um individuelle Interaktionen der beteiligten Teilprozesse zu analysieren und die Reaktion eines biogeochemischen Systems auf eine Änderung der Systembedingungen vorherzusagen. Das in dieser Arbeit untersuchte biogeochemische System ist mikrobiell induzierte Kalzitausfällung (MICP), insbesondere die Nutzung von MICP um Leckagen zu vermindern.

Die Porosität und die Permeabilität eines porösen Mediums werden bei MICP durch die Ansammlung Biomasse und, weitaus wichtiger, die Ausfällung von Kalzit reduziert. Mit MICP kann die Durchströmung des Untergrunds vermindert werden, z.B. zur Erhöhung der Speichersicherheit in der Deckschicht eines Gasspeicherreservoirs in der Umgebung von Injektions- oder Extraktionsbrunnen oder um in einem Grundwasseraquifer eine Schadstofffahne einzudämmen. Für solche Anwendungen ist es wichtig, die resultierende Porositäts- und Permeabilitätsreduktion sowie die dafür benötigte Menge an zu injizierenden Reagenzien wie Kalzium, Harnstoff und Biomasse vorherzusagen. Das Ziel dieser Arbeit ist es, das für die Beantwortung solcher anwendungsbezogener Fragestellungen benötigte numerische Modell bereitzustellen. Um dieses Ziel zu erreichen, wird zunächst ein bestehendes Modell für MICP weiterentwickelt. Das Modell wird daraufhin angewandt um die Planung von Laborexperimenten und einer Anwendungen zu unterstützen, was die Fähigkeiten des Modells und die Vorteile seiner Verwendung aufzeigt. Zudem werden in dieser Arbeit mögliche Maßnahmen zur Verringerung der Rechenzeiten des Modells identifiziert, um eine praktische Nutzung des Modells zur Unterstützung der Planung von Anwendungen zu erleichtern.

Die Verbesserung des Modells konzentriert sich auf die treibende Kraft von MICP, die mikrobiell katalysierte Harnstoffhydrolyse, die die Ausfällung von Kalzit induziert, und die resultierende Permeabilitätsreduktion. Die Modelvorhersagen der Permeabilität werden

mit experimentellen Messwerten verglichen und die Beziehung von Porosität und Permeabilität kalibriert. Während die verwendete Beziehung von Porosität und Permeabilität die Permeabilitätsreduktion aufgrund der Kalzitausfällung zufriedenstellend beschreibt, kann sie die initiale Reduktion durch die Inokulation des porösen Mediums nicht reproduzieren. Anhand von in Mikromodellexperimenten gemessener Porosität und Permeabilität wird eine verbesserte Beziehung von Porosität und Permeabilität entwickelt. Diese verbesserte Beziehung führt zu realistischeren Permeabilitätsreduktionvorhersagen. Implementierung einer artspezifischen Reaktionsrate für die Harnstoffhydrolyse für lebende Zellen von *Sporosarcina pasteurii*, welche üblicherweise für MICP verwendet werden, verbesserte zusätzlich das Modell, da die bisher implementierte Reaktionsrate auf der Kinetik der Harnstoffhydrolyse durch purem, aus Jackbohnen *Canavalia ensiformis* extrahiertem Enzym basierte. Das verbesserte Modell wird durch inverse Modellierung unter der Benutzung von Messdaten aus mehreren Experimenten neu kalibriert. Diese beinhalten auch Messdaten aus zwei neuen Säulenexperimenten mit räumlich und zeitlich aufgelösten Messungen von Kalzium und Ammonium, die das bisherige Modell nicht vorhersagen konnte. Sowohl diese neuen als auch die alten Säulenexperimente können vom verbesserten Modell vorhergesagt werden.

Anwendungsbeispiele sind ein MICP Feldversuch und eine Untersuchung des Einfluss der initialen Menge und Verteilung von Biomasse auf MICP in Säulenexperimenten. Dieser Einfluss wird zusätzlich noch mit dem Effekt verschiedener Injektionsstrategien verglichen. Die Ergebnisse dieser Untersuchung zeigen, dass der Effekt der Injektionsstrategie die Effekte der initialen Menge und Verteilung von Biomasse auf die Menge an ausgefälltem Kalzit deutlich überwiegen, außer für sehr extreme Biomasseverteilungen. Nur für eine der kontinuierlichen Injektionsstrategien ist die Verteilung von Kalzit abhängig von der initialen Biomasseverteilung. Für alle anderen Injektionsstrategien ist die Verteilung von Kalzit für die verschiedenen initialen Biomasseverteilung ähnlich, wieder ausgenommen sehr extreme Biomasseverteilungen, für die an manchen Stellen anfangs keine Biomasse vorhanden ist. Aufgrund der Limitierung der Untersuchung, die Anlagerung von Biomasse wird vernachlässigt, bleiben diese Stellen in der Simulation weiterhin frei von Biomasse weswegen dort nur wenig Kalzit ausfällt. Zusätzlich wird das Modell angewandt um das Ergebnis eines Feldversuchs vorauszusagen. Dafür werden zwei hypothetische Injektionsstrategien vor dem Feldversuch simuliert und nach dem Feldversuch wird die die Simulation mit der verwendeten Injektionsstrategie wiederholt. Der Mangel an Daten ist eine der Herausforderungen der Modellierung von realen Anwendungen von MICP. Wichtige Parameter wie Porosität und Permeabilität oder geometrische Informationen sind meist nur unsichere Schätzwerte. Trotz dieser Unsicherheiten ist Modellierung ein nützliches Werkzeug in der Planung und Auswertung technischer MICP Anwendungen.

Die rechnerische Effizienz des Modells ist ein weiterer Aspekt dieser Arbeit. Besonders bei

3D Simulationen im technischen Maßstab wird die Rechenzeit leicht sehr lang und verhindert dadurch die Verwendung des Modells für mehr als wenige, ausgewählte repräsentative Szenarien. Für eine praktische Verwendung des Modells zur Unterstützung der Planung von realen Anwendungen muss die Rechenzeit verringert werden. Zur Reduktion der Rechenzeit sind verschiedene Methoden verfügbar, vor allem die Nutzung ausgeklügelter numerischer Lösungsschemata, Modellvereinfachungen und andere Maßnahmen, welche die nötigen Berechnungen verringern. Modellvereinfachungen sind ein Ingenieursansatz, der den Fehler durch die Modellvereinfachung mit dem Fehler durch andere Annahmen oder unvollständigem Wissen und der möglichen Verringerung der Rechenzeit abwägt. Im Gegensatz zu optimierten Lösungsschemata ist die Anwendbarkeit solcher vereinfachter Modelle von den Gegebenheiten abhängig und muss deswegen stets überprüft werden. Beispielhaft untersucht werden als Vereinfachungen ein Modell mit initialem Biofilm, welches den Transport und die Anlagerung von suspendierter Biomasse vernachlässigt, und ein Modell mit vereinfachter Chemie, welches die komplexen chemischen Berechnungen vernachlässigt. Von den weiteren Möglichkeiten die Rechenzeit zu reduzieren, werden vergrößerte Zeitschrittweiten untersucht. Sowohl das Modell mit vereinfachter Chemie als auch mit vergrößerten Zeitschrittweiten reduziert sich die Rechenzeit erheblich. Für die untersuchten Bedingungen werden Reduktionen bis zu einer Größenordnung erreicht, aber weitere Möglichkeiten die Rechenzeit zu reduzieren müssen noch untersucht werden.



# 1. Introduction

This thesis reports recent advances in the modeling of biogeochemical and transport processes in the subsurface, the primary focus being the microbially induced calcite precipitation in pore spaces or other preferential flow pathways. Biogeochemical processes typically involve chemical cycles which are either driven by or have an impact on the activity of subsurface microorganisms (microbes).

## 1.1. Microbes in the subsurface

Microbes are ubiquitous in the environment, including the subsurface. Although microbes are most abundant in the shallow subsurface, even at a depth of several hundred meters, the number of, for example, bacterial cells per gram of soil is often only one to two orders of magnitude lower than in the surface soil, e.g. the values given in *Hazen et al.* (1991), averaged over the three different locations, are  $3.8 \cdot 10^8$  cells per gram of surface soil and  $1.9 \cdot 10^7$  cells per gram of a sedimentary formation at a depth of 169 to 296 m. The limiting factor for the survival of microbes at great depths is either the lack of appropriate energy sources, the water content, or increasing temperature (*Pedersen, 1993*).  $110^\circ\text{C}$  is a commonly accepted limit for microbial life (*Stetter et al., 1990*); thus, considering the geothermal gradient, microbial life can reach as deep as several kilometers below surface. Some hints suggest that hyperthermophile microbes might tolerate even higher temperatures (*Amend and Teske, 2005*). In some cases, very low permeability or small pore-size zones which do not allow cells to pass might additionally prevent the colonization of regions below these zones, before the temperature or other limits are reached (*Amend and Teske, 2005*). The metabolism of these microbes influences the geochemical processes occurring in the subsurface (*Lovley and Chapelle, 1995*). The combined interaction of microbial metabolism and geochemical processes is called biogeochemistry.

## 1.2. Biogeochemical processes

In the subsurface, biotechnologies involving biogeochemical processes have already been developed or are currently in the focus of research. Many of these measures aim at controlling biogeochemical processes in order to manipulate them in a favorable way. Some examples are:

- bioremediation of soils by microbial decomposition of organic pollutants (e.g. *Juhasz and Naidu, 2000; Samanta et al., 2002; Bamforth and Singleton, 2005; Hunkeler et al., 1999; Ron and Rosenberg, 2002; Mulligan, 2005*) or by mobilization (for example through acidification, redox transformation, complexation, or methylation) and treatment of adsorbed or chemically bound metal ions (e.g. *Gadd, 2000, 2004*) or immobilization of dissolved heavy metal ions and thus removal from the aqueous solution (by precipitation due to biogenic production of carbonate, oxalate, or phosphate, redox transformation, biosorption, or intracellular accumulation) (e.g. *Gadd, 2000, 2004; Rhee et al., 2012*);
- enhanced recovery of resources as in microbially enhanced oil recovery (MEOR) (e.g. *Bachmann et al., 2014; Huang et al., 2014; Sen, 2008; Lazar et al., 2007; Youssef et al., 2007*), microbially enhanced coal bed methane (MECBM) (e.g. *Ritter et al., 2015; Hamilton et al., 2015; Jones et al., 2010*), and microbial leaching of metal ores (e.g. *Pradhan et al., 2008; Watling, 2006; Rohwerder et al., 2003*);
- blocking of preferential flow paths by the accumulation of biomass or minerals precipitated as a result of the microbial metabolism, e.g. high-permeability zones in an oil reservoir during MEOR (e.g. *Huang et al., 2014; Sen, 2008; Lazar et al., 2007; Raiders et al., 1989*) or targeted sealing of reservoir cap rocks to reduce possible leakage pathways (e.g. *Phillips et al., 2013b; Mitchell et al., 2013; Phillips et al., 2013a*);
- increasing the mechanical strength of the subsurface medium by microbially induced mineral precipitation, e.g. to fortify dikes and stabilize loose-soil building grounds (e.g. *van Wijngaarden et al., 2011; Harkes et al., 2010; van Paassen et al., 2010; Whiffin et al., 2007*).

## 1.3. Role of modeling

However, the manipulation of biogeochemical processes is not easy as they result from the complex interactions of living organisms, usually microbes, and the geochemical environment, (e.g. *Dupraz et al., 2009a*). The complex interplay of the multitude of interactions occurring simultaneously in realistic application conditions is in most cases not yet understood, even

though many of the individual interactions, e.g. the change in pH of the surrounding liquid phase due to the metabolism of a specific species or strain of bacteria, have often been studied in well controlled laboratory experiments (e.g. ureolysis by *Sporosarcina pasteurii* in *Lauchnor et al.* (2015)). Other interactions or processes are not understood in sufficient detail, e.g. the attachment of microbial cells to solid surfaces, often because the measurement of the necessary quantities – in the case of attachment, the number of attached cells – is difficult (*Bouwer et al.*, 2000; *Cunningham et al.*, 2007). In field applications, the influence of indigenous microbes is difficult to quantify for the same reason since they are predominantly present as attached to solid surfaces and biofilms (e.g. *Davey and O'toole*, 2000; *Hazen et al.*, 1991). One way to improve the understanding of such processes or the complex interplay of the various contributing processes of biogeochemistry is to construct numerical models of reactive transport (*Steeffel et al.*, 2015b, 2005). Modeling is particularly beneficial to improved understanding if model development is integrated with a coordinated program of laboratory experimentation.

Numerical models help to design and evaluate laboratory experiments as well as field scale applications. For example, modeling can assist in identifying the most promising strategies for the application of biotechnologies in the field by an individual site-specific prediction of the response of the biogeochemical system to the various sets of possible application input parameters. Additionally, modeling can be used to choose the focus of future experimental research. Some investigations, such as determining the sensitivity of the integral process to its individual subprocesses, are conducted faster and more easily by modeling rather than with experimental parameter studies.

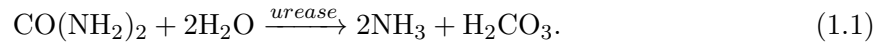
## 1.4. Microbially induced calcite precipitation

In this thesis, the biogeochemical engineering application investigated is microbially induced calcite precipitation (MICP) in the context of sealing possible leakage pathways of subsurface gas ( $\text{CO}_2$ ,  $\text{CH}_4$ ,  $\text{H}_2$ ) reservoirs. The necessary processes are two-phase multi-component reactive transport including precipitation and dissolution of calcite as well as the biomass-related processes: attachment of biomass to surfaces, detachment of biomass from a biofilm, and growth and decay of biomass. Additionally, the reduction in porosity and permeability has to be considered; this results from the presence of the solid phases biofilm and calcite in the pore space.

MICP offers an engineering option that uses controlled biofilm growth to achieve targeted calcite precipitation. In subsurface applications, this process is typically associated with

a reduction of porosity and, even more importantly, of permeability. As an engineering technology, it can be used to alter hydraulic flow conditions and can be applied, for example, to cut off highly permeable pathways such as fractures, faults, or behind-casing defects in boreholes within a geological formation (*Phillips et al.*, 2013b; *Mitchell et al.*, 2013; *Phillips et al.*, 2013a).

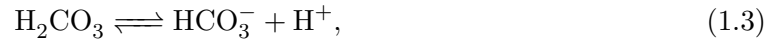
*S. pasteurii* expresses the enzyme urease that catalyzes the hydrolysis reaction of urea ( $\text{CO}(\text{NH}_2)_2$ ) into ammonia ( $\text{NH}_3$ ) and carbon dioxide ( $\text{CO}_2$ ):



Aqueous solutions of ammonia become alkaline as  $\text{H}^+$  is consumed until the equilibrium of ammonium and ammonia is reached. Thus, the ureolysis reaction leads to an increase in pH until the pH is equal to the pKa of ammonia:



This shifts the carbonate balance in an aqueous solution toward higher concentrations of dissolved carbonate ( $\text{CO}_3^{2-}$ ):



Adding calcium ( $\text{Ca}^{2+}$ ) to the system then results in the precipitation of calcium carbonate ( $\text{CaCO}_3$ ):



The resulting overall MICP reaction equation is:



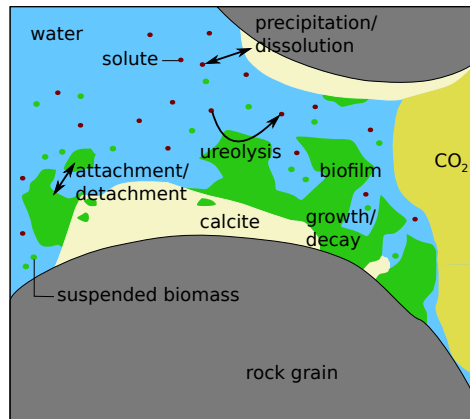


**Figure 1.1.:** Schematic view of relevant processes during MICP.

In a porous medium, this process, which results in the aforementioned impacts on the hydraulic properties, depends on the interplay between biofilm growth, fluid dynamics, and reaction rates. A pore-scale sketch of the most important processes of MICP is shown in Figure 1.1.

A major difficulty for practical engineering applications of MICP is the predictive planning of its use and impact, since it involves a number of complex interacting processes. While the basic chemistry and the flow processes are known, it is the exact quantitative description of the interactions and, in particular, the influence of the biofilm and the developing precipitates that pose challenges to achieving predictability.

## 1.5. Objectives of the thesis

The long-term goal of the research this thesis contributes to is advancing the development of a comprehensive model of the processes relevant for MICP as discussed in Section 1.4 in the context of porous media flow. This thesis contributes to this goal by its three major objectives, which are:

- to improve the model for MICP as proposed by *Ebigbo et al. (2012)* by including advanced experimental insights into relevant processes;
- to apply the model to help design experimental investigations as well as field scale applications;
- to investigate exemplary approaches to reduce the computational time of the model.

## 1.6. Structure of the thesis

This thesis is organized around the main objectives of this thesis, each of the objectives from Section 1.5 having a separate chapter describing the research conducted to reach them. These main chapters are preceded by an introduction to the fundamentals of flow and transport in porous media in Chapter 2 and a description of the previous work in modeling MICP in Chapter 3. Chapter 4 describes the improvements of the numerical model for MICP, which include the implementation of species-specific ureolysis rate equations as well as an investigation of the porosity-permeability relationship. In Chapter 5, it is shown how the improved model from Chapter 4 can be used to help design field applications of MICP and how the model can be used to estimate the potential relevance of the result of an experimental investigation. Chapter 6 presents exemplary approaches to reduce the computational effort such as sequential solution schemes or simplified rate equations and equations of state. This chapter compares the effect of each approach on the computational time and the accuracy with each of the other approaches as well as a reference solution. Finally, the achievements of this thesis are summarized in Chapter 7.

## 2. Fundamentals of modeling flow and transport in porous media

### 2.1. Scale

Depending on the scale of interest, physical and chemical processes and properties can be described using different approaches. On the molecular scale, the properties and interactions of individual molecules are described, which is only feasible for a restricted number of molecules. For larger systems, a continuum approach is used, where properties are averaged over groups of similar molecules, assuming continuous matter. This upscaling by averaging from the molecular scale results in the micro-scale, on which the system is described by the pore geometry and the distribution of distinct fluid phases within the pores. However, for larger laboratory or field-scale applications, the micro-scale is still computationally prohibitively expensive and system descriptions on the macro-scale are used for calculations. The macro-scale description is obtained by averaging over the micro-scale properties within a representative elementary volume (REV), which needs to be large enough to ensure that the averaged properties are independent of the REV size or position. However, it should in turn be much smaller than the entire domain size (*Helmig, 1997*). The detailed pore-geometry and phase-distribution information of the micro-scale is lost on the macro-scale and replaced by volume average quantities, such as porosity, permeability and phase saturation, and relations like the Darcy's law. The macro-scale is also called the REV (or Darcy) scale and is the scale of the models discussed in this thesis.

### 2.2. Porous medium properties

#### 2.2.1. Porosity

The porosity  $\phi$  is defined as the fraction of the volume occupied by fluids in an REV  $V_{\text{fluid}}$  divided by the total volume of the REV  $V_{\text{total}}$ .

$$\phi = \frac{V_{\text{fluid}}}{V_{\text{total}}} = 1 - \frac{V_{\text{solid}}}{V_{\text{total}}}. \quad (2.1)$$

### 2.2.2. Intrinsic permeability

The intrinsic permeability is a measure on the REV scale of the ease of fluid flow through porous media. It relates the potential gradient and the resulting flow velocity in the Darcy equation. As the porous medium may have a structure leading to preferential flow in certain directions, intrinsic permeability is in general a tensorial quantity  $\mathbf{K}$ . For isotropic porous media, it can be reduced to a scalar quantity  $K$ .

## 2.3. Phases and components

A phase is defined as a continuum having distinct properties (e.g. density and viscosity). For MICP in porous media in the context of underground gas storage, there are at least two fluid and three solid phases. Two phases are the immiscible fluid phases water, including dissolved salts and gases, and gas. Additionally, there are the three solid phases biofilm, calcite, and the inert solid matrix, which is assumed not to react or deform. The fluid phases have different affinities to the solid phases. The aqueous phase has a higher affinity to the solid phases and is therefore referred to as the wetting phase and the gas phase as the non-wetting phase. In this thesis, all solid phases are assumed to have the same wettability behavior.

The fluid phases may be composed of several components, while the solid phases are assumed to consist exclusively of a single component. Components are distinct chemical species or a group of chemical species. The composition of the components in a phase can influence the phase properties. For the aqueous phase ( $\alpha = w$ ), this influence on the phase properties is accounted for by the salinity, which represents the cumulative effects of solutes. The salinity  $X_{\text{sal}}$  is defined as the ratio of the mass of solutes to the total mass of the aqueous phase,  $X_{\text{sal}} = \text{mass}_w^{\text{solute}} / \text{mass}_w^{\text{total}}$ .

### 2.3.1. Mass fraction, mole fraction, molality

The composition of a phase is described by mass or mole fractions of the components. The mole fraction  $x_{\alpha}^{\kappa}$  of component  $\kappa$  in phase  $\alpha$  is defined as:

$$x_{\alpha}^{\kappa} = \frac{n_{\alpha}^{\kappa}}{\sum_i n_{\alpha}^i}, \quad (2.2)$$

where  $n_{\alpha}^{\kappa}$  is the number of moles of component  $\kappa$  in phase  $\alpha$ . The mass fraction  $X_{\alpha}^{\kappa}$  is defined similarly using the mass of component  $\kappa$  in phase  $\alpha$  instead of  $n_{\alpha}^{\kappa}$ ,  $X_{\alpha}^{\kappa} = \text{mass}_{\alpha}^{\kappa} / \text{mass}_{\alpha}^{\text{total}}$ . The molar mass  $M^{\kappa}$  of the component  $\kappa$  relates the mass fraction to the mole fraction and vice versa. In this work, mole fractions are used in all models.

The molality  $m^{\kappa}$  of component  $\kappa$  in the aqueous phase is defined as:

$$m^{\kappa} = \frac{n_{\text{w}}^{\kappa}}{\text{mass}_{\text{H}_2\text{O}}}, \quad (2.3)$$

where  $\text{mass}_{\text{H}_2\text{O}}$  is the mass of pure water in the aqueous phase. Molalities are used in the chemical calculations because density effects at higher solute concentrations prohibit the use of concentrations, which depend on the volume. Likewise, the mole fraction of an inert component might change significantly during reactions, see Eq. (2.2). The mass of the solvent, in this case water, is much more constant and, consequently,  $m^{\kappa}$  also has less fluctuation.

## 2.4. Fluid properties

The most important fluid properties to describe fluid flow on the REV scale are density and viscosity.

### 2.4.1. Density

The density  $\rho_{\alpha}$  of a fluid phase  $\alpha$  is defined as the ratio of its mass to its volume ( $\rho_{\alpha} = \text{mass}_{\alpha} / \text{volume}_{\alpha}$ ) while the molar density  $\rho_{\text{mol},\alpha}$  is defined as the ratio of the number of moles per volume ( $\rho_{\text{mol},\alpha} = \text{moles}_{\alpha} / \text{volume}_{\alpha}$ ). In this work, the molar density is used for the fluid phases and the mass density is used for solid phases.

### 2.4.2. Viscosity

The dynamic viscosity  $\mu_{\alpha}$  characterizes the resistance of a fluid to flow. As density, it is a fluid phase property. For Newtonian fluids, it relates the shear stress  $\tau_s$  to the velocity gradient  $dv_{\alpha,x}/dy$ :

$$\tau_s = \mu_\alpha \frac{dv_{\alpha,x}}{dy}. \quad (2.4)$$

Density and viscosity are both dependent on pressure, temperature and phase composition. In this thesis, temperature is assumed to be constant, but both properties may vary according to pressure and composition.

## 2.5. Fluid phase interactions in porous media

If more than a single fluid is present in the porous medium, the fluids interact with each other and the solids, which leads to additional properties for two-phase systems.

### 2.5.1. Saturation

The saturation  $S_\alpha$  of a phase  $\alpha$  is defined as the ratio of the volume occupied by that phase to the total pore volume within an REV. As all pores are filled with some fluid, the sum of the saturations of all present phases is equal to one.

### 2.5.2. Capillary pressure

Immiscible fluids form a sharp interface as a result of differences in their intermolecular forces translating into different adhesive and cohesive forces at the fluid-fluid and fluid-fluid-solid interfaces creating interfacial tension on the microscale. From the mechanical equilibrium which has also to be satisfied at the interface, a difference between the pressures of the fluid phases results defined as the capillary pressure  $p_c$ :

$$p_c = p_n - p_w. \quad (2.5)$$

On the microscale,  $p_c$  can be calculated from the surface tension according to the Laplace equation (see *Helmig*, 1997).

On the REV scale, however, capillary pressure needs to be defined by quantities of that scale. Several empirical relations provide expressions to link  $p_c$  to the wetting-phase saturation  $S_w$ . In this thesis, the relation given by *Brooks and Corey* (1964) is used to determine  $p_c$  based on  $S_e$ , which is the effective wetting-phase saturation, the entry pressure  $p_d$ , and the parameter  $\lambda$  describing the pore-size distribution:

$$p_c = p_d S_e^{-\frac{1}{\lambda}}, \quad (2.6)$$

with

$$S_e = \frac{S_w - S_{w,r}}{1 - S_{w,r}}, \quad (2.7)$$

where  $S_{w,r}$  is the residual wetting phase saturation which cannot be displaced by another fluid phase and remains in the porous medium.

### 2.5.3. Relative permeability

The presence of two fluid phases in the porous medium reduces the space available for flow for each of the fluid phases. This increases the resistance to flow of the phases, which is accounted for by the means of the relative permeability  $k_{r,\alpha}$ , which scales the intrinsic permeability. It is a value between zero and one, depending on the saturation. The relations describing the relative permeabilities of the wetting and non-wetting phase are different as the wetting phase predominantly occupies small pores and the edges of larger pores while the non-wetting phases occupies large pores. The relative permeabilities for the wetting phase  $k_{r,w}$  and the non-wetting phase are calculated as:

$$k_{r,w} = S_e^{\frac{2+3\lambda}{\lambda}} \quad (2.8)$$

and

$$k_{r,n} = (1 - S_e)^2 \left( 1 - S_e^{\frac{2+\lambda}{\lambda}} \right). \quad (2.9)$$

## 2.6. Transport processes in porous media

On the macro-scale, the transport of mass can be grouped according to the driving force of the transport process. Pressure gradients result in the advective transport of a fluid phase and all the components constituting the phase, while concentration gradients result in the diffusion of a component within a phase. Dispersion is a diffusion-like process caused by the approximated description of advection on the macro-scale.

### 2.6.1. Advection

Advective transport is determined by the flow field. On the macro-scale, the velocity  $\mathbf{v}$  is calculated using the Darcy equation depending on the potential gradient  $(\nabla p - \rho \mathbf{g})$ , accounting for both pressure difference and gravitation, the intrinsic permeability of the porous medium, and the viscosity  $\mu$  of the fluid phase:

$$\mathbf{v} = -\frac{\mathbf{K}}{\mu}(\nabla p - \rho \mathbf{g}). \quad (2.10)$$

$\mathbf{v}$  is proportional to  $(\nabla p - \rho \mathbf{g})$  with the proportional factor  $\mathbf{K}/\mu$ . This equation can be extended to calculate the velocity  $\mathbf{v}_\alpha$  of phase  $\alpha$  in the case of two-phase flow by considering the relative permeability  $k_{r,\alpha}$  (Section 2.5.3):

$$\mathbf{v}_\alpha = -\frac{k_{r,\alpha} \mathbf{K}}{\mu_\alpha}(\nabla p_\alpha - \rho_\alpha \mathbf{g}) \quad (2.11)$$

### 2.6.2. Diffusion

Molecular diffusion is a process determined by the concentration gradient. It is commonly modeled as Fickian diffusion following Fick's first law:

$$\mathbf{j}_d = -\rho_{\text{mol},\alpha} D_\alpha^\kappa \nabla x_\alpha^\kappa, \quad (2.12)$$

where  $D_\alpha^\kappa$  is the molecular diffusion coefficient of component  $\kappa$  in phase  $\alpha$ . In a porous medium, the actual path lines are tortuous due to the impact of the solid matrix. This tortuosity and the impact of the presence of multiple fluid phases is accounted for by using an effective diffusion coefficient  $D_{\text{pm},\alpha}^\kappa$ :

$$D_{\text{pm},\alpha}^\kappa = \phi \tau_\alpha S_\alpha D_\alpha^\kappa, \quad (2.13)$$

where  $\tau_\alpha$  is the tortuosity of phase  $\alpha$ .

### 2.6.3. Dispersion

Heterogeneities on a scale smaller than the macro-scale lead to heterogeneous advective transport, which cannot be described using the macro-scale Darcy equation to calculate the velocity field and the resulting transport. Consequently, dispersion is scale-dependent. Dispersion accounts for this diffusion-like spreading due to heterogeneous transport, which is different longitudinally and transversely to the direction of flow. This results in the dispersion being a tensorial quantity.

$$\mathbf{D}_{\text{pm},\alpha}^{\kappa} = \frac{\mathbf{v}_{\text{e},\alpha} \mathbf{v}_{\text{e},\alpha}^{\text{T}}}{\|\mathbf{v}_{\text{e},\alpha}\|} (\alpha_l - \alpha_t) + \mathbf{I} \left( D_{\text{pm},\alpha}^{\kappa} - \alpha_t \right) \|\mathbf{v}_{\text{e},\alpha}\|, \quad (2.14)$$

where  $\mathbf{D}_{\text{pm},\alpha}^{\kappa}$  is the dispersion tensor,  $\mathbf{v}_{\text{e},\alpha} = v_{\alpha}/\phi$  the effective velocity, and  $\alpha_l$  and  $\alpha_t$  are the longitudinal and the transverse dispersivities.

## 2.7. Balance equations

The basic equations for the numerical modeling of transport are the balance equations derived from the continuity of mass and momentum. In porous media, the Reynolds number is usually sufficiently low ( $< 1$ ) to assume a creeping flow regime, where inertial forces can be neglected. This reduces the momentum balance to the Darcy equations for single-phase flow (Eq. (2.10)) or two-phase flow (Eq. (2.11)). As the momentum and the mass balance are decoupled for this case, the velocity obtained using the Darcy equations can be directly used in the mass balance equations. Additionally to the transport processes discussed in Section 2.6, the mass balance equation has to consider storage and sources or sinks.

### 2.7.1. Balance equation for component transport in two-phase flow

For the transport of a component  $\kappa$  in a two-phase flow environment, the balance equation can be written as:

$$\sum_{\alpha} \frac{\partial (\phi S_{\alpha} \rho_{\text{mol},\alpha} x_{\alpha}^{\kappa})}{\partial t} + \nabla \cdot (\rho_{\text{mol},\alpha} x_{\alpha}^{\kappa} \mathbf{v}_{\alpha} \cdot \mathbf{n}) - \mathbf{D}_{\text{pm},\alpha}^{\kappa} \rho_{\text{mol},\alpha} \nabla x_{\alpha}^{\kappa} - q^{\kappa} = 0; \alpha \in \{\text{w}, \text{n}\}, \quad (2.15)$$

where  $q^\kappa$  is the source term of the component  $\kappa$ . For reactive transport,  $q^\kappa$  may consist of external sources or sinks due, for example, to extraction of  $\kappa$  as well as sources or sinks due to the reactions involving  $\kappa$ .

### 2.7.2. Balance equation for solid phases

Mineral phases and biofilm are considered to be rigid and to consist only of one single component each. Thus, their balance equation consists only of a storage and a source term and no summation over different phases is necessary:

$$\frac{\partial (\phi_\lambda \rho_{\text{mol},\lambda})}{\partial t} - q^\lambda = 0. \quad (2.16)$$

Here,  $\phi_\lambda$  is the volume fraction,  $\rho_{\text{mol},\lambda}$  the molar density, and  $q^\lambda$  the source term of the solid phase  $\lambda$ .

## 2.8. Effects of mineral precipitation and biomass growth in porous media

As already mentioned in the introduction, Chapter 1, the growth of biomass and the precipitation of minerals within a porous medium reduce its porosity and permeability. For example, growing a biofilm only at constant hydraulic head may already result in a significant reduction of the porosity (50 - 96%) and the permeability (> 90%) as measured in *Cunningham et al.* (1991).

### 2.8.1. Porosity changes due to mineral precipitation and biomass growth

Modeling changes in porosity is straightforward and commonly done by subtracting the volume fractions of the solid phases  $\phi_\lambda$  from the initial porosity  $\phi_0$ :

$$\phi = \phi_0 - \sum \phi_\lambda. \quad (2.17)$$

### **2.8.2. Permeability changes due to mineral precipitation and biomass growth**

The permeability reductions due to bioclogging measured in a variety of experiments compiled in *Thullner* (2010) range between two and four orders of magnitude. For biofilm-mediated calcite precipitation in sand columns, permeability reductions of 60 - 99% were measured (*Phillips et al.*, 2013b). In fractured sandstone, permeability reductions of up to five orders of magnitude were achieved in *Phillips et al.* (2013b).



### 3. State of the art prior to this work; experiments

Models for simulating MICP processes have been developed by a number of authors (*Martinez et al.*, 2014; *Barkouki et al.*, 2011; *Cuthbert et al.*, 2013; *van Wijngaarden et al.*, 2013, 2011; *Ebigbo et al.*, 2012), each of the models focusing on different processes. Often, the models developed are designed to match a series of experiments. Consequently, they focus on the processes of relevance in the corresponding experiments while neglecting other processes that might be relevant in the field.

The models presented by *Martinez et al.* (2014) and *Barkouki et al.* (2011) use a complex ureolysis rate equation (*Fidaleo and Lavecchia*, 2003) and a saturation-state-dependent precipitation rate, while neglecting changes in permeability and the processes related to bacterial transport, growth, and decay. As a result, the ureolytic activity is assumed to be constant over time for each point in space and the distribution of urease in space is described by a Gamma distribution (*Martinez et al.*, 2014) or an exponential function (*Barkouki et al.*, 2011).

In *Cuthbert et al.* (2013), a first-order kinetic model is assumed for ureolysis, and bacterial transport and attachment are modeled. The precipitation rate is assumed to be stoichiometric to the ureolysis rate. The impact of MICP on the fracture transmissivity is measured in the experiment and included in the model in dependence on a reduction of the fracture aperture related to the volume of precipitated calcite.

Michaelis-Menten kinetics are used to model the ureolysis rate in *van Wijngaarden et al.* (2013, 2011) and, like *Cuthbert et al.* (2013), these authors assume that the precipitation rate is proportional to the ureolysis rate. The permeability is decreased as a result of the porosity reduction caused by the precipitated calcite. A Kozeny-Carman relationship is used to calculate the permeability. Bacteria are assumed to be homogeneously distributed in *van Wijngaarden et al.* (2011), while *van Wijngaarden et al.* (2013) accounts for attachment and detachment due to adsorption and desorption respectively. For special cases, *van Wijngaarden et al.* (2013, 2011) propose analytical solutions.

*Ebigbo et al.* (2012) developed a complex two-phase model including component transport, kinetic reactions, and a reduction of porosity and permeability due to calcite precipitation and biofilm presence. This model uses a complex, biofilm-dependent ureolysis rate equation adapted from *Fidaleo and Lavecchia* (2003) and a calcite precipitation rate equation dependent on interfacial area and saturation state (*Zhong and Mucci*, 1989) as well as on dissolution kinetics (*Compton et al.*, 1989; *Chou et al.*, 1989). Additionally, the model accounts for microbial processes such as attachment, substrate-dependent growth, decay, and detachment due to shear stress as well as for reduced porosity and permeability using a Verma-Pruess relationship. This high complexity is the result of the aim of the model to predict arbitrary MICP setups in the context of CO<sub>2</sub>-storage.

The *Ebigbo et al.* (2012) model will be presented in the following Section 3.1 as it represents the starting point for the investigations in this thesis in Chapters 4, 6, and 5.

### 3.1. Model concept

The conceptual model for MICP follows the one presented by *Ebigbo et al.* (2012). It accounts for two-phase multi-component reactive transport on the continuum scale, including biofilm and calcite as solid phases. The reactions considered are pH-dependent dissociation reactions, microbial growth and decay as well as microbially catalyzed ureolysis and mass-transfer reactions between the different phases. Mass transfer may occur between both fluid phases by mutual dissolution of water and CO<sub>2</sub> in the gas or the aqueous phase. It may also occur between the aqueous phase and the two ‘solid’ phases, biofilm and calcite denoted by subscripts (f) and (c) respectively, by attachment or detachment of biomass and precipitation or dissolution of calcite. The mobile components, denoted by superscripts  $\kappa$ , are water (w), dissolved inorganic carbon (C<sub>tot</sub>), sodium (Na), chloride (Cl), calcium (Ca), urea (u), ammonium and ammonia (N<sub>tot</sub>), substrate (s), oxygen (O<sub>2</sub>), and suspended biomass (b). Substrate is the carbon and energy source of the bacteria and O<sub>2</sub> the electron acceptor.

The primary variables solved are the aqueous-phase pressure  $p_w$ , mole fractions  $x_w^\kappa$  of component  $\kappa$  in the water phase, and, for the solid phases biofilm and calcite, volume fractions  $\phi_\lambda$ . Although the previous model by *Ebigbo et al.* (2012) was formulated using mass fractions  $X_w^\kappa$  as primary variables, this description will be formulated using mole fractions  $x_w^\kappa$  to avoid unnecessary repetitions in later chapters as the models used in this work are all based on the use of mole fractions. All calcium carbonate is assumed to precipitate as calcite, since experimental investigations of *Phillips et al.* (2015); *Mitchell et al.* (2013); *Lauchnor et al.* (2013); *Cuthbert et al.* (2012) confirmed by XRD measurements that calcite is the predominant polymorph of

calcium carbonate precipitates forming under MICP conditions. In *Phillips et al. (2013b)*, calcite and possibly vaterite were observed.

However, the CO<sub>2</sub>-phase saturation is used as primary variable instead of the mole fraction of total inorganic carbon in water  $x_w^{C_{\text{tot}}}$  whenever both fluid phases are present within the same control volume (*Class and Helmig, 2002*). All reactive and mass-transfer processes are incorporated in the mass balance equations for the components (3.1) and (3.2) by component-specific source and sink terms:

$$\sum_{\alpha} \left[ \frac{\partial}{\partial t} (\phi \rho_{\alpha, \text{mol}} x_{\alpha}^{\kappa} S_{\alpha}) + \nabla \cdot (\rho_{\alpha, \text{mol}} x_{\alpha}^{\kappa} \mathbf{v}_{\alpha}) - \nabla \cdot (\rho_{\alpha, \text{mol}} \mathbf{D}_{\text{pm}, \alpha}^{\kappa} \nabla x_{\alpha}^{\kappa}) \right] = q^{\kappa}, \quad \alpha \in \{\text{n}; \text{w}\}. \quad (3.1)$$

Here,  $t$  is time,  $\phi$  porosity,  $\rho_{\alpha, \text{mol}}$ ,  $S_{\alpha}$ , and  $\mathbf{v}_{\alpha}$  the molar density, saturation and the velocity of phase  $\alpha$  respectively,  $x_{\alpha}^{\kappa}$  the mole fraction of component  $\kappa$  in phase  $\alpha$ .  $\mathbf{D}_{\text{pm}, \alpha}$  is the dispersion tensor of phase  $\alpha$  in the porous medium, and  $q^{\kappa}$  is the source term of component  $\kappa$  due to biochemical reactions. However, all components except water, CO<sub>2</sub>, and O<sub>2</sub> are assumed to be restricted to the water phase.

The mass balances for the solid phases calcite and biofilm contain only a storage and source term since they are immobile:

$$\frac{\partial}{\partial t} (\phi_{\lambda} \rho_{\lambda}) = q^{\lambda}, \quad \lambda \in \{\text{c}; \text{f}\}. \quad (3.2)$$

Here,  $\phi_{\lambda}$  and  $\rho_{\lambda}$  are volume fraction and mass density of the solid phase  $\lambda$ , and  $q^{\lambda}$  is the source term of phase  $\lambda$  due to biochemical reactions. The sources and sinks due to reactions  $q^{\kappa}$  and  $q^{\lambda}$  are specific to the components and are discussed in detail in the following Section 3.1.1.

Note that while the model originally published in *Ebigbo et al. (2012)* uses component mass fractions  $X_{\alpha}^{\kappa}$  as primary variables, here, component mole fractions  $x_{\alpha}^{\kappa}$  are used as primary variables.

### 3.1.1. Component-specific reactive source and sink terms

The source and sink terms account for the biogeochemical reactions occurring during MICP and the presence of CO<sub>2</sub>: ureolysis, calcite precipitation and dissolution, biomass growth under consumption of oxygen and substrate, biomass decay, as well as attachment and detachment of biomass.

### Water, sodium and chloride

Sodium and chloride do not participate in the reactions and water is the solute and is abundant, which is why its consumption by the hydrolysis of urea (Eq. (1.6)) is considered negligible. Thus, the reactive source terms for water  $q^w$ , sodium  $q^{\text{Na}}$  and chloride  $q^{\text{Cl}}$  are zero:

$$q^w = q^{\text{Na}} = q^{\text{Cl}} = 0 \quad (3.3)$$

### Urea and total nitrogen

The source term for  $N_{\text{tot}}$ ,  $q^{N_{\text{tot}}}$ , and the sink term for urea  $q^u$  result from ureolysis (Eq. (1.1)). For each mole of urea hydrolyzed, 2 moles of  $N_{\text{tot}}$  are generated. The  $q^s$  are thus:

$$q^u = -r_{\text{urea,old}}, \quad (3.4)$$

$$q^{N_{\text{tot}}} = 2r_{\text{urea,old}}, \quad (3.5)$$

where  $r_{\text{urea,old}}$  is the ureolysis rate from *Ebigbo et al. (2012)*. The rate equation is derived from the complex enzymatic rate equation originally published by *Fidaleo and Lavecchia (2003)* for the ureolysis rate of pure urease extracted from jack bean (*Canavalia ensiformis*) seeds. It accounts for enzyme inactivation due to suboptimal pH, inhibition caused by high product ( $\text{NH}_4^+$ ) concentrations and a Michaelis-Menten type reaction rate dependency of the urea concentration:

$$r_{\text{urea,old}} = \frac{k_{\text{urease,old}}}{1 + \frac{m^{\text{H}^+}}{K_{\text{eu},1}} + \frac{K_{\text{eu},2}}{m^{\text{H}^+}}} Z_{\text{ub}} \frac{m^u}{m^u + K_{\text{u,old}}} \frac{K_{\text{NH}_4^+}}{m^{\text{NH}_4^+} + K_{\text{NH}_4^+}}. \quad (3.6)$$

Here,  $k_{\text{urease,old}}$  is the maximum activity of urease from *Krajewska (2009)*,  $m^{\text{H}^+}$  and  $m^{\text{NH}_4^+}$  are the molalities of  $\text{H}^+$  and  $\text{NH}_4^+$ , calculated from the water phase composition and the mole fractions respectively,  $K_{\text{eu},1}$  and  $K_{\text{eu},2}$  are speciation constants for the protonation and deprotonation of urease (*Fidaleo and Lavecchia, 2003*),  $Z_{\text{ub}}$  the urease mass concentration,  $K_{\text{u,old}}$  (*Krajewska, 2009*) is the half-saturation constant for urea as used in *Ebigbo et al. (2012)*, and  $K_{\text{NH}_4^+}$  is the product inhibition constant from (*Fidaleo and Lavecchia, 2003*). The urease mass concentration  $Z_{\text{ub}}$  is assumed to be related nonlinearly to the attached biomass  $\rho_f \phi_f$ ;  $\rho_f$  and  $\phi_f$  are the density and volume fraction of attached biomass, while the contribution of the suspended biomass to ureolysis is neglected:

$$Z_{\text{ub}} = k_{\text{ub,old}} (\rho_f \phi_f)^{n_{\text{ub}}}, \quad (3.7)$$

where  $k_{\text{ub,old}}$  is the mass ratio of urease to biofilm and  $n_{\text{ub}}$  is an exponent accounting for nonlinear relations between biofilm and urease mass.

### Calcium and calcite

The source terms of calcium  $q^{\text{Ca}}$  and calcite  $q^{\text{c}}$  are determined by the rates of precipitation and dissolution. When the aqueous phase is oversaturated with respect to calcite, it precipitates according to (Eq. (1.5)). In the opposite case, calcite dissolves until the solution is saturated or all calcite is already dissolved:

$$q^{\text{Ca}} = r_{\text{diss}} - r_{\text{prec}}, \quad (3.8)$$

$$q^{\text{c}} = -r_{\text{diss}} + r_{\text{prec}}. \quad (3.9)$$

Here,  $r_{\text{diss}}$  is the rate of calcite dissolution and  $r_{\text{prec}}$  the rate of calcite precipitation. Both reaction rates are calculated as follows, depending on the interfacial area available for the reaction as well as the saturation index  $\Omega$  and, in the case of the dissolution, additionally on the molality of  $\text{H}^+$ . The precipitation rate of calcite is calculated as:

$$r_{\text{prec}} = k_{\text{prec}} A_{\text{sw}} (\Omega - 1)^{n_{\text{prec}}}; \text{ for } \Omega \geq 1, \quad (3.10)$$

$$A_{\text{sw}} = A_{\text{sw},0} \left(1 - \frac{\phi_{\text{c}}}{\phi_0}\right)^{\frac{2}{3}}, \quad (3.11)$$

$$\Omega = \frac{m^{\text{Ca}^{2+}} \gamma^{\text{Ca}^{2+}} m^{\text{CO}_3^{2-}} \gamma^{\text{CO}_3^{2-}}}{K_{\text{sp}}}, \quad (3.12)$$

where  $k_{\text{prec}}$  and  $n_{\text{prec}}$  are empirical precipitation parameters from *Zhong and Mucci (1989)*,  $A_{\text{sw}}$  and  $A_{\text{sw},0}$  are the current and initial interfacial areas respectively between the water phase and the solid phases,  $K_{\text{sp}}$  the calcite solubility product and  $m^{\text{Ca}^{2+}}$  and  $m^{\text{CO}_3^{2-}}$  the molalities of calcium and carbonate respectively. The activity coefficients  $\gamma^{\kappa}$  are calculated using Pitzer equations (*Clegg and Whitfield, 1995; Millero et al., 1984; Wolf et al., 1989*). The dissolution rate of calcite is calculated as:

$$r_{\text{diss}} = (k_{\text{diss},1} m^{\text{H}^+} + k_{\text{diss},2}) A_{\text{cw}} (\Omega - 1)^{n_{\text{diss}}}; \text{ for } \Omega < 1, \quad (3.13)$$

$$A_{\text{cw}} = \min(A_{\text{sw}}, a_{\text{c}}\phi_{\text{c}}), \quad (3.14)$$

where  $k_{\text{diss},1}$ ,  $k_{\text{diss},2}$ , and  $n_{\text{diss}}$  are dissolution parameters (Chou *et al.*, 1989; Compton *et al.*, 1989) and  $a_{\text{c}}$  is the specific surface area and  $\phi_{\text{c}}$  the volume fraction of calcite.

### Dissolved inorganic carbon

Dissolved inorganic carbon is generated by the hydrolysis of urea (Eq. (1.6)) as well as by the dissolution of calcite while it is consumed by the precipitation of calcite (Eq. (1.5)). Thus, the source term of dissolved inorganic carbon  $q^{\text{C}_{\text{tot}}}$  results in:

$$q^{\text{C}_{\text{tot}}} = r_{\text{urea,old}} + r_{\text{diss}} - r_{\text{prec}}, \quad (3.15)$$

### Suspended and attached biomass

The source and sink terms of suspended and attached biomass (biofilm),  $q^{\text{b}}$  and  $q^{\text{f}}$ , include four reaction rates each, corresponding to the biomass-related processes the model accounts for. These processes are growth and decay increasing and decreasing the suspended or attached biomass as well as attachment and detachment describing the transfer of biomass from the suspended to the attached state and vice versa:

$$q^{\text{b}} = \frac{r_{\text{g}}^{\text{b}} - r_{\text{b}}^{\text{b}} - r_{\text{a}} + r_{\text{d}}}{M^{\text{b}}}, \quad (3.16)$$

$$q^{\text{f}} = \frac{r_{\text{g}}^{\text{f}} - r_{\text{b}}^{\text{f}} + r_{\text{a}} - r_{\text{d}}}{M^{\text{f}}} \quad (3.17)$$

where  $r_{\text{g}}^{\text{b}}$  is the growth rate and  $r_{\text{b}}^{\text{b}}$  the decay rate of suspended biomass,  $r_{\text{a}}$  the attachment rate,  $r_{\text{d}}$  the detachment rate and  $M^{\text{b}}$  the molar mass of biomass to convert the rates in the units from mass to moles per volume and time. Accordingly,  $r_{\text{g}}^{\text{f}}$  and  $r_{\text{b}}^{\text{f}}$  are the growth and decay of biofilm and  $M^{\text{f}}$  is the molar mass of biofilm. All rates influencing both attached and suspended biomass are assumed to be of a first-order type, where the rate is calculated by the product of a specific rate and the respective biomass, which is  $C_{\text{w}}^{\text{b}}S_{\text{w}}\phi$  in the case of suspended and  $\phi_{\text{f}}\rho_{\text{f}}$  in the case of attached biomass. Here,  $C_{\text{w}}^{\text{b}}$  is the suspended biomass mass concentration in the water phase,  $S_{\text{w}}$  the water phase saturation.

The growth rates of suspended and attached biomass are as follows:

$$r_g^b = \mu_g C_w^b S_w \phi, \quad (3.18)$$

$$r_g^f = \mu_g \phi_f \rho_f, \quad (3.19)$$

with the specific growth rate  $\mu_g$ .  $\mu_g$  is calculated using double Monod kinetics to reproduce the dependency of the microbial growth on both substrate and oxygen.

$$\mu_g = k_{\mu,old} Y \frac{C_w^s}{K_s + C_w^s} \frac{C_w^{O_2}}{K_{O_2} + C_w^{O_2}}. \quad (3.20)$$

Here,  $k_{\mu,old}$  is the maximum specific growth rate, which was fitted in *Ebigbo et al. (2012)*,  $Y$  the yield coefficient expressing the ratio of biomass generated to the mass of substrate consumed (*Seto and Alexander, 1985*).  $C_w^s$  and  $C_w^{O_2}$  are the mass concentrations of substrate and oxygen in the water phase and  $K_s$  (*Taylor and Jaffé, 1990*) and  $K_{O_2}$  (*Hao et al., 1983*) are the half-saturation coefficients for substrate and oxygen respectively.

The decay rates are calculated similarly to the growth rates:

$$r_b^b = k_b^b C_w^b S_w \phi, \quad (3.21)$$

$$r_b^f = k_b^f \phi_f \rho_f, \quad (3.22)$$

except that the specific decay rates of suspended and attached biomass,  $k_b^b$  and  $k_b^f$  respectively, take different processes into account, increasing inactivation. For suspended biomass, non-optimal, acidic pH is assumed to increase inactivation:

$$k_b^b = b_0 \left( 1 + \frac{K_{pH}}{m_{H^+}^2} \right), \quad (3.23)$$

where  $b_0$  is the endogenous decay rate (*Taylor and Jaffé, 1990*) and  $K_{pH}$  is an empirical constant from *Kim et al. (2000)*, accounting for increased cell inactivation at low pH. High pH is assumed not to influence the inactivation of suspended biomass, as *S. pasteurii* is alkaliphile. On the contrary, attached cells are protected from harsh environmental conditions and the presence of  $CO_2$  within the biofilm by protective mechanisms such as extracellular polymers (*Mitchell et al., 2008*). However, as calcite precipitates mainly in or close to the biofilm, cells may be covered with calcite precipitates or disrupted by crystals inactivating the affected cells

(Dupraz *et al.*, 2009b; Whiffin *et al.*, 2007). Consequently, the precipitation rate is assumed to increase the specific decay rate of attached biomass:

$$k_b^f = b_0 + \frac{r_{\text{prec}} M^c}{\rho_c (\phi_0 - \phi_c)}, \quad (3.24)$$

where  $\frac{r_{\text{prec}} M^c}{\rho_c}$  is the volumetric calcite precipitation rate,  $M^c$  being the molar mass and  $\rho_c$  the density of calcite, and  $\phi_0 - \phi_c$  is the space available for calcite precipitation, which may occur in the biofilm or the pore space.

The attachment rate  $r_a$  quantifies the biomass transfer from the suspended to the attached state. As attachment is modeled assuming a first-order kinetic rather than a sorption-type behavior, it is independent of the amount of attached biomass:

$$r_a = k_a C_w^b \phi S_w, \quad (3.25)$$

where  $k_a$  is the specific attachment rate from *Taylor and Jaffé* (1990). It is considered to consist of two terms,  $c_{a,1} \phi_f$  and  $c_{a,2}$ , whose coefficient  $c_{a,1}$  accounts for preferential attachment to existing biofilm while  $c_{a,2}$  accounts for the unspecific attachment to arbitrary surfaces:

$$k_a = c_{a,1} \phi_f + c_{a,2}. \quad (3.26)$$

Detachment of biomass from biofilm is assumed to be proportional to the shear stress. Additionally, the growth contributes to the detachment rate, as vigorously growing biofilm is typically weaker and as such more susceptible to detachment (*Rittmann*, 1982). As the model of *Ebigbo et al.* (2012) is defined on the Darcy scale but the shear stress is a micro-scale property, it is approximated using the absolute value of the water-phase potential gradient:

$$r_d = k_d \phi_f \rho_f, \quad (3.27)$$

where  $r_d$  is the rate of detachment and  $k_d$  the detachment coefficient:

$$k_d = c_d (\phi S_w |\nabla p_w - \rho_w \mathbf{g}|)^{0.58} + \frac{\phi_f}{\phi_0 - \phi_c} \mu_g. \quad (3.28)$$

Here,  $c_d$  is a coefficient for the shear-stress-dependent detachment,  $|\nabla p_w - \rho_w \mathbf{g}|$  the absolute value of the water-phase potential gradient, and  $\phi_0$  the initial porosity.

### Substrate and oxygen

The consumption of substrate and oxygen is linked to the growth of both suspended and attached biomass by the yield coefficient  $Y$  of substrate:

$$q^s = -\frac{r_g^b + r_g^f}{M^s Y}. \quad (3.29)$$

In the case of oxygen, the coefficient  $F$ , which is the ration of oxygen consumed per substrate consumed, is used to express the biomass yield per oxygen consumed using  $Y$ :

$$q^{O_2} = Fq^s = -F\frac{r_g^b + r_g^f}{M^{O_2} Y}. \quad (3.30)$$

### 3.1.2. Supplementary equations

#### Permeability and porosity

The permeability decreases due to biofilm growth and calcite precipitation as already discussed in Chapter 1. In the model, the reduction of permeability is calculated based on the reduction of porosity:

$$\frac{K}{K_0} = \left( \frac{\phi - \phi_{\text{crit}}}{\phi_0 - \phi_{\text{crit}}} \right)^3. \quad (3.31)$$

Here,  $K_0$  is the initial permeability,  $\phi_{\text{crit}}$  the critical porosity at which the permeability is zero as estimated by *Ebigbo et al.* (2012), and  $\phi_0$  is the initial porosity. The porosity  $\phi$  decreases as the volume fractions of biofilm and calcite increase (Eq. (2.17)):

$$\phi = \phi_0 - \phi_c - \phi_f. \quad (3.32)$$

### Capillary pressure and relative permeability

The capillary pressure saturation relation of Brooks and Corey (e.g. *Brooks and Corey*, 1964; *Corey*, 1994) is used to calculate the capillary pressure based on the wetting phase saturation (Eq. (2.6)), using an entry pressure  $p_d = 10^4$  Pa and a pore-size distribution parameter  $\lambda = 2$  (see *Ebigbo et al.*, 2010). The relative permeabilities of the wetting and the non-wetting phase are also calculated using the relations given by Brooks and Corey, see Section 2.5.3, with identical parameters as for the capillary pressure.

### Fluid properties

The density and the viscosity of the CO<sub>2</sub> phase are calculated using the relation given by *Span and Wagner* (1996) and *Fenghour et al.* (1998) respectively. In these calculations, the effects of the small amounts of water and oxygen are neglected. The density and the viscosity of the aqueous phase are calculated according to *Batzle and Wang* (1992) as a function of salinity. Sodium, chloride and calcium are considered to contribute to the salinity.

### Phase partitioning of components

The dissolution of CO<sub>2</sub> in the aqueous phase is calculated according to *Duan and Sun* (2003) as a function of temperature, pressure and salinity. In the two-phase case, the concentration of H<sub>2</sub>CO<sub>3</sub> is assumed to be equal to the solubility while, in the case of the exclusive presence of the aqueous phase, the concentration of inorganic carbon is exclusively dependent on the precipitation, dissolution and ureolysis reactions. In this case, the solubility represents the maximum possible concentration. The mass fraction of water in the CO<sub>2</sub> phase is assumed to be constant as in *Bielinski* (2006). For the solubility of oxygen in the aqueous phase, Henry's law is used with parameters according to *Sander* (1999), now published in *Sander* (2015).

#### 3.1.3. Diffusion, dispersion and tortuosity

The dispersion of components is accounted for in the model and calculated according to Equation (2.14). The tortuosity is calculated according to *Millington and Quirk* (1961):

$$\tau_\alpha = \frac{(\phi S_\alpha)^{\frac{7}{3}}}{\phi^2}. \quad (3.33)$$

## Dissociation reactions and pH

The dissociation of  $\text{NH}_3$  and  $\text{H}_2\text{CO}_3$  produced by ureolysis, see Equation (1.1), is important for modeling MICP as the precipitation rate is dependent on the activity of  $\text{CO}_3^{2-}$ , which is influenced by the overall geochemistry of the solution but most importantly on the activity of  $\text{H}^+$  (Equations (1.3) and (1.4)). Additionally, the ureolysis rate is influenced by the amount of  $\text{NH}_4^+$  in the solution, as high concentrations are assumed to inhibit the ureolysis (Equation (3.6)).

In the model, the dissociation of  $\text{H}_2\text{CO}_3$  and  $\text{NH}_3$  is calculated using the relations given by *Millero et al.* (2007) and *Bell et al.* (2008) respectively. The activity of  $\text{H}^+$  is calculated using the charge balance of the resulting geochemical system as well as the law of mass action for the dissociation of water:

$$[\text{H}^+][\text{OH}^-] = K_w, \quad (3.34)$$

where  $K_w = 10^{-14}$  is the dissociation constant and  $[\text{H}^+]$  and  $[\text{OH}^-]$  are the activities of  $\text{H}^+$  and  $\text{OH}^-$  respectively. The charge balance in general requires that:

$$\sum_{\kappa=1}^{\text{charged components}} z^\kappa m^\kappa = 0, \quad (3.35)$$

where  $z^\kappa$  is the charge of component  $\kappa$  and  $m^\kappa$  its molality. The resulting charge balance for the specific geochemical system can be written as:

$$0 = 2m^{\text{Ca}^{2+}} + m^{\text{Na}^+} + m^{\text{NH}_4^+} + m^{\text{H}^+} - 2m^{\text{CO}_3^{2-}} - m^{\text{HCO}_3^-} - m^{\text{Cl}^-} - m^{\text{OH}^-}. \quad (3.36)$$

In this equation, the molalities  $m^\kappa$  of  $\text{NH}_4^+$ ,  $\text{CO}_3^{2-}$ ,  $\text{HCO}_3^-$ , and  $\text{OH}^-$  are expressed as a function of  $m^{\text{H}^+}$  using the laws of mass action for the dissociation reactions (Eqs. (1.2), (1.3), (1.4), and (3.34)). The equation is then solved using a Newton algorithm and the resulting  $[\text{H}^+]$  is used to calculate the molalities of the other chemical species involved in the above-mentioned dissociation reactions.

## Activities

For the dissociation reactions discussed in Section 3.1.3, activities are not considered, as empirical relations are used accounting for the activities by the means of apparent dissociation constants, which include the activities and are thus dependent on the geochemistry (*Millero et al.*, 2007; *Bell et al.*, 2008). To determine the saturation index of calcite (Eq. (3.12)), the activities of carbonate and calcium are considered, as precipitation and dissolution are key processes for MICP. The activities of carbonate and calcium are calculated using Pitzer equations as proposed by *Clegg and Whitfield* (1995); *Millero et al.* (1984); *Wolf et al.* (1989).

### 3.1.4. Numerical implementation

The model of *Ebigbo et al.* (2012) is implemented in the simulator MUFTE\_UG. The discretization used is the fully-coupled vertex-centered finite volume (box) scheme (*Helwig*, 1997) for space and the implicit Euler method for time.

## 3.2. Interaction between modeling and experiments

The model of *Ebigbo et al.* (2012) was developed using data from four sand column experiments (C1, C2, C3, and C4) conducted at Montana State University. Two experiments were used to calibrate the model and an additional two columns were used to validate the calibrated model (*Ebigbo et al.*, 2012). The model predictions of the effluent pH match the experimental measurements well for all columns, even though only the resulting calcite precipitation of C1 and C2 were used for calibration. The agreement between the measured and the predicted precipitate distribution for C3 and C4 is also good (*Ebigbo et al.*, 2012).

Additional experimental data are used in this work to improve the model further. Those experiments are used to investigate the model performance for changed experiment geometry, high-pressure environments, different porous media, changed injection medium composition, and ultimately a field-scale application.

For a high-pressure experiment (HP) using a Berea sandstone core as a porous medium instead of sand as in the columns (*Phillips*, 2013), using the model of *Ebigbo et al.* (2012) to predict both the pressure difference and the resulting calcite precipitate distribution shows that while the model of *Ebigbo et al.* (2012) is able to predict the reduction in porosity well the modeled pressure difference does not match the measured pressure difference (*Hommel et al.*, 2013). Fitting the critical porosity using the final measured values of porosity and permeability

improves the prediction of the final pressure difference, but especially in the first 100 h, the discrepancies remain (*Hommel et al.*, 2013). A preliminary 2D micro-model experiment using only biomass without calcite precipitation to clog the pore space gave some insight into the porosity-permeability relation. This experiment was similar to the 2D micro-model experiments conducted by *Connolly* (2015) measuring both the porosity reduction during MICP as well as the resulting increase in the pressure difference. However, the range of valid pressure measurements in those experiments and the artificial, high-porosity geometry of the 2D micro-models used do not allow for representative data sets to develop a porosity-permeability relationship for MICP. In the experiments by *Connolly* (2015), an engineered, fluorescent strain of *Escherichia coli* (*Connolly et al.*, 2013) is used as the calcite-precipitation-inducing microbe, as the fluorescence of the cells allows the biofilm volume to be measured by imaging. However, the particular strain of *E. coli* used in the 2D micro-model forms much thicker biofilms than *S.pasteurii*, the bacteria used in all other experiments, further limiting the potential value of the experimentally measured porosity-permeability relationship. Thus, experimental investigations (*Connolly*, 2015) of the change of porosity and permeability during MICP as well as numerical, pore-scale-based investigations (*Qin and Hassanizadeh*, 2015) of the change of porosity and permeability due to bioclogging have not yet been successful in closing the gap in our knowledge. The HP experiment, the modeling related to it, and the investigation of the porosity-permeability relation for MICP are discussed in Section 4.1.

For another set of sand column experiments, the duplicate columns D1 and D2, the model of *Ebigbo et al.* (2012) is not able to predict the resulting distribution of calcite precipitates as well as for the columns C1-C4. This mismatch can probably be attributed to the change in the composition of the injected MICP medium (*Hommel et al.*, 2015b). Revising the ureolysis kinetics according to the experimental findings on whole-cell catalyzed ureolysis by *Lauchnor et al.* (2015) and recalibrating the model by inverse modeling using an extensive data set of experimental measurements including spatially and temporally resolved ammonium and calcium concentrations lead to a revised model able to predict results of both sets of column experiments (C4 as well as D1 and D2) with a reasonable accuracy (*Hommel et al.*, 2015b). The revision of the model of *Ebigbo et al.* (2012) is discussed in detail in Section 4.2. The setup of experiment D2 is additionally used as a reference setup in the numerical investigation of the influence of initial biomass distribution and the injection strategy on the result of MICP, see Section 5.1.

In addition to the data from the new column experiments, experimental results of a two-dimensional radial-flow experiment conducted within a bicycle rim (BR) are used for the model recalibration as detailed in Section 4.2. For this experiment, both the geometry and the continuous injection strategy are different from the experiments previously discussed. The

recalibration of the revised model to the final calcite distribution of BR lead to parameter values different from those obtained using the column experiments C4, D1, and D2, indicating that some of the processes influenced by the geometry of the experiment, most probably the interactions of biomass and hydraulics, need further revision and experimental investigation (*Hommel et al.*, 2015b).

To improve the understanding of the attachment of *S. pasteurii* to sand, column experiments are conducted using the injection strategies of the experiments D1 and D2 (*Hommel et al.*, 2015a). Six columns are inoculated with an identical concentration of *S. pasteurii*. Two duplicate columns each are rinsed and the attached cells measured directly after the inoculation, after an 8 h batch period, and after the 8 h batch period plus an additional 18 h injection of growth medium (*Hommel et al.*, 2015a). Due to the difficulties associated with getting accurate and reproducible measurements of attached cells, a numerical study on the influence of the initial amount and distribution of attached biomass on MICP is conducted. The results are compared with the influence of the injection strategy in Section 5.1.

Finally, the model is used to gain insight into a field application, where a horizontally fractured sandstone at 341 m below ground surface was sealed within a few days using MICP (*Cunningham et al.*, 2014). The model results and a brief comparison with the experimental data are presented in Section 5.2.

### 3.3. Implementation in DuMu<sup>X</sup>: solution scheme and changes

originally, the model of *Ebigbo et al.* (2012) was implemented in MUFTE\_UG, but the implementation discussed further in this thesis is in DuMu<sup>X</sup>. The open-source simulator DuMu<sup>X</sup> (DUNE for Multi-Phase, Component, Scale, Physics, ...) (*Flemisch et al.*, 2011) is based on DUNE (Distributed and Unified Numerics Environment), which is a framework for solving partial differential equations (*Bastian et al.*, 2008a,b). The discretization used is, identically to *Ebigbo et al.* (2012), the fully-coupled vertex-centered finite volume (box) scheme (*Helmig*, 1997) for space and the implicit Euler method for time. The resulting system of equations is linearized using the Newton-Raphson method and solved using the BiCGStab solver (*van der Vorst*, 1992).

Few changes were made in the course of the transition; they mainly concern the calculations of the mutual dissolution of CO<sub>2</sub> in brine and that of water in the CO<sub>2</sub>-phase. Additionally, the value for the liquid diffusion coefficient was set to a literature value of  $1.587 \cdot 10^{-9} \text{m}^2/\text{s}$  given in *Riquelme et al.* (2007) for the diffusion of NaCl in water.

In the model as implemented in DuMuX, the dissolution of CO<sub>2</sub> in brine (or water) and the dissolution of water in CO<sub>2</sub> is calculated according to *Spycher and Pruess* (2005), with the equilibrium conditions in both phases being dependent on the pressure, temperature and salinity of the aqueous phase. For further details on the phase composition calculations, see *Darcis* (2012).



## 4. Model improvements

### 4.1. Improvement of the porosity-permeability relation \*

Reliable technologies and engineering measures to prevent leakage from reservoirs in the case of unexpected problems is crucial for both the safety and efficiency of carbon capture and storage (CCS). One of the possible sealing technologies is microbially induced calcite precipitation (MICP). Bacteria, calcium and other reactants are injected into the rock, where the metabolism of the bacteria alters the geochemistry, resulting in a super-saturation of calcite. The subsequent calcite precipitation reduces or even completely clogs the pore space, minimizing possible leakage pathways. Experiments in sand-filled columns (*Ebigbo et al.*, 2012) and rock cores (*Phillips et al.*, 2013b) show that it is possible to control the distribution of the precipitated calcite through the column as well as to reduce the permeability of a fractured rock due to mineralization. A model describing the relevant processes of MICP has been developed and validated using the experimental data of the sand column experiments (*Ebigbo et al.*, 2012).

#### 4.1.1. Sandstone core simulations

Recently, MICP experiments were conducted under reservoir-like pressure conditions at 7 MPa using a large fractured sandstone core (*Phillips et al.*, 2013b) as well as small cores of the same sandstone, 5.08 cm in length and 2.54 cm in diameter (*Phillips*, 2013). In this work, the existing model is used to simulate a small sandstone core experiment to find out if the model is able to describe MICP under more realistic conditions, including reservoir-like pressure and a consolidated porous medium.

---

\*Section 4.1.1 is published in J. Hommel, A. B. Cunningham, R. Helmig, A. Ebigbo, and H. Class, Numerical Investigation of Microbially Induced Calcite Precipitation as a Leakage Mitigation Technology. Energy Procedia, 40C (2013), 392–397, DOI: 10.1016/j.egypro.2013.08.045.

**Table 4.1.:** Differences between experiments used for validation of the model (sand columns C1 and C2, *Ebigbo et al. (2012)*) and the experimental setup (high-pressure sandstone core (HP) *Phillips (2013)*) considered in this investigation.

Experiment	Length	Effluent pressure	$\frac{\text{mol}_{\text{Ca}}}{\text{mol}_{\text{urea}}}$	Resuscitation	$\phi_0$	$K_0$
C1 & C2	61 cm	0.1 MPa	3.7	When appropriate	0.4	$2 \cdot 10^{-10} \text{ m}^2$
HP	5.08 cm	7 MPa	1	After $\text{Ca}^{2+}$ injections	0.18	$3.7 \cdot 10^{-14} \text{ m}^2$

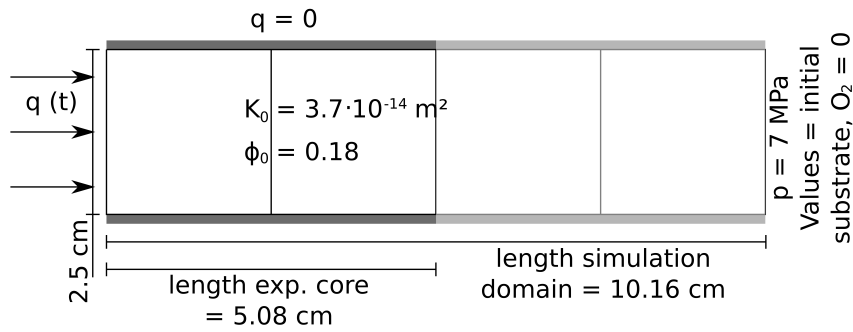


**Figure 4.1.:** Sketch of the domain, boundary conditions and the grid used for simulation.

## Methods and results

The geometry and properties of the porous medium as well as the boundary conditions were adapted to match the conditions of the high-pressure, sandstone-core experiment. Table 4.1 shows the main differences in the porous media, injection and geometry parameters between the new sandstone-core experiment described in *Phillips (2013)* and the sand-filled column experiments, which were used to validate the model in *Ebigbo et al. (2012)*.

Figure 4.1 shows a sketch of the simulation domain with the grid of 4 cells and the boundary conditions. On the left, there is a periodically changing injection of different aqueous media in accordance with the experimental injection scheme. The injected media are equivalent to those in *Phillips et al. (2013b)*. The top and bottom are Neumann no-flow boundaries. The outlet on the right-hand side is implemented as a Dirichlet boundary. For this boundary, all values are set to the initial value except for substrate and oxygen, which are set to zero. The simulation domain is set twice as long as the experimental core in order to avoid boundary effects.

After simulation of the experiment, the simulated permeability was reduced by a factor of

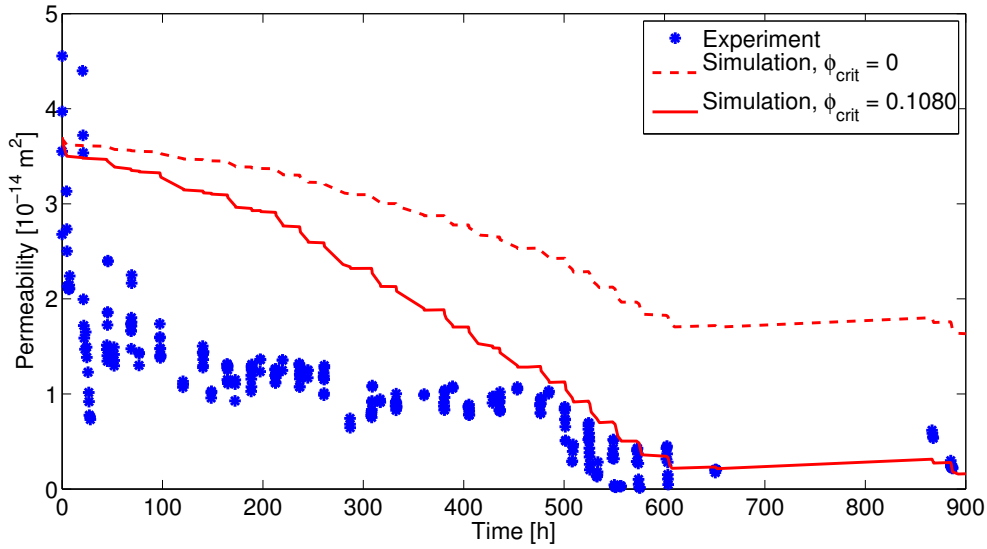


**Figure 4.2.:** Comparison of measured (blue stars) and simulated (red lines) permeability over time. The dashed line represents the permeability as calculated in the original model described in *Ebigbo et al.* (2012), whereas the solid one shows the permeability after fitting  $\phi_{\text{crit}}$  in Equation (3.31) to the experimental data.

roughly 2, whereas the experimental permeability was reduced by a factor of about 10. The implemented relation of porosity to permeability is of a Verma-Prues type, see Equation (3.31).

In the original model, validated against experiments in sand columns,  $\phi_{\text{crit}}$  has been set to zero (*Ebigbo et al.*, 2012). Considering that the permeability of a consolidated sandstone rock may tend to zero before its porosity does, a second simulation was run with a value of  $\phi_{\text{crit}} = 0.108$ , fitted using the measured initial and final porosity and permeability inserted in Equation (3.31). In Figure 4.2, the permeabilities of both simulations are compared with the permeability calculated from the measured pressure drop during injections in the experiment. For the simulation with the fitted critical porosity, the simulated permeability fits the experimentally measured data quite well after a time of 500 hours. The initial drop in measured permeability is not matched by any simulation.

Table 4.2 shows the volume fraction of calcite in the inlet half and the effluent half of the core, the average volume fractions of biofilm and calcite, and the resulting average porosity and permeability for each simulation and for the experiment. Results of simulations with finer discretizations, which are not shown here, are not significantly different from the 4-cell grid results.

The simulation results for calcite decrease with the distance from the inlet, which contradicts the results of the experiment, where the effluent half of the core contains more calcite than

**Table 4.2.:** Comparison of simulated and measured volume fractions of calcite, average volume fraction of biofilm, average porosity and mean permeability at the end of the experiment. The experimental volume fraction of biofilm is calculated as  $\phi_f = \phi_0 - \phi - \phi_c$ , using Equation (3.32).

	inlet $\phi_c$	effluent $\phi_c$	Avg. $\phi_c$	Avg. $\phi_f$	Avg. $\phi$	Mean K
Experiment	0.035	0.039	0.037	0.006	0.137	$2.4 \cdot 10^{-15} \text{m}^2$
Simulation, $\phi_{\text{crit}} = 0$	0.03355	0.02947	0.03151	0.01058	0.1379	$16.3 \cdot 10^{-15} \text{m}^2$
Simulation, $\phi_{\text{crit}} = 0.108$	0.03353	0.02943	0.03148	0.01045	0.1381	$1.6 \cdot 10^{-15} \text{m}^2$

the inlet half. Average volume fractions of calcite are lower for both simulations than for the experiment. However, in a control core, 2.5 mg calcite are measured per g of sandstone (Phillips, 2013), which yields an initial volume fraction of 0.002. Considering this initial calcite, the difference between simulated and experimental calcite is less than 10 % of the measured volume fraction. Biofilm volume fractions are higher in the simulations, but the low volume fraction of biofilm in the experiment might be due to decay prior to the porosity measurement, since the porosity was not measured until weeks after the end of the experiment. Additionally, some biofilm might have been removed by detachment during the permeability measurements. Fitting  $\phi_{\text{crit}}$  increases the calculated shear stresses in the second simulation, as the injection rate is identical while the permeability is reduced compared with the simulation with  $\phi_{\text{crit}} = 0$  (Eq. (3.31)). This results in an increased detachment of biofilm, see Equations (3.27) and (3.28). The volume fraction of precipitated calcite decreases accordingly, since the amount of biofilm determines the amount of catalytic enzyme (Eqs. (3.6) and (3.7)). However, this decrease in biofilm and precipitated calcite for the simulation with the fitted  $\phi_{\text{crit}}$  is very small. The average permeability for the simulations is calculated as a harmonic mean of the local permeabilities.

## Conclusions

The model is capable of simulating MICP under reservoir-like conditions and an injection scheme different from the one used for validating the model, as shown in Table 4.1. Only the simulated permeability deviated from the measured values for the direct implementation of the experimental setting in the existing model as described in Ebigbo *et al.* (2012). Fitting the critical porosity in the porosity-permeability relation led to the simulated permeability matching the measured one for the last 450 hours of the experiment. For the first half of the experiment, processes occur that cannot be described by the model's current implementation of the porosity-permeability relation. We have a hypothesis which explains the dramatic reduction of permeability during the first 100 hours of the experiment. Contrary to the

implemented porosity-permeability relation, relatively small volumes of biofilm might in reality drastically reduce the permeability due to inhomogeneous distribution in the pore space. This inhomogeneity would change the shape of the pores or eventually clog pore throats, shutting off possible flow paths. This explanation is supported by a measured change in the pore-size distribution, which shows selective plugging of specific pore sizes (*Phillips*, 2013).

## Outlook

To show that MICP is a feasible sealing technology for liquid storage reservoirs in the subsurface, further experiments need to be conducted. These experiments will include larger, more complex settings such as heterogeneous porous media, two-phase flow which cannot be simplified as one-dimensional as the experiment in this work or in *Ebigbo et al.* (2012). To gain a better understanding of the permeability reduction due to MICP and test our hypothesis, we will perform additional micro-model experiments with defined and known pore-size distributions. In those micro-models, the permeability and porosity can be measured continuously and non-destructively during MICP. With these porosity and permeability data sets, it will be possible to determine which processes lead to the initial decrease in permeability at the beginning of MICP. Once those processes are identified, the parameters of the appropriate porosity-permeability relation can be fitted to the experimental observations.

### 4.1.2. Literature review on porosity-permeability relations

Most porosity-permeability relations are intended to estimate the permeability of a given porous medium based on constant properties such as the porosity and characteristic grain or pore geometry. The most widely used equation was originally published by *Kozeny* (1927) and later modified by *Carman* (1937):

$$\frac{\Delta p}{L} = \frac{180\mu}{\Phi_s^2 D_p^2} \frac{(1-\phi)^2}{\phi^3} v, \quad (4.1)$$

where  $\frac{\Delta p}{L}$  is the pressure difference over the length  $L$  of the sample,  $\Phi_s$  is the sphericity, a particle geometry parameter, and  $D_p$  is the characteristic particle diameter. With Darcy's law (Equation (2.10)), the Kozeny-Carman equation can be reformulated to directly estimate the permeability:

$$K = \frac{\Phi_s^2 D_p^2}{180} \frac{\phi^3}{(1-\phi)^2}. \quad (4.2)$$

Although proposed to estimate the permeability for a constant porous medium, the Kozeny-Carman relation or relations derived from it are widely used to estimate the changes in permeability due to changes in porosity resulting from mineral precipitation or biofilm accumulation. What is used in many approaches is relating the current permeability to an initial or reference permeability by the Kozeny-Carman relation (Equation (4.2)) (e.g. *van Wijngaarden et al.*, 2011, 2013) or some simplified relations (e.g. *Ebigbo et al.*, 2010, 2012; *Bernabe et al.*, 2003; *Verma and Pruess*, 1988). Negligible geometry changes ( $\Phi_s, D_p \approx \text{constant}$ ) are commonly assumed. For the original Kozeny-Carman equation, this results in:

$$\frac{K}{K_0} = \frac{\phi^3 (1 - \phi_0)^2}{\phi_0^3 (1 - \phi)^2}, \quad (4.3)$$

where  $K_0$  and  $\phi_0$  are the initial or reference values of  $K$  and  $\phi$  respectively. For mineral precipitation in porous media, some porosity-permeability relations have been derived by upscaling considerations and additional empirical relations have been proposed. Those relations are summarized in the top part of Table 4.3.

For the growth of biofilms in porous media, many porosity-permeability relations are available, most of them derived analytically using approaches on the pore or pore-network scale, but none of these relations is widely used. Selected relations are summarized in the middle part of Table 4.3. A pore-network study by *Qin and Hassanizadeh* (2015) finds no unique relationship between the porosity reduction by biomass accumulation and the resulting permeability. Instead, *Qin and Hassanizadeh* (2015) observe that the relation is rather dependent on the biomass morphology and the operating conditions.

However, the effect of bioclogging is strongly dependent on the experimental setup. In a 1D column, for example, the permeability may decrease extremely while for the same porosity reduction in a 2D setup, the overall permeability is hardly affected as long as the flow is able to bypass the clogged areas (*Thullner*, 2010) This is one of the reasons why obtaining a generally valid porosity-permeability relation for bioclogging or biomineralization or even upscaling from 1D column experiments to 2D or 3D setups is extremely difficult (*Thullner*, 2010).

In modeling, usually the relations for mineral precipitation are used (e.g. a *Verma and Pruess* (1988) relation with modified exponent in *Ebigbo et al.* (2010, 2012)) or, in the case of *Cuthbert et al.* (2013) where the reduction of a single fracture's transmissivity is modeled, the reduction is calculated based on geometric considerations and the contribution of the biomass is neglected. *van Wijngaarden et al.* (2013) use the Kozeny-Carman equation (Eq. (4.2)) with  $\Phi_s = 1$  and assuming a constant  $D_p$ , the permeability reduction due to biomass is neglected. In many

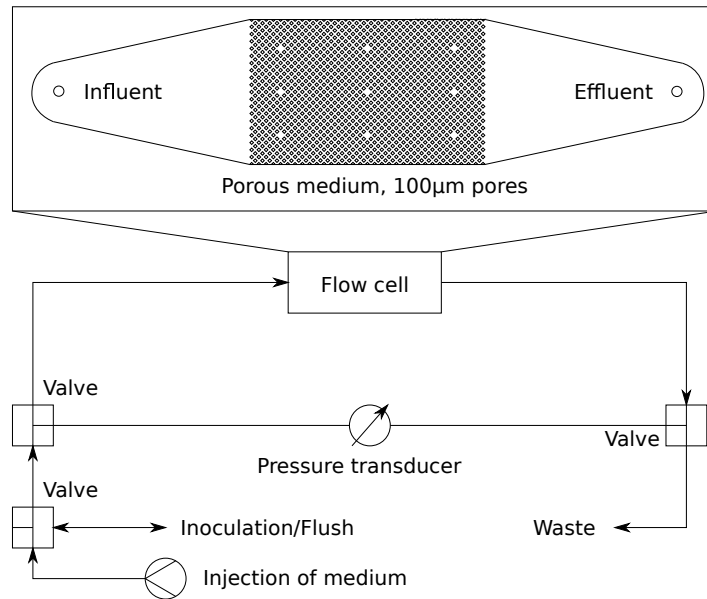


Figure 4.3.: Sketch of the micro-model experiment setup.

studies, the models even completely neglect changes in the permeability (e.g. *Martinez et al.*, 2014; *Barkouki et al.*, 2011).

### 4.1.3. Micro-model investigation

As the model's predictions of the permeability during MICP did not match the experimental results very well, a micro-model experiment was conducted at Montana State University<sup>†</sup> to improve the understanding of pore space alteration due to biofilm growth and calcite precipitation and their effect on pore morphology. The porous region of the micro-model discussed here has a regular 2D geometry with a height of 100  $\mu\text{m}$  and a pore size of 100  $\mu\text{m}$ , see Figure 4.3. Only biomass attachment and growth, not the calcite precipitation, is investigated in this experiment. Follow-up experiments as described in *Connolly* (2015) included the precipitation of calcite and additionally had similar pore widths (112  $\mu\text{m}$ ), but a height of only 18  $\mu\text{m}$ .

The experiment is conducted at a temperature of 37°C to increase the growth rate of the fluorescent strain of *E. coli* MJK2 used to grow the biofilm. Growing the culture from frozen stock and inoculation is done as described in *Connolly et al.* (2013). After inoculation of the micro-model, growth medium according to *Connolly et al.* (2013) is injected continuously

<sup>†</sup>The microscopy and image analysis for this experiment was done by James M. Connolly at Montana State University.

**Table 4.3:** Porosity-permeability relations proposed to account for the permeability reduction caused by changes in porosity related to mineral precipitation and dissolution (top), biomass accumulation only (middle), and combined biofilm growth and mineral precipitation (bottom).

Source	Relation $\frac{K}{K_0} =$	Comment
<i>Verma and Pruess</i> (1988); <i>Lai et al.</i> (2014)	$\left(\frac{\phi - \phi_{\text{crit}}}{\phi_0 - \phi_{\text{crit}}}\right)^\epsilon$	Derived by upscaling from pore size. Here, $\phi_{\text{crit}}$ is the critical porosity, at which $K = 0$ and is $\epsilon$ an exponent. Both $\phi_{\text{crit}}$ and $\epsilon$ are specific to a porous medium.
<i>Berrabe et al.</i> (2003)	$\left(\frac{\phi}{\phi_0}\right)^\eta$	Empirical relation for mechanical deformation as well as mineral dissolution and precipitation, where the exponent $\eta$ is related to changes in the ratio of effective to non-effective porosity.
<i>Tsygkin and Woods</i> (2005)	$\frac{1 - e^{\theta\phi}}{1 - e^{\theta\phi_0}}$	For salt precipitation due to decompression and evaporation in a single fracture. Here, $\theta$ is a parameter describing the relative impact of evaporation and advection.
<i>Lai et al.</i> (2014)	$\left(\frac{\phi}{\phi_0}\right)^3 \left(\frac{(1 - \phi_0)^{2/3} + E_1(\phi_{\text{end}} - \phi_0)^{2/3}}{(1 - \phi)^{2/3} + E_1(\phi_{\text{end}} - \phi)^{2/3}}\right)^2$	This Fair-Hatch relation is derived from dimensional analysis for dissolution of minerals. Here $E_1$ is a parameter and $\phi_{\text{end}}$ is the final porosity after complete dissolution of the soluble mineral.
<i>Lai et al.</i> (2014)	$\frac{\phi^3(1 - \phi_0)^2}{\phi_0^3(1 - \phi)^2}$	See Eq. (4.3).
<i>Vandewere et al.</i> (1995)	$d \left(\frac{\phi}{\phi_0}\right)^2 (1 - d) \frac{k^{\text{bio}}}{(1 - \phi/\phi_0)(1 - k^{\text{bio}})}$	Model considering both biomass growth as biofilm and as plugs. $d = d(\phi/\phi_0)$ distributes biomass into biofilm or biomass plugs and $k^{\text{bio}} \ll K$ is the residual permeability of a biomass plug.
<i>Seki and Mizasaki</i> (2001)	$\left(1 - \frac{((\phi_0 - \phi)/(\beta_e - \beta_e\phi_0) + 1)^{1/3} - 1}{(\tau/(1 - \phi_0))^{1/3} - 1}\right)^3$	Here, $\tau$ is a shape factor and $\beta_e$ a so-called enveloping factor describing the ratio of the volume occupied by biomass to the volume that could be occupied for a given maximum biofilm thickness.
<i>Thalner et al.</i> (2002) colony model	$a \left(\frac{\phi - \phi_{\text{crit}}}{\phi_0 - \phi_{\text{crit}}}\right)^3 + (1 - a) \left(\frac{\phi - \phi_{\text{crit}}}{\phi_0 - \phi_{\text{crit}}}\right)^2$	Derived from pore network models considering exclusively colonies. Here $a$ is a fitting parameter and $\phi_{\text{crit}}$ the critical porosity, at which $K = 0$ .
<i>Thalner et al.</i> (2002) biofilm model	$\left(\left(\frac{\phi - \phi_{\text{crit}}}{\phi_0 - \phi_{\text{crit}}}\right)^b + k^{\text{min}}\right) \frac{1}{1 + k^{\text{min}}}$	Derived from pore network models considering exclusively biofilm. here, $b$ is a fitting parameter and $\phi_{\text{crit}}$ the critical porosity, at which $K$ is equal to the minimum permeability $k^{\text{min}}$ .
<i>Ehligbo et al.</i> (2012)	$\left(\frac{\phi - \phi_{\text{crit}}}{\phi_0 - \phi_{\text{crit}}}\right)^3$	Using a Verma-Pruess relation ( <i>Verma and Pruess</i> , 1988) with $\epsilon = 3$ .
<i>van Wijngaarden et al.</i> (2013)	$\frac{\phi^3(1 - \phi_0)^2}{\phi_0^3(1 - \phi)^2}$	See Eq. (4.3), considering only changes in porosity due to calcite.

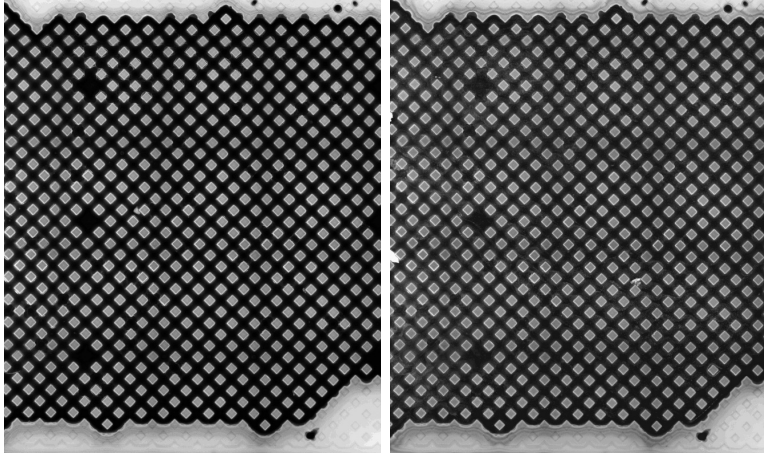


**Figure 4.4.:** Depth-averaged microscopy images of the first half of the micro-model’s porous region. Flow is from left to right. The left shows the clean porous medium before inoculation, the right shows the final biofilm developed within the porous medium after 13.6 h.

at a rate of  $1 \text{ ml/h}$ . The pressure is recorded continuously using a pressure transducer and microscopy images are taken at intervals of 2 h (Table A.1).

A Navier-Stokes model is used to calculate the hydraulic losses over the micro-model, including the porous, the influent, and the effluent region *Connolly* (2015). This hydraulic loss is compared with the measured pressure difference for the empty micro-model to calculate the hydraulic losses in the tubing between the pressure transducer and the micro-model, see Figure 4.3. Assuming the hydraulic losses outside the porous region are constant, the resulting pressure difference over the porous region can be calculated. The pressure difference in the porous region alone is used to calculate the experimental permeability using an inverse Darcy equation (Equation (2.10)). Confocal laser scanning microscopy is used to measure the biofilm volume in this and the follow-up experiments by *Connolly* (2015). The initial and final microscopy images are shown in Figure 4.4.

An attempt is made to improve the porosity-permeability relationship for MICP. Two approaches are investigated, all based on the relation from *Ebigbo et al.* (2012) used previously. The first approach is to fit the exponent of the relation, the second is to find a shape coefficient  $S$  as a function of the biofilm volume fraction.  $S$  is a factor to the relation used previously and is assumed to account for changes in the pore geometry and connectivity (e.g. the plugging of pore throats) due to biofilm. This second approach is motivated by the fact that the largest discrepancies between model results and measurements for the HP experiment occur during the early time period, when little calcite precipitated and the porosity reduction can be mainly attributed to the presence of biofilm. This results in a porosity-permeability relation:

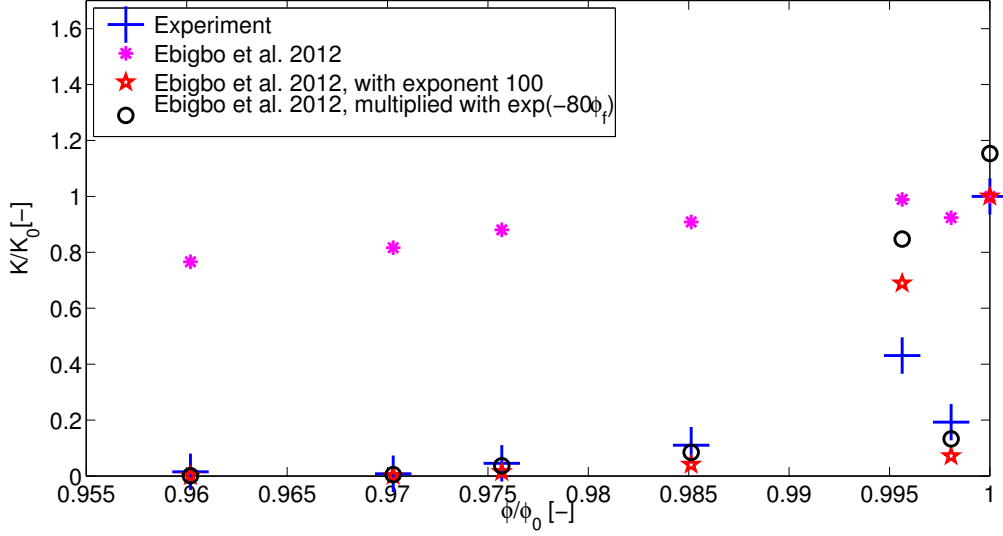


**Figure 4.5.:** Permeability and porosity measured in the first, biomass-only micro-model experiment. And the permeability predictions based on the measured porosity using different relations.

$$K = K_0 \left( \frac{\phi - \phi_{\text{crit}}}{\phi_0 - \phi_{\text{crit}}} \right)^n S. \quad (4.4)$$

Fitting to the porosity and permeability data (Table A.1) results in the new relations for both approaches shown in Figure 4.5, with an exponent of  $n = 100$  and  $S = 1$  for the first approach and  $n = 3$  and  $S = e^{-80\phi_f}$  for the second.

#### 4.1.4. Conclusions from the micro-model investigation

As shown in Figure 4.6, the model results for the permeability in the HP experiment improve using the relation resulting from the second approach:

$$K = K_0 \left( \frac{\phi - \phi_{\text{crit}}}{\phi_0 - \phi_{\text{crit}}} \right)^3 e^{-80\phi_f}. \quad (4.5)$$

However, even with this updated porosity-permeability relation (Equation (4.5)), the initial reduction of the permeability directly after the inoculation for the HP experiment is still underestimated by the model. This is surprising as the relation is fitted to the results of a 2D setup and the HP experiment setup is rather 3D, although it is modeled as a 1D setup in Section 4.1.1. Usually, porosity-permeability relations obtained at a lower dimensional level

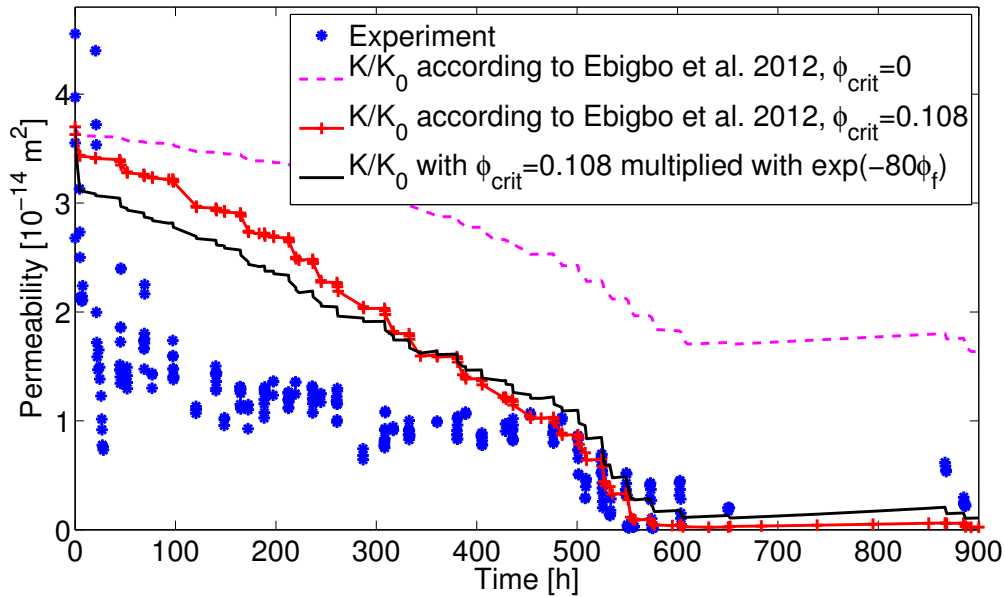


**Figure 4.6.:** More sophisticated porosity-permeability relations improve the permeability predictions slightly. The additional shape coefficient  $S = e^{-80\phi_f}$  is determined by fitting to results of micro-model experiments.

overestimate the permeability when used for higher dimensions, as more bypassing of clogged areas is possible for higher dimensions (e.g. *Thullner*, 2010).

The regular pattern of the porous region of the micro-model as well as the high porosity are unrealistic for the sandstone core discussed previously. Additionally, the bacteria used (fluorescent strain of *E. coli*) form much thicker biofilms than *S.pasteurii*, the bacteria used in the high-pressure core as well as the other experiments. However, the fluorescent *E. coli* strain is still used, as biofilm is difficult to image since it provides low X-ray contrast and the fluorescence allows for biofilm volume measurement by confocal laser scanning microscopy (*Connolly*, 2015). Further, the range of porosity and pressure measurements is limited in the preliminary experiment with biofilm only (see Figure 4.5 and Table A.1) as well as in the experiments from *Connolly* (2015). This, together with the artificial, high-porosity geometry of the 2D micro-models, does not yield representative data sets to develop a porosity-permeability relationship for MICP.

Also in the follow-up experiments by *Connolly* (2015), the best fit of the porosity-permeability relation is achieved with a similar relation, with the parameters in Equation (4.4) fitted to  $S = 1$ ,  $n = 62$  and  $\phi_{\text{crit}} = 0$ . In *Connolly* (2015), full MICP is investigated instead of only biomass growth. However, the study does not add much insight as it has identical limitations, such as a very high initial porosity, uniform pore geometries, and a very limited range of

porosity and permeability reductions.

For further investigations of the porosity-permeability relation during MICP, more experimental data are needed, especially at realistically low porosities and for changes in permeability of several orders of magnitude. Finally, with improved imaging technologies, it might be possible to use 3D micro-models as well as *S.pasteurii* for the investigation of the porosity-permeability relation, further increasing the similarity to the conditions at which the other experiments as well as the field applications are conducted.

The literature review in Section 4.1.2 indicates that biomass accumulation in porous media has different effects on permeability than mineral precipitation. In Table 4.3, the various relations proposed to describe the permeability change dependent on the change in porosity are, in general, more complex for the relations proposed for biomass accumulation than for mineral precipitation. This is supported by the results from the HP-experiment simulations (Figures 4.2 and 4.6), where the initial permeability reduction in the experiment due to biomass inoculation is not matched by the model predictions, but, during later times, the reduction due to calcite precipitation is predicted much more accurately with both relations used (Eq. (3.31) and (4.5)).

However, in the following Section 4.2 and Chapters 5 and 6, the more general porosity-permeability relation from *Ebigbo et al.* (2012) (Eq. (3.31)) is used because of the lack of experimental support for the porosity-permeability relation fitted to the micro-model data (Eq. (4.5)).

## 4.2. Improvement of the ureolysis rate equation <sup>‡</sup>

Models for simulating MICP processes have been developed by a number of authors (*Martinez et al.*, 2014; *Barkouki et al.*, 2011; *Cuthbert et al.*, 2013; *van Wijngaarden et al.*, 2013, 2011; *Ebigbo et al.*, 2012), each focusing on different processes. Often, the models are designed to match a series of experiments. Consequently, they focus on the processes of relevance in the corresponding experiments while neglecting other processes that might be relevant in the field.

The models presented by *Martinez et al.* (2014) and *Barkouki et al.* (2011) use a complex ureolysis rate equation (*Fidaleo and Lavecchia*, 2003) and a saturation-state-dependent precipitation rate, while neglecting changes in permeability and the processes related to bacterial transport, growth, and decay. As a result, the ureolytic activity is assumed to be constant over time for each point in space and the distribution of urease in space is described by a Gamma distribution (*Martinez et al.*, 2014) or an exponential function (*Barkouki et al.*, 2011).

In *Cuthbert et al.* (2013), a first-order kinetic model is assumed for ureolysis, and bacterial transport and attachment are modeled. The precipitation rate is assumed to be stoichiometric to the ureolysis rate. The impact of MICP on the fracture transmissivity is measured in the experiment and included in the model in dependence on a reduction of the fracture aperture related to the volume of precipitated calcite.

Michaelis-Menten kinetics are used to model the ureolysis rate in *van Wijngaarden et al.* (2013, 2011) and, like *Cuthbert et al.* (2013), these authors assume that the precipitation rate is proportional to the ureolysis rate. The permeability is decreased as a result of the porosity reduction caused by the precipitated calcite. A Kozeny-Carman relationship is used to calculate the permeability. Bacteria are assumed to be homogeneously distributed in *van Wijngaarden et al.* (2011), while *van Wijngaarden et al.* (2013) accounts for attachment and detachment due to adsorption and desorption respectively. For special cases, *van Wijngaarden et al.* (2013, 2011) propose analytical solutions.

*Ebigbo et al.* (2012) developed a complex two-phase model including component transport, kinetic reactions, and a reduction of porosity and permeability due to calcite precipitation and biofilm presence. This model uses a complex, biofilm-dependent ureolysis rate equation adapted from *Fidaleo and Lavecchia* (2003) and a calcite precipitation rate equation dependent on interfacial area and saturation state (*Zhong and Mucci*, 1989) as well as on dissolution kinetics (*Compton et al.*, 1989; *Chou et al.*, 1989). Additionally, the model accounts for

---

<sup>‡</sup>This section is published in J. Hommel, E. G. Lauchnor, A. J. Phillips, R. Gerlach, A. B. Cunningham, R. Helmig, A. Ebigbo, and H. Class, A revised model for microbially induced calcite precipitation - improvements and new insights based on recent experiments. *Water Resources Research*, 51 (2015)(5), 3695–3715, DOI: 10.1002/2014WR016503.

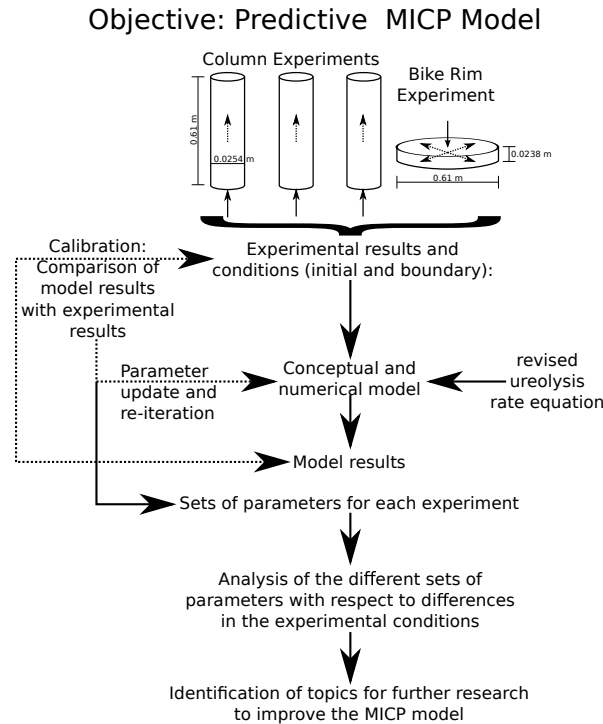


**Figure 4.7.:** Overview of steps taken in the course of model revision.

microbial processes such as attachment, substrate-dependent growth, decay, and detachment due to shear stress as well as for reduced porosity and permeability using a Verma-Pruess-type relationship (Verma and Pruess, 1988).

The model used in this study is an extension of the model presented in Ebigbo *et al.* (2012) after revisions such as the replacement of some of the fitted parameter values with updated literature values and an updated ureolysis rate equation (Lauchnor *et al.*, 2015). All rate equations, except the updated one for ureolysis, as well as the constitutive relationships used in Ebigbo *et al.* (2012) are assumed to be still valid.

The aims of this study are to investigate the predictive performance of the model developed in Ebigbo *et al.* (2012) (described in detail in Chapter 3) for new column experiments and a 2D radial flow experiment, to examine the effect of the implementation of a rate equation for ureolysis based on recent research on the ureolysis of *S. pasteurii* (Lauchnor *et al.*, 2015), and to assess the range of fitting-parameter values obtained by inverse modeling. This should lead to the identification of areas on which to focus further research, prioritizing future experimental investigations as well as defining strategies for the model development with the long-term perspective of a predictive field-scale MICP model. Figure 4.7 shows the sequential steps and objectives of this study.

### 4.2.1. Processes and recent experiments

#### Overview and experiments

The original model was calibrated for columns using a certain set of conditions (*Ebigbo et al.*, 2012). However, after changes in the solution chemistry subsequently implemented in the experiments, modeling results no longer accurately predicted the measurements. For a substantial revision of the complex model of *Ebigbo et al.* (2012), the processes needed to be reconsidered in detail. Our considerations and hypotheses are based on a series of new experimental data from column experiments similar to those described in *Ebigbo et al.* (2012).

Data from three column experiments are used in the inverse modeling and determination of the fitting parameters. One column from the previous study, Column 4 (C4), is used to ensure reproducibility. Two more column studies were performed with modifications to the previous study. As these columns were operated as duplicates, they are denoted column D1 and column D2.

All columns were constructed from clear PVC pipe of 2.54 cm diameter and 61 cm length, filled with 40-mesh quartz sand (0.5 mm effective filtration size, manufacturer information, Unimin Corp., Emmet, ID), packed under water and vertically positioned. They were inoculated with *S. pasteurii* and subjected to a 16 h attachment period, after which a 24 h growth period was initiated by continuous addition of growth medium in an upflow configuration at 10 ml/min. Following the growth period, calcium additions commenced, consisting of injecting two pore volumes of a medium containing calcium, followed by a no-flow period to allow reaction and precipitation to occur. This mineralization period was followed by injection of growth medium to resuscitate the microorganisms and the procedure was repeated until calcium had been injected 22 times for column C4 and 30 times for columns D1 and D2.

Differences between the operating parameters for the columns C4, D1 and D2 are presented in Table B.1, while the composition of injected fluids is given in Table B.2. The first modification to the columns D1 and D2 was a reduction in the  $\text{Ca}^{2+}$  concentration to 0.33 M, which is equal to the molar concentration of urea in the mineralization medium. Second, the no-flow period for biomineralization was reduced from 24 h to 4 h, as successfully implemented by (*Phillips et al.*, 2013b) to increase  $\text{Ca}^{2+}$ -precipitation efficiency and decrease the time necessary to achieve the desired permeability reduction. Finally, the column studies used in the improved model calibration were constructed with five sampling ports at locations 10, 20, 30, 40 and 50 cm downstream of the inlet. Ports were made by drilling 1.252 cm holes in the PVC and securing rubber stoppers in the holes, allowing for sampling of pore fluid via a 23 gauge needle

and 5 ml syringe. The sampling took place along the direction of flow and over time during the experiments, providing additional measurements for model calibration.

While columns D1 and D2 were operated, pore fluid was sampled from the ports at 1-hour intervals during selected no-flow mineralization periods. The effluent pH,  $\text{NH}_4^+$  and  $\text{Ca}^{2+}$  were monitored at the end of each mineralization and growth period, in addition to the  $\text{NH}_4^+$  and  $\text{Ca}^{2+}$  measured in sampling ports over time during mineralization periods. Viable bacterial counts were performed on effluent samples, ensuring that *S. pasteurii* remained the active organism during the experiments. Finally, the columns were cut into eight sections to measure the precipitated calcite.

Additionally, a 2D radial flow experiment was conducted in a radial flow reactor constructed from two Plexiglas plates and a bicycle rim (BR), which enabled us to investigate the influence of a radial flow field on MICP. The radial flow experiment is valuable for investigating differences between different fluid-dynamic cases and making the model more broadly applicable to various environments, especially for field-relevant radial flow conditions.

The radial flow reactor was constructed from two 31 cm-diameter, 1/4" Plexiglas plates that sandwiched a pack of the 40-mesh quartz sand, which was sealed on the outer diameter by squeezing the Plexiglas onto a metal ring (bicycle rim) with clamps. In between the Plexiglas and metal was a bead of Teflon putty which sealed the edge to prevent leaks when clamped tightly. Sixteen 1/4" NPT threads were inserted around the circumference of the top Plexiglas plate (outlet) as well as one thread in the center (inlet); these were all attached by barbed fittings to silicone tubing. The central inlet was connected via tubing to a peristaltic pump; the outlet tubes emptied into an elevated effluent collection tub.

The radial flow reactor was inoculated with 3 l of an overnight culture of *S. pasteurii* which was allowed to attach for 16.5 hours and then subjected to a 12-hour growth stage. After the growth period, a medium containing calcium was injected under constant flow conditions for 12 hours followed by an overnight precipitation period. At the termination of the experiment, the Plexiglas plates were removed and the sand was sampled at 2.5, 4, 6.5 and 9 inches from the center in eight radial directions. Relevant experimental design parameters are summarized in Table B.1, while Table B.2 gives the composition of the injected fluids.

Microbially, whole-cell-catalyzed ureolysis is the driving force of MICP, increasing pH to the pKa of  $\text{NH}_3\text{-NH}_4^+$  by the production of  $\text{NH}_3$ . At this pH, a substantial amount of carbonate is present in the solution (the pKa of  $\text{HCO}_3^- \text{-CO}_3^{2-}$  is approximately one order of magnitude higher), which in turn, in the presence of calcium ions, can lead to a supersaturation of calcium carbonate in the solution, thereby promoting the precipitation of calcium carbonate. The

dissociation coefficients of  $\text{H}_2\text{CO}_3$  and  $\text{NH}_3$  are calculated using relations given by *Millero et al.* (2007) and *Bell et al.* (2008) respectively.

Another key parameter is the distribution of biomass within the porous medium, since the presence of ureolytic microbes is a prerequisite for MICP. As the distribution of biomass is not exactly known for the MICP experiments, it is not possible to validate the equations governing the distribution of biomass directly by comparison with biofilm measurements. However, the ureolytic activity of the bacteria, which is monitored by measuring the product  $\text{NH}_4^+$  in recent column experiments, allows for an indirect evaluation of the ability of the model to predict the biomass distribution.

### Revised ureolysis kinetics

Most studies on ureolysis kinetics either focus on the kinetics of extracted enzyme (*Cuthbert et al.*, 2012; *Stocks-Fischer et al.*, 1999; *Tobler et al.*, 2011) or, when whole-cell systems are investigated, simplify kinetics to zero- or first-order reaction rates depending only on urea concentrations (*Cuthbert et al.*, 2012; *Ferris et al.*, 2003; *Okwadha and Li*, 2010; *Tobler et al.*, 2011). Few models for whole-cell systems use complex kinetics; e.g. (*Ebigbo et al.*, 2012) uses a Michaelis-Menten-type ureolysis kinetic adapted from *Fidaleo and Lavecchia* (2003).

Urease extracted from *S. pasteurii* has been shown to have higher half-saturation coefficients than plant urease and an optimum rate at a pH of 8 (*Stocks-Fischer et al.*, 1999), whereas the optimal pH determined for the jack bean urease in *Fidaleo and Lavecchia* (2003) is at a pH of 7. In whole-cell systems, additional mass-transfer (transport) processes of reactants and products across the cell wall and regulatory processes within the cells are likely to influence the observed reaction rates in the bulk medium. This has been circumvented in continuum scale approaches through lumped apparent kinetic parameters.

The kinetic rates of biofilm cells might be different from the kinetics of suspended cells, as described in *Carrera et al.* (2004). Even in the case of pure immobilized enzyme, there may be a decrease in the apparent reaction rates attributed to immobilization (*Bachmeier et al.*, 2002). Other studies observed no significant difference between the kinetics of suspended and biofilm cells (*Shreve and Vogel*, 1993; *Mirpuri et al.*, 1997). However, in thick biofilms, the diffusive transport of urea and  $\text{NH}_4^+$  within the biofilm might significantly reduce the apparent ureolysis rate. In the light of the available information on this topic, we consider the assumption of no significant difference between biofilm and suspended cell kinetics to be the most appropriate at this point, especially since no satisfactory parametrizations of the processes possibly leading to differences in the reaction kinetics are available on the Darcy scale.

In batch experiments, *Lauchnor et al. (2015)* investigated the influences of urea,  $\text{NH}_4^+$ , cell concentration, and pH of the medium on the ureolysis of whole cells of *S. pasteurii*. These new observations and measurements can be accounted for in the MICP model by adjusting the Michaelis-Menten kinetics and parameters:

$$r_{\text{urea}} = k_{\text{urease}} k_{\text{ub}} \rho_f \phi_f \frac{m^{\text{u}}}{m^{\text{u}} + K_{\text{u}}}. \quad (4.6)$$

$r_{\text{urea}}$  represents the revised rate of ureolysis according to *Lauchnor et al. (2015)*,  $k_{\text{urease}}$  the revised maximum activity of urease adapted from *Lauchnor et al. (2015)*,  $\rho_f$  and  $\phi_f$  the density and volume fraction of biofilm respectively,  $k_{\text{ub}}$  the mass ratio of urease to biofilm as given in *Bachmeier et al. (2002)*,  $m^{\text{u}}$  the molality of urea calculated from the water phase composition, and  $K_{\text{u}}$  is the half saturation constant for urea adapted from *Lauchnor et al. (2015)*.

To convert the new half-saturation constant given by *Lauchnor et al. (2015)*  $K = 355 \text{ mmol/l}$  to molalities  $\text{mol/kg}_{\text{H}_2\text{O}}$ , we assume that the concentrations used in the experiments did not affect the density. Thus, the half-saturation constant  $K_{\text{u}}$  in the model is set to  $0.355 \text{ mol/kg}_{\text{H}_2\text{O}}$ .

The value of the apparent urease activity  $k_{\text{urease}}$  in a whole-cell system is calculated by dividing the maximum reaction rate  $V_{\text{max}}$  by the urease content of a bacterial cell  $k_{\text{ub}}$ . According to *Bachmeier et al. (2002)*, the urease content in *S. pasteurii* is at most 1% of the dry cell mass. As the cells in *Lauchnor et al. (2015)* are in late exponential phase with urea-replete conditions, it is assumed that they produce the maximum amount of urease possible. Thus, for further analysis, it is assumed that  $k_{\text{ub}}$  is equal to 0.01. To convert the units of  $V_{\text{max}}$  given in *Lauchnor et al. (2015)* from  $\text{mmol/CFU}\cdot\text{h}$  (CFU standing for colony-forming units) to SI units for compatibility with the conceptual model, the same cell weight of  $2.5 \cdot 10^{-16} \text{ kg/CFU}$  is used as in *Ebigbo et al. (2012)*, originally given in *Norland et al. (1987)*. The resulting updated value for  $k_{\text{urease}}$  is  $706.7 \text{ mol/kg}_{\text{biomass}}\cdot\text{s}$ , calculated from the value of the maximum reaction rate  $V_{\text{max}} = 6.4 \cdot 10^{-9} \text{ mmol/CFU}\cdot\text{h}$  given in *Lauchnor et al. (2015)*.

As the observed ureolysis rates in *Lauchnor et al. (2015)* are directly proportional to the cell concentration, the exponent previously fitted in Equation (3.6) (*Ebigbo et al., 2012*) is set to  $n_{\text{ub}} = 1$  to achieve this linear dependence.

### Biofilm-hydraulics interactions

Accumulation of biofilm in a porous medium reduces the pore space available for flow, thereby reducing the permeability. For constant flow, it increases the effective flow velocity in the pores and thus the pressure gradient required to maintain constant flow. This process continues until

the pores are either completely filled with biofilm, blocking the flow, or a point is reached at which the increased detachment due to shear forces is in equilibrium with the accumulation of biomass by growth or attachment. Such an equilibrium will probably lead to local preferential flow paths where shear stress detaches the biofilm and neighboring regions are blocked by the biofilm. This can result in a sub-continuum-scale structure where different processes are dominant in each region on separate time scales. A dual-continuum approach as used in *Ebigbo et al.* (2010) is able to represent such sub-continuum-scale features on the Darcy scale. However, for the sake of computational efficiency and simplicity, as well as because of the lack of data available regarding biofilm transport processes, we refrain from using a dual-continuum approach in this study.

Microbial attachment is often modeled either as an adsorption equilibrium or according to colloid filtration theory. In the literature, there is a multitude of different approaches for describing attachment and detachment, depending on chemical conditions in the fluid or physical properties of the cells and the porous medium. For example, *Torkzaban et al.* (2008), observe that attachment of *Escherichia coli* increases with the ionic strength of the fluid. In microbially enhanced oil recovery simulations by *Nielsen et al.* (2014), microbial attachment is calculated either as adsorption following a Langmuir isotherm or according to the colloid filtration theory if the ratio of the cell size to the pore diameter is sufficiently large. However, in this study, it is assumed that the first-order-rate equation (see Equations (3.25) and (3.26) in Chapter 3) describing the transfer of biomass from the water phase (suspended biomass) to the biofilm phase by microbial attachment as given in *Ebigbo et al.* (2012) is still valid and only the values of the attachment coefficients have to be calibrated.

The total amount of biofilm in the system  $\phi_f \rho_f$  is determined by biofilm volume fraction and density.  $\phi_f$  is limited by the volume fraction available for biofilm ( $\phi_0 - \phi_c$ ) The smaller  $\rho_f$ , the smaller the maximum amount of attached biomass that can accumulate in the system. Additionally,  $\phi_f$  of a given amount of biofilm is higher for low  $\rho_f$ , thereby increasing its influence on porosity and permeability. Reduced permeability leads to increased detachment, as  $|\nabla p_w - \rho_w \mathbf{g}|$  increases. For complex 2D or 3D systems, low  $\rho_f$  might not necessarily increase detachment, as it inevitably would for 1D systems, but lead to increased clogging and the formation of flow channels, increasing heterogeneity and dispersivity. Thus, the biofilm density is a key parameter of the model which greatly influences the amount of interaction between biofilm and flow processes.

The biofilm densities provided in the available literature vary over two orders of magnitude. *Melo* (2005) gives dry matter biofilm densities from 2.5 to 91 kg/m<sup>3</sup>, *Zhang and Bishop* (1994) provide densities from 29 to 38 kg/m<sup>3</sup>, while *Paul et al.* (2012) measure dry densities ranging from 5 to 39 kg/m<sup>3</sup>. In *Taylor and Jaffé* (1990), the lowest value given is 2.5 kg/m<sup>3</sup>, while the

value used in the previous model is  $10 \text{ kg/m}^3$  (*Ebigbo et al.*, 2012). As described in *Paul et al.* (2012), biofilm density is variable in space and time, changing with shear stress and growth conditions. However, to our knowledge, no parametrization is currently available that can duly account for these processes in the context of such a model. Thus, in the model, the biofilm density is a constant value representing both the dry cell density as well as the total dry biofilm density, neglecting the contribution of extracellular polymers.

### Fitting procedure

The number of fitting parameters is reduced compared with *Ebigbo et al.* (2012) by replacing some fitted values with literature values as discussed in Section 4.2.3.

The fitting parameters of the conceptual model are the biofilm density  $\rho_f$ , the attachment coefficient of bacteria to existing biofilm  $c_{a,1}$ , and the attachment coefficient of bacteria to arbitrary solid surfaces  $c_{a,2}$ . It is assumed that the first-order-rate equation (Equation (3.25)) describing microbial attachment as given in *Ebigbo et al.* (2012) is still valid and only the values of the attachment coefficients have to be calibrated.

For some of the inverse model runs (Section 4.2.2),  $k_{ub}$ , the parameter that has been identified in *Ebigbo et al.* (2012) as being most sensitive, is included in the set of calibration parameters to improve fitting. This can be additionally interpreted as a test of the hypothesis that the ureolysis rates of suspended and biofilm cells are equal, since the value of  $k_{urease}$  was calculated using this assumption (see Section 4.2.1).

#### 4.2.2. Model calibration

Inverse modeling is used to recalibrate the numerical model implemented in the open-source simulator DuMu<sup>x</sup> (*Flemisch et al.*, 2011) using the experimental results of a variety of experimental setups. The grid used for the DuMu<sup>x</sup> model is chosen in such a way that the grid nodes match the experimental sampling locations. Additionally, a grid-convergence study confirmed that the resolution of the grid used is sufficiently fine to avoid grid-induced artifacts as shown in Figure B.1.

We perform inverse modeling rather than trial-and-error-based methods as used in *Ebigbo et al.* (2012) for the recalibration. Inverse modeling provides some analysis of parameter sensitivity and correlations between the different fitting parameters. To this end, iTOUGH2 and its PEST Protocol (*Finsterle*, 2007, 2011) were used as inverse model and coupled to the DuMu<sup>x</sup>

**Table 4.4.:** Selected parameter sets obtained by inverse modeling of column experiment D2 data, used for the plots in Figures 4.12, 4.13, and 4.14.

Name	$c_{a,1}$ [1/s]	$c_{a,2}$ [1/s]	$\rho_f$ [kg/m <sup>3</sup> ]	$k_{ub}$ [-]
low $c_{a,1}$ & $c_{a,2}$	$10^{-11.29}$	$10^{-14.59}$	4.80	0.0045
low $\rho_f$	$10^{-5.70}$	$10^{-6.66}$	0.062	0.01*
low $k_{ub}$	$10^{-4.81}$	$10^{-5.30}$	13.35	0.0014
best fit	$10^{-7.08}$	$10^{-6.07}$	6.9	0.00032

\*  $k_{ub} = 0.01$  not fitted, but set according to *Bachmeier et al. (2002)*.

forward model using parameter input files. For details of the inverse modeling procedure, we refer interested readers to *Finsterle (2007, 2011)*.

Various experimental results are used for the calibration of the model, including three column experiments, Column 4 (C4) (*Ebigbo et al., 2012*), two duplicate columns (D1, D2) and a 2D radial flow experiment within a bicycle rim (BR). The latter is used to investigate possible influences of the flow field on the fitted parameter values, which would indicate inconsistencies in the conceptual model. For experiments C4 and BR, only the calcite volume-fraction distribution data at the end of the experiment were available for calibration; see Table B.3. For experiments D1 and D2, additional in-situ measurements of pore-fluid  $\text{Ca}^{2+}$  and  $\text{NH}_4^+$  concentrations during the experiments at 10 cm intervals (i.e. 10, 20, 30, 40, and 50 cm from the injection point) are available and used as observation data for the inversions. These concentration measurements were conducted for each of the two experiments at six different points in time (i.e. 0, 0.5, 1, 2, 3 and 4 hours after the end of selected  $\text{Ca}^{2+}$ -rich injections), each measurement being repeated six (for D1) or seven (for D2) times; see Tables B.4 to B.7.

Finally, to be able to obtain parameter values averaged over all experimental setups, inverse modeling is performed using data of multiple experiments (C4, D2, BR), henceforth denoted (M). Since D2 is the experimental data set providing the most observations, the detailed discussions and plots (Figures 4.12, 4.13 and 4.14 in Section 4.2.3) focus on selected parameter sets obtained using this data set. These parameter sets are given in Table 4.4 while the respective parameter sensitivities as well as the correlations for the “best fit” parameter set are shown in Table 4.5.

The initial guesses of the fitting parameters are based on parameter values given previously (*Ebigbo et al., 2012*) and for later inverse model runs based on estimates from previous inverse model runs. The other important parameters for inverse modeling, the standard deviations of the groups of observations, were estimated using experimentally determined standard deviations of the individual measurements. For the data sets D1 and D2 with in-situ measurements of  $\text{Ca}^{2+}$ - and  $\text{NH}_4^+$ , the contribution of  $\text{CaCO}_3$  to the objective function was

**Table 4.5.:** Parameter and data sensitivities for the parameter sets given in Table 4.4 and direct correlations for the fitted parameters of the “best fit” as given by iTOUGH2.

Parameter and data sensitivity							
	$\rho_f$	$c_{a,1}$	$c_{a,2}$	$k_{ub}$	$\text{NH}_4^+$	$\text{Ca}^{2+}$	$\text{CaCO}_3$
low $c_{a,1}$ & $c_{a,2}$	22328.0	615970.7	226.9	26.6	216384.9	368056.1	54111.2
low $\rho_f$	2293.4	263.4	549.0	*	1851.4	447.3	806.9
low $k_{ub}$	20.3	417.0	817.9	735.4	658.7	1294.6	37.3
best fit	59.2	583.1	642.2	1686.9	1086.9	1431.6	453.0
Direct correlations for the “best fit”**							
	$\rho_f$	$c_{a,1}$	$c_{a,2}$	$k_{ub}$			
$\rho_f$	1	-0.416	-0.804	0.277			
$c_{a,1}$	-0.416	1	-0.504	0.473			
$c_{a,2}$	-0.804	-0.504	1	0.502			
$k_{ub}$	0.277	0.473	0.502	1			

\*  $k_{ub} = 0.01$  not fitted, but set according to *Bachmeier et al. (2002)*.

\*\* The direct correlations for most other parameter sets are in the same range ( $\pm 0.2$ ).

weighted with a factor of 10 compared with those of the concentrations to compensate for the difference in the number of measurements (8 for  $\text{CaCO}_3$ , over 100 for  $\text{Ca}^{2+}$  and  $\text{NH}_4^+$ ). This was done to achieve approximately equal initial sensitivity for each data set ( $\text{CaCO}_3$ ,  $\text{Ca}^{2+}$ , and  $\text{NH}_4^+$  measurements). Approximately equal sensitivity is considered necessary to ensure that every data set contributes to the parameter estimation, especially the application-relevant calcite data set which would otherwise be outnumbered. For inverse model runs where  $\text{Ca}^{2+}$  and  $\text{NH}_4^+$  concentrations were considered a single data set, equal, averaged standard deviations were assumed as required by iTOUGH2, while for inverse model runs where each pulse was considered a separate data set, individual standard deviations for each pulse were used. The standard deviations were estimated based on a 5% reproducibility for the ion chromatography measurements.

The values obtained from the model calibration by inverse modeling for the biofilm density  $\rho_f$  range from 0.01 to 35  $\text{kg}/\text{m}^3$  (Figure 4.8), depending on the data set used for inverse modeling as well as the inverse modeling setup (i.e. the initial guess or the use of  $\text{Ca}^{2+}$  and  $\text{NH}_4^+$  as one single observation set or the use of pulse-wise sets of observation). If the very low values obtained in the inverse model runs, which exclude  $k_{ub}$  from the set of fitting parameters, were neglected, the values for each experimental data set were within one order of magnitude. Calibration using the bicycle-rim data yielded exclusively higher  $\rho_f$  ranging from 6.4 to 35  $\text{kg}/\text{m}^3$  compared with the calibrations to any of the column experiments, where the highest value was 14.7  $\text{kg}/\text{m}^3$ . The values of  $\rho_f$  obtained by using the multi-experiment data set M are 4.3 and 8.3  $\text{kg}/\text{m}^3$ ; note that M consists of all data from C4, D2 and BR, the calcite data of each

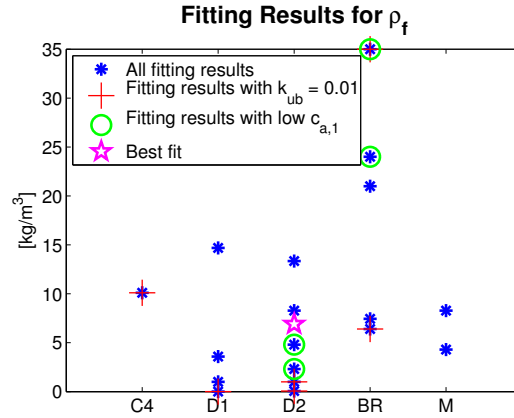


**Figure 4.8.:** Values obtained for the biofilm density  $\rho_f$  for each experiment through parameter estimation using iTOUGH2. Multiple experiments (C4, D2, and BR) are combined in the data set M to fit averaged parameters values.

experiment and the  $\text{Ca}^{2+}$  and  $\text{NH}_4^+$  data of D2 receive initially approximately equal weight.  $\rho_f = 4.3\text{kg/m}^3$  was obtained when the  $\text{Ca}^{2+}$  and  $\text{NH}_4^+$  data of D2 was input as pulse-wise sets of observations, while  $\rho_f = 8.3\text{kg/m}^3$  was obtained for the inverse model run on the data set M when considering the  $\text{Ca}^{2+}$  and  $\text{NH}_4^+$  data of D2 a single observation set each. These values compare well with the lower values fitted against BR data and the intermediate range of the values fitted to the column experiments. They also match the parameter set “best fit”, where the biofilm density obtained is  $6.9\text{ kg/m}^3$ . Low biofilm densities are observed for calibration against any experiment when  $k_{ub}$  is excluded from the set of fitting parameters and set to the constant literature value of 0.01 (*Bachmeier et al.*, 2002).

Figure 4.9 shows the coefficient  $c_{a,1}$  which varies between  $10^{-12.81}$  and  $10^{-1.81}$  1/s. However, most values for  $c_{a,1}$  are in the much narrower range of  $10^{-7.08}$  to  $10^{-4.56}$ .

The values of  $c_{a,1}$  obtained by calibration against the combined data set of M,  $10^{-5.78}$  ( $\text{Ca}^{2+}$  and  $\text{NH}_4^+$  single observation sets each) and  $10^{-4.56}$  1/s ( $\text{Ca}^{2+}$  and  $\text{NH}_4^+$  pulse-wise observation sets), are intermediate, while the “best fit” to D2,  $c_{a,1} = 10^{-7.08}$  1/s, is very low. Some calibrations using the column D2 data yield even lower values for  $c_{a,1}$  ( $10^{-12.81}$  and  $10^{-11.92}$ ). For the bicycle-rim experiment, remarkably low values of  $c_{a,1} = 10^{-10}$  1/s occur in sets of parameters in which the biofilm density is high (24 and  $35\text{ kg/m}^3$ ).

Figure 4.10 indicates that the parameter  $c_{a,2}$  varies between  $10^{-14.59}$  and  $10^{-5.43}$  1/s. Note that the extremely low values of  $10^{-14.59}$  and  $10^{-14.27}$  1/s obtained by fitting to column experiment D2 data are outliers. Most values are higher and range from  $10^{-8.00}$  to  $10^{-5.43}$  1/s. For almost all data sets,  $10^{-6}$  1/s is a representative value for the order of magnitude. In fact, for the

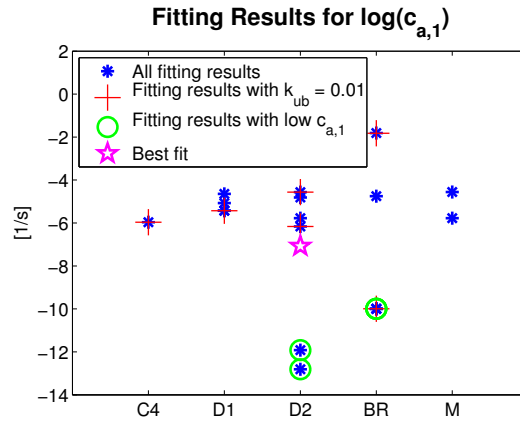


**Figure 4.9.:** Values obtained for the attachment coefficient to biofilm  $c_{a,1}$  through parameter estimation using iTOUGH2. Multiple experiments (C4, D2, and BR) are combined in the data set M to fit averaged parameters values.

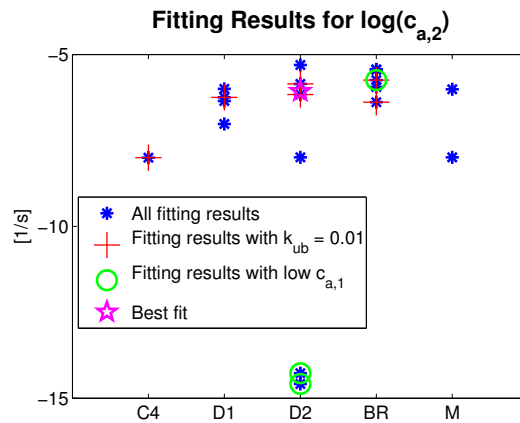


**Figure 4.10.:** Values obtained for the attachment coefficient to arbitrary surfaces  $c_{a,2}$  through parameter estimation using iTOUGH2. Multiple experiments (C4, D2, and BR) are combined in the data set M to fit averaged parameters values.

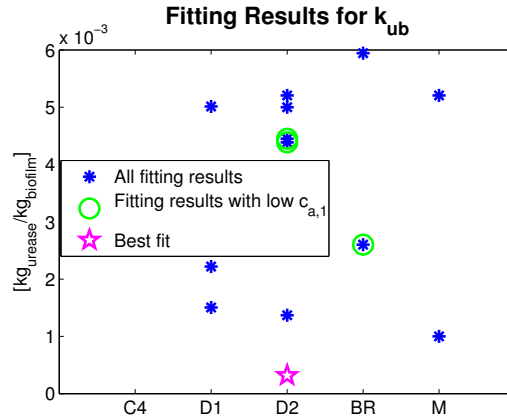


**Figure 4.11.:** Values obtained for the urease content of biofilm  $k_{ub}$  through parameter estimation using iTOUGH2. Multiple experiments (C4, D2, and BR) are combined in the data set M to fit averaged parameters values. For C4,  $k_{ub}$  was not included in the set of fitting parameters for the inverse modeling.

bicycle-rim data set, the  $c_{a,2}$  values are within one order of magnitude, between  $10^{-6.39}$  and  $10^{-5.43}$  1/s.

In most sets of parameters,  $c_{a,2}$  is between 1 and 2.5 orders of magnitude lower than  $c_{a,1}$ . Contrary to this general trend,  $c_{a,1}$  is several orders of magnitude lower than the corresponding  $c_{a,2}$  in some of the fits using the bicycle-rim experiment data. This is also the case for the parameter set “best fit”, where  $c_{a,1} = 10^{-7.08}$  1/s is one order of magnitude lower than  $c_{a,2} = 10^{-6.07}$  1/s.

In the inverse model runs including  $k_{ub}$  as a fourth fitting parameter, the resulting values are all below the literature value of 0.01 given in *Bachmeier et al.* (2002) (see Figure 4.11). This result indicates that the apparent ureolysis rate or urease production of *S. pasteurii* growing as a biofilm is probably lower than the rate of suspended cells investigated in *Lauchnor et al.* (2015). This might be caused by transport limitations as observed in *Bachmeier et al.* (2002) or due to a different metabolic activity of biofilm cells (*Carrera et al.*, 2004).

For the duplicate column experiments, the range of calibrated  $k_{ub}$  values was from 0.00032 to 0.0052, the “best fit” parameter value being the lowest. As in the case of the biofilm density  $\rho_f$ , the values of  $k_{ub}$  obtained by fitting to bicycle-rim data are higher and range from 0.0026 to 0.0059. The values of  $k_{ub}$  obtained for the two inverse model runs using the data set M (0.001 and 0.0052) are in the range of the values fitted to D1 and D2.  $k_{ub} = 0.001$  was obtained when the  $\text{Ca}^{2+}$  and  $\text{NH}_4^+$  data of D2 were input as pulse-wise sets of observations, while  $k_{ub} = 0.0052$  was obtained for the inverse model run on the data set M when considering these data a single observation set each.

If  $k_{\text{ub}}$  is included in the set of fitting parameters and the model is calibrated to the bicycle-rim data, the values of the biofilm density are moderate, while assuming a fixed  $k_{\text{ub}} = 0.01$  yields the lowest ( $6.4 \text{ kg/m}^3$ ) and the highest ( $35 \text{ kg/m}^3$ ) densities obtained for this experimental setup. If  $k_{\text{ub}}$  is included in the set of fitting parameters for the column experiments, higher biofilm densities are obtained, while the values of the attachment coefficients do not change.

This can be explained by both  $k_{\text{ub}}$  and  $\rho_f$  occurring in the ureolysis rate equation, in which they are multiplied by each other, see Equation (4.6). However,  $k_{\text{ub}}$  and  $\rho_f$  are not correlated ( $r = 0.277$  for the “best fit” parameter set, see Table 4.5), since the biofilm density also determines the volume fraction of a given mass of biofilm. Low densities lead to high volume fractions and a corresponding decrease in porosity and permeability. This increases the pressure gradient, thereby increasing detachment and limiting the maximum biomass ( $\rho_f \phi_f$ ) present in the system.

*S. pasteurii* is aerobic and requires oxygen to synthesize urease (Martin *et al.*, 2012). According to simulations, all oxygen is consumed during no-flow periods, which in reality would decrease the enzyme content of cells because de novo urease cannot be produced anaerobically. Hence, the low values for  $k_{\text{ub}}$  are comparable with the average urease contents of the cells under alternately aerobic and anaerobic conditions, since the model assumes that the urease content of the cells is constant. The higher values of  $k_{\text{ub}}$  fitted using the BR data support this hypothesis as the constant flow injection scheme for this experiment reduces oxygen limitation of the cells. However, even in this experiment, the fitted values are considerably lower than the literature value of 0.01.

For a more detailed investigation of the parameters obtained, the simulation results for selected sets of parameters as given in Table 4.4 are plotted together with experimental data of column experiment D2 in Figures 4.12, 4.13, and 4.14. The concentrations of  $\text{Ca}^{2+}$  and  $\text{NH}_4^+$  shown in Figures 4.12 and 4.13 are measured and calculated at 0.3 m distance from the injection point. The data for the other measurement locations at 0.1, 0.2, 0.4, and 0.5 m distance are not shown here because of space constraints, but show similar trends.

Parameter sets with extremely low attachment coefficients  $c_{a,1}$  and  $c_{a,2}$  predict hardly any ureolysis and, hence, no calcite precipitation for the first three measured pulses. On the other hand, the parameter sets with higher  $c_{a,1}$  and  $c_{a,2}$  overestimate both ureolysis and precipitation and predict that nearly all  $\text{Ca}^{2+}$  would precipitate in all of the measurement pulses, while measurements show complete precipitation of dissolved calcium only for the last four pulses.

The “best fit” parameter set is able to predict most  $\text{Ca}^{2+}$  and  $\text{NH}_4^+$  measurements. All other sets of parameters have in common that the reaction rates are overestimated although they were fitted to the same data set, which can best be seen in the comparison of measured

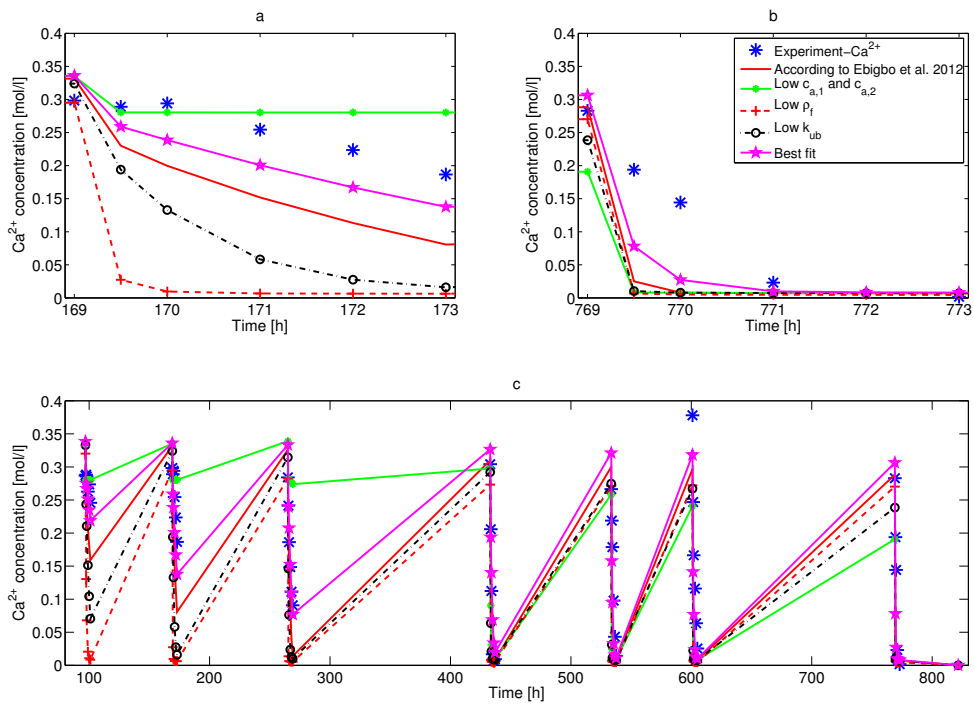


**Figure 4.12.:** Simulation results for selected parameter sets in comparison with measured  $\text{Ca}^{2+}$  concentrations for column experiment D2 at 0.2 m distance from the injection point. A total of 7 measurement series were conducted after the end of  $\text{Ca}^{2+}$ -rich injection pulses (c). For a better temporal resolution, (a) shows a zoom of the second measurement series and (b) one of the last (seventh). The parameter values corresponding to each parameter set are given in Table 4.4.

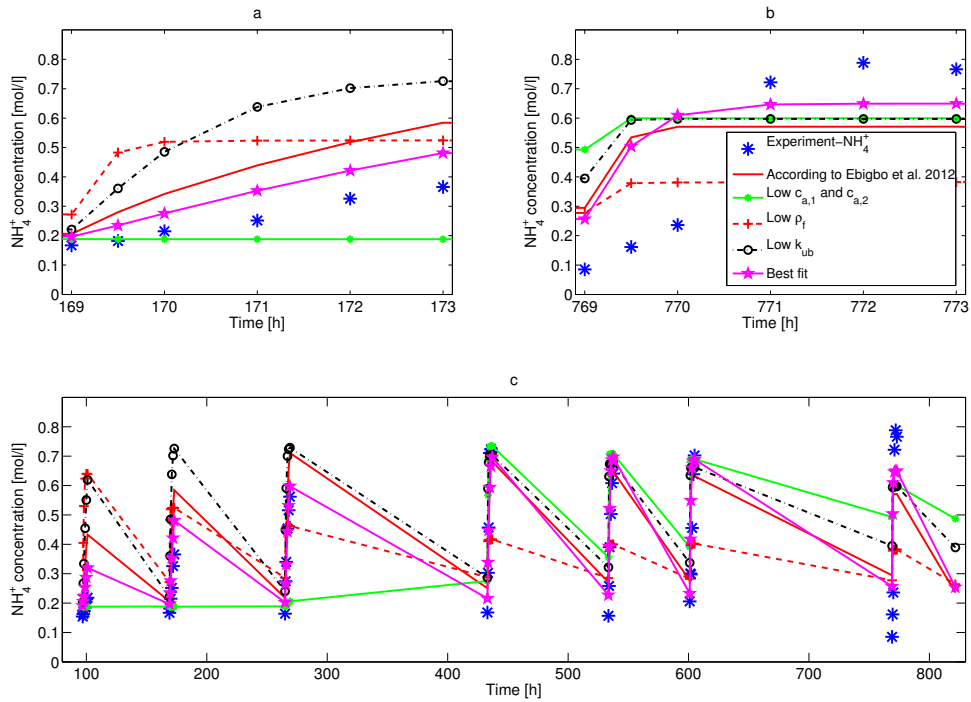


**Figure 4.13.:** Simulation results for selected parameter sets in comparison with measured  $\text{NH}_4^+$  concentrations for column experiment D2 at 0.2 m distance from the injection point. A total of 7 measurement series were conducted after the end of  $\text{Ca}^{2+}$ -rich injection pulses (c). For a better temporal resolution, (a) shows a zoom of the second measurement series and (b) one of the last (seventh). The parameter values corresponding to each parameter set are given in Table 4.4.

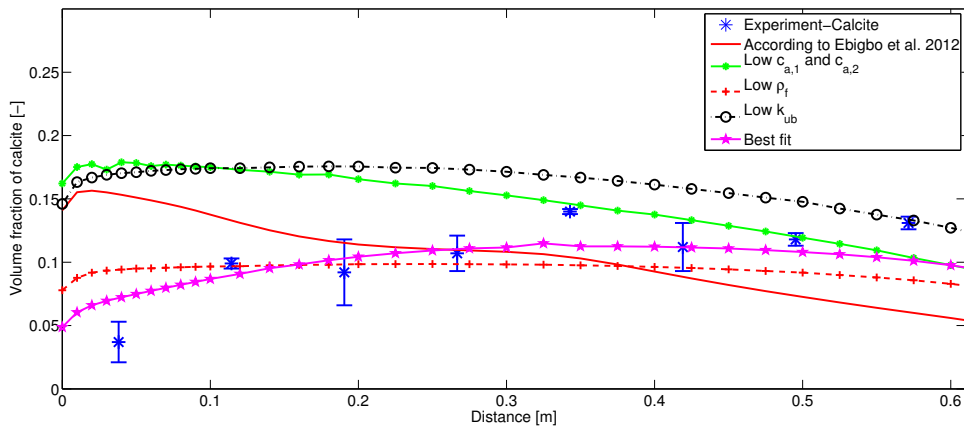


**Figure 4.14.:** Simulation results for selected parameter sets in comparison with measured final volume fractions of calcite for column experiment D2. The error bars on the experimental values represent the standard deviation of triplicate measurements. The parameter values corresponding to each set of parameters are given in Table 4.4.

and simulated  $\text{NH}_4^+$  concentrations in Figure 4.13. Especially for later times, the simulated  $\text{NH}_4^+$  concentrations right after the corresponding  $\text{Ca}^{2+}$ -rich injection are higher than the experimentally observed concentrations. This shows that the model predicts significant urea hydrolysis as early as during the injection phase while the experimental measurements do not confirm this prediction.

With a constant weight of the seven pulses of the in-situ measurements over time after a  $\text{Ca}^{2+}$ -rich injection, the first three pulses of measured  $\text{Ca}^{2+}$  and  $\text{NH}_4^+$  concentrations do not match the data set D2 as seen in the plot for the parameter set “low attachment” in Figures 4.12 and 4.13. For the data set D1, a similar trend was observed (data not shown). Consequently, the weight of the first pulses was increased because the attachment of bacteria is most relevant during the early times of the column experiment and thus determines the amount of attached biomass before significant growth occurs.

With the higher weighting of the first three  $\text{Ca}^{2+}$ -rich injections, the fitted model is able to match the measured concentrations of  $\text{NH}_4^+$  and  $\text{Ca}^{2+}$  more appropriately, although none of the parameter sets obtained resulted in model predictions matching the characteristic shape of both early and late measurements. For most measurements, however, the predictions for experiment D2 using the “best fit” parameter set (see Table 4.4) are closer to the measurements than for any other parameter set fitted using the data of experiment D2, see Table B.8.

The final distribution of calcite obtained by modeling has a different shape from that of the experiments. Even when the weight of the calcite data set was very high, the estimated parameters did not significantly improve the shape of the modeled calcite distribution, especially in the inlet region. This is somewhat unexpected, because the sensitivity analysis provided by iTOUGH2 suggests that at least the inverse model runs leading to the parameter sets “low  $\rho_f$ ” and “best fit” were sensitive to the  $\text{CaCO}_3$  data, see Table 4.5. Most modeled volume fractions of calcite for D1 and D2 are higher than those measured, especially in the influent region. When the first 10 cm of the influent region are neglected, the two parameter sets most sensitive to the  $\text{CaCO}_3$  data, the “low  $\rho_f$ ” and especially the “best fit” parameter set, result in modeled calcite distributions almost within the standard deviations of the experimental measurements. This result is additionally supported by the model predictions of both parameter sets resulting in very low residuals when compared with the calcite measurement (see Table B.8). Figure 4.14 compares the measured and the simulated calcite distribution.

As expected, the calibrated values of the fitting parameters are different depending on the experimental setup used for calibration, the initial guess of the parameters, and the weight (weighted standard deviation) of the observations. However, similar experimental setups, as in D1 and D2, lead to similar best-fit parameter values for identical inverse model parameters. The

calibration results using multiple experimental data sets M yield intermediate parameter values. Thus, the values calibrated using the data set M can be interpreted as values averaged over the individual experimental setups. Consequently, these values represent a good approximation of the experiment-independent, true values of the fitting parameters. The values of the parameter set fitted to M that has the low value of  $k_{\text{ub}} = 0.001$  are additionally quite similar to the parameter set “best fit” of data set D2.

The calibrated parameter values ( $\rho_f$  and  $c_{a,1}$ ) for the bicycle-rim data set encompass a wide range compared with the values calibrated to the other experimental data, except the extremely low attachment coefficients for some inverse model runs using D2 data. This might indicate that the inverse problem is ill-posed when using exclusively the limited BR data. For this experiment, no time-dependent measurements of pore fluids are available for calibration.

### 4.2.3. Discussion

Most fitted values of the biofilm density  $\rho_f$  compare well with the values given in the literature. Only some values fitted to D1 and D2 data are extremely low ( $< 1 \text{ kg/m}^3$ ). However, these low values are obtained in inverse modeling runs which excluded the urease content of the cells  $k_{\text{ub}}$  from the set of parameters and assumed it to be equal to the maximum value given in *Bachmeier et al.* (2002). In the inverse model runs including  $k_{\text{ub}}$  as fitting parameter, all estimates are lower than this maximum value. The calibrated values of the attachment coefficient  $c_{a,2}$  are, in general, 2 orders of magnitude lower than the values given for *E. coli* in *Torkzaban et al.* (2008). Both  $\rho_f$  and  $c_{a,2}$  are species-dependent parameters, which limits the comparability of the calibrated values to literature data, because specific literature on the properties of *S. pasteurii* is sparse.

For most sets of parameters, except for the fits to the bicycle-rim experiment with  $k_{\text{ub}}$  set to the literature value of 0.01, the coefficient of attachment to existing biofilm  $c_{a,1}$  is usually 1 to 2.5 orders of magnitude higher than the coefficient of attachment to arbitrary surfaces  $c_{a,2}$ . In the attachment coefficient equation (Eq. (3.26)),  $c_{a,1}$  is multiplied by the volume fraction of biofilm, which is bounded by the value of the initial porosity. Thus, for realistic biofilm volume fractions ( $\phi_f$  being typically less than 1% and initially no biofilm being present) and attachment-coefficient values as fitted, Equation (3.26) is dominated by  $c_{a,2}$  and the impact of  $c_{a,1}\phi_f$  is negligible. The sets of parameters obtained from inverse modeling of the bicycle-rim experiment with  $k_{\text{ub}}$  set to 0.01 yield values for  $c_{a,1}$  which are 4 orders of magnitude lower than the values for  $c_{a,2}$ , which would indicate that preferential attachment to biofilm does not occur during this experiment. Similarly, in the “best fit” parameter set,  $c_{a,1}$  is one order of magnitude lower than  $c_{a,2}$ . Thus, preferential attachment to biofilm is not necessary to

match the experimental results using the description of MICP currently implemented in the conceptual model.

The residuals between model predictions and the experimental results are reduced compared with the model of *Ebigbo et al.* (2012) by some of the parameter sets, while other parameter sets lead to increased residuals (see Table B.8). One explanation might be that the objective function has local minima which lead to non-optimal parameter sets, depending on the initial guess of the fitted parameters. However, the parameter set “best fit” does not only have very low residuals when compared with the data set of experiment D2 used for calibration, but also matches quite well both the effluent pH measurements of experiment D2 (see Figure B.5) which were not used as observations in inverse modeling as well as the calcite distributions of the other column experiments C4 and D1, see Figures B.2 and B.3.

Sections 4.2.3 and 4.2.3 discuss the experimental needs identified in this study as prerequisites for improving the conceptual understanding of MICP. Prior to this, the revised model is compared with the model of *Ebigbo et al.* (2012).

### Comparison with the previous model

The main difference between the revised model used in this study and the MICP model developed previously (*Ebigbo et al.*, 2012) is the ureolysis rate equation. The previous model features complex Michaelis-Menten-type ureolysis kinetics adapted from *Fidaleo and Lavecchia* (2003) (Eq. (3.6)).

This complex kinetic model accounts for a reduction of the maximum reaction rate by enzyme inactivation caused by non-optimal pH and inhibition by high product ( $\text{NH}_4^+$ ) concentrations as well as for varying biofilm mass and urea concentrations. Within the context of a MICP model, the main uncertainty of this ureolysis rate equation is that it was developed for the pure enzyme extracted from jack beans while, in most proposed MICP applications, whole cells of the bacterium *S. pasteurii* are used instead.

The revised model uses the ureolysis rate equation (Equation (4.6)) updated according to recent experimental investigations on the ureolysis kinetics of whole cells of *S. pasteurii* (*Lauchnor et al.*, 2015); see Section 4.2.1. The new rate equation is specific for whole-cell systems of *S. pasteurii* and has neither pH dependency nor  $\text{NH}_4^+$  inhibition since *Lauchnor et al.* (2015) demonstrated that neither process influences to ureolysis in whole-cell systems of *S. pasteurii*.

Further, the maximum specific growth rate  $k_\mu = 2.89 \cdot 10^{-5} \text{ 1/s}$ , one of the parameters used to fit the model in *Ebigbo et al.* (2012), was replaced by a recently published literature value of

$k_\mu = 4.1667 \cdot 10^{-5} \text{ 1/s}$  given in *Connolly et al. (2013)*. Additionally, the molecular diffusion coefficient in the water phase  $D_w$  was set to  $1.587 \cdot 10^{-9} \text{ m}^2/\text{s}$ , as given in *Riquelme et al. (2007)*. Table 4.6 compares the parameters used in *Ebigbo et al. (2012)* with the parameters used in the revised model.

The performance of both the previous (*Ebigbo et al., 2012*) and the revised model proposed here in predicting the calcite distributions of various experiments (C4, D1 and BR) is shown in Figures B.2 to B.4. Figures 4.12, 4.13, and 4.14 give more detailed comparisons of the predictions of both models and column D2 data. These figures illustrate the improved match of model predictions and experimental observations gained with the revised model using the parameter set “best fit”. This is confirmed by the calculated residuals given in Table B.8.

The improvement of the revised model is a result of the increase in the quantity and quality of the experimental data available, improving both the conceptual understanding of MICP as well as increasing the information for model recalibration. The ureolysis kinetics for the ureolysis of *S. pasteurii* (*Lauchnor et al., 2015*) resulted in the updated ureolysis rate equation which, together with the maximum specific growth rate for *S. pasteurii* (*Connolly et al., 2013*), allowed a reduction of the number of fitting parameters.

For the model recalibration, additional MICP experiments were available, providing measurements for an increased range of experimental conditions such as the injection strategy and injection rate (Table B.1), the injected concentration (Table B.2), and geometry (Section 4.2.1 and Figure 4.7). Additionally, for the experiments D1 and D2, spatially and temporally resolved measurements of  $\text{NH}_4^+$  and  $\text{Ca}^{2+}$  were available for recalibration, increasing the number of observations from the 8 calcite measurements up to more than 400 for each of the experiments.

Finally, the parameter estimation was more systematic as inverse modeling, rather than trial-and-error, methods were used for recalibration using the extended set of experimental observations as input, which resulted in additional insights, e.g. a sensitivity analysis of the model to both the observations used and the parameters estimated. The sensitivity analysis provided by iTOUGH2 indicated that the model is most sensitive to changes in the ureolysis rate equation.  $k_{\text{ub}}$  (and  $\rho_f$  instead, if  $k_{\text{ub}}$  was excluded from the fitting parameters) was identified as the most sensitive parameter, followed by the attachment coefficients.

## Ureolysis

All parameter sets including  $k_{\text{ub}}$  as a fitting parameter yield values smaller than the literature value of 0.01, indicating that the rate of ureolysis is overpredicted by Equation (4.6) using the

Table 4.6.: Comparison of revised, refitted, and other parameter values used to the values given in *Ebigbo et al. (2012)*.

Param.	Unit	Revised Value	Revised reference	<i>Ebigbo et al. (2012)</i>	Ref. <i>Ebigbo et al. (2012)</i>
$\phi_0$	-	0.4	<i>Ebigbo et al. (2012)</i>	0.4	Measured
$\phi_{\text{crit}}$	-	0	<i>Ebigbo et al. (2012)</i>	0	Estimated
$K_0$	$\text{m}^2$	$2 \cdot 10^{-10}$ ; $1.82 \cdot 10^{-10}$	Measured; <i>Ebigbo et al. (2012)</i>	$1.79 - 2.30 \cdot 10^{-10}$	Measured
$\rho_c$	$\text{kg}/\text{m}^3$	2710	<i>Ebigbo et al. (2012)</i>	2710	-
$\rho_f$	$\text{kg}/\text{m}^3$	<b>0.01 - 35</b>	<b>Refitted</b>	10	Fitted
$D_w^k$	$\text{m}^2/\text{s}$	<b><math>1.587 \cdot 10^{-9}</math></b>		$10^{-9}$	-
$\alpha_1$	m	0.025	<i>Riquelme et al. (2007)</i>	0.025	<i>Frippiat et al. (2008)</i>
$A_{\text{sw},0}$	$\text{m}^2/\text{m}^3$	5000	<i>Frippiat et al. (2008)</i>	5000	Estimated
$a_c$	$\text{m}^2/\text{m}^3$	20000	<i>Ebigbo et al. (2012)</i>	20000	Estimated
$k_{\text{prec}}$	$\text{mol}/\text{m}^2\text{s}$	$1.5 \cdot 10^{-10}$	<i>Zhong and Mucci (1989)</i>	$1.5 \cdot 10^{-10}$	<i>Zhong and Mucci (1989)</i>
$\eta_{\text{prec}}$	-	3.27	<i>Zhong and Mucci (1989)</i>	3.27	<i>Zhong and Mucci (1989)</i>
$k_{\text{diss},1}$	$\text{kg}_{\text{H}_2\text{O}}/\text{m}^2\text{s}$	$8.9 \cdot 10^{-1}$	<i>Chou et al. (1989)</i>	$8.9 \cdot 10^{-1}$	<i>Chou et al. (1989)</i>
$k_{\text{diss},2}$	$\text{mol}/\text{m}^2\text{s}$	$6.5 \cdot 10^{-7}$	<i>Chou et al. (1989)</i>	$6.5 \cdot 10^{-7}$	<i>Chou et al. (1989)</i>
$\eta_{\text{diss}}$	-	1	<i>Flukiger and Bernard (2009)</i>	1	<i>Flukiger and Bernard (2009)</i>
$k_{\mu}$	1/s	<b><math>4.1667 \cdot 10^{-5}</math></b>	<i>Connolly et al. (2013)</i>	$2.89 \cdot 10^{-5}$	Fitted
$K_s$	$\text{kg}/\text{m}^3$	$7.99 \cdot 10^{-4}$	<i>Taylor and Jaffé (1990)</i>	$7.99 \cdot 10^{-4}$	<i>Taylor and Jaffé (1990)</i>
$K_{\text{O}_2}$	$\text{kg}/\text{m}^3$	$2 \cdot 10^{-5}$	<i>Hao et al. (1983)</i>	$2 \cdot 10^{-5}$	<i>Hao et al. (1983)</i>
$Y$	-	0.5	<i>Seto and Alexander (1985)</i>	0.5	<i>Seto and Alexander (1985)</i>
$F$	-	0.5	<i>Mateles (1971)</i>	0.5	<i>Mateles (1971)</i>
$b_0$	1/s	$3.18 \cdot 10^{-7}$	<i>Taylor and Jaffé (1990)</i>	$3.18 \cdot 10^{-7}$	<i>Taylor and Jaffé (1990)</i>
$K_{\text{pH}}$	$\text{mol}^2/\text{kg}_{\text{H}_2\text{O}}$	$6.15 \cdot 10^{-10}$	<i>Kim et al. (2000)</i>	$6.15 \cdot 10^{-10}$	<i>Kim et al. (2000)</i>
$c_{a,1}$	1/s	<b><math>1.55 \cdot 10^{-13} - 1.55 \cdot 10^{-2}</math></b>	<b>Refitted</b>	0.0443	Fitted
$c_{a,2}$	1/s	<b><math>2.57 \cdot 10^{-15} - 3.72 \cdot 10^{-6}</math></b>	<b>Refitted</b>	$9.19 \cdot 10^{-4}$	Fitted
$c_d$	1/s	$2.89 \cdot 10^{-8}$	<i>Ebigbo et al. (2010)</i>	$2.89 \cdot 10^{-8}$	<i>Ebigbo et al. (2010)</i>
$k_{\text{urease}}$	$\text{mol}/\text{kg}_s$	<b>706.7</b>	<i>Lauchnor et al. (2015)</i>	41.7	<i>Krajewska (2009)</i>
$K_u$	$\text{mol}/\text{kg}_{\text{H}_2\text{O}}$	<b>0.355</b>	<i>Lauchnor et al. (2015)</i>	0.0173	<i>Krajewska (2009)</i>
$K_{\text{eu},1}$	$\text{mol}/\text{kg}_{\text{H}_2\text{O}}$	Removed	<i>Lauchnor et al. (2015)</i>	$7.57 \cdot 10^{-7}$	<i>Fidaleo and Lavecchia (2003)</i>
$K_{\text{eu},2}$	$\text{mol}/\text{kg}_{\text{H}_2\text{O}}$	Removed	<i>Lauchnor et al. (2015)</i>	$1.27 \cdot 10^{-8}$	<i>Fidaleo and Lavecchia (2003)</i>
$K_{\text{NH}_4^+}$	$\text{mol}/\text{kg}_{\text{H}_2\text{O}}$	Removed	<i>Lauchnor et al. (2015)</i>	0.0122	<i>Fidaleo and Lavecchia (2003)</i>
$k_{\text{ub}}$	-	<b><math>0.01</math>; <math>0.0014 - 0.0059</math></b>	<i>Bachmeier et al. (2002)</i> ; <b>Refitted</b>	0.11	Fitted
$\eta_{\text{ub}}$	-	<b>1.0</b>	<i>Lauchnor et al. (2015)</i>	1.5	Fitted
$T$	$^{\circ}\text{C}$	25	<i>Ebigbo et al. (2012)</i>	25	Constant

kinetic parameters for suspended cells from *Lauchnor et al.* (2015). This is supported by the comparison of modeled with measured concentrations, as shown exemplarily in Figure 4.13, and by re-calibrated sets of parameters with fixed  $k_{\text{ub}} = 0.01$  resulting in low biofilm density, thereby favoring detachment and reducing the amount of ureolytic biomass in the simulations to match a lower reaction rate.

Another reason for the small  $k_{\text{ub}}$  estimates can be that *S. pasteurii* needs oxygen both to grow and produce urease (*Martin et al.*, 2012). In the simulations of the column experiments, all oxygen is consumed during the batch periods following a  $\text{Ca}^{2+}$ -rich injection leading to anoxic conditions. These anoxic conditions could have led to less urease production in the biofilm, which would account for the lower average value of  $k_{\text{ub}}$  in the model. Additionally, the measurements show that the  $\text{NH}_4^+$  concentration right at the end of the  $\text{Ca}^{2+}$ -rich injections is equal to the injected concentration of  $0.177 \text{ mol/l}$ , indicating that no significant amount of urea is hydrolyzed during flow, rather that urea was hydrolyzed during no-flow periods. On the contrary, the model predicts that  $\text{NH}_4^+$  concentrations already increase during the flow period for the later pulses for any set of parameters fitted (see Figure 4.13 a and b).

This overestimation is caused by the model assumptions that the ureolysis rate is dependent on the bulk urea concentration (see Equation (4.6)) and that the kinetic parameters are equal to those proposed by *Lauchnor et al.* (2015) (see Section 4.2.1). Therefore, the use of suspended-cell kinetics will probably not be the final approach for MICP models, as most of the cells during MICP in subsurface systems are in biofilms (*Ebigbo et al.*, 2012; *Cuthbert et al.*, 2012). It is important to investigate experimentally whether this overestimation is due to neglected additional mass transfer processes within the porous medium and the biofilm, as suggested by *Bachmeier et al.* (2002), or caused by a change in the kinetics resulting from the change in the growth mode, as suggested by *Carrera et al.* (2004). Extracellular urease changes the apparent ureolysis kinetics of microbial cells in biofilms (*Klose and Tabatabai*, 1999) and the production of urease in cells within a biofilm might be different from that in suspended cells. Additionally, the assumption of well-mixed conditions is dependent on the heterogeneity of the porous medium. For the experiments, single-grain-size sand was used and packed carefully to avoid initial heterogeneities as described in Section 4.2.1. Preferential flow paths and stagnant regions developing during the experiments could have led to concentration and reaction-rate differences on the pore scale which are difficult to represent with an averaged bulk-concentration-dependent reaction rate in the Darcy-scale model.

A key step is to determine whether the reduced apparent reaction rates in biofilm systems occur because of mass-transfer limitations or because of significant differences in metabolism between biofilm and suspended cells. A combination of small to micro-scale experiments and pore-scale modeling is a promising approach for determining which of these processes is responsible for the

observed discrepancies. If the discrepancies are caused by locally heterogeneous concentrations, the model can be improved by implementing additional equations describing the mass transfer between biofilm and liquid phase as well as diffusion within the biofilm. To give an example, mass transfer processes within the biofilm can be implemented using a double-continuum model as used in *Ebigbo et al. (2010)*. If locally heterogeneous concentrations are not able to explain the difference in the reaction rates observed, the biofilm-based kinetics parameters have to be determined experimentally for *S. pasteurii*. Alternatively, independently of what causes the discrepancy, upscaled biofilm-related kinetics parameters can be used which explicitly account for the metabolism of attached cells as well as heterogeneous concentrations and additional mass transfer. However, the conceptual understanding of biofilm-catalyzed ureolysis and of the potential influence of biofilm-fluid mass transfer needs to be improved. Further experimental research should focus especially on determining the apparent ureolysis rates of *S. pasteurii* biofilms and the resulting calcite precipitation rates, since these are the key processes of MICP.

### Attachment and biofilm density

The best-fit attachment coefficients  $c_{a,1}$  and  $c_{a,2}$  vary over several orders of magnitude, indicating that the model is not very sensitive to them although the sensitivity analysis carried out by iTOUGH2 shows that the attachment coefficients have medium to high sensitivity compared with the other parameters fitted; see Table 4.5. Thus, a better knowledge of bacterial attachment would substantially improve the model. The model is especially sensitive to  $c_{a,1}$  and  $c_{a,2}$  at the beginning of the simulation, where the biofilm distribution is determined by attachment and not yet dominated by the interplay of growth and detachment, see Figures 4.12a and 4.13a. Especially for field-scale applications in which oxygen is not readily available, attachment of injected cells or cells detached from upstream regions might be the dominant process determining the distribution of biofilm. Experiments might show whether preferential attachment of *S. pasteurii* to existing biofilms, as assumed in Equation (3.26), can be observed or not.

Further, the biofilm density is assumed to be constant in the conceptual model. In the literature, however, it is shown that the density of biofilms depends on various environmental factors such as exposure to shear stress, compaction of biofilm due to external stress, the history of exposure to external and shear stress during growth, and the type of electron acceptor available during growth (*Paul et al., 2012*). Biofilm density may also change with the thickness of the biofilm as shown in *Zhang and Bishop (1994)*. The validity of the assumption of a constant biofilm density used in the conceptual model has to be investigated in experiments, since the biofilm density strongly influences the amount of simulated attached biomass in the

**Table 4.7.:** Focal points to improve the conceptual understanding of MICP by targeted experiments and numerical investigations as identified in this study.

Focal point	Suggested investigation method	Purpose of research on this focal point
Biofilm-based ureolysis kinetics for <i>S. pasteurii</i>	experimental	Improve the understanding of biofilm-catalyzed ureolysis, determine the apparent ureolysis rate and find a suitable parametrization and the corresponding parameters
Density of <i>S. pasteurii</i> biofilms	experimental	Determine whether the assumption of constant biofilm density holds, if yes, give estimates of the density of <i>S. pasteurii</i> biofilms if not, identify the governing processes, and find a suitable parametrization and the corresponding parameters
Attachment of <i>S. pasteurii</i>	experimental	Determine whether preferential attachment to existing biofilm is relevant and estimate the attachment coefficient(s)
Accuracy of simplified models	numerical	Assess the modeling error of MICP models of different complexity in comparison to uncertainties resulting from unknown parametrizations of processes as well as unknown porosity and permeability for applications in the field

system. A better knowledge of the biofilm density is crucial to the success of any further investigation of the interactions of biofilm and hydraulic conditions. These interactions govern the distribution of catalytically active biofilm in the porous medium, thereby controlling the distribution of the precipitated calcite.

#### 4.2.4. Summary

Given the recent insight into and experimental data on ureolysis and biofilm-hydraulics interactions, the possible reduction of model uncertainty is restricted by the current insufficient knowledge of those processes and a lack of parametrizations which could crucially improve the successful modeling of MICP. The focal points of future research as identified in this study are summarized in Table 4.7.

The difference between the experimental and the modeled calcite distributions indicates that at least one relevant process for MICP is not yet implemented in sufficient detail in the

---

conceptual model. Before a more detailed calibration of the numerical model is attempted, the conceptual understanding of all relevant processes, including the biofilm-catalyzed ureolysis, resulting calcite precipitation as well as the interplay of hydraulics and biofilm processes, has to be improved. Pore-scale investigations of ureolysis catalyzed by *S. pasteurii* biofilms might help in determining which of the processes involved have to be considered in more detail.

Hence, a systematic experimental approach is needed for the investigation of the processes related to *S. pasteurii* biofilms in relevant conditions. Experiments are needed to derive apparent biofilm-based, volume-averaged parameter values which can be used for both engineering applications of MICP and numerical models used to design and evaluate future MICP experiments and applications.

Parallel to further experimentation, an investigation of simplified models designed to answer specific engineering questions is a promising approach for future modeling work, since knowledge of the relevant processes is limited and parametrizations are not available. For field-scale applications, the reduced accuracy of such simplified models is probably acceptable, since important site-specific modeling input parameters such as permeability and porosity are often not known in sufficient detail, resulting in an accuracy reduction which is greater than the reduction caused by simplifying model assumptions. Additionally, simplified models might prove to be computationally more efficient, thereby facilitating the use of MICP.



## 5. Application of the model to guide experimental investigations

### 5.1. Investigation of the influence of initial biomass and injection strategy \*

#### 5.1.1. Introduction

It has been suggested that the distribution of cells in the porous medium during MICP is a key parameter (*Barkouki et al.*, 2011). Yet it is very difficult to control or even reliably measure the concentrations of attached microbial cells (e.g. *Bower et al.*, 2000; *Cunningham et al.*, 2007). The presence of ureolytic microbes is a prerequisite for MICP. However, in the deep subsurface, the number of ureolytic microbes initially present might be limited. Hence, to achieve MICP in such environments, the injection of cells with the desired activity would be necessary.

Any process responsible for the transfer of suspended biomass to the solid phase can be referred to as attachment (*Clement et al.*, 1999). These processes, which may occur simultaneously, include straining, sorption, sedimentation, and interception. Descriptions of the relevant mechanisms and various approaches of quantifying these processes can be found in e.g. *Corapcioglu and Haridas* (1984); *Harvey and Garabedian* (1991); *Clement et al.* (1999); *Stevik et al.* (2004); *Tufenkji* (2007). Depending on the dominant mechanisms, the quantification of attachment may require knowledge of geometry (e.g. pore-size distribution, heterogeneities, cell sizes), physicochemical properties of the bulk fluid (e.g. pH, ionic strength, temperature), surface properties (e.g. hydrophobicity, surface charge and roughness) of the porous medium and the biofilm, and flow conditions (velocity). Attachment is typically incorporated in flow and transport models via a rate function. Various expressions have been used for this function,

---

\*This section is published in J. Hommel, E. G. Lauchnor, R. Gerlach, A. B. Cunningham, A. Ebigbo, R. Helmig, and H. Class, Investigating the Influence of the Initial Biomass Distribution and Injection Strategies on Biofilm-Mediated Calcite Precipitation in Porous Media. *Transport in Porous Media*, (2015), 1-23, DOI: 10.1007/s11242-015-0617-3

many based on filtration theory (e.g. *Harvey, 1991; Scheibe et al., 2007*), several others on first-order kinetics (e.g. *Clement et al., 1996; Murphy et al., 1997*), and a few assuming that biofilms increase the attachment rate (e.g. *Taylor and Jaffé, 1990; Ebigbo et al., 2010*). In her review, *Tufenkji (2007)* points out that the incorporation of many of the factors which influence attachment rates “in predictive models remains a challenge”. *Clement et al. (1999)* stress the lack of research work on attachment rates to pre-existing biofilms in porous media.

Laboratory column experiments are commonly used to investigate the attachment process and to measure attachment coefficients, (e.g. *Cunningham et al., 2007*). However, any inquiry regarding the final distribution of metabolically active cells in porous media will be associated with high uncertainties due to the challenges in measuring the number and activity of metabolically active microbes attached to the porous medium (*Cunningham et al., 2007; Gerlach, 2001*). These uncertainties will at least increase the number of experiments needed to measure statistically significant coefficient values.

As a consequence of this lack of information and data, many models assume the resulting distribution of biomass or enzyme based on conceptual considerations or experimental observations, e.g. homogeneous distribution of biomass (*van Wijngaarden et al., 2011*), exponentially decreasing biomass with increasing distance to the injection (*Barkouki et al., 2011*), or biomass being distributed according to a Gamma distribution (*Martinez et al., 2014*).

### **Preliminary Experiments**

A preliminary investigation of initial bacterial attachment and biofilm growth was performed with vertical sand-filled columns. Three sets of duplicate column experiments were carried out, including (1) initial attachment during injection, (2) attachment over an 8-hour no-flow period, and (3) attachment and biofilm growth over 24 hours. The six columns were constructed using clear PVC pipes of 61 cm length and 2.54 cm inner diameter, which were filled with 40-mesh quartz sand (0.5 mm effective filtration size, manufacturer information, Unimin Corp., Emmet, ID, identical to the sand used for the experiments described in *Ebigbo et al. (2012); Hommel et al. (2015b)*), packed under water and vertically positioned. They were inoculated simultaneously with 300 ml (two pore volumes) of cell suspension of identical cell concentration of *S. pasteurii* ( $3.2 \cdot 10^7 \frac{\text{CFU}}{\text{ml}}$ ) at a flow rate of  $10 \frac{\text{ml}}{\text{min}}$  in an upflow configuration. The first pair of duplicate columns was rinsed immediately after the inoculation for 30 min with cell-free medium at a flow rate of  $10 \frac{\text{ml}}{\text{min}}$  to wash out cells that were not tightly attached while the cells injected into the remaining four columns were allowed to attach for 8 hours. After this batch period, the next pair of duplicate columns was rinsed while the remaining pair was subject to an 18-hour injection of growth medium at  $10 \frac{\text{ml}}{\text{min}}$ . The last pair of duplicate columns was

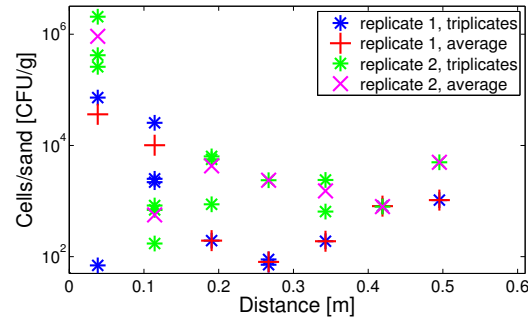


**Figure 5.1.:** Measured cells for two attachment-experiment replicates with inoculation and 8 hour no-flow period. The total number of attached cells measured in those experiments was used to estimate the initial amount of biomass for the numerical study.

rinsed with two pore volumes of cell-free medium after the growth-medium injection period, washing out cells that were not tightly attached. Effluent samples were collected from each column during inoculation and rinse. After rinsing, the columns were gravity drained and cut into eight sections of 7.62 cm length and triplicate samples of the thoroughly mixed sand of each section were taken for analysis of the number of culturable attached cells.

For the analysis of the attached cells, the samples were treated with a diluted desorption solution (1:5 in phosphate buffer saline (PBS)) as described in *Cunningham et al.* (2007), originally published in *Camper et al.* (1985). An aliquot (5 ml) of this solution was added to approximately 1 g of sand in a test tube, which was vortexed for 1 second. The test tube was placed on a horizontal shaker (150 rpm) for 30 min and then vortexed again for 3 seconds. The supernatant was sampled immediately after the coarse particles had settled and subsamples of various dilution in PBS were plated on Brain-Heart-Infusion (BHI) agar containing 2% urea. High concentrations of the desorption solution appeared to inhibit growth of *S. pasteurii* cells on BHI urea plates. After 1 day of incubation at 30°C, the bacterial colonies developed on the plates were counted and the dried sand samples were weighed to determine the number of cells attached per mass of sand.

Figure 5.1 shows the measured cells over the distance for the duplicate attachment experiments that were inoculated, subject to no-flow conditions for 8 hours, and rinsed to remove suspended cells. The cell distributions measured in these experiments are very scattered and the values of some of the triplicate measurements vary over more than two orders of magnitude although they were taken from the same, well-mixed section of the column. For most sections, even the section-wise averages of each replicate column differ by more than an order of magnitude. Additionally, some of the plates did not show any growth of cells at all, e.g. there are no results for the effluent section (Figure 5.1).

## Objectives

In this study, preliminary experiments investigated the attachment of *S. pasteurii* to packed sand in 0.61 m columns as described in Section 5.1.1. Still, the number of experiments is insufficient, granting only limited insight into a process understanding of the attachment of *S. pasteurii*. Thus, prior to repeating the attachment experiments, a numerical study is conducted which investigates the influence of initial biomass distributions, representing attachment, on the model predictions of the resulting distribution of calcite and biomass. To this end, various scenarios were simulated using the numerical model proposed by *Hommel et al.* (2015b), discussed in Section 4.2. In other words, this study aims at answering the question whether the initial amount and distribution of biomass (and thus the process of cell attachment) are prerequisites for modeling MICP or not. If not, it would not justify the potentially immense effort of the experimental investigations necessary to determine the exact attachment behavior of *S. pasteurii*.

Additionally, the sensitivity to various injection strategies is tested as the influence and importance of the initial distribution of biomass might be different for the various injection strategies. Further, the injection strategies themselves might have an impact on the result of MICP since the injection strategy directly determines important reaction parameters such as the residence time. The inclusion of differing injection strategies broadens the scope of the study as the results are not limited to a single set of injection conditions. The three hypotheses investigated in this study are:

- the initial distribution of attached biomass determines the resulting final distributions of both biomass and calcite;
- the total amount of attached biomass influences the final distributions of both biomass and calcite;
- the injection strategy (flow rate and number of injections) determines the final distributions of both biomass and calcite resulting from the application of MICP.

## Methods

Despite the different mechanisms potentially involved, cell attachment is only relevant when many suspended cells are present and available to attach. In most setups, this is only the case during the initial inoculation period when the suspended cell concentration in the pore liquid is high. At later times, the only source of suspended cells is the detachment of cells from the developed biofilm. This consideration is supported by model calculations using the model

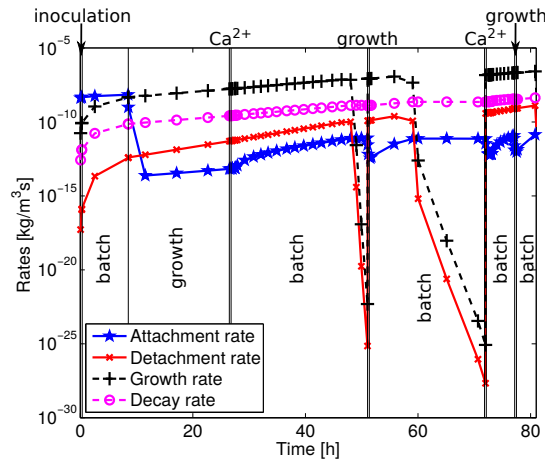


**Figure 5.2.:** Comparison of the attachment rate to the other rates influencing the biomass distribution as predicted by the model for the first 80 h of experiment D2 by *Hommel et al. (2015b)*. During the initial cell injection (first 0.5 h, labeled ‘inoculation’) and the following batch period (next 8.0 h, labeled ‘batch’), the attachment rate is high. During the following injections and batch periods the attachment rate is significantly lower. The subsequent time periods are labeled according to the main purpose of the injection: ‘growth’ for calcium-free medium injection and ‘Ca<sup>2+</sup>’ for calcium-rich medium injection. A figure comparing the rates for the entire duration of the simulation is included in Figure C.1.

described in Section 5.1.1. Figure 5.2 compares the order of magnitude of all rates (attachment, detachment, growth, decay) influencing the amount of attached biomass during the simulation of the column experiment D2 discussed in *Hommel et al. (2015b)*. This figure shows that only during the initial injection of the cells into the column and the following 8-hour batch period, the attachment rate is the highest rate. After this first 8.5-hour inoculation phase, the high inoculation cell concentration is replaced by fresh, cell-free growth medium, and the growth rate of attached cells quickly becomes more important than the attachment rate. For the remainder of the experiment, the attachment rate is several orders of magnitude lower than the growth rate of attached cells. Even with ceasing growth during the batch periods, in which all oxygen is consumed (Figure 5.2, between 60 and 73 hours), growth is the dominant process increasing attached biomass.

### Model Concept

The conceptual model for MICP used in this study follows the model published by *Ebigbo et al. (2012)* and revised by *Hommel et al. (2015b)*. The only difference to the model presented in *Hommel et al. (2015b)* is that the attachment of cells is represented by a given initial distribution of biomass. Thus, in the context of this study, it is assumed that the attachment rate is negligible,  $r_a = 0$ , as the simulations start after the inoculation period with a high

concentration of suspended cells, assuming pre-determined distributions of attached biomass. The resulting source term for attached biomass as used in this study is:

$$q^f = r_g^f - r_b^f - r_d \quad (5.1)$$

where  $r_g^f$ ,  $r_b^f$ , and  $r_d$  are the rates of growth, decay, and detachment respectively (*Ebigbo et al.*, 2012; *Hommel et al.*, 2015b). The other source and sink terms are, similar to the ones in Equation (5.1), based on the rates of the reactions in which the corresponding component is involved.

Replacing the initial inoculation and attachment by initial biomass distributions does not change the model results very much, which is confirmed by the comparison of the full model accounting for inoculation and attachment (*Hommel et al.*, 2015b) with the results obtained by assuming the various initial biomass distributions. This comparison is shown in Figure C.2.

### Initial biomass distributions

The various initial biomass distributions are chosen such that the total mass of biomass within the system is constant. The total mass of initially attached biomass is estimated based on the average total biomass measured in the replicate attachment column experiments (see Section 5.1.1). To adjust for the higher inoculation cell concentration in the experimental setup used (experiment D2 (*Hommel et al.*, 2015b) ( $5.6 \cdot 10^7 \frac{\text{CFU}}{\text{ml}}$ )) compared with the attachment experiments ( $3.2 \cdot 10^7 \frac{\text{CFU}}{\text{ml}}$ ), the number of cells measured in the attachment experiments is scaled by the ratio of the inoculation cell concentrations. Thus, it is estimated that a total of  $4 \cdot 10^9$  cells are distributed throughout the column, which translates into a total biomass volume of approximately  $110 \text{ mm}^3$  using a cell weight of  $2.5 \cdot 10^{-16} \frac{\text{kg}}{\text{cell}}$  (*Norland et al.*, 1987) and an approximate biofilm density of  $10 \frac{\text{kg}}{\text{m}^3}$  (*Ebigbo et al.*, 2012).

Five different initial biomass distributions are investigated (Figure 5.3):

- *homogeneous distribution* (as assumed by e.g. *van Wijngaarden et al.* (2011)); the initial biomass volume fraction along the simulation domain is constant, the initial biomass volume fraction for the *homogeneous* case being  $\phi_{f,0,h} = 2.597 \cdot 10^{-4}$ . This represents a case with a very low attachment coefficient at very high inoculation cell concentration or sorptive attachment under conditions at which the sorption capacity is exceeded;
- *first-order* distribution; the volume fraction of initially attached biomass decreases exponentially with increasing distance  $z$  from the inlet, following the equation:

$$\phi_{f,0,1st}(z) = 5\phi_{f,0,h}e^{-8.18z}.$$

This exponential distribution corresponds to the approximate first-order distributions that were observed in our attachment experiment with *S. pasteurii* (Figure 5.1);

- *inverse first-order* distribution, as proposed by *Barkouki et al.* (2011), which corresponds to a change of the direction of flow after inoculation. *Barkouki et al.* (2011) propose that this distribution of cells will lead to a more homogeneous distribution of precipitated calcite, as the reduction of reactants along the flow path is counteracted by an increase in catalyzing enzyme. Even though this initial biomass distribution is likely to be unrealistic for subsurface applications, it provides an upper bound for how much the resulting calcite precipitation can be influenced by the initial biomass distribution. Consequently, the initial attached biomass volume fraction increases with the distance  $z$  from the inlet for this initial distribution:

$$\phi_{f,0,inverse\ 1st}(z) = 5\phi_{f,0,h}e^{8.18(z-0.61)};$$

- *influent spike* of biomass; the initially attached biomass is concentrated in the influent region, decreasing rapidly with increasing distance  $z$ :

$\phi_{f,0,spike}(z) = 192.86\phi_{f,0,h}e^{-817.69z}$ . This represents a rock with low permeability and small pore sizes such as a low permeability sandstone or silty or clayey material (e.g. shale rock), into which cells are unable to penetrate very far, but instead form a coating (often referred to as a filter cake) in the influent region;

- *random* biomass; the constant biomass volume fraction of the *homogeneous* initial biomass distribution is multiplied at each grid point by a random number  $R(z)$  between 0 and 2 as given in Table C.1, which is adjusted by a common factor to ensure that the sum of the initial biomass is preserved. The *random* distribution represents heterogeneous attachment caused by not yet determined processes such as chemotactic movement prior to attachment or preferential attachment to certain minerals and surfaces with certain properties (e.g. roughness, charge) that lead to a non-monotonous, more or less random attachment behavior as observed in the preliminary attachment experiment (Figure 5.1) that cannot be described by simple exponential distributions:

$$\phi_{f,0,random}(z) = \phi_{f,0,h}R(z).$$

The volume fractions of biomass for each of the five initial biomass distributions are given for each grid node in Table C.1.

Additionally, since attachment does not only influence the distribution, but also the total amount of attached biomass, it was also investigated whether a 5-fold increase or decrease of the initial biomass distribution affects the results of MICP. This is done using the initial

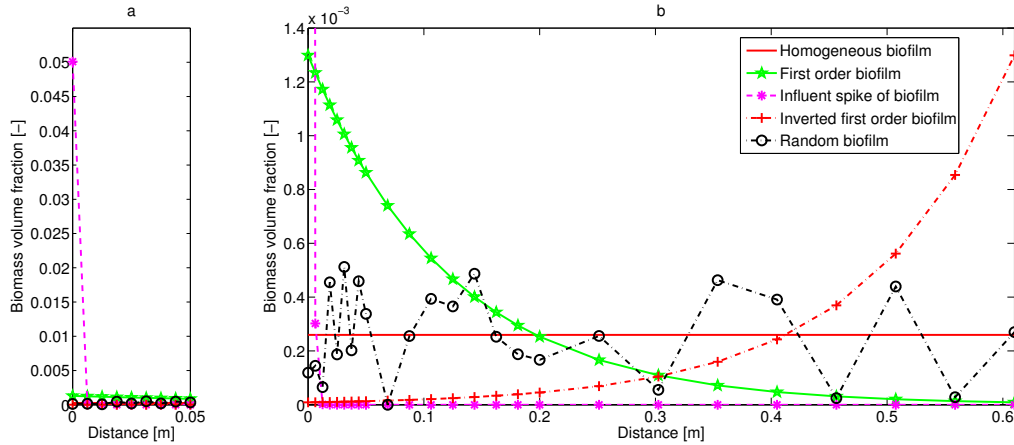


**Figure 5.3.:** Initial distributions of attached biomass investigated in the numerical study. Subfigure (a) on the left visualizes the very high initial biomass for the *influent spike* in the influent region, while subfigure (b) on the right focuses on the other initial biomass distributions over the total length of the column.

biomass distributions already discussed with an additional factor of 5 or 0.2 for high or low attachment of biomass respectively.

### Injection strategies

Further, various injection strategies are simulated to investigate whether the influence of the initial biomass distribution (and thus the influence of attachment) on the final calcite and biomass distribution is dependent on the injection strategy. The six injection strategies are based on the column experiment D2 described in *Hommel et al. (2015b)*. This injection strategy is based on the pulsed injection of growth medium and calcium-rich medium, each injection being followed by 4-hour batch periods during which urea hydrolysis and calcite precipitation occurred. The total number of injections during the experiment D2 was 30 calcium-rich injections and 29 growth-media injections, each with the compositions given in Table B.2. The injection strategy of this experiment is used as the reference case for which experimental measurements are available.

The other injection strategies have not necessarily been implemented experimentally but have been considered as possible alternatives to continuous injections at the same flow rate as the pulsed injections described in *Hommel et al. (2015b)* and *Ebigbo et al. (2012)*.

These six injection strategies can be divided into 3 pulsed and 3 continuous injection strategies with fast, normal and slow injection speed each. The reference strategy is the normal-speed, pulsed injection strategy. It is identical to the injection strategy of the experiment D2 described

**Table 5.1.:** Injection strategies investigated in this study. The reference values  $Q_{\text{ref}}$  and  $t_{\text{ref}}$  are based on the experiment D2 from *Hommel et al. (2015b)*. The time  $t_{\text{ref}}$  is the duration of the experiment D2 without the initial inoculation and the first batch period (Figure 5.2). Also, the time of the batch periods is not reduced; only the time of the injection periods is adapted to conserve the total amount of injected components.

Injection strategy	Flow rate $Q$ $\left[\frac{\text{ml}}{\text{min}}\right]$	Time of injection $t$	# of pulses
Fast pulsed	$5 \cdot Q_{\text{ref}} = 50$	$0.2 \cdot t_{\text{ref}}$	30
Pulsed	$Q_{\text{ref}} = 10$	$t_{\text{ref}}$	30
Slow pulsed	$0.2 \cdot Q_{\text{ref}} = 2$	$5 \cdot t_{\text{ref}}$	30
Fast continuous	$5 \cdot Q_{\text{ref}} = 50$	$0.2 \cdot t_{\text{ref}}$	1
Continuous	$Q_{\text{ref}} = 10$	$t_{\text{ref}}$	1
Slow continuous	$0.2 \cdot Q_{\text{ref}} = 2$	$5 \cdot t_{\text{ref}}$	1

in *Hommel et al. (2015b)*, but the initial inoculation injection and the following batch period are replaced by assuming the initial biomass distribution as discussed in Section 5.1.1. The fast-pulsed and slow-pulsed injection strategies are derived from the reference case by a change of both the flow rate of injection and the time for injection by a factor of 5, see Table 5.1.

An increase in the flow rate and a corresponding decrease of the duration of the injection result in the fast-pulsed injection strategy, while the flow rate is decreased and the duration increased for the slow-pulsed injection strategy. The batch period between the pulses of injections was not changed and remained at 4 hours for all the pulsed injection strategies.

The continuous-flow injection strategies were derived from the pulsed strategies by aggregating all injections of one type into one continuous injection of the same type but increased length. Thus, instead of the 30 repeating pulses of the pulsed strategies, as in experiment D2, the continuous injection strategies consist of one single pulse of first growth medium and second  $\text{Ca}^{2+}$ -rich medium, followed by a no-flow period of the cumulative length of all 30 batch periods of the pulsed injection strategies.

The injection methods were aligned such that the total amount of reactants injected, such as urea and calcium, as well as the composition of the injected fluids were equal for each method. This normalization allowed for fairly straightforward comparisons between the various injection strategies. These injection strategies are summarized in Table 5.1.

In an application of MICP, a faster injection might be motivated by restricted time of access to the target formation while a slower injection might be motivated by constraints of the injection pressure, which, for application of MICP as a leakage mitigation technology, has to be lower than the fracking pressure of the surrounding rock. Similarly, the continuous injections requires less time for the injection of the same amount of reactants.

These changes in both the flow rate and the general injection strategy allow for an assessment of the influence of the residence time of the components (i.e. urea,  $\text{Ca}^{2+}$ , substrate,  $\text{O}_2$ ) on the resulting distribution of calcite and biomass.

### 5.1.2. Results

First, we present the impact of the various initial biomass distributions as defined in Section 5.1.1 for the selected injection strategies defined in Table 5.1. The effect of the various initial biomass distributions on the resulting distributions of calcite and biomass is shown exemplarily for both the pulsed and the continuous injection strategy in Figures 5.4 and 5.5 respectively. Except for the extreme initial biomass distribution of the *influent spike*, the resulting distributions of calcite and biomass are quite similar, and seemingly more dependent on the injection strategy than on the initial distribution of attached biomass. Generally, for the pulsed injection strategy, the model results are less dependent on the initial biomass distribution, while for the continuous injection, the initial distribution has a higher influence on the results. This is expected, as the residence time of the pulsed injection strategy includes the 4-hour batch period. For the pulsed injection strategy, which is equal to the injection strategy used in the experiment D2 of *Hommel et al.* (2015b), the model predictions of precipitated calcite obtained by assuming the *homogeneous*, the *first-order*, the *inverse first-order*, and the *random* initial biomass distribution (see Section 5.1.1) match the experimentally measured calcite distribution very well.

The various initial biomass distributions influence the predicted final distribution of calcite in a straightforward manner. Wherever there is initially more biomass, there will be more calcite at the end. While this tendency can be seen for both pulsed and continuous injections, it is much more noticeable for the continuous injection strategy (Figure 5.4). Thus, comparison with the initially *homogeneous* biomass distribution, the *first-order* distribution increases the final calcite volume fraction in the influent region, while it decreases the volume fraction of calcite towards the effluent; the *inverse first-order* distribution behaves in the opposite way to the *first-order* distribution, decreasing calcite towards the influent and increasing it towards the effluent; the *random* initial biomass leads to a deviation of the calcite precipitated around the calcite results for the *homogeneous* case, which corresponds to the distribution of the initial biomass, as can be observed when comparing Figure 5.4 with Figure 5.3. Only the *influent spike* initial distribution of biomass leads to completely different results, caused by the dramatic changes in the order of magnitude of initial biomass with distance from the inlet.

For the pulsed injection strategy, the various initial biomass distributions do not change the distribution of calcite and biomass throughout the column. The pulsed injection strategy leads

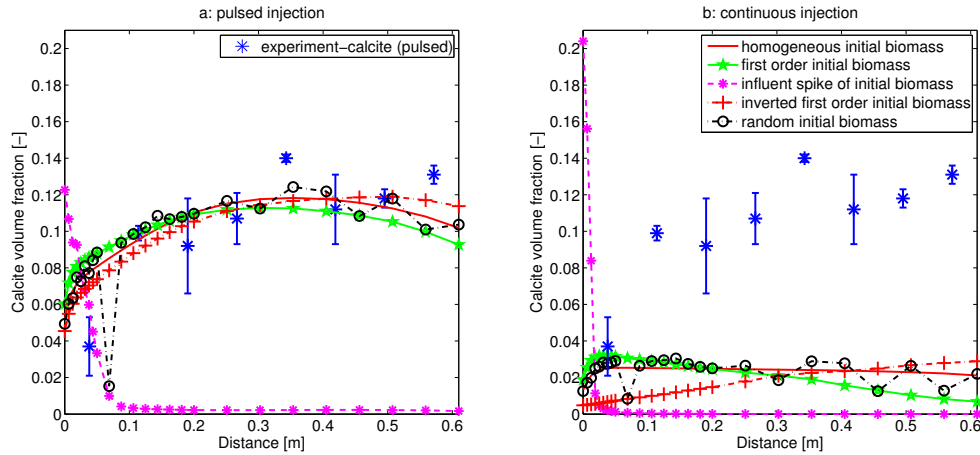


**Figure 5.4.:** Comparison of experimental calcite measurements and the resulting calcite volume fractions using the various initial biomass distributions as defined in Section 5.1.1 and shown in Figure 5.3. The results for the pulsed injection strategy are shown on the left (a) and those for the continuous injection strategy on the right (b).

to average final calcite volume fractions of more than 0.1, with only small differences between the results of *homogeneous*, *first-order*, *inverse first-order*, and *random* initial biomass distributions  $\Delta\phi_{c,\max} \approx 0.02$ . An exception is the *random* biomass distribution at  $z = 0.06875$  m, where the initial biomass is zero (Table C.1).

For the continuous injection strategy, the average final calcite volume fraction is in the order of  $\phi_c \approx 0.025$ , while the maximum difference in the final calcite volume fraction for the various initial distribution is approximately the same as for the pulsed injection strategy,  $\Delta\phi_{c,\max} \approx 0.02$ . Thus, for the continuous injection strategy, the final distribution of calcite strongly depends on the initial biomass distribution, as the variation of the final calcite volume fraction is almost as high as its average value. Here, the initially *homogeneous* and *random* biomass distributions lead to approximately constant final calcite volume fractions of  $\phi_c = 0.025$ , while the *first-order* initial biomass distribution leads to a calcite distribution decreasing from  $\phi_c = 0.035$  at the influent region to  $\phi_c = 0.008$  at the effluent. The *inverse first-order* initial biomass distribution leads to a calcite distribution increasing from  $\phi_c = 0.007$  at the influent region to  $\phi_c = 0.032$  at the effluent.

The final biomass distribution shows the same trends as those of calcite, see Figures 5.5 and 5.4. For the pulsed injection strategy, all initial biomass distributions, except for the *influent spike*, result in a more or less linearly decreasing final distribution of biomass between approximately  $\phi_f \approx 0.07$  at the influent and  $\phi_f \approx 0.02$  at the effluent end of the column. The final biomass distributions for the continuous injection strategy are very similar to the final calcite distributions for this injection strategy.

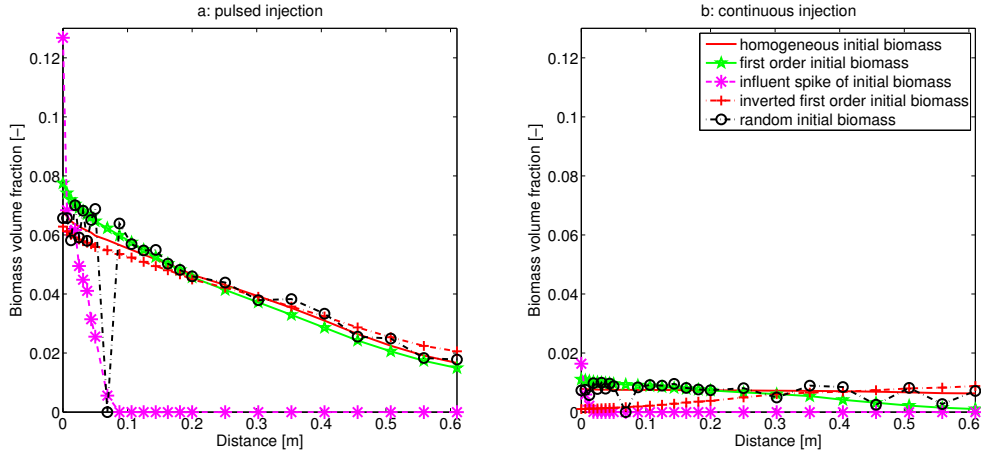


**Figure 5.5.:** Comparison of the resulting biomass volume fractions using the various initial biomass distributions as defined in Section 5.1.1 and shown in Figure 5.3. The results for the pulsed injection strategy are shown on the left (a) and those for the continuous injection strategy on the right (b).

The effect of the various initial biomass distributions on the results for the fast and slow continuous as well as the fast and slow pulsed injection strategies (Table 5.1) is similar to their effects for the reference injection rates (pulsed and continuous injection strategy) shown in Figures 5.5 and 5.4. However, the effect of the various initial biomass distributions for both the fast and the slow continuous injection strategy are not as pronounced as for the continuous injection strategy. The detailed results for both fast and slow injection strategies are available in Figures C.3-C.8.

In general, it can be observed that for the fast injection strategies, the differences caused by the various initial biomass distributions decrease, while they increase for the slow injection strategies. This becomes obvious when comparing the  $\text{Ca}^{2+}$  precipitation efficiencies  $\epsilon$  of the various injection strategies, which are presented in Table 5.2.

$$\epsilon = \frac{\Sigma \left( \text{Ca}_{\text{precipitated}}^{2+} \right)}{\Sigma \left( \text{Ca}_{\text{injected}}^{2+} \right)} \quad (5.2)$$

For both pulsed and continuous injections, the slow injections lead to higher  $\epsilon$ , while the fast injections result in very low  $\epsilon$ . For each injection rate, the pulsed injections lead to higher precipitation efficiencies than the continuous injections. Thus, higher residence times lead to higher  $\epsilon$ . The effect of longer residence times is amplified by the higher amount of biomass, which increases with residence time, resulting additionally in higher ureolysis rates. The highest  $\text{Ca}^{2+}$ -precipitation efficiency ( $\epsilon = 0.5$ ) is achieved by the slow-pulsed injection strategy

**Table 5.2.:** Impact of the initial biomass distribution, representing different attachment mechanisms, on the precipitation efficiency  $\epsilon$  of  $\text{Ca}^{2+}$  (sum of precipitated  $\text{Ca}^{2+}$  normalized by the amount of injected  $\text{Ca}^{2+}$ ) as predicted by the numerical model for the various injection strategies.

Injection strategy	Homogeneous $\phi_{f,0}$	First-order $\phi_{f,0}$	Influent spike $\phi_{f,0}$	Inverse first-order $\phi_{f,0}$	Random $\phi_{f,0}$
fast pulsed	0.217	0.214	0.015	0.216	0.214
pulsed	0.292	0.285	0.025	0.290	0.288
slow pulsed	0.492	0.484	0.135	0.500	0.486
fast continuous	0.013	0.013	0.003	0.013	0.013
continuous	0.066	0.055	0.011	0.052	0.064
slow continuous	0.401	0.399	0.069	0.402	0.387

**Table 5.3.:** Impact of the initial biomass distribution, representing different attachment mechanisms, on the shape coefficient  $\sigma$  of the calcite distribution, quantified as the ratio of the influent region calcite (at  $z = 0.10625$  m) to the effluent region calcite (at  $z = 0.5075$  m).

Injection strategy	Homogeneous $\phi_{f,0}$	First-order $\phi_{f,0}$	Influent spike $\phi_{f,0}$	Inverse first-order $\phi_{f,0}$	Random $\phi_{f,0}$
fast pulsed	0.65	0.69	0.49	0.61	0.65
pulsed	0.83	0.93	1.47	0.74	0.84
slow pulsed	3.25	3.56	2.61	3.00	3.28
fast continuous	1.00	1.02	2.80	1.01	0.98
continuous	1.10	2.82	15.4	0.37	1.10
slow continuous	3.29	3.51	41.7	3.06	3.36

when assuming the *inverse first-order* initial biomass distribution. However, for this injection strategy, assuming the *homogeneous* or the *first-order* initial biomass distribution results in almost similar  $\text{Ca}^{2+}$ -precipitation efficiencies of 0.49 or 0.48 respectively. The fast continuous injection strategy results in the lowest  $\epsilon$ . It leads to  $\epsilon = 0.013$  for the *homogeneous*, *first-order*, *inverse first-order* and *random* initial biomass distribution and  $\epsilon = 0.003$  for the *influent spike*. The *influent spike* initial biomass distribution results in very low  $\epsilon$  for all injection strategies because the biomass-catalyzed ureolysis is limited to the inlet, where the biomass is concentrated. Even the high reaction rates due to the initially high amount of biomass cannot compensate for the very short residence time of the injected fluids in the part of the column that has biomass. The values of  $\epsilon$  given in Table 5.2 are visualized in Figure C.14.

To compare the shape of the resulting distributions, it is useful to define a shape coefficient  $\sigma$  of the distribution of calcite, which quantifies the ratio of the influent region calcite ( $\phi_c$  at  $z = 0.10625$  m) to the effluent region calcite ( $\phi_c$  at  $z = 0.5075$  m):

$$\sigma = \frac{\phi_c(z = 0.10625 \text{ m})}{\phi_c(z = 0.5075 \text{ m})} \quad (5.3)$$

High values of  $\sigma$  indicate that the calcite distribution decreases with distance from the influent, while values close to 1 indicate evenly distributed calcite and values smaller than 1 indicate that the calcite increases with distance. The resulting values of  $\sigma$  are shown in Table 5.3 for all initial biomass distributions and injection strategies used in this study. Additionally, they are visualized in Figure C.15.

Slow injections lead not only to high precipitation efficiencies, but also to  $\sigma \gg 1$ , whether the injection is pulsed or continuous. Fast pulsed injections, on the contrary, result in  $\sigma \approx 0.65 < 1$  and fast continuous injections result in  $\sigma \approx 1$ . At the intermediate injection rate,  $\sigma$  of *homogeneous*, *first-order*, *inverse first-order*, and *random* initial biomass distribution is less than one ( $\sigma \approx 0.8$ ) for the pulsed injection strategy. When comparing the calcite volume fractions at  $z = 0.05 \text{ m}$  to those at  $z = 0.5075 \text{ m}$ , the influence of the various initial biomass distributions on  $\sigma$  increases, see Table C.2.

The shape coefficient  $\sigma$  only varies noticeably for the various initial biomass distributions when the injection is continuous at the intermediate injection rate. Thus, for this injection strategy, the residence time and the characteristic times for calcite precipitation are balanced in a way that the changes in the reaction rate due to varying amounts of catalytic biomass have some influence on the distribution of the precipitated calcite. *Homogeneous* and *random* initial biomass distribution lead to an almost even distribution of calcite with  $\sigma = 1.1$ , while for *first-order* and *inverse first-order* initial biomass distribution  $\sigma$  is different. *First-order* initial biomass distribution results in calcite volume fractions decreasing with distance and a corresponding  $\sigma = 2.82 \gg 1$ ; the *inverse first-order* initial biomass results in  $\sigma = 0.37 \ll 1$ . The resulting  $\sigma$  of the *homogeneous*, the *first-order*, and the *inverse first-order* initial biomass distribution are visualized in Figure 5.6. In this figure, it can be seen that the *inverse first-order* initial biomass distribution leads to a lower  $\sigma$ , i.e. less precipitation in the influent relative to the deeper distances into the column, when switching from the pulsed to the continuous injection, while the *first-order* initial biomass distribution shows an increase in  $\sigma$ , i.e. greater precipitation in the influent region relative to the deeper sections of the column, when changing from the pulsed to the continuous injection. However, for the *inverse first-order* initial biomass distribution,  $\sigma$  is always smaller than for the *first-order* initial biomass distribution, but for all injection strategies except for the continuous injection strategy, this difference in  $\sigma$  is very small, see Figure 5.6 and Table 5.3.

Figures 5.7 and 5.8 visualize the impact of changed injection strategies on the distributions of calcite and biomass for the *homogeneous* and the *first-order* initial biomass distribution. For

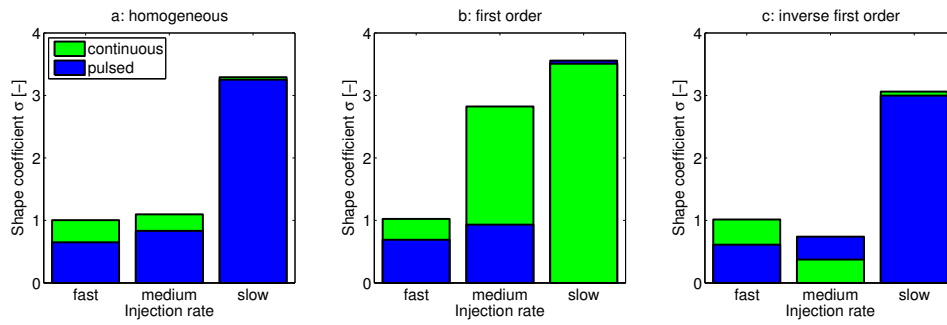


**Figure 5.6.:** Comparison of the resulting shape coefficients  $\sigma$  as given in Table 5.3 for the pulsed and continuous injections at various injection rates (Table 5.1) using the *homogeneous* (a), the *first-order* (b), and the *inverse first-order* (c) initial biomass distribution. The shape coefficients  $\sigma$  of the other initial biomass distributions for all the injection strategies are shown in Figure C.15.

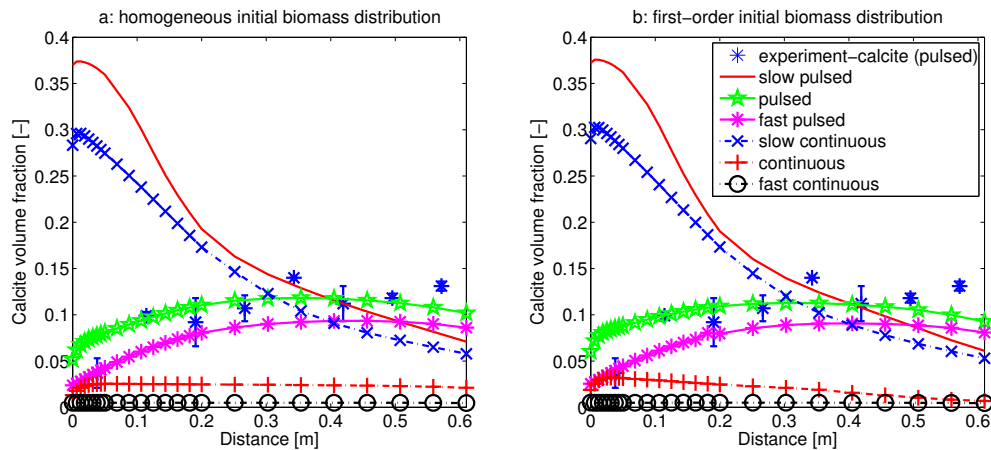


**Figure 5.7.:** Comparison of the resulting calcite volume fractions for the various injection strategies (see Table 5.1) using the *homogeneous* (a) and the *first-order* (b) initial biomass distribution.

the other distributions, the impact is similar as shown in the Figures C.9-C.13.

For all injection rates, the biomass volume fractions are always greater for the pulsed injections than for the continuous injections, presumably due to the repeated supply of oxygen, the limiting nutrient for growth in this system, which allows for biomass growth in between calcium precipitation periods. Additionally, the biomass distribution is more even for the continuous injection strategies. In general, decreased injection rates lead to an increase in the biomass volume fraction, especially towards the influent. However, the final biomass distribution of the slow pulsed (and to a lesser extent the slow continuous) injection strategy (Figure 5.8) are reduced, at least at the influent, as a result of the high precipitation of calcite (Figure 5.7) which leads to inactivation of biomass in the influent region (Ebigbo *et al.*, 2012).

Because attachment does not only determine the distribution but also the total amount of

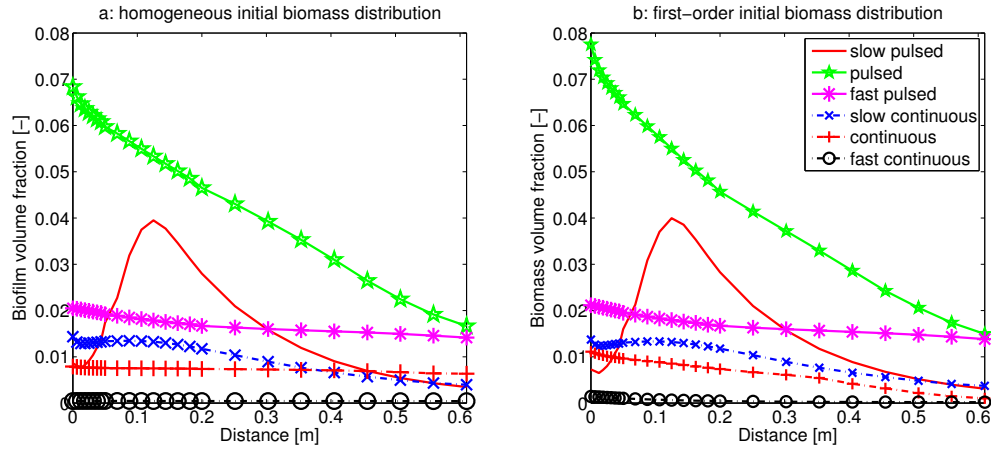


**Figure 5.8.:** Comparison of the resulting biomass volume fractions for the various injection strategies (see Table 5.1) using the *homogeneous* (a) and the *first-order* (b) initial biomass distribution.

attached cells, the impact of varying initial amounts of biomass is investigated as well.

Figures 5.9 and 5.10 compare the resulting final volume fractions of calcite for the *homogeneous* and the *first-order* initial biomass distributions for three different amounts of total initial biomass and two injection strategies, the pulsed and the continuous injection strategy. As expected, increased initial amounts of biomass lead to increased final volume fractions of both biomass and calcite. It is very interesting that the pulsed injection strategy with increased initial biomass results in a decreased final biomass volume fraction for the second half of the column, which is not the case for the continuous injection strategy. This behavior is probably caused by the overall higher biomass concentrations, achieved through the pulsed injection strategies. These increased biomass concentrations result in almost complete consumption of the limiting nutrient, oxygen, in the first half of the column at later times, see Figures C.16 and C.17. The significantly reduced oxygen concentrations then result in significantly reduced biomass growth in the second half of the column relative to the first half of the column. The same effect can be observed when comparing the biomass volume fractions for the second half of the column resulting from pulsed and slow pulsed injection strategies (Figure 5.8 and Figures C.16 and C.17).

Further, for increased initial biomass, the shape coefficient  $\sigma$  of the calcite distribution increases as well as the precipitation efficiency  $\epsilon$  (Table 5.4). For the *homogeneous* initial biomass distribution,  $\epsilon$  increases more than for the *first-order* initial biomass distribution. But for  $\sigma$ , the increase is higher for the *first-order* than for the *homogeneous* initial biomass distribution.

Thus, the impact of increased initial biomass is similar to the impact of decreased injection rate, but is not as pronounced. This becomes evident when comparing the results of *homogeneous*

**Table 5.4.:** Impact of the initial amount of biomass on the precipitation efficiency of  $\text{Ca}^{2+}$   $\epsilon$  (sum of precipitated  $\text{Ca}^{2+}$  normalized by the amount of injected  $\text{Ca}^{2+}$ ) and the shape coefficient  $\sigma$  of the distribution of calcite quantified as the ratio of the influent region calcite (at  $z = 0.10625$  m) to the effluent region calcite (at  $z = 0.5075$  m) as predicted by the numerical model for the pulsed and continuous injection strategy and *first-order* and *homogeneous* initial biomass distribution.

Injection strategy	Biomass	$\epsilon$	$\sigma$
pulsed, first-order	high $\phi_f$	0.301	1.07
	$\phi_f$ (Sec. 5.1.1)	0.285	0.93
	low $\phi_f$	0.275	0.87
pulsed, homogeneous	high $\phi_f$	0.315	0.87
	$\phi_f$ (Sec. 5.1.1)	0.292	0.83
	low $\phi_f$	0.280	0.82
continuous, homogeneous	high $\phi_f$	0.087	1.14
	$\phi_f$ (Sec. 5.1.1)	0.066	1.10
	low $\phi_f$	0.051	1.06

and *first-order* initial biomass for the pulsed injection strategy given in Table 5.4 with those for the pulsed injections and *homogeneous* and *first-order* initial biomass in Tables 5.2 and 5.3.

However, the increase in both the final volume fraction of biomass and calcite with increasing initial biomass concentration is surprisingly low. The resulting calcite volume fraction is only increased by approximately a maximum of 20% in the influent region for the 5-fold increased initial biomass for the pulsed injection strategy when assuming the *first-order* distribution, while for the second half of the column, there are only very small differences.

For the *homogeneous* initial distribution, the 5-fold increased initial biomass volume fraction leads to an increase of the final calcite volume fraction of approximately 10%, but for this initial biomass distribution the increase is approximately constant over the length of the column, which is supported by the small changes in  $\sigma$  shown for the *homogeneous* initial biomass (Table 5.4). The impact of a varied initial amount of biomass on the resulting final calcite volume fractions of the continuous injection is approximately similar to the impact on the results of the pulsed injection.

For a decrease in the initial biomass, the results of both the *homogeneous* and the *first-order* initial distribution of biomass show a trend that is expected from the case of increased initial biomass, i.e.  $\sigma$  and  $\epsilon$  both decrease with decreasing initial biomass.

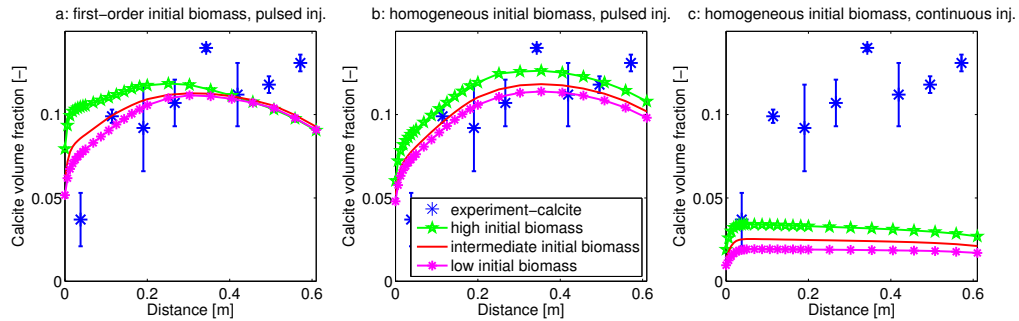


**Figure 5.9.:** Comparison of the resulting calcite volume fractions for various initial amounts of biomass (high: initial biomass distribution multiplied by 5; intermediate: initial biomass distribution as specified in Section 5.1.1; low: initial biomass distribution divided by 5). The final calcite distribution resulting from the varied initial amount of biomass for the *first-order* distribution of biomass when using the pulsed injection strategy is shown on the left (a); the results for for the *homogeneous* initial biomass using the pulsed injection strategy in the middle (b) and for the *homogeneous* initial biomass distribution using the continuous injection strategy on the right (c).

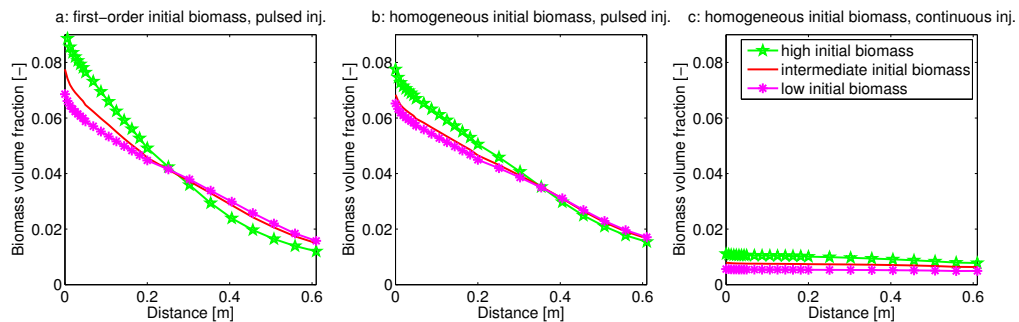


**Figure 5.10.:** Comparison of the resulting biomass volume fraction or various initial amounts of biomass (high: initial biomass distribution multiplied by 5; intermediate: initial biomass distribution as specified in Section 5.1.1; low: initial biomass distribution divided by 5). The final biomass distribution resulting from the varied initial amount of biomass for the *first-order* distribution of biomass when using the pulsed injection strategy is shown on the left (a); the results for for the *homogeneous* initial biomass using the pulsed injection strategy is shown in the middle (b) and for the *homogeneous* initial biomass distribution using the continuous injection strategy on the right (c).

### 5.1.3. Discussion

The initial distribution of biomass generally has only a minor influence on the distribution of cells and calcite throughout the columns (Figure 5.4 and 5.5; Tables 5.2 and 5.3), although the initial distribution of biomass can become important if very large spatial differences in biomass concentration are present. For instance, cases (such as for the *influent spike* biomass distribution) with very high biomass concentrations in the influent result in very high volume fractions of calcite in the influent region of the column. This case simulates a very low permeability formation into which microbial cultures are injected. Cells would mostly attach to the first few centimeters of the formation and, in the field, MICP in such a situation would probably result in complete plugging of the injection well unless specific injection strategies were developed and applied.

In contrast, if no biomass is present in certain areas of the columns, very little to no precipitation was observed. This is because of the lack of urea-hydrolyzing biomass in these areas. In the simulations, the effect of this initial lack of biomass is exacerbated because the only way for biomass to reach those areas would be growth of biomass into these areas from adjacent areas or detachment and reattachment from upstream areas. All of these mechanisms were excluded from the simulations since the purpose of this study was to evaluate the effect of initial biomass distributions and injection strategies on the effectiveness of MICP technologies.

The injection strategy (i.e. pulsed vs. continuous; fast vs. slow) has a much more obvious influence on the final distribution of biomass and calcite (Figures 5.8 and 5.7; Tables 5.2 and 5.3). Specifically, the  $\text{Ca}^{2+}$  precipitation efficiency  $\epsilon$  varies between 0.285 (*first-order* initial biomass) and 0.292 (*homogeneous* initial biomass) for the pulsed injection strategy and all initial biomass distributions, except for the *influent spike* initial distribution of biomass. The latter always has much lower  $\text{Ca}^{2+}$  precipitation efficiencies compared to the other initial biomass distributions, see Table 5.2. In contrast, the  $\text{Ca}^{2+}$  precipitation efficiency varies for the various injection strategies for the initially *homogeneous* biomass distribution from 0.013 (fast continuous injection) to 0.492 (slow pulsed injection). This again emphasizes how much more important the injection strategy is relative to the initial distribution of biomass when the desired outcome is efficient and homogeneously distributed calcite precipitation. This is demonstrated in Figure 5.11, which compares the  $\text{Ca}^{2+}$  precipitation efficiency for *homogeneous* and *first-order* initial biomass distribution for the various injection strategies (Table 5.1).

As discussed previously, the most notable exception is the very extreme *influent spike* initial biomass distribution, where all biomass is concentrated at the influent of the column. As a result, the precipitation efficiency of the simulations starting with this biomass distribution

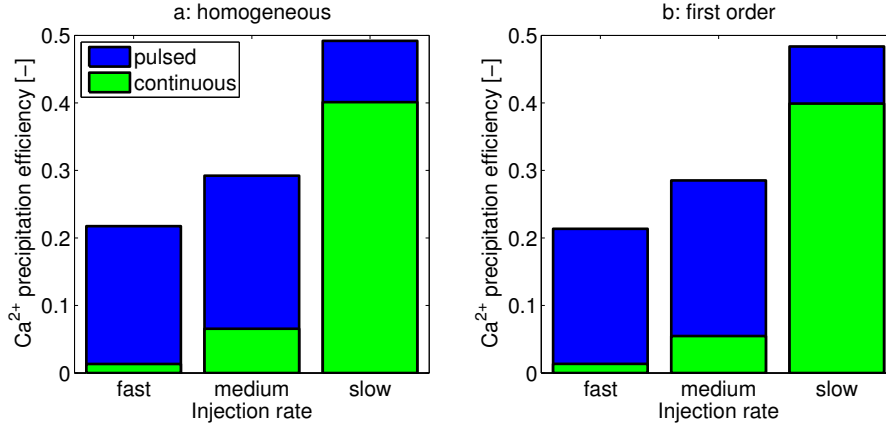


**Figure 5.11.:** Comparison of the resulting  $\text{Ca}^{2+}$  precipitation efficiency  $\epsilon$  as given in Table 5.2 for the pulsed and continuous injections at various injection rates (Table 5.1) using the *homogeneous* (a) and the *first-order* (b) initial biomass distribution. The  $\text{Ca}^{2+}$  precipitation efficiencies of the other initial biomass distributions for all the injection strategies are shown in Figure C.14.

is more than an order of magnitude lower than for the other initial biomass distributions. But even when considering the extreme case of the *influent spike*, the precipitation efficiency varies more due to differences in the injection strategy compared with a change in the initial distribution.

The explanation for the low influence of the various initial biomass distributions on the final distribution of calcite is that the final biomass distributions are very similar for all the initial distributions investigated. The most prominent exceptions are locations where there is no biomass initially, i.e. the *influent spike* at  $z > 0.1$  m and the *random* initial biomass at  $z = 0.06875$  m. As attachment of cells is neglected in this study (Section 5.1.1), there is no possibility to establish a biofilm at these locations.

Thus, the initial distribution of biomass (except for the *influent spike*) does not influence the characteristic shape of the final precipitated calcite very much (and thereby the shape coefficient  $\sigma$ ; see Table 5.3), but only leads to minor shifts of the location of maximum calcite precipitation; for the *influent spike* and the *first-order* case to the upstream part of the column and for the *inverse first-order* distribution to the downstream side of the column relative to the *homogeneous* initial biomass distribution. The exception here is the continuous injection strategy, where the shape of the final calcite distribution is clearly influenced by the initial biomass distribution, see Figures 5.4 and 5.5. The location of maximum calcite precipitation also clearly depends on the initial biomass distribution. This is visualized in Figure 5.6 comparing the shape coefficients for all injections obtained by simulations with the *homogeneous*, *first-order*, and *inverse first-order* initial biomass distribution.

Similarly to the initial distribution, the total amount of initial biomass does not influence the

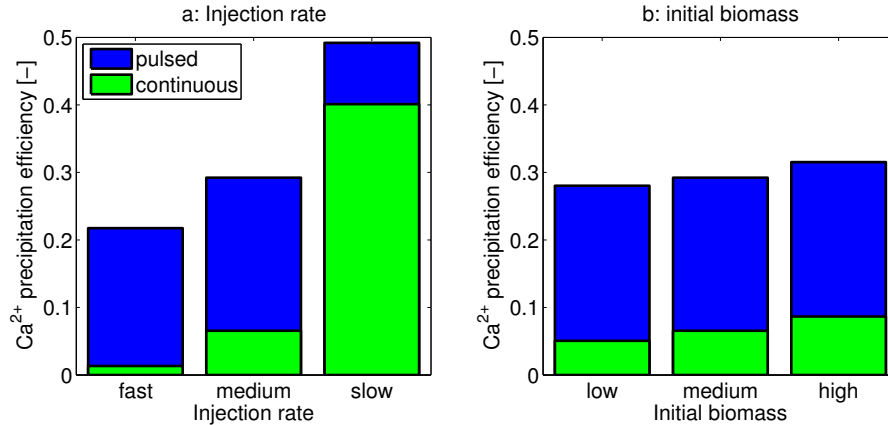


**Figure 5.12.:** Comparison of the resulting Ca<sup>2+</sup> precipitation efficiency  $\epsilon$  for the *homogeneous* initial biomass distribution for both pulsed and continuous injections when (a) varying the injection rate (see Table 5.1) for the medium initial amount of biomass or (b) varying the initial amount of biomass at medium injection rate.  $\epsilon$  of the other initial biomass distributions for all the injection strategies are shown in Figure C.14.

model results as much as the injection strategies, although it appears to be greater than the impact of the various initial biomass distributions. An increase in initial biomass changes the resulting biomass and calcite distributions similarly to a decrease in injection rate. This can be explained by the changes in the characteristic time for transport relative to the characteristic time for reaction, which can also be expressed as the dimensionless Damköhler number  $Da$ :

$$Da = \frac{\text{time of advection}}{\text{time of reaction}} \quad (5.4)$$

Both the increase in ureolytically active biomass and the decrease in injection rate increase the  $Da$  number. Thus, initially, before significant growth of biomass has occurred, the  $Da$  number of, for example, the slow pulsed injection strategy with a medium initial amount of biomass is equal to the  $Da$  of the pulsed injection strategy with a high initial amount of biomass. The differences in the results develop later during the course of the simulation, as the amount of biomass changes due to growth, decay and detachment. In the model, the rate of detachment increases with increased shear stress (potential gradient), (*Ebigbo et al.*, 2012; *Hommel et al.*, 2015b). Thus, detachment will reduce the accumulation of biomass due to growth much more for the pulsed injection strategy than for the slow pulsed injection strategy. Figure 5.12 visualizes this effect, comparing the impact of varying the injection rate with the impact of varying the amount of initial biomass for the *homogeneous* initial biomass distribution. Similarly, the shape of the final calcite distribution does not change much with varying initial biomass, as shown in Figure 5.13 comparing the shape coefficients for varying injection rates and varying initial biomass for the *homogeneous* initial biomass distribution.

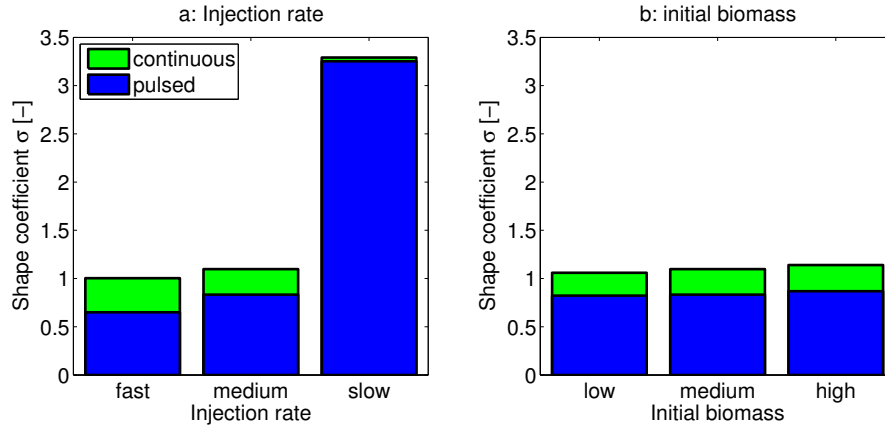


**Figure 5.13.:** Comparison of the resulting shape coefficients  $\sigma$  for the *homogeneous* initial biomass distribution for both pulsed and continuous injections when (a) varying the injection rate (see Table 5.1) for the medium initial amount of biomass or (b) varying the initial amount of biomass at medium injection rate.  $\sigma$  of the other initial biomass distributions for all the injection strategies are shown in Figure C.15.

These observations again emphasize that the injection strategy has the greatest influence on the model results. In general, pulsed injection strategies and low injection rates lead to higher precipitation efficiencies, since the amount of precipitated calcite increases while the mass of injected  $\text{Ca}^{2+}$  is constant. The high  $\text{Ca}^{2+}$  precipitation efficiency  $\epsilon$  of pulsed injection strategies is a result of the discontinuous injections with the 4-hour batch periods. During the batch periods, there is no flow and, thus, the residence time is drastically increased. Specifically, the residence time for the whole column during the injection phases (pulsed or continuous) is much shorter than for the no-flow ('batch') periods. The average hydraulic residence times during the flow phases are 3 minutes for the fast, 15 minutes for the intermediate and 75 minutes for the slow injection rate. During the no-flow phases ('batch periods'), the  $Da$  increases drastically and increases both the extent of precipitation and biomass growth. However, for the slow injection rate, the relative increase of the  $Da$  between the flow and batch periods is smaller than for the fast pulsed injections. This is the reason for the increasing differences between the results of pulsed and continuous injection strategies for the fast injection rate relative to the slower injection rates.

Fast injections lead to distributions where the calcite volume fraction increases with the distance from the influent. For these injections, the reactions are slow relative to the transport, resulting in low  $Da$  and precipitation farther away from the influent. Slow injections, on the contrary, result in high  $Da$  and lead to more precipitation in the influent region relative to the more distant parts of the columns (Table 5.3). In the extreme case, this could lead to massive precipitation in the influent region and complete clogging of the column.

The various initial distributions of biomass (Section 5.1.1) do not only lead to similar results

when compared with each other (Figures 5.4-5.5 and Figures C.3-C.8) but similarly match the full model accounting for inoculation and attachment (Hommel *et al.*, 2015b) quite well (Figure C.2). Thus, neglecting attachment, the component suspended biomass, and starting the simulation with an assumed, pre-established distribution of biomass might be a promising step for the development of models with reduced complexity and computational time.

## Summary

The results of this study indicate that the initial distribution and the initial amount of biomass have less influence on the result of an engineered MICP process than the injection strategy. The initial distribution of biomass can have an influence on the distribution of the precipitated calcite as shown for the continuous injection strategy (Figure 5.6). However, even for this injection strategy, there are only minor differences between the various initial biomass distributions when the resulting precipitation efficiencies are compared. Extreme biomass distributions can also significantly influence the distribution of calcite as exemplified by the *influent spike* scenario, where cells are not able to travel into a porous medium and form a filter cake close to the injection point, resulting in large amounts of biomass and, as a result, calcite at the influent and basically the absence of calcite further downstream.

Optimization in the field, where biomass distribution cannot be controlled very easily, should therefore focus on the development of optimal injection strategies for an assumed biomass distribution. Flow rates low enough to allow for high precipitation efficiency but fast enough to reduce immediate precipitation at the injection point and therefore potential clogging of the influent region should be pursued. Furthermore, no-flow ('batch') periods which would allow for extensive reaction (i.e. urea hydrolysis and calcite precipitation) are recommended regardless of the biomass distribution. Additionally, high flow rates during the injection periods lead to a more homogeneous distribution of calcite or even calcite volume fractions increasing with distance from the influent.

Pulsed injection strategies will lead to higher precipitation efficiencies and fast injection rates will reduce the potential for immediate precipitation of calcite regardless of the distribution of biomass. Additional advantages can be obtained if biomass distribution can be controlled, but this strategy is probably limited in the field.

## 5.2. Application of the model on the field scale <sup>†</sup>

As part of the preparation of a field application of MICP, two different injection strategies (*simple* and *ideal*) are modeled for two different geometrical scenarios (small and large) each. After the field application, a third set of simulations (*real*) is carried out based on the injection strategy of the real application including sampling and changes due to technical problems.

### 5.2.1. Field site and resulting simulation scenarios

The field site is a well located at the Southern Company Gorgas Power Plant in Alabama, USA (*Cunningham et al.*, 2014). The target formation is the Fayette sandstone at 341 m below ground surface which is hydraulically fractured forming a single, horizontal and radial fracture (*Cunningham et al.*, 2014). The formation porosity and permeability are estimated to be 0.12 and 10 mD =  $1.0856 \cdot 10^{-14} \text{ m}^2$  respectively, based on a petrophysical analysis prepared by Schlumberger Carbon Services.

To address the uncertainty in the extent of the radial fracture, two scenarios are investigated: the small scenario with a fracture radius of 1.6 m and the large scenario with a fracture radius of 4 m. The total simulation domains are  $22.5^\circ$  slices, the height as well as the radial extent being adjusted to the fracture radius, resulting in a height and radius of 2.4 m for the small and 8 m for the large scenario, see Figure 5.14. For each scenario, the fracture is approximated as a thin highly permeable layer in the vertical center of the simulation domain.

<sup>†</sup>This section is based on joint work with Elena Shigorina, undertaken during her master's thesis: E. Shigorina (2014). Numerical investigation of microbially induced calcite precipitation at field scale. Master's thesis, Institut für Wasser- und Umweltsystemmodellierung, Universität Stuttgart.

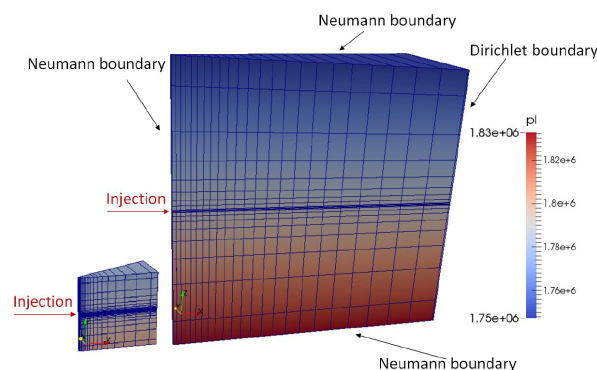


**Figure 5.14.:** Sketch of the grid for the small and the large scenario and the initial pressure as well as the boundary conditions used (*Shigorina*, 2014).

**Table 5.5.:** Main characteristic parameters of the injection strategies investigated for the field application. The complete injection strategies are given in the Appendix, Tables D.2-D.4.

Injection strategy	Brief description	Biomass pulses	Ca <sup>2+</sup> -rich pulses	Mass of Ca <sup>2+</sup> injected [kg]	Duration [h]
<i>simple</i>	few long pulses	1	4	64.3	117.4
<i>ideal</i>	many short pulses	7	34	36.8	93.4
<i>real</i>	many short pulses	6*	24*	21.1	74.3

\* For the *real* injection strategy, the last injection of biomass and the last 3 injections of calcium-rich medium were split into several subinjections as the injection pressure rose above a critical pressure, see Table D.4.

The representative fracture-layer permeability  $K_{\text{frac}} = 1.645 \cdot 10^{-12} \text{ m}^2$  is estimated by fitting single-phase flow simulation results for the large scenario to the data from the field site pumping tests conducted by Schlumberger Carbon Services. The fracture-layer porosity is assumed to be identical to the formation porosity. The critical porosity in the porosity-permeability relation (see Equation (3.31)) is estimated to be  $\phi_{\text{crit}} = 0.1$ , based on the  $\phi_{\text{crit}}$  previously fitted for sandstone cores (Hommel *et al.*, 2013), see Section 4.1.

The computational grid is refined towards the well and around the fracture, see Figure 5.14. The initial conditions are chosen as hydrostatic pressure distribution with a pressure of  $1.79 \cdot 10^6 \text{ Pa}$  at the vertical center of the domain. The initial mole fractions are zero except for total carbon  $x_{\text{w}}^{\text{Ctot}} = 1.79 \cdot 10^{-7}$  as well as Na and Cl, which are set to  $x_{\text{w}}^{\text{Na}} = x_{\text{w}}^{\text{Cl}} = 0.007$  to match the formation salinity of  $X_{\text{sal}} = 24 \text{ g/l}$  reported in Cunningham *et al.* (2014). All other components are assumed not to be present initially. The boundary conditions are set to no-flow boundaries by default, except for the injection into the fracture-layer at the inner radius and a Dirichlet boundary condition for the entire outer radius, which is set to the initial values. The parameters of the injection are discussed in Section 5.2.2.

### 5.2.2. Investigated injection strategies

Two injection strategies were considered during the planning of the field experiment, one with a low number of injections of a long duration each, referred to in the following as the *simple* injection strategy, and one with a high number of short injections, referred to in the following as the *ideal* injection strategy. The *ideal* injection strategy was chosen to be applied in the field as injections with long duration as required in the *simple* strategy were not technically feasible. A third injection strategy implemented is the *real* injection strategy, which is based on the injections carried out in the field, including technical problems, delays and sampling. The three injection strategies are summarized in Table 5.5. The detailed injection strategies are given in Appendix D, Tables D.2-D.4.

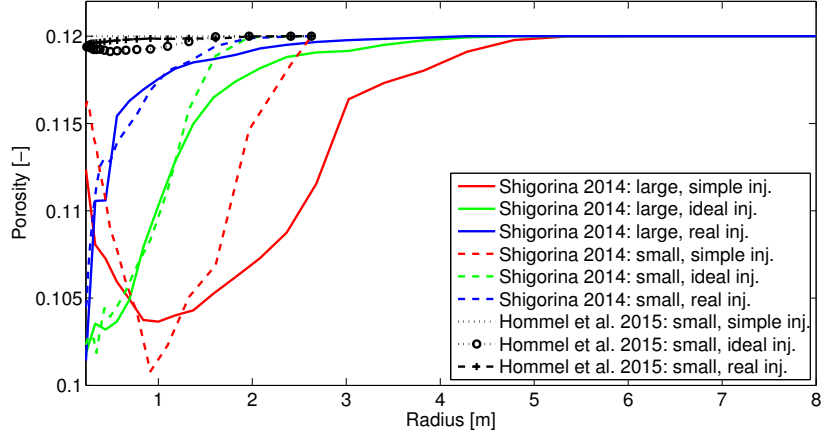


**Figure 5.15.:** Predicted porosity along the fracture layer for the simulations done by *Shigorina* (2014) and using the parameter set from *Hommel et al.* (2015b). Note that in *Shigorina* (2014), the injections were erroneously assumed to enter the  $22.5^\circ$  simulation domain completely, leading to an 8-fold increased injection rate and total mass of injected components.

It is important to note that in *Shigorina* (2014), the fluids were erroneously assumed to be injected only into the  $22.5^\circ$  simulation domain, which led to an 8-fold increased injection rate and mass of the injected components, when assuming radial symmetry. This is corrected in new simulations using the model published in *Hommel et al.* (2015b) (Section 4.2). As the results for the small and the large scenario do not differ much (see Figures 5.15 and 5.16) and due to the significant computational time requirements of the large grid (see Table 5.6), those new simulations are only run for the small scenario.

### 5.2.3. Comparison of model predictions

As expected, the injection strategy influences both the amount and the distribution of biofilm and calcite. Except for the *simple* injection strategy, the simulation results by *Shigorina* (2014) are similar for the small and the large scenario. In general, the simulations for the large scenarios lead to a slightly higher reduction of the porosity and the permeability further away from the injection region, see Figures 5.15 and 5.16. The reduction of porosity and permeability is mainly caused by the precipitated calcite ( $\phi_{c,\max} \approx 0.02$ ), see Figures D.1 and D.2.

For the simulations of *Shigorina* (2014), the *simple* injection strategy resulted in high precipitation efficiencies (28% for the small and 34% for the large scenario). The *ideal* and *real* injection strategies resulted in precipitation efficiencies of approximately 4% (3.2-4.8%), see Table 5.6. This is consistent with the injection rate dependency of the precipitation efficiency found

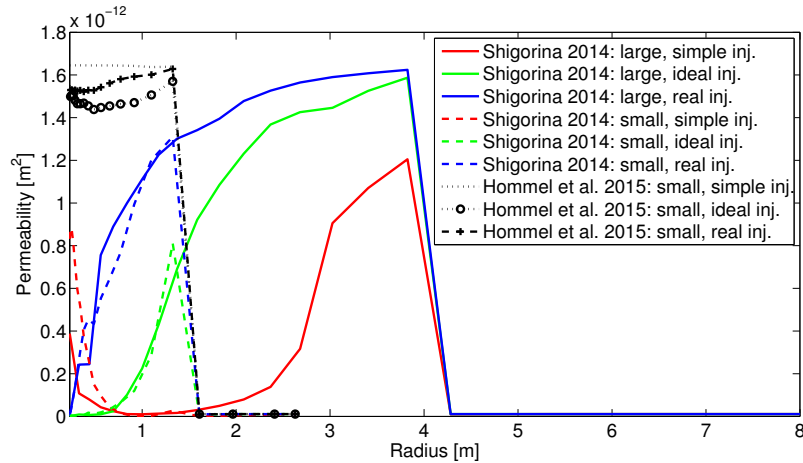


**Figure 5.16.:** Predicted permeability along the fracture layer for the simulations done by *Shigorina* (2014) and using the parameter set from *Hommel et al.* (2015b). The fracture was estimated to extend until 4 m for the large scenario and until 1.6 m for the small scenario. The initial formation permeability is  $K_0 = 1.0856 \cdot 10^{-14} \text{ m}^2$  while the initial fracture-layer permeability is  $K_{\text{frac}} = 1.645 \cdot 10^{-12} \text{ m}^2$ . Note that in *Shigorina* (2014), the injections were erroneously assumed to enter the 22.5° simulation domain completely, leading to an 8-fold increased injection rate and total mass of injected components.

in *Hommel et al.* (2015a), see Section 5.1, where it is found that the precipitation efficiency increases with decreasing injection rate. The injection rate of the *simple* injection strategy ( $1.0515 \cdot 10^{-5} \text{ m}^3/\text{s}$ ) is lower than the typical injection rates of the calcium-rich injections for the *ideal* ( $5.5 \cdot 10^{-5} \text{ m}^3/\text{s}$ ) or the *real* ( $3.2 \cdot 10^{-5} \text{ m}^3/\text{s}$ ) ones.

The simulations with the “best fit” parameter set from *Hommel et al.* (2015b) (Section 4.2) and the corrected injection rate lead to only minor changes in porosity and permeability, see Figures 5.15 and 5.16. Much less calcite is predicted to precipitate compared with the simulations of *Shigorina* (2014). The precipitation efficiencies are less than 2% for all scenarios when using the “best fit” parameter set from *Hommel et al.* (2015b), see Table 5.6. The biofilm volume fractions (Figure D.1) are not significantly lower than the biofilm volume fractions predicted by *Shigorina* (2014).

#### 5.2.4. Discussion

For the simulations done by *Shigorina* (2014), most scenarios required a considerable computational time, see Table 5.6, especially the simulations for the large scenario. However, the results are very similar for both scenarios for radii smaller than 1.6 m, which is the assumed radius of the fracture layer in the small scenario. Even with the improved model, the computational time remains significant.

**Table 5.6.:** Computational and simulation time for the investigated injection strategies and scenarios. Additionally, the number of  $\text{Ca}^{2+}$ -rich injections until the assumed plugging and the mass of  $\text{Ca}^{2+}$  injected until plugging are given, together with the precipitation efficiency defined in Section 5.1.2, Equation (5.2):  $\text{Ca}_{\text{precipitated}}^{2+}/\text{Ca}_{\text{injected}}^{2+}$ . The mass of  $\text{Ca}^{2+}$  injected here is not the total mass of  $\text{Ca}^{2+}$  planned to be injected (see Table D.1), but the mass of  $\text{Ca}^{2+}$  injected until the model predicts plugging and the simulation is terminated\*. The top part gives the values for the simulations done by *Shigorina* (2014), the bottom part the values for simulations using the parameter set “best fit” from *Hommel et al.* (2015b) and the corrected injection rate. The field test was terminated after 24  $\text{Ca}^{2+}$ -rich injections, 74.3 hours after starting the first injection.

Injection and scenario	comput. time [h]	Time simulated * [h]	$\text{Ca}^{2+}$ -rich injections	Mass $\text{Ca}^{2+}$ inj. [kg]	Precipitation efficiency [%]
<i>simple</i> small	1.30	56.26	1.8	29.5	27.7
<i>simple</i> large	96.8	54.59	1.7	29.5	34.3
<i>ideal</i> small	0.96	70.93	25	27.1	3.2
<i>ideal</i> large	26.06	70.94	25	27.1	4.1
<i>real</i> small	93.49	41.25	9	8.9	4.8
<i>real</i> large	38.55	27.76	9	8.8	4.0
field test	-	74.26	24	21.1	unknown
Using the parameters given in <i>Hommel et al.</i> (2015b) and corrected injection rate					
<i>simple</i> small**	381.82	78.37	2.7	43.3	0.6
<i>ideal</i> small	74.94	69.67	24	26.0	1.3
<i>real</i> small***	99.81	74.26	24	21.1	0.4

\* This is the simulated time until the simulation was terminated due to numerical problems related to the decrease in permeability. These numerical problems were interpreted as the time when plugging occurred as it was not possible in the simulation to inject further at the given injection rate.

\*\* The simulation of the *simple* injection strategy using the parameters given by *Hommel et al.* (2015b) was terminated due to the very long computational time but without numerical problems.

\*\*\* The simulation of the *real* injection strategy using the parameters given by *Hommel et al.* (2015b) did not lead to numerical problems and the entire time of the field experiment could be simulated.

As the experimental data are limited due to the depth of 341 m below ground surface, it is difficult to conclude which of the models and which parameter sets most represent the reality. The sensitivity of the model to the estimated formation porosity and permeability, to the assumed fracture-layer porosity and permeability, and to the assumed critical porosity is not investigated. Especially the choice of the critical porosity, at which the permeability becomes zero, strongly influences the permeability predictions of the model.

The low amount of calcite precipitated in the simulations using the corrected injection rate and the parameters from *Hommel et al.* (2015b) (Figure D.2) is consistent with the results in *Hommel et al.* (2015b) (Section 4.2), where the “best fit” parameter set is able to predict the results of all column experiments used while underestimating the precipitation for the radial-flow experiment BR, see Figure B.4.

This is most probably caused by the value of the urease content  $k_{\text{ub}} = 3.81 \cdot 10^{-4}$  being much lower than the preliminary estimate ( $k_{\text{ub}} = 0.0014$ ) used by *Shigorina* (2014), leading to lower ureolysis rates (Eq. (4.6)) and, ultimately, less calcite precipitating. This is supported by the biofilm volume fractions (Figure D.1) being only slightly inferior to the biofilm volume fractions predicted by *Shigorina* (2014). Additionally, the biofilm density  $\rho_f = 6.9 \text{ kg/m}^3$  of the “best fit” parameter set is also lower than the value used by *Shigorina* (2014) ( $\rho_f = 10 \text{ kg/m}^3$ ), leading to less biomass for identical biofilm volume fractions and further reduced ureolysis rates. Thus, the reduced precipitation is probably caused by the decrease in  $k_{\text{ub}}$  and  $\rho_f$  used for the simulations.

### 5.2.5. Summary and outlook

The field-scale application at the Gorgas well is successfully modeled. A comparison of the small and the large scenario indicates that large simulation domains might not be necessary to model MICP as the results of both scenarios are quite similar.

The simulation results using the planned (*ideal*) injection strategy match the field-application results very well, as they predict plugging after 25  $\text{Ca}^{2+}$ -rich and 6 biomass injections. In the field, plugging occurred after 24  $\text{Ca}^{2+}$ -rich and 6 biomass injections. However, using the injection strategy actually used in the field, including delays due to technical problems, variations in the flow rate, and sampling, the simulations done by *Shigorina* (2014) predict plugging much earlier, already after 9  $\text{Ca}^{2+}$ -rich injections, while using the “best fit” parameter set (*Hommel et al.*, 2015b) does not lead to significant plugging.

The computational time for such field-scale applications quickly increases with increasing simulation domain size and the need for a fine spatial discretization able to capture small-sized heterogeneities as a highly permeable region. Consequently, research on models with reduced computational effort is important for further field-scale applications to be able to assist decision-making. Further research should explore the possibilities to reduce the computational effort of the model for MICP without reducing the predictive accuracy. Faster simulations would enable the investigation of more scenarios, e.g. with varying initial porosity and permeability, increasing the confidence in the model results by providing a range of model predictions matching the range of initial parameter estimates. Further, such investigations would provide site-specific sensitivity analyses.



## 6. Perspectives for efficient solution strategies

As discussed in Chapter 4, the description of the microbial ureolysis kinetics was improved based on new experimental findings by *Lauchnor et al.* (2015) and the model was recalibrated using improved experimental data (*Hommel et al.*, 2015b). This increased the capability of the model to predict laboratory experiments while simplifying some of the reaction rates. However, the model complexity and thus the computational effort are still high, which limits the use of the model for designing field-scale applications of MICP. Different strategies for reducing the computational effort are possible, e.g. optimized numerical approaches or simplified physics and chemistry.

First in Section 6.1, this chapter gives an overview of the possible ways of improving the efficiency of numerical models for multi-component reactive transport. Second, Section 6.2 presents the preliminary results of an investigation of the effect of some selected possibilities discussed in Section 6.1 on the computational efficiency and accuracy of the MICP model discussed in Section 4.2 (*Hommel et al.*, 2015b).

### 6.1. Options to reduce computational time

There are several options for reducing the computational time. What they have in common is that they mainly focus on reducing the number of unknowns or the non-linear coupling between the equations, which are the main sources of numerical difficulties (*Carrayrou et al.*, 2010; *Kräutle and Knabner*, 2007).

#### 6.1.1. Optimized numerical solution approaches

The most commonly used solution approaches are the globally implicit approach (GIA) and sequential approaches such as the sequential iterative approach (SIA) and the sequential non-iterative approach (SNIA) (*Steeffel et al.*, 2015a). All of the numerical solution approaches are able to accurately predict the distributions of components as well as the resulting reaction rates even for complex multicomponent reactive transport setups as shown in the benchmark of

*Carrayrou et al.* (2010). Sequential approaches are often used in modeling reactive transport in porous media, since they allow the use of specific methods to solve the transport and chemical equations (e.g. *Carrayrou et al.*, 2004). Sequential approaches are usually computationally more efficient than GIAs (*Yeh and Tripathi*, 1989), but this is not always the case. For example, *Saaltink et al.* (2001) demonstrated that for cases with high influence of the solid phases on the transport behavior, GIAs perform better. In general, SNIA is more efficient than SIA, as SNIA does not iterate (*Carrayrou et al.*, 2004). The MICP model discussed in Section 4.2 uses a GIA (*Hommel et al.*, 2015b).

All sequential approaches introduce a splitting error due to the decoupled calculation of transport and reactions (e.g. *Steeffel et al.*, 2015a; *Carrayrou et al.*, 2010, 2004; *Kanney et al.*, 2003) as well as possibly decrease the robustness of the model (*Kräutle and Knabner*, 2005). For first-order kinetic reactions, the size of the splitting error is controlled by the ratio of the time-step size to the characteristic time of reaction, which is  $1/k$ ,  $k$  being the reaction rate coefficient (*Carrayrou et al.*, 2004). Thus, the splitting error can be limited by decreasing the time step of the sequential calculation to satisfy the Courant criterion, increasing the exchange of information between both sub-problems or by iterative sequential approaches (e.g. *Carrayrou et al.*, 2010; *MacQuarrie and Mayer*, 2005; *Xu et al.*, 1999).

All approaches can be accurate for advection-dominated setups, while SNIA is not well suited to diffusion- or dispersion-dominated setups. For these latter, SNIA either loses accuracy or involves additional computational costs. The accuracy of SIA and GIA approaches does not depend on whether the setup is dispersion- or advection-dominated, but for SIA, the computational costs are generally comparatively high. Both SIA and SNIA are very modular and thus free in the choice of the chemical solvers, which is not the case for GIA. Additionally, in such a sequential approach, the immobile solid phases can be eliminated from the system of equations for the transport part of the calculations, reducing the number of primary variables for the transport calculations. Reducing the number of unknowns also decreases the computational effort (e.g. *Carrayrou et al.*, 2010).

Irrespective of the solution approach, schemes reducing the number of unknowns have a high potential for improving the computational efficiency while maintaining accuracy (e.g. *Hoffmann et al.*, 2012; *Kräutle and Knabner*, 2007, 2005) and could be used to improve any of the solution approaches. In a benchmark, the code of *Hoffmann et al.* (2010) based on a GIA including the reduction scheme performed well in terms of both accuracy and efficiency. For systems with a large number of minerals without a-priori knowledge of the exact presence of the minerals, determining which set of minerals is present might require subsequent iterations and therefore be time-consuming, if not done in a rigorous way. An optimized method of determining the minerals present is given in *Kräutle* (2011).

Still another option might be to use a sequential calculation of pressure and transport as in the IMPET approach by for example *Faigle et al. (2015)* in addition to a sequential calculation of transport and reaction. In the IMPET scheme, only the pressure field is calculated implicitly and the transport of the components is calculated explicitly, based on the pressure.

For the investigation of the influence of the numerical scheme on the computational efficiency, the globally implicit model (*Hommel et al., 2015b*) as well as a sequential non-iterative approach are compared. The sequential non-iterative approach used was successfully tested for a simplified reactive-transport setup (dissolution of calcite due to the injection of  $\text{CO}_2$ ) in the Master's thesis of *Song (2014)*. It uses an adaptive time-stepping dependent on the coupling error and solves the transport equations implicitly. The solid phases biofilm and calcite are neglected in the transport calculations of this model; only their influence on porosity and permeability is modeled. The transport calculation is identical to the globally implicit model discussed in Section 4.2 or *Hommel et al. (2015b)*.

The coupling error  $CE$  is evaluated similarly to the convergence criterion of the non-linear Newton solver (Eq. (6.8)). However, instead of comparing the primary variables  $pV$  for the same calculation before and after an iteration of the solver, the  $pV$  of the transport  $pV_{\text{transport}}$  and the reaction  $pV_{\text{reactions}}$  calculations are compared:

$$CE = \frac{2|pV_{\text{transport}} - pV_{\text{reactions}}|}{pV_{\text{transport}} + pV_{\text{reactions}}}. \quad (6.1)$$

For the primary variables  $pV < 1$ , the absolute value of the primary variable difference is used, as this is more stable in the case of vanishing components (e.g.  $x_w^\kappa \rightarrow 0$ ):

$$CE = |pV_{\text{transport}} - pV_{\text{reactions}}|. \quad (6.2)$$

The primary variable updates due to reactions  $\Delta pV^\kappa$  are calculated explicitly for each reaction sub-problem time step  $\Delta t_{\text{chem}}$  at each grid node in the reaction calculations, using the same rate equations as for the globally implicit model. To transform the units, the resulting  $q^\kappa$  is divided with the molar density of the aqueous phase  $\rho_{\text{mol,w}}$  and multiplied by the time-step size of the reaction calculation  $\Delta t_{\text{chem}}$ . For components with the mole fraction  $x_w^\kappa$  as primary variable (see Section 3.1), this results in:

$$\Delta x^\kappa = q^\kappa \frac{\Delta t_{\text{chem}}}{\rho_{\text{mol,w}}}. \quad (6.3)$$

For the solid phases, the update  $\Delta pV^\lambda$  is calculated similarly to Equation (6.3), but using the molar density of the solid phase  $\rho_{\text{mol},\lambda}$  instead of  $\rho_{\text{mol},w}$ :

$$\Delta\phi^\lambda = q^\lambda \frac{\Delta t_{\text{chem}}}{\rho_{\text{mol},\lambda}}. \quad (6.4)$$

A SIA approach or a reduction scheme similar to the ones proposed by *Hoffmann et al.* (2012), *Kräutle and Knabner* (2007, 2005) are beyond the scope of this thesis since they require a substantial amount of implementation work.

### 6.1.2. Simplification of physics and chemistry

Models with simplified physics or chemistry are an engineering approach, since they neglect certain processes; these need to be identified beforehand dependent on the setup.

The main disadvantage of this approach is that the potential for simplification has to be identified prior to simulation, requiring additional investigations or expert knowledge, and that these potential simplifications are specific to a given setup, limiting the general applicability of such simplified models. For this approach, the reduction in computational effort is achieved by reducing the complexity of the equations of state or the source terms related to (bio)chemical reactions, which makes it easier to solve the system of equations. For example, reaction rates and phase properties like density or viscosity are in general dependent on concentrations of multiple components or even the total composition of the phase. A reduction of the coupling of the mass balance equations also reduces the computational time (e.g. *Hoffmann et al.*, 2012; *Kräutle and Knabner*, 2007, 2005). In some cases, even a reduction of the number of balance equations might be possible, which would additionally decrease the computational time.

In addition to a possible reduction of computational time, another motivation for the simplification approach is the uncertainty of important model input parameters (e.g. porosity and permeability) in the field. In light of this input-parameter uncertainty, excessively detailed equations might be an unnecessary burden on modeling as the overall reliability of the model predictions is already limited by the reliability of the input parameter estimation. Such simplified models might be able to increase the computational efficiency while, in contrast to sequential approaches, conserving the robustness of the globally implicit approach.

Two model simplifications are investigated:

- an *initial biofilm* model (IB), neglecting the components suspended biomass and starting with a pre-established biofilm;

- a *simple chemistry* model (SC), setting the precipitation rate equal to the ureolysis rate. This model assumes that the precipitation is instantaneous following the overall reaction equation (Eq. (1.6)).

The IB model additionally avoids simulating the inoculation and the attachment periods, saving extra computational effort by a reduced process length to be simulated. This model simplification is motivated by the findings of *Hommel et al.* (2015a), discussed in Section 5.1. The initial biofilm distribution  $\phi_{f,0}$  is assumed to follow the distribution dependent on the radius  $r$  as described by Equation (6.5) which is fitted to the FC model biofilm distribution predictions:

$$\phi_{f,0} = -0.00911r^3 - 0.000111r^2 - 0.000035r + 0.0000808. \quad (6.5)$$

Setting the precipitation rate equal to the ureolysis rate (Eq. (4.6)) in the SC model avoids the calculation of the precipitation rate and the associated calculation of the saturation state (Eq. (3.12)) and of the carbonate and calcium activities, which are expensive due to exponential functions and logarithms. Additionally, this reduces the coupling of the mass balance equations for the different components as the activities in the full model are dependent on the overall aqueous phase chemistry (*Hommel et al.*, 2015b). Further, the dissociation of carbonic acid (and ammonia) can be neglected, as the molalities of bicarbonate and especially carbonate are no longer needed, as is the case for the precipitation rate calculation in the full model, see Equation (3.10). This assumption of instantaneous precipitation is commonly used in model studies on MICP (e.g. *Cuthbert et al.*, 2013; *van Wijngaarden et al.*, 2013, 2011).

Other model simplifications not investigated in this study might be the implementation of simplified calculations of the activity coefficients, e.g. using the Debye-Hückel approach:

$$\log \gamma^\kappa = -\frac{A(z^\kappa)^2\sqrt{I}}{1 + Ba^\kappa\sqrt{I}} + b^\kappa I, \quad (6.6)$$

where  $\gamma^\kappa$  is the activity coefficient and  $z^\kappa$  the charge of component  $\kappa$ .  $A$  and  $B$  are parameters depending on temperature,  $I = 1/2 \sum m^\kappa (z^\kappa)^2$  is the ionic strength, and  $a^\kappa$  and  $b^\kappa$  are ion-specific fitting parameters. The Debye-Hückel approach does not use ion-specific terms to calculate  $\gamma^\kappa$  as the Pitzer approach used in *Hommel et al.* (2015b); *Ebigbo et al.* (2012), simplifying the calculation of  $\gamma^\kappa$ . However, for the Debye-Hückel approach, the activities are still dependent on  $I$  and thus on the total aqueous phase composition. Due to the dependence on  $I$ , this does not reduce the non-linear coupling between the mass balance equations.

A more promising model simplification might be the use of a single-phase model. As the model discussed in Section 4.2 is a two-phase model, the phase presence is checked for changes at each iteration. For the simulation of MICP in saturated conditions, this is an unnecessary burden, which could be avoided by the development of a single-phase model.

### 6.1.3. Other possible ways of reducing computational effort

Optimizing the time-step size through adaptive time stepping is a good way of improving the computational efficiency as seen in *Carrayrou et al.* (2010). The model of *Hommel et al.* (2015b) for MICP already uses adaptive time stepping based on the number of non-linear iterations needed for convergence. Thus, relaxing the convergence criterion of the non-linear Newton solver makes it easy to test the effect of increased time steps on the computational efficiency.

Multi-chemistry approaches are also a possible way. Such an approach can be implemented similarly to the multi-physics approaches already implemented in DuMu<sup>X</sup> (e.g. *Faigle et al.*, 2015, 2014). The multi-chemistry approaches can save computational time by calculating activity coefficients or complex reaction equations only in those parts of the domain where suitable indicators show the need for such expensive calculations. Indicators might be the Damköhler number, the presence of certain reactive components, or a threshold concentration of a certain reactive component. In the other parts of the domain, a simplified model can be used, see Section 6.1.2.

Refinement of the computational grid around heterogeneities also increases the computational efficiency compared with uniform grids (e.g. *Carrayrou et al.*, 2010), as this allows the grid to coarsened at other locations, thereby reducing the global number of unknowns. For known heterogeneities in the simulation domain, this grid refinement can be done beforehand, but grid refinement might also be useful for refining concentration gradients or heterogeneities that develop during the simulation, e.g. due to the accumulation of biofilm of minerals. For such cases, which cannot be addressed by initially refining the grid, the use of adaptive grids might be a promising solution. Adaptive grid refinement schemes might refine the computational grid based on indicators dependent on concentration gradients or reaction rates. For example, refinement based on concentration gradients prevents numerical diffusion which usually increases the reaction rates by artificial mixing. Schemes for grid adaption are already implemented in DuMu<sup>X</sup> for two-phase models and the cell-centered finite volume space discretization (*Faigle et al.*, 2015, 2014), but not for the box scheme used in this thesis, see Section 3.3.

## 6.2. Investigation of selected methods for increasing computational efficiency

This section presents the results of an investigation of selected options for reducing the computational effort, see Section 6.1, applied to the model of *Hommel et al.* (2015b) for MICP presented in Section 4.2. For each option, the accuracy and the efficiency are evaluated. The efficiency is expressed using the computational time. Other numerical performance parameters such as the number of linear and non-linear (Newton) iterations are given as well. To determine the accuracy, the result for the precipitated calcite is compared with the resulting calcite precipitate for a simulation using the globally implicit model with high spatial resolution, a strict convergence criterion for the Newton solver of  $N = 10^{-8}$ , and a maximum time-step size of  $\Delta t_{\max} = 100$  s. This comparison is based on the error  $E$  introduced by the simplification, which is calculated as:

$$E = \sqrt{\sum_{i=1}^{\text{nodes}} (\phi_{c,i} - \phi_{c,\text{ref},i})^2}, \quad (6.7)$$

where  $\phi_{c,i}$  is the calcite volume fraction and  $\phi_{c,\text{ref},i}$  the reference calcite volume fraction at the node  $i$ .

The setup for the investigation is the BR Experiment discussed in Section 4.2. The simulation domain is the entire  $360^\circ$  to be able to compare the errors introduced by the sequential solution approach (Section 6.2.1), the model simplifications (Section 6.2.2), or the manipulation of the time-stepping scheme (Section 6.2.3) with the error introduced by the assumption of a homogeneously permeable porous medium. In many applications, the assumption of a homogeneously permeable porous medium is frequently made as the permeability field in the porous medium is unknown in most cases.

In a recent investigation by *Kurz* (2015), the model error due to the assumption of a homogeneous permeability was estimated to be  $6.6 \cdot 10^{-4}$  for the BR-experiment setup using Equation (6.7). This error was estimated using literature data from *Carsel and Parrish* (1988) to create a probable heterogeneous permeability distribution. To correct for the different number of grid nodes for this investigation and the grid used in *Kurz* (2015), it is assumed that the average error per grid node is constant. The resulting error for comparison is  $E_{\text{comp}} = \sqrt{720/144} \cdot 6.6 \cdot 10^{-4} = 3.3 \cdot 10^{-3}$ . For the following, it is important to note that  $E_{\text{comp}}$  is only an estimate based on literature values.

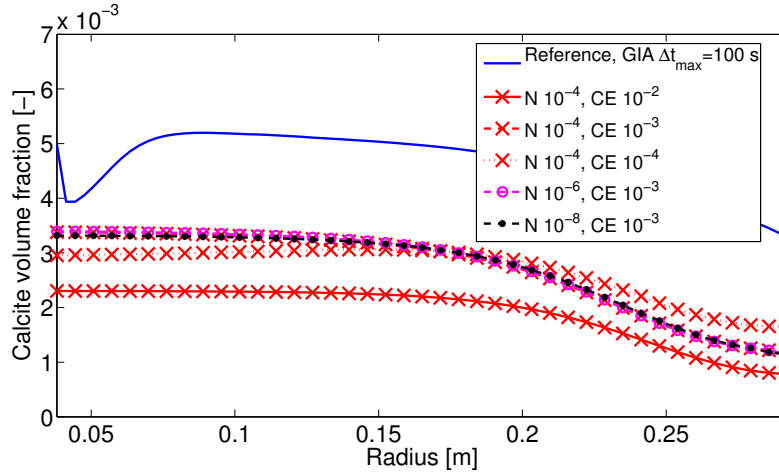


**Figure 6.1.:** Results of the sequential model for the BR experiment (*Hommel et al.*, 2015b) comparing the predicted calcite precipitation with the globally implicit reference simulation.

### 6.2.1. Optimized numerical solution approaches

The implemented SNIA model led to a significant reduction of CPU-time, but the results do not match with the results of the globally implicit model of *Hommel et al.* (2015b), see Figure 6.1. This is probably due to a not yet fully developed time-stepping scheme leading to prohibitively large splitting errors.

Despite the fact that the splitting error is very large, Figure 6.1 also demonstrates that, at least for the maximum tolerable  $CE$  investigated in this study, the Newton solver convergence criterion  $N$  of the transport calculation does not influence the results significantly when compared with the effect of the maximum tolerable  $CE$ .  $CE$  has a higher influence than  $N$  on the computational time as well, see Table 6.2.

As illustrated in Figure 6.2, the sequential model converges towards the globally implicit model for smaller maximum macro-time-step sizes. This shows that the time-stepping scheme currently implemented allows large time-step sizes, resulting in the extreme errors seen in Figures 6.1 and 6.2. Thus, before the performance of this sequential model can be evaluated, the macro-time-stepping scheme determined by the coupling error  $CE$  has to be revised to further satisfy the Courant criterion (the Courant number being smaller or equal to one) to ensure accurate results (e.g. *Steeffel et al.*, 2015a).

**Table 6.1.:** Numerical parameters for various combinations of the coupling error  $CE$  for the time-step management of the coupling between transport and reaction calculations and convergence criteria of the Newton solver  $N$  of the transport subproblem. For comparison, the computational time (CT) of the GIA model with  $N = 1 \cdot 10^{-6}$  is 32110 s, see Table 6.2.

$N$	$CE$	CT [s]
$1 \cdot 10^{-4}$	$1 \cdot 10^{-2}$	2883
	$1 \cdot 10^{-3}$	3857
	$1 \cdot 10^{-4}$	7486
$1 \cdot 10^{-6}$	$1 \cdot 10^{-2}$	3136
	$1 \cdot 10^{-3}$	4191
	$1 \cdot 10^{-4}$	7568
$1 \cdot 10^{-8}$	$1 \cdot 10^{-2}$	3266
	$1 \cdot 10^{-3}$	4465

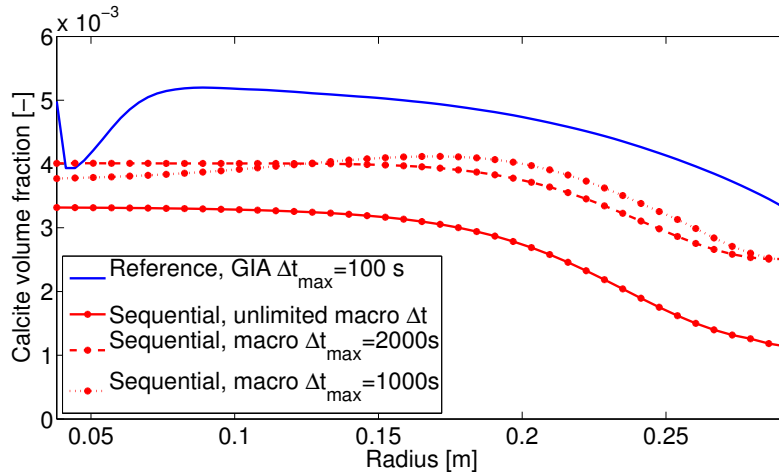


**Figure 6.2.:** Comparison of the results for the sequential model with unlimited macro-time steps to the results with limited time steps and the globally implicit reference simulation.

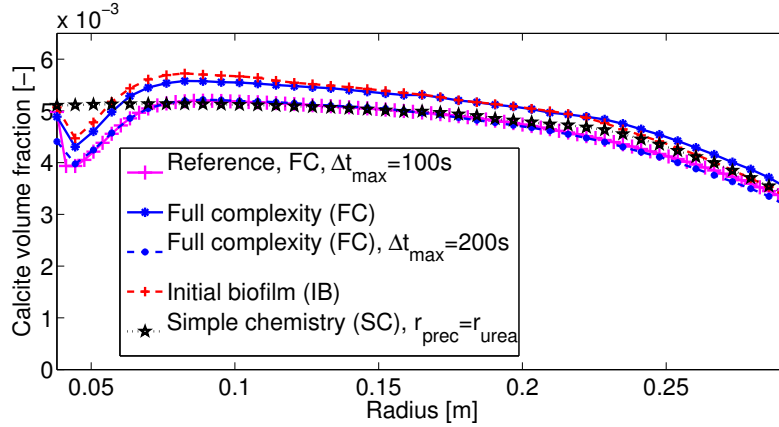


**Figure 6.3.:** Results of the model simplification using the initial biofilm, simple chemistry, and the full complexity model for calcite for the BR experiment (*Hommel et al., 2015b*).

### 6.2.2. Simplification of physics and chemistry

Both simplified models (IB and SC, defined in Section 6.1.2) are compared with the full model discussed in Section 4.2 and published in *Hommel et al. (2015b)*. Further, all three models are compared with a reference solution obtained using the full complexity model on a refined grid and with a limited time-step size.

The predictions of the models are presented in Figure 6.3. The IB model and the full complexity model predict a very similar final distribution of calcite for the BR experiment (*Hommel et al., 2015b*). Both models agree with the reference results in general but overestimate the amount of calcite precipitated compared with the reference solution. The difference between the FC model and the reference results is mainly due to the different time-step sizes. While the time-step size is unrestricted and only dependent on the convergence of the Newton solver, the time-step size is limited to 100 s for the reference. The FC model with a restricted time-step size of 200 s yields almost the same result on the coarse grid as the reference simulation with a maximum time-step size of 100 s on the refined grid. The SC model matches the reference solution quite well for a radius of more than 8 cm, but does not show the dynamics of the other models for smaller radii. However, all models show a satisfactory agreement in the amount and distribution of calcite.

For all models, the error  $E$  is less than or equal to  $3E_{\text{comp}}$ . When compared with the FC model with unlimited time-step size and non-refined grid, the error is lower for the FC and the IB model and comparable with the error of neglecting the heterogeneous permeability distribution, see Table 6.2. For the SC model, both  $E$  and  $E_{\text{FC},8}$  are identical.

Unlike the results, the numerical parameters show a difference between the models. While

**Table 6.2.:** Numerical parameters and the error compared with the reference solution of the different models (FC, IB, and SC). CT is the computational time, NLIT is the number of non-linear (Newton) iterations needed, LIT is the number of linear iterations needed, and  $E$  is the error defined in Equation (6.7).  $E_{\text{FC},8}$  is the error defined in Equation (6.7) using the FC model with a strict Newton convergence criterion ( $N = 1 \cdot 10^{-8}$ ) but unlimited time-step size and non-refined grid as a reference solution. For comparison, the estimated error for neglecting the effect of a heterogeneous permeability distribution in the porous medium is  $E_{\text{comp}} = 0.0033$ .

Model	CT [s]	NLIT	LIT/NLIT	NLIT/ $\Delta t$	$E$	$E_{\text{FC},8}$
FC	32110	4971	15.2	8.6	0.009	0.003
IB	28089	5053	14.9	8.8	0.010	0.004
SC	5758	1094	14.9	5.5	0.007	0.007

the IB model does not reduce the computational time (CT) much, the SC model needs only 18% of the CT of the full model, see Table 6.2. The reduction of the CT in the initial biofilm model is only 13%, which corresponds to a reduction in the time simulated of 13% as well, because the initial inoculation and the first 8 h of growth are neglected. The number of linear iterations per non-linear Newton iteration is almost constant for the three models, suggesting that the reduction on CT of the SC model is mainly due to the reduced number of non-linear (Newton) iterations (NLIT). While the FC model needs 4971 NLIT, the SC model only needs 1094 NLIT, 22% of the NLIT of the FC model. Some part of this reduction in the number of NLIT for the SC model results from the SC model needing on average only 5.5 NLIT/ $\Delta t$ , while the FC and the IB model need 8.6 and 8.8 NLIT/ $\Delta t$  respectively. The remaining reduction in CT of the SC model results from the adaptive time-stepping scheme increasing  $\Delta t$  for low NLIT/ $\Delta t$ , which leads to larger time steps for the SC model (*Flemisch et al.*, 2011).

### 6.2.3. Other possibilities for reducing computational effort

Of the methods to optimize the computational effort in Section 6.1.3, only the optimization of the time-stepping scheme was investigated. A significant reduction of the computational effort can be achieved by increasing the time-step size by relaxing the Newton convergence criterion controlling the time-step adaption scheme for the model of *Hommel et al.* (2015b) as well as the simplifications discussed in Section 6.1.2 and 6.2.2.

For convergence, the maximum relative shift  $R$  of any primary variable  $pV$  at any point of the simulation domain within an iteration of the Newton solver has to be less than the convergence criterion  $N$ . At each point and for each  $pV$ , the relative shift  $R$  is calculated as:

$$R = \frac{|pV_{\text{before}} - pV_{\text{after}}|}{\max\left(1, \frac{pV_{\text{before}} + pV_{\text{after}}}{2}\right)}, \quad (6.8)$$

**Table 6.3.:** Numerical parameters and the error compared with the reference solution of the different models (FC, IB, and SC) for different convergence criteria of the Newton solver (Eq. (6.8)). The values for  $N = 1 \cdot 10^{-6}$  are already given in Table 6.2.  $E_{\text{FC},8}$  is the error defined in Equation (6.7) using the FC model with a strict Newton convergence criterion ( $N = 1 \cdot 10^{-8}$ ) but unlimited time-step size and non-refined grid as a reference solution. For comparison, the estimated error for neglecting the effect of a heterogeneous permeability distribution in the porous medium is  $E_{\text{comp}} = 0.0033$ .

Model, $N$	CT [s]	NLIT	LIT	LIT/NLIT	NLIT/ $\Delta t$	$E$	$E_{\text{FC},8}$
FC, $1 \cdot 10^{-8}$	57533	9051	108437	12.0	9.3	0.007	0.0
FC, $1 \cdot 10^{-6}$	32110	4971	75335	15.2	8.6	0.009	0.003
FC, $1 \cdot 10^{-4}$	4861	776	5103	6.6	3.4	0.010	0.007
IB, $1 \cdot 10^{-8}$	48100	8687	143591	16.5	9.3	0.008	0.003
IB, $1 \cdot 10^{-6}$	28089	5053	75335	14.9	8.8	0.010	0.004
IB, $1 \cdot 10^{-4}$	3816	689	6160	8.9	3.8	0.008	0.005
SC, $1 \cdot 10^{-8}$	111662	22745	126870	5.6	12.2	0.007	0.008
SC, $1 \cdot 10^{-6}$	5758	1094	16303	14.9	5.5	0.007	0.007
SC, $1 \cdot 10^{-4}$	2002	396	5203	13.1	2.6	0.008	0.010

where  $pV_{\text{before}}$  and  $pV_{\text{after}}$  are the values of the primary variable before and after the update. Increasing the convergence criterion leads to fewer iterations necessary for convergence, increasing  $\text{NLIT}/\Delta t$ , and, through the adaptive time-stepping scheme (*Flemisch et al.*, 2011), to increasing time steps. This is the case for all GIA models, the FC model and both the simplified models, IB and SC, see Table 6.3.

For all models, relaxing the Newton solver's convergence criterion  $N$  leads to decreasing  $\text{NLIT}/\Delta t$ , increasing the time-step size  $\Delta t$  (*Flemisch et al.*, 2011), which leads to fewer but larger time steps. The number of linear iterations per non-linear iteration  $\text{LIT}/\text{NLIT}$  also decreases with decreasing  $N$ , further decreasing the computational time, except for the FC and the SC model and  $N = 1 \cdot 10^{-8}$  (Table 6.3). The very high CT for the SC model with  $N = 1 \cdot 10^{-8}$  is probably due to convergence problems of the Newton solver, which is indicated by the high ratio of  $\text{NLIT}/\Delta t = 12.2$ .

NLIT is the best predictor of the CT of a model. For the FC model, the CT needed for each NLIT is approximately 6.4 s for all  $N$  investigated. The NLIT for the IB model requires a constant time of 5.5 s. The  $\text{CT}/\text{NLIT}$  for the SC model is more variable, from 4.9 s for  $N = 1 \cdot 10^{-8}$  to 5.3 s for  $N = 1 \cdot 10^{-6}$ .

The error introduced by relaxing the convergence criterion increases with an increasing convergence criterion. However, even for  $1 \cdot 10^{-4}$ , the error  $E$  is still less than an order of magnitude higher than the estimated error of the assumption of homogeneous permeability  $E_{\text{comp}} = 0.0033$  (Table 6.3). The error is more dependent on the model simplification than on

the convergence criterion and relaxing the convergence criterion does not dramatically increase the error compared with the assumption of homogeneous permeability, which is difficult to avoid for realistic scenarios where the permeability distribution is unknown.

Using the FC model with  $N = 1 \cdot 10^{-8}$  results in  $E = 0.007$  compared with  $E = 0.010$  using  $N = 1 \cdot 10^{-4}$ . Thus, the increase in  $E$  for increasing the tolerance of the Newton solver by  $10^4$ , is still in the range of  $E_{\text{comp}}$ , but the reduction in the computational effort is more than one order of magnitude (91.6%). For the IB model, the computational effort is reduced similarly to 7.9%, while  $E$  does not change. For the SC model, the reduction is even more than 98%, resulting from the very high computational time using  $N = 1 \cdot 10^{-8}$ .

### 6.3. Preliminary conclusions

The sequential approach needs to be improved to satisfy the Courant criterion. This will increase the number of time steps and the computational time accordingly. Thus, at the moment, no final assessment of the performance of this approach can be made. Another option might be to implement an SIA. Additionally, the implementation of a reduction scheme similar to the ones proposed by *Hoffmann et al. (2012)*; *Kräutle and Knabner (2007, 2005)*, providing a reduction of the computational time by factors between 17% and 35% in the examples investigated in *Kräutle and Knabner (2005)*. Finally, for SNIA, it might be worth further sequentializing the transport calculations using an IMPET scheme (*Faigle et al., 2015*), which would further reduce the number of primary variables solved implicitly on a global level.

As presented in Section 6.2.2, model simplification can reduce the computational time significantly. Other simplifications than those investigated might include: a single-phase model for MICP as most applications of MICP do not include two-phase systems, a model with fewer components, e.g. substrate might be neglected in addition to suspended biomass as substrate is usually injected in excess compared with oxygen and thus does not influence biomass growth, or a model using simplified physical equations of state to calculate e.g. density and viscosity. Further simplifying the SC model, e.g. a single-phase SC model, might result in a model with a computational time reduced by an order of magnitude or more compared with the FC model. Even the most simplified SC model has a relatively low error of  $E = 0.008$ , which is still less than one order of magnitude more than  $E_{\text{comp}} = 0.0033$ .

Optimizing the time-step size also has a high potential to reduce the computational time, see Section 6.2.3. For the cases investigated, relaxing the convergence criterion of the Newton solver does not significantly increase the error compared with the reference solution, see Table 6.3. Thus, it is a first important step for reducing the computational time to choose

optimized convergence criteria to improve the adaptive time-step size. However, increasing time-step sizes also lead to larger model errors.

The errors introduced by the model simplifications or a relaxed convergence criterion still seem tolerable when compared with the assumption of homogeneous permeability, which is difficult to avoid for application scenarios where the permeability distribution is unknown. It is important to balance the modeling error introduced by the choice of the model simplification and other modeling assumptions with the possible associated gain in computational efficiency.

Adaptive grids might help to reduce computational time by reducing the number of grid nodes as, during the simulation, the grid is adaptively refined at locations where this is necessary for accuracy or convergence and is coarsened at all other locations. Adaptive grids might reduce the computational time, especially for larger simulation domains with heterogeneities as for example in the case of the field application of MICP in Section 5.2 or in cases where the heterogeneities develop over time due to the reactions. Finally, multi-model-complexity approaches analogous to the multi-physics model from (e.g. *Faigle et al., 2015*) might reduce computational time as for such approaches, only the relevant regions of the simulation domain are calculated using the expensive full-complexity model, while the rest of the domain can be calculated using simplified models discussed in Section 6.1.2 with significantly reduced computational effort, see Section 6.2.2. Both adaptive grids and multi-physics approaches are already implemented in DuMu<sup>X</sup> (*Faigle et al., 2015, 2014*).

## 7. Summary

Biogeochemical processes are ubiquitous in the subsurface, which is increasingly utilized for various purposes. Understanding those biogeochemical processes and manipulating them becomes more and more important. However, as biogeochemical processes result from the complex interactions of a multitude of minerals, fluids and microbes, understanding and influencing them is not easy. This motivates the use of models, which represent simplified and parametrized versions of complex reality. Such models can be used to test hypotheses or, particularly important for engineering applications, predict the outcome of a certain action. This thesis focuses on the modeling of microbially induced calcite precipitation (MICP), which can be used for various engineering applications, including for example soil stabilization, concrete and limestone remediation, groundwater remediation, and subsurface barriers (e.g. *Phillips et al.*, 2013a). The technology of interest for this thesis is the creation of subsurface barriers by MICP, reducing the porosity and permeability in the barrier area by the precipitation of calcite.

Chapter 2 outlines the fundamental quantities and processes necessary for modeling reactive transport in the subsurface. The processes considered necessary are two-phase flow combined with multi-component transport, precipitation and dissolution of calcite, and the accumulation of biomass within the porous medium. Additionally, Chapter 2 includes a brief discussion of the effects of biomass and calcite accumulation on the flow field and the resulting component transport.

Chapter 3 discusses in detail the model for MICP of *Ebigbo et al.* (2012) developed previously as it is the basis on which the investigations of this thesis are built. First, the basic model concept is outlined and the balance equations are given. Second, the various component-specific source and sink terms due to biogeochemical reactions are discussed. Following the source and sink terms, the supplementary equations are discussed. The supplementary equations are used to calculate the change in the the porous medium properties such as porosity and permeability due to MICP, fluid-phase properties like density and viscosity, and the chemical composition of the aqueous phase, including for example the calculation of the activities of the components or their subspecies and the partitioning of  $N_{\text{tot}}$  and  $C_{\text{tot}}$  into the subspecies  $\text{NH}_3$  and  $\text{NH}_4^+$  and  $\text{CO}_2$ ,  $\text{H}_2\text{CO}_3$ ,  $\text{HCO}_3^-$ ,  $\text{H}_2\text{CO}_3^{2-}$  respectively. Finally, Chapter 3 also discusses the interaction

between modeling investigations and experimental work and provides a brief overview of the implementation of the model. These interactions between modeling and experimental investigations are extremely valuable to both the model development and further experimental work. Consequently, most of the modeling investigations conducted in this thesis are linked to experimental investigations, either by using insights and data from experiments to improve the model for MICP as discussed in Chapter 4 or by using the model to test hypotheses to determine a-priori promising experimental designs and to gain insight into processes that are difficult to measure in experiments or field applications, as shown in Chapter 5.

Chapters 4-6 correspond to the objectives of the thesis defined in Section 1.5:

- to improve the model for MICP as proposed by *Ebigbo et al. (2012)* by including advanced experimental insights on relevant processes;
- to apply the model to help design experimental investigations as well as field-scale applications;
- to investigate exemplary approaches to reduce the computational time of the model.

The following summarizes the steps undertaken to reach these objectives.

### **Model improvement**

The model improvements based on recent experimental data (Chapter 4) have been successful, although further improvements may be possible in the future as soon as additional experimental data on MICP are available. Both the porosity-permeability relation (Section 4.1) and the ureolysis rate equation (Section 4.2) are improved.

The general Verma-Prueess type porosity-permeability relation performs well compared with experimental measurements when predicting the precipitation of calcite, but it cannot predict the drastic initial decrease in permeability due to inoculation of the porous medium. A brief literature review on porosity-permeability relations for bioclogging and mineral precipitation confirms that the effect of biomass on permeability is much more variable and more difficult to predict than the effect of mineral precipitates. An updated porosity-permeability relation fitted to data from micro-model experiment with simultaneous measurement of biomass volume and pressure difference improved the match of the permeability predictions of the model. However, the extent of the initial decrease in permeability is still not captured by the updated relation.

Recent insight into the ureolysis rate kinetics of *S. pasteurii* allowed the ureolysis rate equation in the model to be improved. Together with further experimental insights into the growth rate

of *S. pasteurii*, it also enabled a reduction in the number of fitting parameter in the model. The improved model is recalibrated using inverse modeling and experimental data from four different experiments, one “old” column experiment from *Ebigbo et al. (2012)* and a radial-flow experiment for which only the final calcite data are available for calibration and two “new” column experiments of which temporally and spatially resolved in-situ measurements of  $\text{NH}_4^+$  and  $\text{Ca}^{2+}$  are available in addition to the final calcite distribution. The recalibration leads to parameter values that result in good model predictions for both the “old” and the “new” column experiments with different injection strategies and composition of the injected media. However, the same set of parameters lead to an underestimation of the calcite precipitation for the radial-flow experiment. This indicates that, despite the improvement of the ureolysis rate equation, the conceptual model of MICP may still be improved further. As the agreement between the model predictions and experimental data seems to be dependent on the dimension of the experiment, the most likely reason is the interactions between hydraulics and MICP.

The key improvements compared with the model for MICP proposed by *Ebigbo et al. (2012)* are:

- the updated porosity-permeability relation;
- the updated ureolysis rate equation;
- the reduction of the fitting parameters;
- the recalibration using inverse modeling instead of a trial-and-error approach;
- the resulting improved accuracy of the model predictions for a variety of experimental setups.

As the flow field is the main difference between 1D columns and 2D radial flow, this indicates that the interaction of biomass accumulation in the porous medium and the hydraulics might not yet be implemented in the model in sufficient detail. Further research on the interactions of flow and transport in a porous medium with the growth, decay, attachment, and detachment of biomass can be expected to result in a further improved model for MICP, whose prediction accuracy is independent of the flow conditions. The highest gain is expected from insights into the attachment and the detachment of biomass as well as into the influence of the accumulation of biomass on the permeability. The preliminary investigation of the porosity-permeability relation based on micro-model experiments increased the match of model predictions of the permeability to the measured permeability but, as of now, the micro-model porosity and permeability data are scarce and not representative for realistic porous media. New micro-model experiments with representative initial porosity, permeability, and pore-size distributions would increase confidence in the obtained porosity-permeability relation used for modeling

MICP on the REV scale. Further, such micro-model experiments might give additional insight into the attachment behavior of microbes.

### **Model application**

The interactions between hydraulic conditions and the accumulation of biomass are difficult to study in experiments; this was confirmed by preliminary attachment experiments. Instead of repeating the time-consuming experiments, a numerical study is used to investigate the influence of the initial amount and distribution of biomass on the resulting MICP (Section 5.1) for various injection strategies. The initial biomass distributions here represent different attachment mechanisms and various porous medium properties. Both the precipitation efficiency, the ratio of the  $\text{Ca}^{2+}$  precipitated to the  $\text{Ca}^{2+}$  injected, and the shape of the resulting calcite distribution are evaluated. In general, the effect of the initial amount and distribution of biomass on the precipitation efficiency is minor compared with the effect of the injection strategy. The same holds for the shape of the resulting calcite distribution, except for one of the continuous injection strategies. Thus, for column experiments, additional information on the attachment of biomass and thereby on the initial amount and distribution of biomass will probably increase the model accuracy significantly only for a limited range of injection strategies.

The results presented in Section 5.2 show that it is possible to use the MICP model to predict the results of field-scale applications of MICP. In the specific field-scale application of MICP investigated, 6 injections of biomass and 24 injections of calcium-rich biomineralization medium are used to seal a single fracture in a sandstone formation at 341 m below ground surface. For the modeling, the fracture is approximated as a thin, highly permeable layer in the vertical center of the simulation domain.

Three different injection strategies are modeled, two hypothetical ones and the injection strategy later used in an actual field application, which is based on one of the hypothetical strategies. To address some of the uncertainties related to the geology, two different scenarios are investigated. The results of the simulations show considerable differences in the precipitation efficiencies, the distribution of the precipitates along and perpendicular to the fracture, as well as the predicted times of sealing.

For the improved model, it is shown that it can be successfully applied to:

- test hypotheses about and gain insights into the relative importance of parameters of MICP such as the initial amount and distribution of biomass or the injection strategy;
- predict field-scale applications of MICP.

The use of models to help design experiments to investigate MICP and applications of MICP is beneficial for both the experiment or application and the model development. Modeling can be used to test the sensitivity of the overall MICP process to the parameters under investigation in the experiment or the design parameters of a field application. The model predictions might then allow a reduction of the number of experimental investigations by providing a-priori estimates of the experimental outcomes for a variety of experimental setups. Similarly, the model predictions for a field application of MICP can be used to estimate the required amounts of inoculum, growth and mineralization media or help to choose the injection strategy. During and after the field application or the experiment, measurements can be compared with the model predictions which in turn can be used to evaluate the model performance. However, especially for field applications where the simulation domains need to account for complex geometries and contain a rather large volume, the computational effort of the globally implicit model with full complexity quickly becomes prohibitive. For such engineering purposes, the computational time needs to be reduced to facilitate the use of the model on site and during the planning.

### **Effective solution strategies**

The computational effort of the MICP model is the major obstacle to its use in planning engineering applications of MICP. For each model application, depending on its purpose, the computational effort of the model and the model accuracy have to be balanced. Both the accuracy and the computational effort are dependent on the model assumptions, the numerical solution scheme of the model, and the processes considered in the model. Several ways of reducing the computational effort of the MICP model are investigated in Chapter 6.

Sophisticated numerical solution schemes might reduce the computational effort of the MICP model. However, the sequential approach investigated in this study is not suitable as, although it significantly reduced the computational time: it does not predict the results accurately enough.

The computational effort can be reduced significantly by optimizing the convergence criteria and thereby the adaptive time-step size or by simplifying the model neglecting certain processes as shown in Chapter 6. The simplification approach needs a-priori expert knowledge to be able to decide which of the processes can be neglected without causing intolerable effects on the accuracy of the model. Simplifying the calculation of the reactions results in an a decrease of the computational time of almost an order of magnitude. Even higher reductions are possible by optimizing the time-step size by the choice of an appropriate convergence criterion for the non-linear solver.

For the model simplifications, the reduction of non-linearities and coupling between the different balance equations have a much higher effect on the computational time than reducing the number of primary variables. Reduced non-linear coupling of the balance equations results in fewer iterations needed by the non-linear solver for convergence. Due to an adaptive time-stepping scheme, the faster convergence additionally leads to increased time-step sizes, further decreasing the computational effort. Equally, choosing a higher convergence criterion for the non-linear solver results in faster convergence, larger time-step sizes and reduced computational effort.

It is demonstrated that the computational effort can be reduced significantly by:

- simplifying the reactive source and sink calculations;
- optimizing the time-step size by the choice of an appropriate convergence criterion.

The sequential solution approach implemented currently has to be improved to guarantee a sufficient accuracy until its computational effort can be meaningfully compared with the globally implicit models. Further simplifications might additionally reduce the computational effort. Such further simplifications might include a one-phase model, neglecting further components, or the use of simplified equations of state analogously to the simplified chemical reaction calculations already investigated.

What is not investigated in this thesis but also has great potential to further reduce the computational effort is the use of adaptive grids and a multi-complexity model approach. Adaptive grids as well have a great potential to reduce the number of grid nodes necessary as they automatically refine or coarsen the computational grid based on suitable indicators. This might reduce the size of the system of equations that needs to be solved and thereby decrease the computational effort. In a multi-complexity model approach, models of different complexity are used in different regions of the simulation domain and coupled spatially. The choice of the model complexity for a region is based on the processes occurring in this region. This approach reduces the use of the highly complex model, presumably leading to faster convergence and thereby reducing the computational effort.

# Bibliography

- J. P. Amend and A. Teske, *Expanding frontiers in deep subsurface microbiology. Palaeogeography, Palaeoclimatology, Palaeoecology*, 219 (2005)(1-2), 131–155.
- R. T. Bachmann, A. C. Johnson, and R. G. Edyvean, *Biotechnology in the petroleum industry: An overview. International Biodeterioration & Biodegradation*, 86 (2014), 225–237.
- K. L. Bachmeier, A. E. Williams, J. R. Warmington, and S. S. Bang, *Urease activity in microbiologically-induced calcite precipitation. Journal of Biotechnology*, 93 (2002)(2), 171–81.
- S. M. Bamforth and I. Singleton, *Bioremediation of polycyclic aromatic hydrocarbons: current knowledge and future directions. Journal of Chemical Technology & Biotechnology*, 80 (2005)(7), 723–736.
- T. H. Barkouki, B. C. Martinez, B. M. Mortensen, T. S. Weathers, J. D. De Jong, T. R. Ginn, N. F. Spycher, R. W. Smith, and Y. Fujita, *Forward and inverse bio-geochemical modeling of microbially induced calcite precipitation in half-meter column experiments. Transport in Porous Media*, 90 (2011)(1), 23–39.
- P. Bastian, M. Blatt, a. Dedner, C. Engwer, R. Klöfkorn, R. Kornhuber, M. Ohlberger, and O. Sander, *A generic grid interface for parallel and adaptive scientific computing. Part II: Implementation and tests in DUNE. Computing (Vienna/New York)*, 82 (2008a)(2-3), 121–138.
- P. Bastian, M. Blatt, a. Dedner, C. Engwer, R. Klöfkorn, M. Ohlberger, and O. Sander, *A generic grid interface for parallel and adaptive scientific computing. Part I: Abstract framework. Computing (Vienna/New York)*, 82 (2008b)(2-3), 103–119.
- M. Batzle and Z. Wang, *Seismic Properties of Pore Fluids. Geophysics*, 57 (1992)(11), 1396–1408.
- T. G. Bell, M. T. Johnson, T. D. Jickells, and P. S. Liss, *Ammonia/ammonium dissociation coefficient in seawater: A significant numerical correction. Environmental Chemistry*, 5 (2008)(3), 183–186.

- Y. Bernabe, U. Mok, and B. Evans, *Permeability-porosity Relationships in Rocks Subjected to Various Evolution Processes. pure and applied geophysics*, 160 (2003)(5-6), 937–960.
- A. Bielinski (2006). *Numerical simulation of CO<sub>2</sub> sequestration in geological formations*. Ph.D. thesis, Institut für Wasserbau, Universität Stuttgart.
- E. Bouwer, H. Rijnaarts, A. Cunningham, and R. Gerlach (2000). *Biofilms II: Process Analysis and Applications*, chapter Biofilms in Porous Media, pages 123–158. Wiley-Liss, Inc.
- A. N. Brooks and A. Corey (1964). *Hydraulic Properties of Porous Media*. In C. S. University, editor, *Hydrology Papers*. Colorado State University.
- A. K. Camper, M. W. LeChevalier, S. C. Broadaway, and G. A. McFeters, *Evaluation of procedures to desorb bacteria from granular activated carbon. Journal of Microbiological Methods*, 3 (1985), 187–198.
- P. C. Carman, *Fluid flow through granular beds. Transactions, Institution of Chemical Engineers (London)*, 15 (1937), 150–166.
- J. Carrayrou, J. Hoffmann, P. Knabner, S. Kräutle, C. de Dieuleveult, J. Erhel, J. Van der Lee, V. Lagneau, K. U. Mayer, and K. T. B. MacQuarrie, *Comparison of numerical methods for simulating strongly nonlinear and heterogeneous reactive transport problems—the MoMaS benchmark case. Computational Geosciences*, 14 (2010)(3), 483–502.
- J. Carrayrou, R. Mosé, and P. Behra, *Operator-splitting procedures for reactive transport and comparison of mass balance errors. Journal of Contaminant Hydrology*, 68 (2004)(3-4), 239–268.
- J. Carrera, I. Jubany, L. Carvallo, R. Chamy, and J. Lafuente, *Kinetic models for nitrification inhibition by ammonium and nitrite in a suspended and an immobilised biomass systems. Process Biochemistry*, 39 (2004)(9), 1159–1165.
- R. F. Carsel and R. S. Parrish, *Developing joint probability distributions of soil water retention characteristics. Water Resources Research*, 24 (1988)(5), 755–769.
- L. Chou, R. M. Garrels, and R. Wollast, *Comparative study of the kinetics and mechanisms of dissolution of carbonate minerals. Chemical Geology*, 78 (1989), 269–282.
- H. Class and R. Helmig, *Numerical simulation of non-isothermal multiphase multicomponent processes in porous media. 2. Applications for the injection of steam and air. 25 (2002)*, 551–564.

- S. L. Clegg and M. Whitfield, *A chemical model of seawater including dissolved ammonia and the stoichiometric dissociation constant of ammonia in estuarine water and seawater from -2 to 40°C*. *Geochimica et Cosmochimica Acta*, 59 (1995)(12), 2403–2421.
- T. P. Clement, B. S. Hooker, and R. S. Skeen, *Numerical modeling of biologically reactive transport near nutrient injection well*. *Journal Of Environmental Engineering-ASCE*, 122 (1996)(9), 833–839.
- T. P. Clement, B. M. Peyton, T. R. Ginn, and R. S. Skeen, *Modeling Bacterial Transport and Accumulation Processes in Saturated Porous Media: A Review*. *Advances in Nuclear Science and Technology*, 26 (1999), 59–78.
- R. G. Compton, K. L. Pritchard, and P. R. Unwin, *The dissolution of calcite in acid waters: Mass transport versus surface control*. *Freshwater Biology*, 22 (1989)(2), 285–288.
- J. M. Connolly (2015). *Biofilm-induced carbonate precipitation at the pore-scale*. Ph.D. thesis, Montana State University, Bozeman, Montana.
- J. M. Connolly, M. Kaufman, A. Rothman, R. Gupta, G. Redden, M. Schuster, F. Colwell, and R. Gerlach, *Construction of two ureolytic model organisms for the study of microbially induced calcium carbonate precipitation*. *Journal of Microbiological Methods*, 94 (2013)(3), 290–9.
- M. Y. Corapcioglu and A. Haridas, *Transport and fate of microorganisms in porous media: A theoretical investigation*. *Journal of Hydrology*, 72 (1984)(1-2), 149–169.
- A. T. Corey (1994). *Mechanics of Immiscible Fluids in Porous media*. Water Resources Publications.
- A. B. Cunningham, W. G. Characklis, F. Abedeen, and D. Crawford, *Influence of Biofilm Accumulation on Porous Media Hydrodynamics*. *Environmental Science & Technology*, 25 (1991), 1305–1311.
- A. B. Cunningham, A. J. Phillips, E. Troyer, E. G. Lauchnor, R. Hiebert, R. Gerlach, and L. H. Spangler, *Wellbore leakage mitigation using engineered biomineralization*. *Energy Procedia*, 63 (2014), 4612–4619.
- A. B. Cunningham, R. R. Sharp, F. Caccavo, and R. Gerlach, *Effects of starvation on bacterial transport through porous media*. *Advances in Water Resources*, 30 (2007), 1583–1592.
- M. O. Cuthbert, L. A. McMillan, S. Handley-Sidhu, M. S. Riley, D. J. Tobler, and V. R. Phoenix, *A field and modeling study of fractured rock permeability reduction using microbially induced calcite precipitation*. *Environmental Science & Technology*, 47 (2013)(23), 13637–13643.

- M. O. Cuthbert, M. S. Riley, S. Handley-Sidhu, J. C. Renshaw, D. J. Tobler, V. R. Phoenix, and R. Mackay, *Controls on the rate of ureolysis and the morphology of carbonate precipitated by *S. pasteurii* biofilms and limits due to bacterial encapsulation*. *Ecological Engineering*, 41 (2012), 32–40.
- M. Darcis (2012). *Coupling Models of Different Complexity for the Simulation of CO<sub>2</sub> Storage in Deep Saline Aquifers*. Ph.D. thesis, Institut für Wasser- und Umweltsystemmodellierung, Universität Stuttgart.
- M. E. Davey and G. A. O’toole, *Microbial biofilms: from ecology to molecular genetics*. *Microbiology and Molecular Biology Reviews*, 64 (2000)(4), 847–867.
- Z. Duan and R. Sun, *An improved model calculating CO<sub>2</sub> solubility in pure water and aqueous NaCl solutions from 273 to 533 K and from 0 to 2000 bar*. *Chemical Geology*, 193 (2003)(3-4), 257–271.
- C. Dupraz, R. P. Reid, O. Braissant, A. W. Decho, R. S. Norman, and P. T. Visscher, *Processes of carbonate precipitation in modern microbial mats*. *Earth-Science Reviews*, 96 (2009a)(3), 141–162.
- S. Dupraz, M. Parmentier, B. Ménez, and F. Guyot, *Experimental and numerical modeling of bacterially induced pH increase and calcite precipitation in saline aquifers*. *Chemical Geology*, 265 (2009b)(1-2), 44–53.
- A. Ebigbo, R. Helmig, A. B. Cunningham, H. Class, and R. Gerlach, *Modelling biofilm growth in the presence of carbon dioxide and water flow in the subsurface*. *Advances in Water Resources*, 33 (2010)(7), 762–781.
- A. Ebigbo, A. J. Phillips, R. Gerlach, R. Helmig, A. B. Cunningham, H. Class, and L. H. Spangler, *Darcy-scale modeling of microbially induced carbonate mineral precipitation in sand columns*. *Water Resources Research*, 48 (2012)(7), W07519.
- B. Faigle, M. A. Elfeel, R. Helmig, B. Becker, B. Flemisch, and S. Geiger, *Multi-physics modeling of non-isothermal compositional flow on adaptive grids*. *Computer Methods in Applied Mechanics and Engineering*, 292 (2015), 16–34.
- B. Faigle, R. Helmig, I. Aavatsmark, and B. Flemisch, *Efficient multiphysics modelling with adaptive grid refinement using a MPFA method*. *Computational Geosciences*, (2014), 625–636.
- A. Fenghour, W. Wakeham, and V. Vesovic, *The viscosity of carbon dioxide*. *Journal of Physical and Chemical Reference Data*, 27 (1998)(1), 31–44.

- F. G. Ferris, V. Phoenix, Y. Fujita, and R. W. Smith, *Kinetics of calcite precipitation induced by ureolytic bacteria at 10 to 20°C in artificial groundwater. Geochimica et Cosmochimica Acta*, 67 (2003)(8), 1701–1710.
- M. Fidaleo and R. Lavecchia, *Kinetic study of enzymatic urea hydrolysis in the pH range 4-9. Chemical and Biochemical Engineering Quarterly*, 17 (2003), 311–318.
- S. Finsterle (2007). *iTOUGH2 user's guide*. Technical Report LBNL-40040 Updated Reprint, Earth Science Division, Lawrence Berkeley National Laboratory, University of California, Berkeley, CA 94720.
- S. Finsterle (2011). *iTOUGH2 universal optimization using the PEST protocol user's guide*. Technical Report LBNL-3698E (revised), Earth Science Division, Lawrence Berkeley National Laboratory, University of California, Berkeley, CA 94720.
- B. Flemisch, M. Darcis, K. Erbertseder, B. Faigle, a. Lauser, K. Mosthaf, S. Müthing, P. Nuske, a. Tatomir, M. Wolff, and R. Helmig, *DuMu<sup>X</sup>: DUNE for multi-{phase, component, scale, physics, ...} flow and transport in porous media. Advances in Water Resources*, 34 (2011)(9), 1102–1112.
- F. Flukiger and D. Bernard, *A new numerical model for pore scale dissolution of calcite due to CO<sub>2</sub> saturated water flow in 3D realistic geometry: Principles and first results. Chemical Geology*, 265 (2009)(1-2), 171–180.
- C. C. Frippiat, P. C. Pérez, and A. E. Holeyman, *Estimation of laboratory-scale dispersivities using an annulus-and-core device. Journal of Hydrology*, 362 (2008)(1-2), 57–68.
- G. M. Gadd, *Bioremedial potential of microbial mechanisms of metal mobilization and immobilization. Current Opinion in Biotechnology*, 11 (2000)(3), 271–279.
- G. M. Gadd, *Microbial influence on metal mobility and application for bioremediation. Geoderma*, 122 (2004)(2-4 SPEC. IIS.), 109–119.
- R. Gerlach (2001). *Transport and activity of dissimilatory metal reducing bacteria in porous media for the remediation of heavy metals and chlorinated hydrocarbons*. Ph.D. thesis, Montana State University, College of Engineering.
- S. Hamilton, S. Golding, K. Baublys, and J. Esterle, *Conceptual exploration targeting for microbially enhanced coal bed methane (MECoM) in the Walloon Subgroup, eastern Surat Basin, Australia. International Journal of Coal Geology*, 138 (2015), 68–82.

- O. J. Hao, M. G. Richard, D. Jenkins, and H. W. Blanch, *The half-saturation coefficient for dissolved oxygen: A dynamic method for its determination and its effect on dual species competition*. *Biotechnology and Bioengineering*, 25 (1983)(2), 403–16.
- M. P. Harkes, L. a. van Paassen, J. L. Booster, V. S. Whiffin, and M. C. van Loosdrecht, *Fixation and distribution of bacterial activity in sand to induce carbonate precipitation for ground reinforcement*. *Ecological Engineering*, 36 (2010)(2), 112–117.
- R. W. Harvey (1991). *Modeling the Environmental Fate of Microorganisms*, chapter Parameters Involved In Modeling Movement of Bacteria In Groundwater, pages 89–114. American Society for Microbiology, Washington, D.C.
- R. W. Harvey and S. P. Garabedian, *Use of colloid filtration theory in modeling movement of bacteria through a contaminated sandy aquifer*. *Environmental Science & Technology*, 25 (1991)(1), 178–185.
- T. C. Hazen, L. Jiménez, G. López de Victoria, and C. B. Fliermans, *Comparison of bacteria from deep subsurface sediment and adjacent groundwater*. *Microbial Ecology*, 22 (1991)(1), 293–304.
- R. Helmig (1997). *Multiphase Flow and Transport Processes in the Subsurface - A Contribution to the Modeling of Hydrosystems*. Springer Verlag.
- J. Hoffmann, S. Kräutle, and P. Knabner, *A parallel global-implicit 2-D solver for reactive transport problems in porous media based on a reduction scheme and its application to the MoMaS benchmark problem*. *Computational Geosciences*, 14 (2010)(3), 421–433.
- J. Hoffmann, S. Kräutle, and P. Knabner, *A general reduction scheme for reactive transport in porous media*. *Computational Geosciences*, 16 (2012)(4), 1081–1099.
- J. Hommel, A. B. Cunningham, R. Helmig, A. Ebigbo, and H. Class, *Numerical Investigation of Microbially Induced Calcite Precipitation as a Leakage Mitigation Technology*. *Energy Procedia*, 40C (2013), 392–397.
- J. Hommel, E. G. Lauchnor, R. Gerlach, A. B. Cunningham, A. Ebigbo, R. Helmig, and H. Class, *Investigating the influence of the initial biomass distribution and injection strategies on biofilm-mediated calcite precipitation in porous media*. *Transport in Porous Media*, (2015a), 1–23.
- J. Hommel, E. G. Lauchnor, A. J. Phillips, R. Gerlach, A. B. Cunningham, R. Helmig, A. Ebigbo, and H. Class, *A revised model for microbially induced calcite precipitation:*

- Improvements and new insights based on recent experiments. Water Resources Research*, 51 (2015b)(5), 3695–3715.
- L. Huang, L. Yu, Z. Luo, S. Song, H. Bo, and C. Zheng, *A Microbial-enhanced Oil Recovery Trial in Huabei Oilfield in China. Petroleum Science and Technology*, 32 (2014)(5), 584–592.
- D. Hunkeler, R. Aravena, and B. J. Butler, *Monitoring microbial dechlorination of tetrachloroethene (PCE) in groundwater using compound-specific stable carbon isotope ratios: Microcosm and field studies. Environmental Science and Technology*, 33 (1999)(16), 2733–2738.
- E. J. P. Jones, M. a. Voytek, M. D. Corum, and W. H. Orem, *Stimulation of Methane Generation from Nonproductive Coal by Addition of Nutrients or a Microbial Consortium. Applied and Environmental Microbiology*, 76 (2010)(21), 7013–7022.
- A. L. Juhasz and R. Naidu, *Bioremediation of high molecular weight polycyclic aromatic hydrocarbons: A review of the microbial degradation of benzo[a]pyrene. International Biodeterioration and Biodegradation*, 45 (2000)(1-2), 57–88.
- J. F. Kanney, C. T. Miller, and C. T. Kelley, *Convergence of iterative split-operator approaches for approximating nonlinear reactive problems. Advances in Water Resources*, 26 (2003), 247–261.
- D. S. Kim, S. Thomas, and H. S. Fogler, *Effects of pH and trace minerals on long-term starvation of Leuconostoc mesenteroides. Applied and Environmental Microbiology*, 66 (2000)(3), 976–81.
- S. Klose and M. Tabatabai, *Urease activity of microbial biomass in soils. Soil Biology and Biochemistry*, 31 (1999)(2), 205–211.
- J. Kozeny, *Über kapillare Leitung des Wassers im Boden. Sitzungsber. Akad. Wiss., Wien*, 136 (1927)(2a), 271–306.
- B. Krajewska, *Ureasases I. Functional, catalytic and kinetic properties: A review. Journal of Molecular Catalysis B: Enzymatic*, 59 (2009)(1-3), 9–21.
- S. Krättele, *The semismooth Newton method for multicomponent reactive transport with minerals. Advances in Water Resources*, 34 (2011), 137–151.
- S. Krättele and P. Knabner, *A new numerical reduction scheme for fully coupled multicomponent transport-reaction problems in porous media. Water Resources Research*, 41 (2005)(9), W09414.

- S. Kräutle and P. Knabner, *A reduction scheme for coupled multicomponent transport-reaction problems in porous media: Generalization to problems with heterogeneous equilibrium reactions*. *Water Resources Research*, 43 (2007)(3), W03429.
- T. Kurz (2015). *Numerische Untersuchung des Einflusses von Heterogenitäten im porösen Medium auf mikrobiell induzierte Kalzitausfällung*. Bachelor's thesis, Institut für Wasser- und Umweltsystemmodellierung, Universität Stuttgart.
- K.-H. Lai, J.-S. Chen, C.-W. Liu, and S.-Y. Yang, *Effect of permeability-porosity functions on simulated morphological evolution of a chemical dissolution front*. *Hydrological Processes*, 28 (2014)(1), 16–24.
- E. Lauchnor, D. Topp, A. Parker, and R. Gerlach, *Whole cell kinetics of ureolysis by *Sporosarcina pasteurii**. *Journal of Applied Microbiology*, 118 (2015)(6), 1321–1332.
- E. G. Lauchnor, L. N. Schultz, S. Bugni, A. C. Mitchell, A. B. Cunningham, and R. Gerlach, *Bacterially Induced Calcium Carbonate Precipitation and Strontium Co-Precipitation in a*. *Environmental Science & Technology*, 47 (2013)(3), 1557–1564.
- I. Lazar, I. G. Petrisor, and T. F. Yen, *Microbial Enhanced Oil Recovery (MEOR)*. *Petroleum Science and Technology*, 25 (2007)(11), 1353–1366.
- D. R. Lovley and F. H. Chapelle, *Deep subsurface microbial processes*. *Review of Geophysics*, 33 (1995)(3), 365–381.
- K. T. B. MacQuarrie and K. U. Mayer, *Reactive transport modeling in fractured rock: A state-of-the-science review*. *Earth-Science Reviews*, 72 (2005)(3-4), 189–227.
- D. Martin, K. Dodds, B. T. Ngwenya, I. B. Butler, and S. C. Elphick, *Inhibition of *Sporosarcina pasteurii* under anoxic conditions: implications for subsurface carbonate precipitation and remediation via ureolysis*. *Environmental Science & Technology*, 46 (2012)(15), 8351–5.
- B. Martinez, J. T. De Jong, and T. R. Ginn, *Bio-geochemical reactive transport modeling of microbial induced calcite precipitation to predict the treatment of sand in one-dimensional flow*. *Computers and Geotechnics*, 58 (2014), 1–13.
- R. I. Mateles, *Calculation of the oxygen required for cell production*. *Biotechnology and Bioengineering*, 13 (1971)(4), 581–582.
- L. F. Melo, *Biofilm physical structure, internal diffusivity and tortuosity*. *Water Science Technology*, 52 (2005)(7), 77–84.

- F. Millero, F. Huang, T. Graham, and D. Pierrot, *The dissociation of carbonic acid in NaCl solutions as a function of concentration and temperature. Geochimica et Cosmochimica Acta*, 71 (2007)(1), 46–55.
- F. J. Millero, P. J. Milne, and V. L. Thurmond, *The solubility of calcite, strontianite and witherite in NaCl solutions at 25° C. Geochimica et Cosmochimica Acta*, 48 (1984), 1141–1143.
- R. J. Millington and J. P. Quirk, *Permeability of porous solids. Transaction of the Faraday Society*, 57 (1961)(8), 1200–1207.
- R. Mirpuri, W. Jones, and J. D. Bryers, *Toluene degradation kinetics for planktonic and biofilm-grown cells of Pseudomonas putida 54G. Biotechnology and Bioengineering*, 53 (1997)(6), 535–546.
- A. C. Mitchell, A. J. Phillips, M. A. Hamilton, R. Gerlach, W. K. Hollis, J. P. Kaszuba, and A. B. Cunningham, *Resilience of planktonic and biofilm cultures to supercritical CO<sub>2</sub>. Journal of Supercritical Fluids*, 47 (2008)(2), 318–325.
- A. C. Mitchell, A. J. Phillips, L. Schultz, S. Parks, L. H. Spangler, A. B. Cunningham, and R. Gerlach, *Microbial CaCO<sub>3</sub> mineral formation and stability in an experimentally simulated high pressure saline aquifer with supercritical CO<sub>2</sub>. International Journal of Greenhouse Gas Control*, 15 (2013), 86–96.
- C. N. Mulligan, *Environmental applications for biosurfactants. Environmental Pollution*, 133 (2005)(2), 183–198.
- E. M. Murphy, T. R. Ginn, A. Chilakapati, C. T. Resch, J. L. Phillips, T. W. Wietsma, and C. M. Spadoni, *The influence of physical heterogeneity on microbial degradation and distribution in porous media. Water Resources Research*, 33 (1997)(5), 1087–1103.
- S. M. Nielsen, I. Nesterov, and A. A. Shapiro, *Simulations of microbial-enhanced oil recovery: Adsorption and filtration. Transport in Porous Media*, 102 (2014)(2), 227–259.
- S. Norland, M. Heldal, and O. Tmyr, *On the relation between dry matter and volume of bacteria X-ray analysis. Microbial Ecology*, 13 (1987), 95–101.
- G. D. O. Okwadha and J. Li, *Optimum conditions for microbial carbonate precipitation. Chemosphere*, 81 (2010)(9), 1143–1148.
- E. Paul, J. C. Ochoa, Y. Pechaud, Y. Liu, and A. Liné, *Effect of shear stress and growth conditions on detachment and physical properties of biofilms. Water research*, 46 (2012)(17), 5499–5508.

- K. Pedersen, *The deep subterranean biosphere*. *Earth-Science Reviews*, 34 (1993)(4), 243–260.
- A. J. Phillips (2013). *Biofilm-Induced Calcium Carbonate Precipitation: Application in the Subsurface*. Ph.D. thesis, Montana State University.
- A. J. Phillips, J. Eldring, R. Hiebert, E. Lauchnor, A. C. Mitchell, A. B. Cunningham, L. H. Spangler, and R. Gerlach, *Design of a meso-scale high pressure vessel for the laboratory examination of biogeochemical subsurface processes*. *Journal of Petroleum Science and Engineering*, 126 (2015), 55–62.
- A. J. Phillips, R. Gerlach, E. G. Lauchnor, A. C. Mitchell, A. B. Cunningham, and L. H. Spangler, *Engineered applications of ureolytic biomineralization: a review*. *Biofouling*, 29 (2013a)(6), 715–733.
- A. J. Phillips, E. G. Lauchnor, J. J. Eldring, R. Esposito, A. C. Mitchell, R. Gerlach, A. B. Cunningham, and L. H. Spangler, *Potential CO<sub>2</sub> leakage reduction through biofilm-induced calcium carbonate precipitation*. *Environmental Science & Technology*, 47 (2013b), 142–149.
- N. Pradhan, K. Nathsarma, K. Srinivasa Rao, L. Sukla, and B. Mishra, *Heap bioleaching of chalcopyrite: A review*. *Minerals Engineering*, 21 (2008)(5), 355–365.
- C.-Z. Qin and S. M. Hassanizadeh, *Pore-Network Modeling of Solute Transport and Biofilm Growth in Porous Media*. *Transport in Porous Media*, (2015)(September).
- R. a. Raiders, R. M. Knapp, and M. J. Mcinerney, *Microbial Selective Plugging and Enhanced Oil-Recovery*. *Journal of Industrial Microbiology*, 4 (1989)(3), 215–229.
- Y. Rhee, S. Hillier, and G. Gadd, *Lead Transformation to Pyromorphite by Fungi*. *Current Biology*, 22 (2012)(3), 237–241.
- R. Riquelme, I. Lira, C. Pérez-López, J. A. Rayas, and R. Rodríguez-Vera, *Interferometric measurement of a diffusion coefficient: comparison of two methods and uncertainty analysis*. *Journal of Physics D: Applied Physics*, 40 (2007)(9), 2769–2776.
- D. Ritter, D. Vinson, E. Barnhart, D. M. Akob, M. W. Fields, A. B. Cunningham, W. Orem, and J. C. McIntosh, *Enhanced microbial coalbed methane generation: A review of research, commercial activity, and remaining challenges*. *International Journal of Coal Geology*, 146 (2015), 28–41.
- B. E. Rittmann, *The effect of shear stress on biofilm loss rate*. *Biotechnology and Bioengineering*, XXIV (1982)(2), 501–506.

- T. Rohwerder, T. Gehrke, K. Kinzler, and W. Sand, *Bioleaching review part A: Applied Microbiology and Biotechnology*, 63 (2003)(3), 239–248.
- E. Z. Ron and E. Rosenberg, *Biosurfactants and oil bioremediation. Current Opinion in Biotechnology*, 13 (2002)(3), 249–252.
- M. W. Saaltink, J. Carrera, and A. C., *On the behavior of approaches to simulate reactive transport. Journal of Contaminant Hydrology*, 48 (2001), 213–235.
- S. K. Samanta, O. V. Singh, and R. K. Jain, *Polycyclic aromatic hydrocarbons: Environmental pollution and bioremediation. Trends in Biotechnology*, 20 (2002)(6), 243–248.
- R. Sander (1999). *Compilation of Henry's Law Constants for Inorganic and Organic Species of Potential Importance in Environmental Chemistry (version 3)*. <http://www.henrys-law.org>.
- R. Sander, *Compilation of Henry's law constants (version 4.0) for water as solvent. Atmospheric Chemistry and Physics*, 15 (2015), 4399–4981.
- T. D. Scheibe, H. Dong, and Y. Xie, *Correlation between bacterial attachment rate coefficients and hydraulic conductivity and its effect on field-scale bacterial transport. Advances in Water Resources*, 30 (2007)(6-7), 1571–1582.
- K. Seki and T. Miyazaki, *A mathematical model for biological clogging of uniform porous media. Water Resources Research*, 37 (2001)(12), 2995–2999.
- R. Sen, *Biotechnology in petroleum recovery: The microbial EOR. Progress in Energy and Combustion Science*, 34 (2008)(6), 714–724.
- M. Seto and M. Alexander, *Effect of bacterial density and substrate concentration on yield coefficients. Applied and Environmental Microbiology*, 50 (1985)(5), 1132–1136.
- E. Shigorina (2014). *Numerical investigation of microbially induced calcite precipitation at field scale*. Master's thesis, Institut für Wasser- und Umweltsystemmodellierung, Universität Stuttgart.
- G. S. Shreve and T. M. Vogel, *Comparison of substrate utilization and growth kinetics between immobilized and suspended Pseudomonas cells. Biotechnology and Bioengineering*, 41 (1993)(3), 370–379.
- N. Song (2014). *Investigation of a decoupling scheme for modeling reactive transport*. Master's thesis, Institut für Wasser- und Umweltsystemmodellierung, Universität Stuttgart.

- R. Span and W. Wagner, *A new equation of state for carbon dioxide covering the fluid region from the triple-point temperature to 1100 K at pressures up to 800 MPa*. *Journal of Physical and Chemical Reference Data*, 25 (1996)(6), 1509–1596.
- N. Spycher and K. Pruess, *CO<sub>2</sub>-H<sub>2</sub>O mixtures in the geological sequestration of CO<sub>2</sub>. II. Partitioning in chloride brines at 12–100° C and up to 600 bar*. *Geochimica et Cosmochimica Acta*, 69 (2005)(13), 3309–3320.
- C. Steefel, D. Depaolo, and P. Lichtner, *Reactive transport modeling: An essential tool and a new research approach for the Earth sciences*. *Earth and Planetary Science Letters*, 240 (2005)(3-4), 539–558.
- C. I. Steefel, C. A. J. Appelo, B. Arora, D. Jacques, T. Kalbacher, O. Kolditz, V. Lagneau, P. C. Lichtner, K. U. Mayer, J. C. L. Meeussen, S. Molins, D. Moulton, H. Shao, J. Šimůnek, N. Spycher, S. B. Yabusaki, and G. T. Yeh, *Reactive transport codes for subsurface environmental simulation*. *Computational Geosciences*, 19 (2015a)(3), 445–478.
- C. I. Steefel, S. B. Yabusaki, and K. U. Mayer, *Reactive transport benchmarks for subsurface environmental simulation*. *Computational Geosciences*, 19 (2015b)(3), 439–443.
- K. O. Stetter, G. Fiala, G. Huber, R. Huber, and a. Seegerer, *Hyperthermophilic microorganisms*. *FEMS Microbiology Reviews*, 75 (1990), 117–124.
- T. K. Stevik, K. Aa, G. Ausland, and J. F. Hanssen, *Retention and removal of pathogenic bacteria in wastewater percolating through porous media: a review*. *Water Research*, 38 (2004)(6), 1355 – 1367.
- S. Stocks-Fischer, J. K. Galinat, and S. S. Bang, *Microbiological precipitation of CaCO<sub>3</sub>*. *Soil Biology and Biochemistry*, 31 (1999), 1563–1571.
- S. W. Taylor and P. R. Jaffé, *Substrate and biomass transport in a porous-medium*. *Water Resources Research*, 26 (1990)(9), 2181–2194.
- M. Thullner, *Comparison of bioclogging effects in saturated porous media within one- and two-dimensional flow systems*. *Ecological Engineering*, 36 (2010)(2), 176–196.
- M. Thullner, J. Zeyer, and W. Kinzelbach, *Influence of microbial growth on hydraulic properties of pore networks*. *Transport in Porous Media*, 49 (2002)(1), 99–122.
- D. J. Tobler, M. O. Cuthbert, R. B. Greswell, M. S. Riley, J. C. Renshaw, S. Handley-Sidhu, and V. R. Phoenix, *Comparison of rates of ureolysis between *Sporosarcina pasteurii* and an indigenous groundwater community under conditions required to precipitate large volumes of calcite*. *Geochimica et Cosmochimica Acta*, 75 (2011)(11), 3290–3301.

- S. Torkzaban, S. S. Tazehkand, S. L. Walker, and S. A. Bradford, *Transport and fate of bacteria in porous media: Coupled effects of chemical conditions and pore space geometry*. *Water Resources Research*, 44 (2008)(4), W04403.
- G. G. Tsyppkin and A. W. Woods, *Precipitate formation in a porous rock through evaporation of saline water*. *Journal of Fluid Mechanics*, 537 (2005), 35–53.
- N. Tufenkji, *Modeling microbial transport in porous media: Traditional approaches and recent developments*. *Advances In Water Resources*, 30 (2007)(6-7), 1455–1469.
- H. A. van der Vorst, *BI-CGSTAB: A Fast and Smoothly Converging Variant of BI-CG for the Solution of Nonsymmetric Linear Systems*. *SIAM Journal on Scientific and Statistical Computing*, 13 (1992)(2), 631–644.
- L. A. van Paassen, R. Ghose, T. J. M. van der Linden, W. R. L. van der Star, and M. C. M. van Loosdrecht, *Quantifying Biomediated Ground Improvement by Ureolysis: Large-Scale BiogROUT Experiment*. *Journal of Geotechnical and Geoenvironmental Engineering*, 136 (2010)(12), 1721–1728.
- W. K. van Wijngaarden, F. J. Vermolen, G. A. M. Meurs, and C. Vuik, *Modelling BiogROUT: A new ground improvement method based on microbial-induced carbonate precipitation*. *Transport in Porous Media*, 87 (2011)(2), 397–420.
- W. K. van Wijngaarden, F. J. Vermolen, G. A. M. Meurs, and C. Vuik, *A mathematical model for BiogROUT*. *Computational Geosciences*, 17 (2013)(3), 463–478.
- P. Vandevivere, P. Baveye, D. S. de Lozada, and P. DeLeo, *Microbial Clogging of Saturated Soils and Aquifer Materials: Evaluation of Mathematical Models*. *Water Resources Research*, 31 (1995)(9), 2173–2180.
- A. Verma and K. Pruess, *Thermohydrological conditions and silica redistribution near high-level nuclear wastes emplaced in saturated geological formations*. *Journal of Geophysical Research: Solid Earth*, 93 (1988)(B2), 1159–1173.
- H. Watling, *The bioleaching of sulphide minerals with emphasis on copper sulphides — A review*. *Hydrometallurgy*, 84 (2006)(1-2), 81–108.
- V. S. Whiffin, L. a. van Paassen, and M. P. Harkes, *Microbial Carbonate Precipitation as a Soil Improvement Technique*. *Geomicrobiology Journal*, 24 (2007)(5), 417–423.
- M. Wolf, O. Breitkopf, and R. Puk, *Solubility of calcite in different electrolytes at temperatures between 10 and 60°C and at CO<sub>2</sub> partial pressures of about 1 kPa*. *Geochemical Journal*, 76 (1989), 291–301.

- T. Xu, J. Samper, C. Ayora, M. Manzano, and E. Custodio, *Modeling of non-isothermal multi-component reactive transport in field scale porous media flow systems*. *Journal of Hydrology*, 214 (1999)(1-4), 144–164.
- G. T. Yeh and V. S. Tripathi, *A critical evaluation of recent developments in hydrogeochemical transport models of reactive multichemical components*. *Water Resources Research*, 25 (1989)(1), 93–108.
- N. Youssef, D. R. Simpson, K. E. Duncan, M. J. McInerney, M. Folmsbee, T. Fincher, and R. M. Knapp, *In Situ Biosurfactant Production by Bacillus Strains Injected into a Limestone Petroleum Reservoir*. *Applied and Environmental Microbiology*, 73 (2007)(4), 1239–1247.
- T. C. Zhang and P. L. Bishop, *Density, porosity, and pore structure of biofilms*. *Water Research*, 28 (1994)(11), 2267–2277.
- S. Zhong and A. Mucci, *Calcite and aragonite precipitation from seawater solutions of various salinities: Precipitation rates and overgrowth compositions*. *Chemical Geology*, 78 (1989), 283–299.

## **A. Model improvement: porosity-permeability relation**

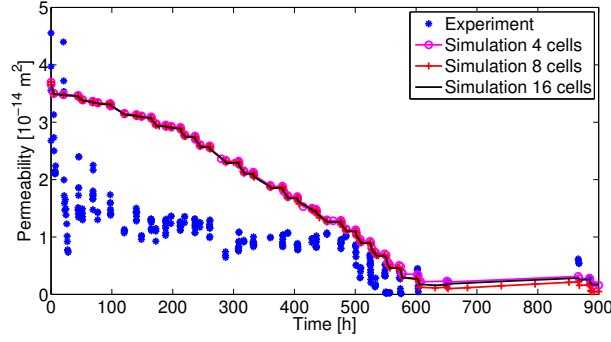


**Figure A.1.:** Grid convergence study for the high pressure core simulation.

**Table A.1.:** Porosity and corrected, porous-medium-only pressure difference  $\Delta p_{\text{corr}}$  measured in the micro model experiment as well as the permeability calculated from the pressure difference. The injection rate is 1 ml/h, the cross sectional area  $605291 \mu\text{m}^2$ , the viscosity 0.72 Pas (at  $37^\circ\text{C}$ ), the porous medium length  $9729 \mu\text{m}$ . For each porosity measurement, the permeability is calculated using the averaged  $\Delta p_{\text{corr}}$  of the duration of taking the microscopy image. The tubing and non-porous region pressure difference is assumed to be constant and estimated to be 17.2 Pa.

Time [h]	$\phi$	$\Delta p_{\text{corr}}$ [Pa]	$K$ [ $\text{m}^2$ ]
0.34	0.6239	27.3	$1.3 \cdot 10^{-10}$
2.34	0.6211	63.3	$5.6 \cdot 10^{-11}$
4.34	0.6250	93.7	$3.8 \cdot 10^{-11}$
6.34	0.6226	141.7	$2.5 \cdot 10^{-11}$
8.34	0.6146	247.2	$1.4 \cdot 10^{-11}$
10.34	0.6087	600.6	$5.9 \cdot 10^{-12}$
12.34	0.6053	3448.6	$1.0 \cdot 10^{-12}$
13.6	0.5990	1795.1	$2.5 \cdot 10^{-12}$

This appendix contains the grid convergence study for the simulation of the HP experiment (Figure A.1) and detailed information on the porosity and permeability data of the micro-model experiment in Table A.1.

## **B. Model improvement: ureolysis**

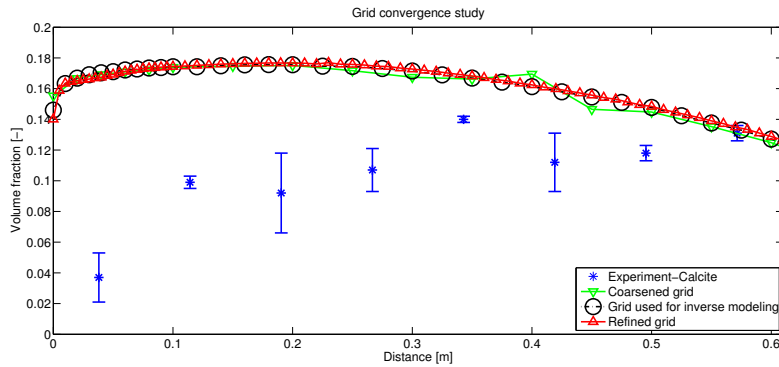


**Figure B.1.:** Results of a grid convergence study comparing different grid resolutions.

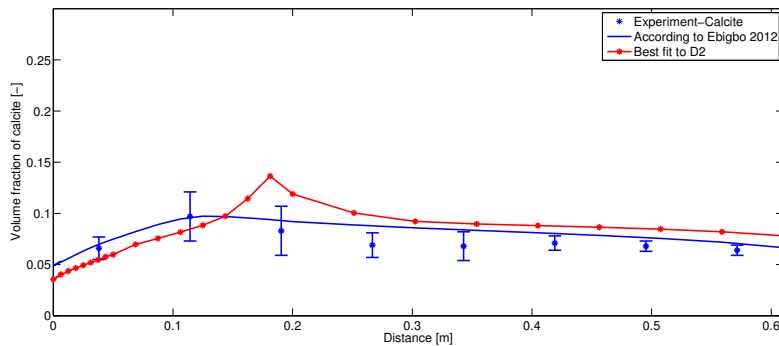


**Figure B.2.:** Comparison of the column C4 experiment results for calcite with predictions of the *Ebigbo et al.* (2012) model and the revised model. The fit to the data is approximately similar for both models.

This appendix contains several figures and tables, giving the data used in Section 4.2 or supporting the its conclusions. Figure B.1 gives the results of a grid convergence study indicating that grid induced effects did not affect the results obtained in this study. Figures B.2 to B.4 compare measured and modeled calcite distributions for experiments C4, D1 and BR, which are not shown in the manuscript itself. Further, Figure B.5 compares measured and modeled effluent pH for experiment D2.

Table B.1 gives relevant experimental design parameters and Table B.2 the composition of the fluids injected during the experiments. Experimental measurements used as observations in inverse modeling are given in the Tables B.3 to B.7. Table B.8 summarizes the sums of squared residuals of model predictions for selected parameter sets (see Table 4.4) to the experimental measurements of D2. This Table additionally gives the residuals between measurements and the predictions of the previous model proposed by (*Ebigbo et al.*, 2012).

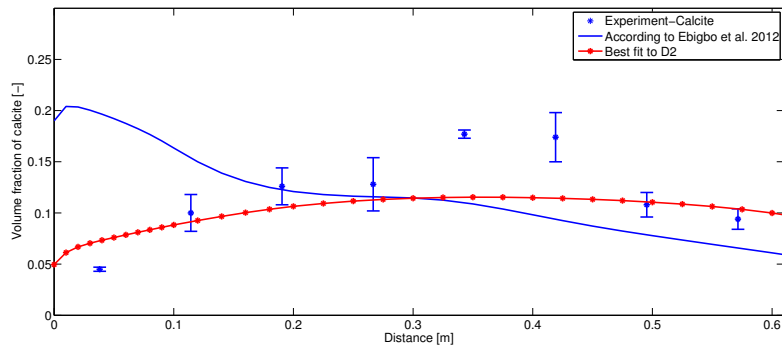


**Figure B.3.:** Comparison of the column D1 experiment results for calcite with predictions of the *Ebigo et al. (2012)* model and the revised model. The model and parameters determined in this study for D2 provide a better fit to the D1 results than the model and parameters proposed by *Ebigo et al. (2012)*.

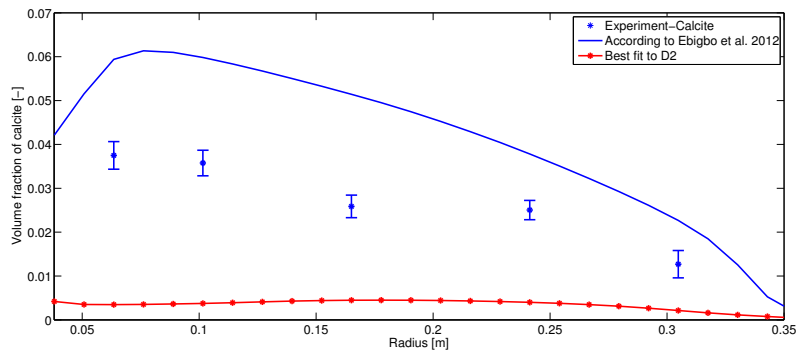


**Figure B.4.:** Comparison of the bicycle rim experiment results for calcite with predictions of the *Ebigo et al. (2012)* model and the revised model. The *Ebigo et al. (2012)* model overpredicts the amount of calcite precipitated, while the revised model with parameters determined for D2 underestimates it.

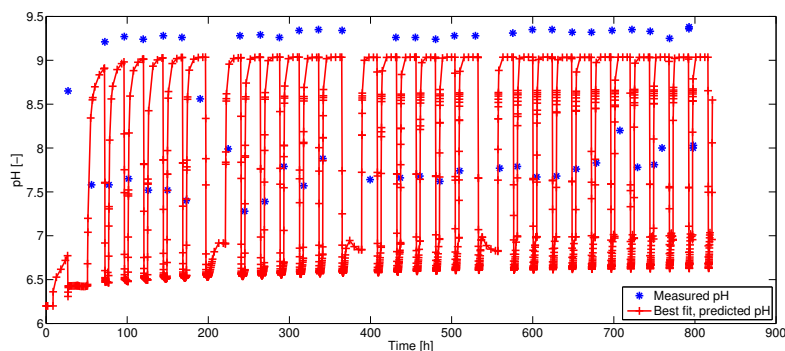


**Figure B.5.:** Comparison of experimentally measured pH of column experiment D2 to predictions of the revised model. Outgassing of  $\text{CO}_2$  probably increased the measured pH, as the pH measurements were not conducted in-situ, but in samples extracted from the column and exposed to atmospheric conditions prior to pH measurement.

**Table B.1.:** Experimental parameters of the experiments used in inverse modeling. Values of column C4 are taken from *Ehigbo et al.* (2012). The given concentrations are in the units of  $\text{g/l}$ , except for *S. pasteurii*.

Experiment	Inoculum [CFU/ml]	Flow rate [ml/min]	Residence time during flow [min]	No. of $\text{Ca}^{2+}$ rich pulses	Mineralization Period	No. of re- suscitation events	Resuscitation frequency
Column C4	$1.3 \cdot 10^7$	10	15	22	Overnight flow	no	9 Every 4-5 days
Column D1	$2.7 \cdot 10^8$	10	15	30	4 h no flow	29	Daily
Column D2	$5.6 \cdot 10^7$	10	15	30	4 h no flow	29	Daily
Bicycle Rim BR	$1.6 \cdot 10^8$	57	48	1	12 h constant flow	0	-

**Table B.2.:** Injected fluid composition for the experiments used in inverse modeling. The given concentrations are in the units of  $\text{g/l}$ , except for *S. pasteurii*.

Injection type	$\text{CaCl}_2$	Urea	$\text{NH}_4\text{Cl}$	$\text{C}_{\text{tot}}$	Substrate*	$\text{O}_2$	<i>S. pasteurii</i>	pH
Inoculation	0	0	10	0.00058	3	0.008	Exp. specific **	6.2
Resuscitation	0	20	10	0.00058	3	0.008	0	6.2
Calcium rich	$139.7 / 36.9^{***}$	20	10	0.00058	3	0.008	0	5.4

\*Substrate represents the carbon and energy source of *S. pasteurii* used in the experiments (Difco Nutrient Broth).

\*\*The specific inoculation concentrations of each experiment are given in Table B.1.

\*\*\*The concentration of  $\text{CaCl}_2$  is  $139.7 \text{ g/l}$  for column C4 and  $36.9 \text{ g/l}$  for all other experiments.

**Table B.3.:** Measured final volume fractions of calcite at given distance (Columns) or radius (Bicycle Rim) used as observations in inverse modeling. Values of C4 are taken from *Ebigbo et al. (2012)*. The values given here are the averages of triplicate measurements at each measurement location. For column D1 and D2, interpolated values are tabulated at locations that match the nearest grid point. These values were obtained through linear interpolation between the two surrounding measurements. The distance between measurement location and the nearest grid node was never greater than 1 cm. The experimental data presented here is also used in the Figures 4.14, B.2, B.3, and B.4.

Location measured	3.81 cm	11.43 cm	19.05 cm	26.67 cm	34.29 cm	41.91 cm	49.53 cm	57.15 cm
Column C4	0.066	0.097	0.083	0.069	0.068	0.071	0.068	0.064
Column D1	0.045	0.100	0.126	0.128	0.177	0.174	0.108	0.094
Column D2	0.037	0.099	0.092	0.107	0.140	0.112	0.118	0.131
Location grid*	4.0 cm	12.0 cm	20.0 cm	27.5 cm	35.0 cm	42.5 cm	50.0 cm	57.5cm
Column D1* interpolated	0.047	0.102	0.126	0.133	0.177	0.169	0.107	0.093
Column D2* interpolated	0.040	0.099	0.094	0.110	0.137	0.113	0.119	0.132
Location measured	6.35 cm	10.16 cm	16.51 cm	24.13 cm	30.48 cm			
Bicycle Rim BR**	0.037	0.036	0.026	0.025	0.013			

\*Grid location the measured calcite values were interpolated to in order to match the grid nodes and the interpolated values.

\*\*The values given for the Bicycle Rim experiment are averages of measurements in 8 radial segments.

**Table B.4.:** Measured concentrations of ammonium [ $\text{mol/l}$ ] for column experiment D1 used as observations in inverse modeling.

Pulse	Time [h]	10 cm	20 cm	30 cm	40 cm	50 cm
5	151.35	0.157	0.157	0.154	0.156	0.155
	151.85	0.173	0.170	0.177	0.184	0.190
	152.35	0.192	0.190	0.213	0.224	0.230
	153.35	0.206	0.212	0.274	0.287	0.302
	154.35	0.240	0.244	0.357	0.353	0.367
	155.35	0.260	0.287	0.430	0.407	0.416
7	218.85	0.150	0.155	0.149	0.155	0.159
	219.35	0.171	0.166	0.180	0.192	0.198
	219.85	0.192	0.183	0.191	0.224	0.247
	220.85	0.235	0.230	0.275	0.323	0.326
	221.85	0.283	0.289	0.370	0.421	0.436
	222.85	0.326	0.365	0.456	0.544	0.516
10	290.85	0.151	0.161	0.161	0.158	0.163
	291.35	0.215	0.211	0.238	0.214	0.187
	291.85	0.286	0.290	0.395	0.290	0.219
	292.85	0.375	0.419	0.547	0.431	0.257
	293.85	0.463	0.552	0.613	0.592	0.293
	294.85	0.518	0.642	0.685	0.657	0.408
22	626.85	0.160	0.163	0.167	0.172	0.174
	627.35	0.242	0.234	0.251	0.227	0.204
	627.85	0.294	0.269	0.288	0.244	0.202
	628.85	0.397	0.386	0.411	0.300	0.244
	630.85	0.511	0.551	0.521	0.360	0.273
24	698.85	0.184	0.191	0.191	0.207	0.213
	699.35	0.279	0.268	0.266	0.260	0.249
	699.85	0.384	0.362	0.372	0.344	0.310
	700.85	0.456	0.460	0.472	0.332	0.345
	701.85	0.522	0.612	0.552	0.429	0.349
	702.85	0.616	0.660	0.602	0.454	0.395
30	866.85	0.159	0.163	0.160	0.163	0.162
	867.35	0.259	0.255	0.276	0.299	0.294
	867.85	0.340	0.321	0.366	0.417	0.378
	868.85	0.495	0.511	0.558	0.586	0.357
	869.85	0.596	0.609	0.644	0.612	0.432
	870.85	0.628	0.679	0.690	0.679	0.397

**Table B.5.:** Measured concentrations of calcium [ $\text{mol/l}$ ] for column experiment D1 used as observations in inverse modeling.

Pulse	Time [h]	10 cm	20 cm	30 cm	40 cm	50 cm
5	151.35	0.277	0.275	0.270	0.254	0.273
	151.85	0.196	0.277	0.263	0.264	0.266
	152.35	0.218	0.262	0.265	0.235	0.250
	153.35	0.241	0.262	0.224	0.207	0.206
	154.35	0.161	0.249	0.189	0.176	0.171
	155.35	0.175	0.227	0.154	0.164	0.152
7	218.85	0.258	0.256	0.249	0.252	0.250
	219.35	0.239	0.245	0.241	0.220	0.230
	219.85	0.204	0.234	0.202	0.193	0.211
	220.85	0.159	0.218	0.199	0.179	0.163
	221.85	0.158	0.210	0.172	0.144	0.133
	222.85	0.137	0.168	0.128	0.089	0.091
10	290.85	0.260	0.264	0.262	0.253	0.254
	291.35	0.231	0.248	0.232	0.239	0.255
	291.85	0.175	0.209	0.156	0.210	0.239
	292.85	0.120	0.156	0.086	0.133	0.218
	293.85	0.083	0.061	0.047	0.047	0.193
	294.85	0.042	0.022	0.013	0.024	0.138
22	626.85	0.263	0.262	0.256	0.255	0.255
	627.35	0.217	0.227	0.228	0.235	0.246
	627.85	0.193	0.203	0.191	0.210	0.216
	628.85	0.117	0.153	0.137	0.171	0.217
	630.85	0.070	0.076	0.092	0.181	0.202
24	698.85	0.303	0.299	0.286	0.288	0.290
	699.35	0.236	0.255	0.252	0.258	0.264
	699.85	0.187	0.222	0.205	0.224	0.241
	700.85	0.134	0.164	0.153	0.150	0.231
	701.85	0.113	0.083	0.115	0.177	0.222
	702.85	0.068	0.062	0.080	0.180	0.196
30	866.85	0.257	0.262	0.247	0.243	0.239
	867.35	0.193	0.209	0.188	0.179	0.188
	867.85	0.163	0.162	0.124	0.120	0.140
	868.85	0.085	0.084	0.058	0.050	0.063
	869.85	0.036	0.023	0.014	0.038	0.127
	870.85	0.017	0.001	0.001	0.004	0.136

**Table B.6.:** Measured concentrations of ammonium [ $\text{mol/l}$ ] for column experiment D2 used as observations in inverse modeling. The measurements at 20 cm distance from the inlet are used in Figure 4.13.

Pulse	Time [h]	10 cm	20 cm	30 cm	40 cm	50 cm
3	97	0.154	0.154	0.158	0.157	0.161
	97.5	0.160	0.163	0.167	0.171	0.174
	98	0.166	0.173	0.163	0.186	0.194
	99	0.178	0.184	0.192	0.216	0.227
	100	0.192	0.213	0.218	0.248	0.243
	101	0.215	0.218	0.269	0.257	0.289
6	169	0.162	0.166	0.169	0.171	0.172
	169.5	0.189	0.181	0.217	0.229	0.272
	170	0.222	0.214	0.238	0.284	0.323
	171	0.227	0.251	0.304	0.357	0.391
	172	0.245	0.325	0.394	0.423	0.462
	173	0.263	0.365	0.418	0.441	0.444
9	265	0.159	0.163	0.156	0.188	0.198
	265.5	0.229	0.274	0.315	0.346	0.392
	266	0.322	0.340	0.386	0.401	0.430
	267	0.371	0.453	0.521	0.498	0.500
	268	0.436	0.516	0.577	0.582	0.583
	269	0.444	0.562	0.637	0.625	0.646
15	433	0.157	0.168	0.179	0.184	0.199
	433.5	0.208	0.303	0.328	0.346	0.354
	434	0.264	0.457	0.471	0.517	0.532
	435	0.364	0.710	0.663	0.686	0.652
	436	0.545	0.723	0.709	0.658	0.690
	437	0.582	0.714	0.706	0.686	0.697
19	533.5	0.156	0.157	0.159	0.169	0.173
	534	0.170	0.258	0.282	0.291	0.332
	534.5	0.253	0.390	0.411	0.409	0.441
	535.5	0.293	0.503	0.591	0.669	0.625
	536.5	0.361	0.608	0.691	0.734	0.628
	537.5	0.398	0.641	0.723	0.677	0.644
21	601	0.190	0.206	0.236	0.171	0.180
	601.5	0.246	0.301	0.457	0.308	0.317
	602	0.290	0.298	0.465	0.440	0.421
	603	0.357	0.456	0.585	0.608	0.589
	604	0.398	0.639	-	0.683	0.658
	605	0.448	0.703	0.710	0.696	0.634
28	769	0.085	0.085	0.092	0.092	0.100
	769.5	0.114	0.162	0.181	0.165	0.165
	770	0.155	0.236	0.252	0.232	0.224
	771	0.524	0.722	0.732	0.642	0.649
	772	0.636	0.788	0.780	0.754	0.741
	773	0.650	0.766	0.740	0.743	0.715

**Table B.7.:** Measured concentrations of calcium [ $\text{mol/l}$ ] for column experiment D2 used as observations in inverse modeling. The measurements at 20 cm distance from the inlet are used in Figure 4.12.

Pulse	Time [h]	10 cm	20 cm	30 cm	40 cm	50 cm
3	97	0.286	0.287	0.290	0.292	0.287
	97.5	0.272	0.288	0.287	0.285	0.293
	98	0.289	0.286	0.270	0.277	0.274
	99	0.269	0.263	0.258	0.249	0.249
	100	0.260	0.274	0.250	0.231	0.215
	101	0.277	0.246	0.233	0.197	0.219
6	169	0.298	0.298	0.295	0.292	0.285
	169.5	0.280	0.289	0.285	0.260	0.236
	170	0.258	0.294	0.259	0.238	0.218
	171	0.258	0.254	0.222	0.182	0.185
	172	0.250	0.224	0.176	0.169	0.149
	173	0.241	0.187	0.167	0.157	0.116
9	265	0.287	0.284	0.251	0.273	0.270
	265.5	0.261	0.241	0.217	0.197	0.157
	266	0.218	0.186	0.172	0.176	0.134
	267	0.189	0.149	0.123	0.123	0.114
	268	0.161	0.111	0.082	0.083	0.078
	269	0.128	0.091	0.047	0.052	0.038
15	433	0.276	0.304	0.284	0.268	0.266
	433.5	0.250	0.206	0.201	0.191	0.179
	434	0.210	0.112	0.103	0.114	0.094
	435	0.169	0.017	0.029	0.037	0.040
	436	0.097	0.007	0.016	0.037	0.025
	437	0.058	0.009	0.016	0.022	0.027
19	533.5	0.277	0.266	0.266	0.271	0.250
	534	0.228	0.219	0.208	0.211	0.183
	534.5	0.223	0.179	0.136	0.162	0.129
	535.5	0.151	0.098	0.052	0.044	0.062
	536.5	0.132	0.043	0.009	0.002	0.028
	537.5	0.096	0.014	0.003	-	0
21	601	0.334	0.378	0.372	0.255	0.247
	601.5	0.314	0.247	0.280	0.190	0.187
	602	0.273	0.166	0.161	0.169	0.153
	603	0.215	0.116	0.057	0.045	0.052
	604	0.139	0.064	0.086	0.035	0.014
	605	0.124	0.025	0.007	0.024	0.021
28	769	0.279	0.283	0.273	0.254	0.261
	769.5	0.206	0.194	0.180	0.193	0.177
	770	0.153	0.144	0.120	0.159	0.138
	771	0.087	0.023	0.021	0.057	0.052
	772	0.042	-	0.003	0.011	0.018
	773	0.021	0.002	0.002	0.002	0.012

**Table B.8.:** Sum of squared residuals and normalized squared residuals of model predictions for the data sets  $\text{NH}_4^+$ ,  $\text{Ca}^{2+}$ , and  $\text{CaCO}_3$ . The squared residuals are summed over the 7 measurement pulses with each 6 measurements at the 5 locations for data sets  $\text{NH}_4^+$  (total of 419 measurements; See Table B.6) and  $\text{Ca}^{2+}$  (total of 418 measurements; See Table B.7) and the 8 measurements along the column length for  $\text{CaCO}_3$  (See Table B.3). The values presented here are for the selected parameter sets from Table 2 using the revised model and the parameters and equations as given in *Ehligbo et al. (2012)*.

Data set	<i>Ehligbo et al. (2012)</i>	Low attachment	Low $\rho_f$	Low $k_{ub}$	Best fit
Sum of squared residuals					
$\text{NH}_4^+$	4.11	12.25	11.37	13.90	3.42
$\text{Ca}^{2+}$	2.05	2.56	4.54	2.56	0.97
$\text{CaCO}_3$	0.024	0.034	0.008	0.037	0.003
Total	6.18	14.84	15.92	16.50	4.40
Sum of normalized squared residuals					
$\text{NH}_4^+$	95	295	207	283	82
$\text{Ca}^{2+}$	3890	240	142	129	278
$\text{CaCO}_3$	9.3	14.3	2.3	13.3	0.9
Total	3995	546	351	425	360

## **C. Model application to guide experimental investigations**

This appendix contains additional information and results. Additional information on the grid and boundary conditions used in this study are discussed in Section C.1. Section C.2 contains two figures comparing the rates of the processes influencing the attached biomass (Figure C.1). A comparison of the results of the full model (*Hommel et al.*, 2015b) and the initial biomass model used in this study is also provided. The full model considers inoculation and attachment throughout the duration of each experiment while the simplified approach used in this study, neglects both and starts with an assumed, pre-established attached biomass distribution (Figure C.2).

Section C.3 gives an overview of the initial attached biomass distributions used in this study, containing a table presenting the initial biomass volume fractions of all distributions investigated (Table C.1). Further, Section C.4 presents additional results, Figures C.3-C.8 comparing the resulting final calcite and biomass distributions for all the initial biomass distributions as shown in Table C.1 for each of the injection strategies used in the study, Table C.2 giving alternative shape coefficients calculated using  $\sigma_{5\text{ cm}} = \frac{\phi_c(0.05)}{\phi_c(0.5075)}$  instead of  $\sigma = \frac{\phi_c(0.10625)}{\phi_c(0.5075)}$  as in the main paper, and Figures C.9-C.13 comparing the resulting final calcite and biomass distributions for all the injection strategies used for each of the initial biomass distributions as shown in Table C.1. The  $\text{Ca}^{2+}$  precipitation efficiencies and shape coefficients for all combinations of initial biomass distributions and injection strategies are presented in Figures C.14 and C.15, respectively.

Finally, Figures C.16 and C.17 show the oxygen mass fraction over time at  $z = 0.10625\text{ m}$  and  $z = 0.5075\text{ m}$  for homogeneous initial biomass distributions and pulsed injection strategies.

## C.1. Grid and boundary conditions used in this study

The grid that is used for spatial discretization in this study is identical to the grid used in *Ebigbo et al.* (2012). The discretization along the column is given in the first column of both the Table C.1. It is refined towards the influent and at the effluent it is extended by eight cells (and a distance of 19 cm) to minimize any influence of the Dirichlet boundary condition imposed at the effluent on the results of the first 61 cm, the length of the column as used in the attachment experiments as well as the experiment D2 (*Hommel et al.*, 2015b) used to generate the various injection strategies.

Initially, the column is filled with growth medium as given in Table B.2. The boundary conditions used in this study are identical to those used in *Hommel et al.* (2015b) for this experiment: no-flow boundaries at the sides, a Dirichlet boundary at the effluent ( $z = 0.8$ ) which is set equal to the initial conditions, except for oxygen and substrate, which are set

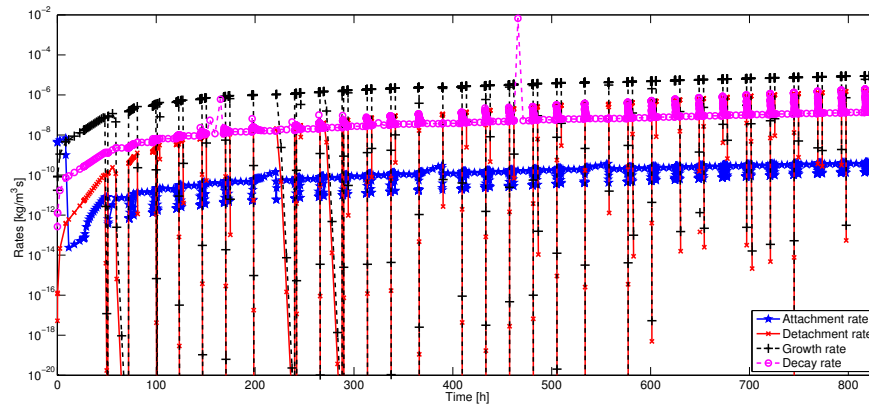
to zero. A time-dependent Neumann boundary is used at the influent ( $z = 0$ ). The time-dependent Neumann boundary accounts for the different composition of the injected fluids described in *Hommel et al.* (2015b).

The composition of the injected fluids for each injection type is given in Table B.2. Omitting the inoculation and the first batch period, the injection starts with an 18 h pulse of growth medium, followed by 0.5 h of calcium-rich with a 23.5 h batch period and 0.5 h of growth medium with a 20.5 h batch period. Starting with the second calcium-rich injection at a simulation time of 64 h, the regular injection cycle begins consisting of 0.5 h calcium-rich medium injection, a 4 h batch period, 0.5 h growth medium injection, and a 19 h batch period starts, which is repeated until the end of the experiment.

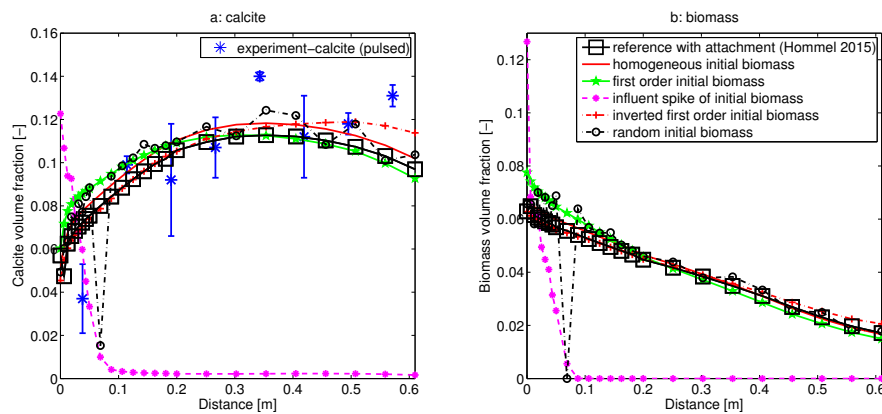
## C.2. Rates influencing the attached biomass

Figure C.1 shows the rates influencing the attached biomass over the entire duration of the column experiment D2 (*Hommel et al.*, 2015b) used to derive the injection strategies used in this study. The attachment rate is lower for the entire duration except the inoculation at the very beginning.

The reference model (*Hommel et al.*, 2015b), including inoculation and attachment, tends to predict slightly lower volume fractions for both biomass and calcite than the average of the results of the initial biomass distributions investigated, see Figure C.2. For biomass, the final distribution of the reference solution is similar to a combination of the resulting biomass of the inverse first-order (for the first half of the column) and homogeneous initial biomass distribution (for the second half of the column). For calcite, the final distribution of the reference solution is similar to a combination of the resulting biomass of the inverse first-order (for the first half of the column) and first-order initial biomass distribution (for the second half of the column).



**Figure C.1.:** Comparison of the attachment rate to the other rates influencing the biomass distribution as predicted by the model for column experiment D2 (*Hommel et al., 2015b*).



**Figure C.2.:** Comparison of the reference calcite (a) and biomass (b) distribution (including initial inoculation and attachment according to (*Hommel et al., 2015b*)) with the final calcite (a) and biomass (b) distributions obtained assuming the various initial biomass distributions investigated in this study (Table C.1) for the pulsed injection strategy.

### C.3. Initial biomass distributions

Five different initial biomass distributions are investigated:

- homogeneous distribution (as assumed by (e.g. *van Wijngaarden et al.*, 2011)); the initial biomass volume fraction along the simulation domain is constant, the initial biomass volume fraction for the homogeneous case being  $\phi_{f,0,h} = 2.597 \cdot 10^{-4}$ . This represents a case with very low attachment coefficient at very high inoculation cell concentration or sorptive attachment at full sorption capacity;

- first order distribution; the volume fraction of biomass decreases exponentially with increasing distance  $z$  to the inlet, following the equation:

$$\phi_{f,0,1^{st}}(z) = 5\phi_{f,0,h}e^{-8.18z}.$$

This exponential distribution corresponds to the approximate first order distributions that was observed in our attachment experiment with *S. pasteurii*;

- inverse first order distribution, as proposed by *Barkouki et al.* (2011), which corresponds to a change of the direction of flow after inoculation. *Barkouki et al.* (2011) propose that this distribution of cells will lead to a homogeneous distribution of precipitated calcite, as the reduction of reactants along the flow path is counteracted by an increase in catalyzing enzyme. Consequently, the initial biomass volume fraction is increasing with the distance  $z$  from the inlet for this initial distribution:

$$\phi_{f,0,inverse\ 1^{st}}(z) = 5\phi_{f,0,h}e^{8.18(z-0.61)};$$

- influent spike of biomass; the biomass is concentrated in the influent region, decreasing rapidly with increasing distance  $z$ :

$\phi_{f,0,spike}(z) = 192.86\phi_{f,0,h}e^{-817.69z}$ . This represents a tight rock (such as a low permeability sandstone) or silty or clayey material (e.g. shale rock) with low permeability and small pore sizes, into which cells are unable to penetrate very far, but instead form a coating (often referred to as a filter cake) in the influent region;

- random biomass; the constant biomass volume fraction of the *homogeneous* initial biomass distribution is multiplied at each grid point by a random number  $R(z)$  between 0 and 2 as given in Table C.1, which is adjusted by a common factor to ensure that the sum of the initial biomass is preserved. The *random* distribution represents heterogeneous attachment caused by not yet determined processes such as chemotactic movement prior to attachment or preferential attachment to certain minerals and surfaces with certain properties (i. e. roughness, charge) that lead to a non-monotonous, more or less random attachment behavior as observed in the preliminary attachment experiment that can

not be described by simple exponential distributions as for the other, idealized initial distributions:

$$\phi_{f,0,\text{random}}(z) = \phi_{f,0,h}R(z).$$

**Table C.1.:** Values of the initial biomass volume fraction  $\phi_{f,0}$  for all distributions investigated as well as the random numbers between 0 and 2 used to generate the random initial biomass distribution.

Distance [m]	Homogeneous	First order	Inverted first order	Influent spike	Random	Random number used for $\phi_{f,0,\text{random}}$
	$\phi_{f,0,h}$	$\phi_{f,0,1^{\text{st}}}$	$\phi_{f,0,\text{inverse 1}^{\text{st}}}$	$\phi_{f,0,\text{spike}}$	$\phi_{f,0,\text{random}}$	
0.0	$2.597 \cdot 10^{-4}$	$12.99 \cdot 10^{-4}$	$0.089 \cdot 10^{-4}$	0.05	$1.194 \cdot 10^{-4}$	0.4598
0.00625	$2.597 \cdot 10^{-4}$	$12.49 \cdot 10^{-4}$	$0.093 \cdot 10^{-4}$	$3.022 \cdot 10^{-4}$	$1.449 \cdot 10^{-4}$	0.5578
0.0125	$2.597 \cdot 10^{-4}$	$12.01 \cdot 10^{-4}$	$0.098 \cdot 10^{-4}$	$1.823 \cdot 10^{-6}$	$0.655 \cdot 10^{-4}$	0.2521
0.01875	$2.597 \cdot 10^{-4}$	$11.55 \cdot 10^{-4}$	$0.103 \cdot 10^{-4}$	$1.100 \cdot 10^{-8}$	$4.550 \cdot 10^{-4}$	1.7521
0.025	$2.597 \cdot 10^{-4}$	$11.11 \cdot 10^{-4}$	$0.109 \cdot 10^{-4}$	$6.634 \cdot 10^{-11}$	$1.872 \cdot 10^{-4}$	0.7206
0.03125	$2.597 \cdot 10^{-4}$	$10.69 \cdot 10^{-4}$	$0.114 \cdot 10^{-4}$	$4.002 \cdot 10^{-13}$	$5.121 \cdot 10^{-4}$	1.9720
0.0375	$2.597 \cdot 10^{-4}$	$10.28 \cdot 10^{-4}$	$0.120 \cdot 10^{-4}$	$2.415 \cdot 10^{-15}$	$2.021 \cdot 10^{-4}$	0.7782
0.04375	$2.597 \cdot 10^{-4}$	$9.890 \cdot 10^{-4}$	$0.127 \cdot 10^{-4}$	$1.457 \cdot 10^{-17}$	$4.591 \cdot 10^{-4}$	1.7680
0.05	$2.597 \cdot 10^{-4}$	$9.512 \cdot 10^{-4}$	$0.133 \cdot 10^{-4}$	$8.787 \cdot 10^{-20}$	$3.377 \cdot 10^{-4}$	1.3001
0.06875	$2.597 \cdot 10^{-4}$	$8.464 \cdot 10^{-4}$	$0.155 \cdot 10^{-4}$	$1.929 \cdot 10^{-26}$	0	0.0000
0.0875	$2.597 \cdot 10^{-4}$	$7.532 \cdot 10^{-4}$	$0.181 \cdot 10^{-4}$	$4.002 \cdot 10^{-33}$	$2.553 \cdot 10^{-4}$	0.9829
0.10625	$2.597 \cdot 10^{-4}$	$6.702 \cdot 10^{-4}$	$0.211 \cdot 10^{-4}$	0	$3.935 \cdot 10^{-4}$	1.5153
0.125	$2.597 \cdot 10^{-4}$	$5.964 \cdot 10^{-4}$	$0.246 \cdot 10^{-4}$	0	$3.655 \cdot 10^{-4}$	1.4073
0.14375	$2.597 \cdot 10^{-4}$	$5.307 \cdot 10^{-4}$	$0.287 \cdot 10^{-4}$	0	$4.869 \cdot 10^{-4}$	1.8747
0.1625	$2.597 \cdot 10^{-4}$	$4.722 \cdot 10^{-4}$	$0.334 \cdot 10^{-4}$	0	$2.527 \cdot 10^{-4}$	0.9731
0.18125	$2.597 \cdot 10^{-4}$	$4.202 \cdot 10^{-4}$	$0.390 \cdot 10^{-4}$	0	$1.878 \cdot 10^{-4}$	0.7230
0.2	$2.597 \cdot 10^{-4}$	$3.739 \cdot 10^{-4}$	$0.454 \cdot 10^{-4}$	0	$1.669 \cdot 10^{-4}$	0.6425
0.25125	$2.597 \cdot 10^{-4}$	$2.718 \cdot 10^{-4}$	$0.691 \cdot 10^{-4}$	0	$2.559 \cdot 10^{-4}$	0.9852
0.3025	$2.597 \cdot 10^{-4}$	$1.976 \cdot 10^{-4}$	$1.051 \cdot 10^{-4}$	0	$0.555 \cdot 10^{-4}$	0.2139
0.35375	$2.597 \cdot 10^{-4}$	$1.436 \cdot 10^{-4}$	$1.598 \cdot 10^{-4}$	0	$4.630 \cdot 10^{-4}$	1.7827
0.405	$2.597 \cdot 10^{-4}$	$1.044 \cdot 10^{-4}$	$2.429 \cdot 10^{-4}$	0	$3.911 \cdot 10^{-4}$	1.5058
0.45625	$2.597 \cdot 10^{-4}$	$0.759 \cdot 10^{-4}$	$3.694 \cdot 10^{-4}$	0	$0.249 \cdot 10^{-4}$	0.0958
0.5075	$2.597 \cdot 10^{-4}$	$0.551 \cdot 10^{-4}$	$5.616 \cdot 10^{-4}$	0	$4.397 \cdot 10^{-4}$	1.6931
0.55875	$2.597 \cdot 10^{-4}$	$0.401 \cdot 10^{-4}$	$8.540 \cdot 10^{-4}$	0	$0.283 \cdot 10^{-4}$	0.1088
0.61	$2.597 \cdot 10^{-4}$	$0.291 \cdot 10^{-4}$	$12.99 \cdot 10^{-4}$	0	$2.701 \cdot 10^{-4}$	1.0399

Continued on next page

End of the physical column

Table C.1 – *Continued from previous page*

Distance [m]	Homogeneous	First order	Inverted first order	Influent spike	Random	Random number used for $\phi_{f,0,\text{random}}$
	$\phi_{f,0,h}$	$\phi_{f,0,1^{\text{st}}}$	$\phi_{f,0,\text{inverse } 1^{\text{st}}}$	$\phi_{f,0,\text{spike}}$	$\phi_{f,0,\text{random}}$	
0.63375	$2.597 \cdot 10^{-4}$	$0.251 \cdot 10^{-4}$	$15.77 \cdot 10^{-4}$	0	$0.527 \cdot 10^{-4}$	0.2028
0.6575	$2.597 \cdot 10^{-4}$	$0.217 \cdot 10^{-4}$	$19.15 \cdot 10^{-4}$	0	$4.818 \cdot 10^{-4}$	1.8552
0.68125	$2.597 \cdot 10^{-4}$	$0.187 \cdot 10^{-4}$	$23.25 \cdot 10^{-4}$	0	$3.137 \cdot 10^{-4}$	1.2078
0.705	$2.597 \cdot 10^{-4}$	$0.161 \cdot 10^{-4}$	$28.24 \cdot 10^{-4}$	0	$0.462 \cdot 10^{-4}$	0.1780
0.72875	$2.597 \cdot 10^{-4}$	$0.139 \cdot 10^{-4}$	$34.29 \cdot 10^{-4}$	0	$0.848 \cdot 10^{-4}$	0.3264
0.7525	$2.597 \cdot 10^{-4}$	$0.120 \cdot 10^{-4}$	$41.64 \cdot 10^{-4}$	0	$2.264 \cdot 10^{-4}$	0.8717
0.77625	$2.597 \cdot 10^{-4}$	$0.104 \cdot 10^{-4}$	$50.56 \cdot 10^{-4}$	0	$1.657 \cdot 10^{-4}$	0.6379
0.8	$2.597 \cdot 10^{-4}$	$0.089 \cdot 10^{-4}$	$61.40 \cdot 10^{-4}$	0	$2.296 \cdot 10^{-4}$	0.8842

## C.4. Results

Here, additional results for every injection strategy and every initial biomass distribution are presented. First, Figures C.3-C.8 show the resulting biomass and calcite distributions for the various initial biomass distributions used in this study (Table C.1) for every of the injection strategies investigated: fast pulsed (Figure C.3), pulsed (Figure C.4), and slow pulsed (Figure C.5) as well as fast continuous (Figure C.6), continuous (Figure C.7), and slow continuous (Figure C.8). Second, Table C.2 presents values for an alternative shape coefficient  $\sigma_{5\text{ cm}}$ , where the influent region calcite is approximated using the calcite volume fraction at  $z = 0.05\text{ m}$  instead of  $z = 0.10625\text{ m}$ :

$$\sigma_{5\text{ cm}} = \frac{\phi_c(0.05)}{\phi_c(0.5075)} \quad (\text{C.1})$$

This alternative shape coefficient  $\sigma_{5\text{ cm}}$  leads to more extreme values, especially for the initial biomass distribution “influent spike”. Third, Figures C.9-C.13 show the effect of all injection strategies used in this study on the results for each initial biomass distribution investigated (Table C.1): homogeneous (Figure C.9), first-order (Figure C.10), inverse first-order (Figure C.11), influent spike (Figure C.12), and random (Figure C.13). Figures C.14 and C.15 present the  $\text{Ca}^{2+}$  precipitation efficiencies and shape coefficients  $\sigma$  for all combinations of injection strategy and initial biomass distribution investigated, respectively. Additionally, those Figures include the  $\text{Ca}^{2+}$  precipitation efficiencies and shape coefficients  $\sigma$  for the pulsed injection strategy and the homogeneous initial biomass distribution with varying initial amounts of biomass. Finally, the temporal development of the oxygen mass fractions for homogeneous initial biomass distributions is shown in Figures C.16 and C.17. The results for varying injection rates and initial amounts of biomass illustrate that oxygen penetrates much further into the column for fast injection rates or for low initial amounts of biomass, which leads to a more uniform distribution of biomass and, thus, calcite.

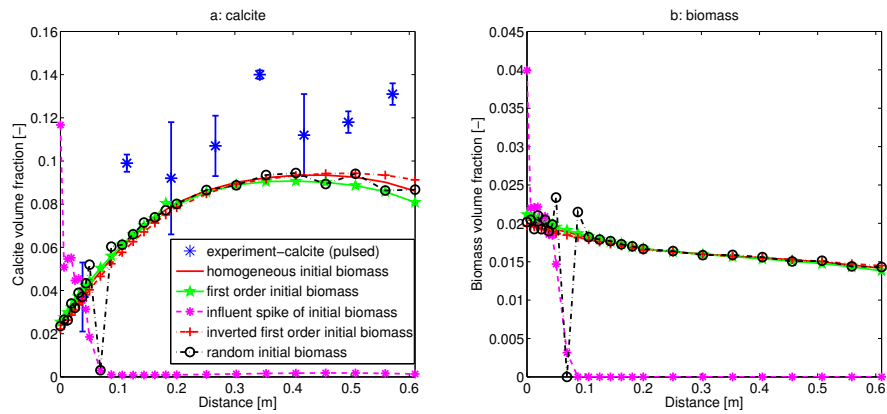


**Figure C.3.:** Comparison of the resulting calcite (a) and biomass (b) distributions for the various initial biomass distributions (Table C.1) and the fast pulsed injection strategy.

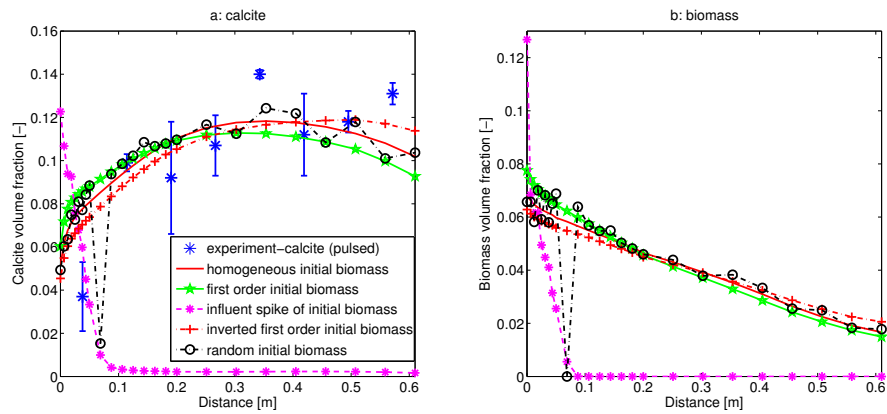


**Figure C.4.:** Comparison of the resulting calcite (a) and biomass (b) distributions for the various initial biomass distributions (Table C.1) and the pulsed injection strategy.

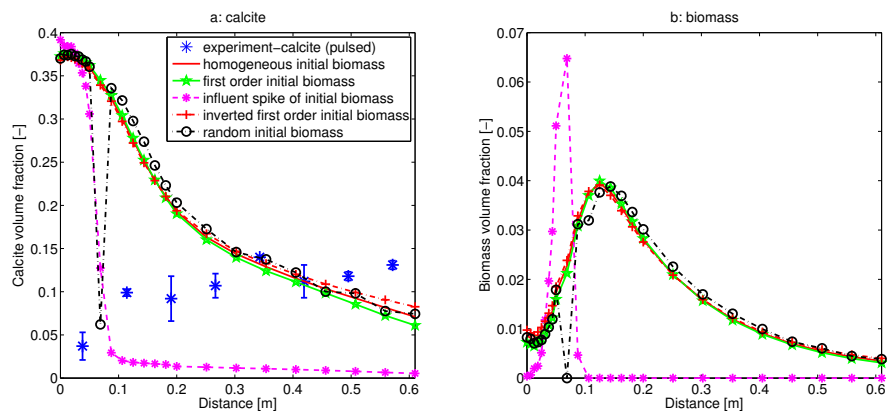


**Figure C.5.:** Comparison of the resulting calcite (a) and biomass (b) distributions for the various initial biomass distributions (Table C.1) and the slow pulsed injection strategy.

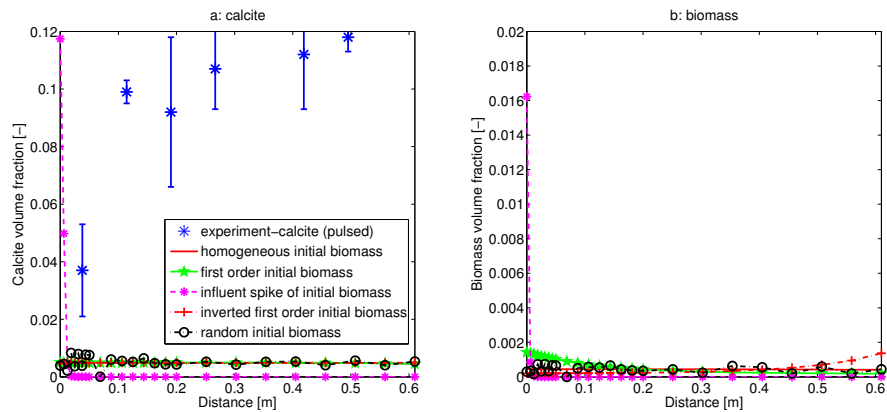


**Figure C.6.:** Comparison of the resulting calcite (a) and biomass (b) distributions for the various initial biomass distributions (Table C.1) and the fast continuous injection strategy.

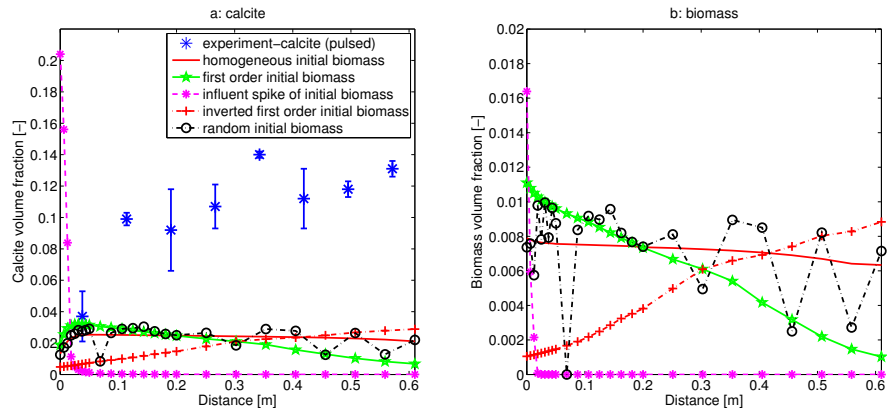


**Figure C.7.:** Comparison of the resulting calcite (a) and biomass (b) distributions for the various initial biomass distributions (Table C.1) and the continuous injection strategy.

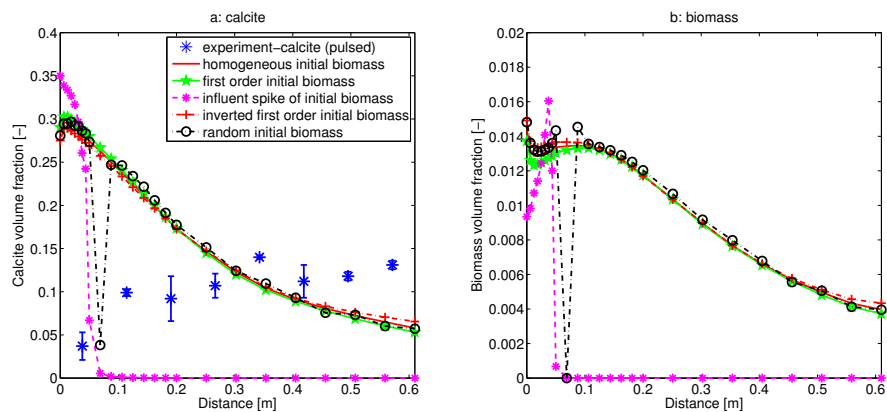


**Figure C.8.:** Comparison of the resulting calcite (a) and biomass (b) distributions for the various initial biomass distributions (Table C.1) and the slow continuous injection strategy.

**Table C.2.:** Impact of the initial biomass distribution, representing different attachment mechanisms, on the shape of the distribution of calcite measured by the shape coefficient  $\sigma_{5\text{ cm}}$  quantified as the ratio of the influent region calcite (at  $z = 0.05\text{ m}$ ) to the effluent region calcite (at  $z = 0.5075\text{ m}$ ). Thus high values indicate that the calcite distribution decreases with distance from the influent, while values close to 1 indicate evenly distributed calcite and values smaller than 1 indicate that the calcite is increasing with distance.

Injection strategy	Homogeneous $\phi_{f,0}$	First-order $\phi_{f,0}$	Influent spike $\phi_{f,0}$	Inverse first-order $\phi_{f,0}$	Random $\phi_{f,0}$
fast pulsed	0.46	0.50	10.34	0.43	0.55
pulsed	0.72	0.84	14.92	0.62	0.75
slow pulsed	3.89	4.23	39.31	3.60	3.67
fast continuous	1.00	1.02	5.42	1.01	1.34
continuous	1.10	3.06	54.68	0.28	1.10
slow continuous	3.80	4.08	2931	3.52	3.74

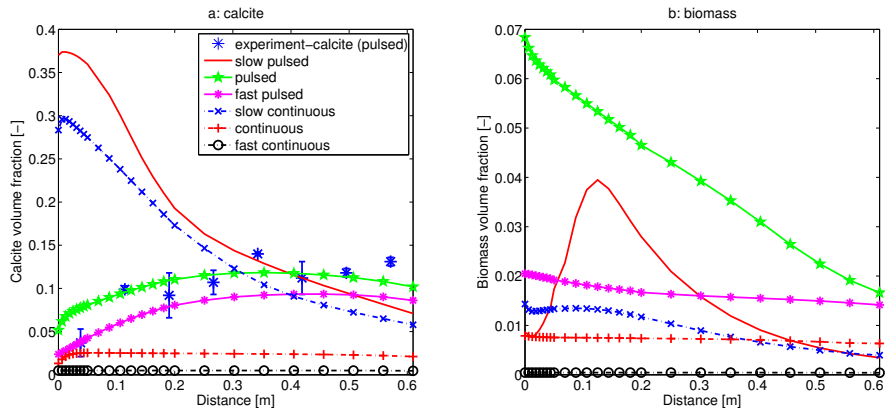


**Figure C.9.:** Comparison of the resulting calcite (a) and biomass (b) distributions for the homogeneous initial biomass distribution (Table C.1) and the various injection strategies investigated in this study.

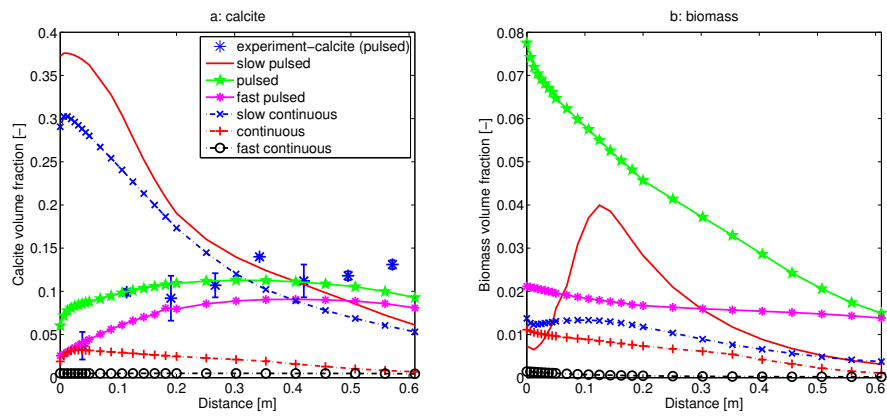


**Figure C.10.:** Comparison of the resulting calcite (a) and biomass (b) distributions for the first-order initial biomass distribution (Table C.1) and the various injection strategies investigated in this study.

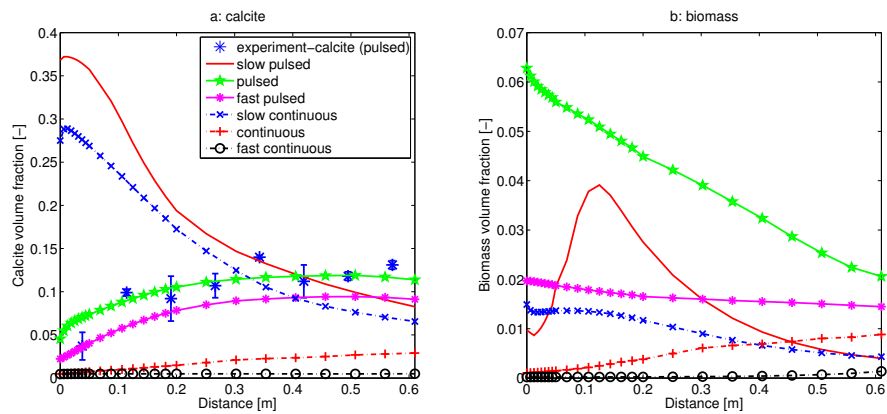


**Figure C.11.:** Comparison of the resulting calcite (a) and biomass (b) distributions for the inverse first-order initial biomass distribution (Table C.1) and the various injection strategies investigated in this study.

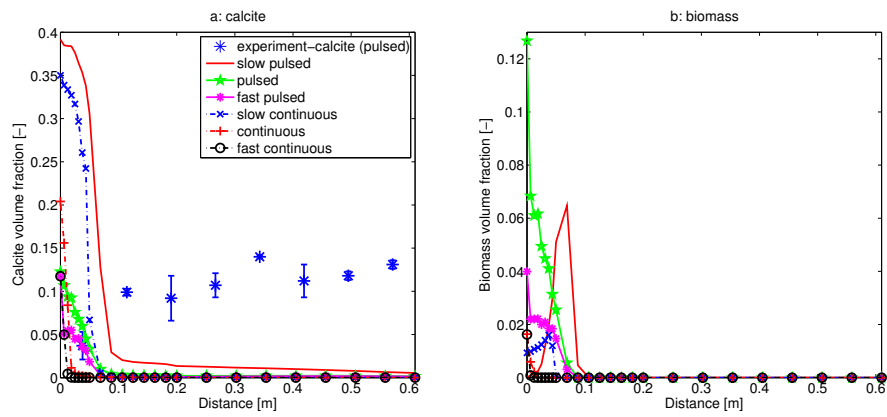


**Figure C.12.:** Comparison of the resulting calcite (a) and biomass (b) distributions for the “influent spike” initial biomass distribution (Table C.1) and the various injection strategies investigated in this study.

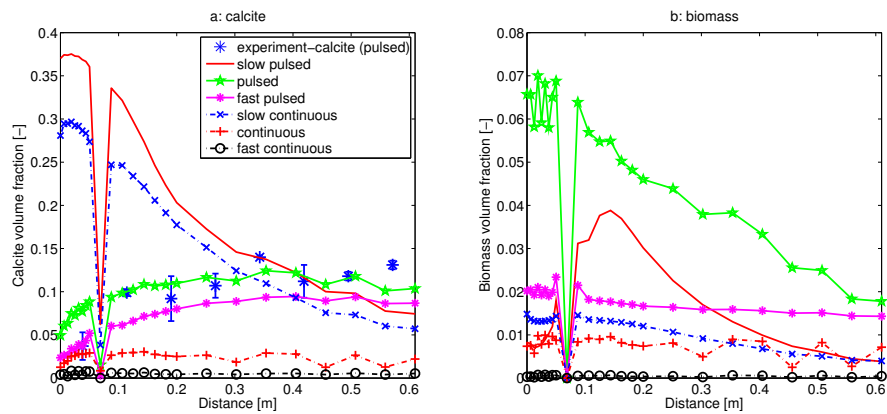


**Figure C.13.:** Comparison of the resulting calcite (a) and biomass (b) distributions for the random initial biomass distribution (Table C.1) and the various injection strategies investigated in this study.

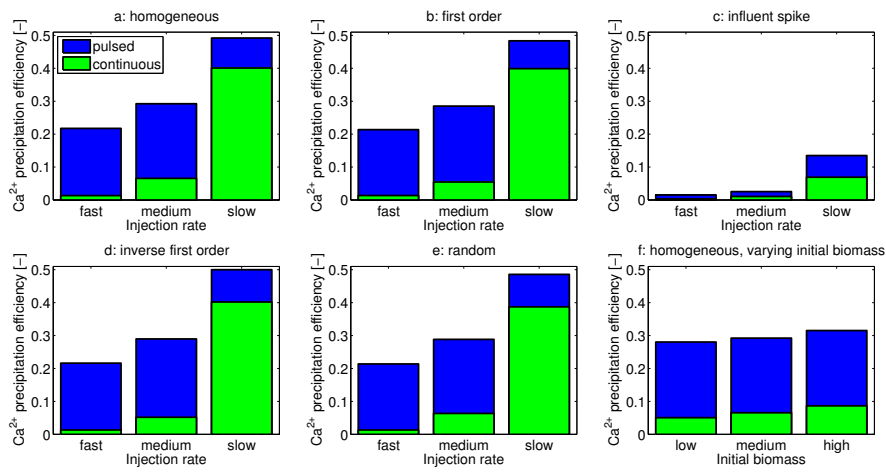


**Figure C.14.:** Ca<sup>2+</sup> precipitation efficiencies for all injection strategies and initial biomass distributions. The subfigures compare the precipitation efficiencies for the various injection strategies for one initial biomass distribution: (a) homogeneous, (b) first order, (c) influent spike, (d) inverse first-order, (e) random. Additionally, subfigure (f) compares the effect of varying initial amount of biomass on the Ca<sup>2+</sup> precipitation efficiency for the pulsed injection strategy and the homogeneous initial biomass distribution.

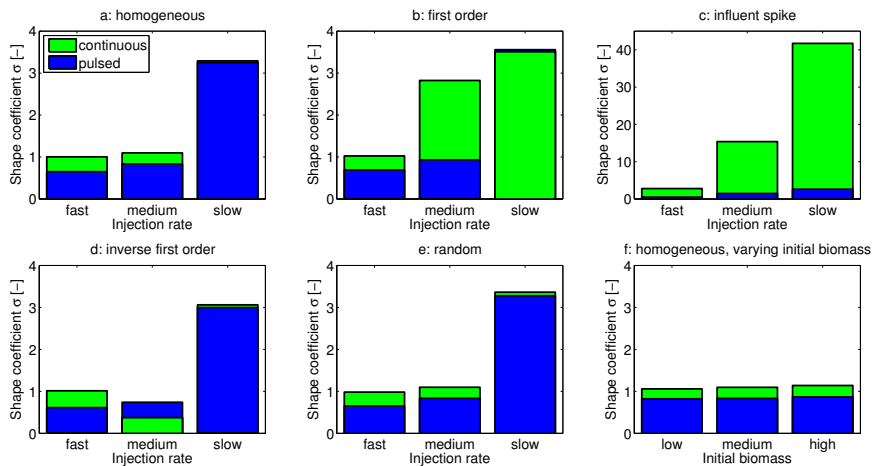


**Figure C.15.:** Shape coefficients  $\sigma$  for all injection strategies and initial biomass distributions. The subfigures compare  $\sigma$  for the various injection strategies for one initial biomass distribution: (a) homogeneous, (b) first order, (c) influent spike, (d) inverse first-order, (e) random. Additionally, subfigure (f) compares the effect of varying initial amount of biomass on  $\sigma$  for the pulsed injection strategy and the homogeneous initial biomass distribution.

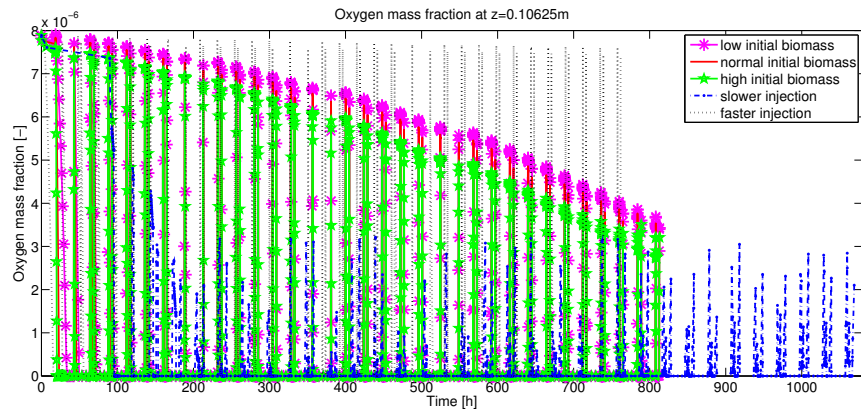


**Figure C.16.:** Oxygen mass fractions for homogeneous initial biomass distributions over time at  $z = 0.10625\text{m}$  distance from the injection for different initial amounts of biomass and injection rates.

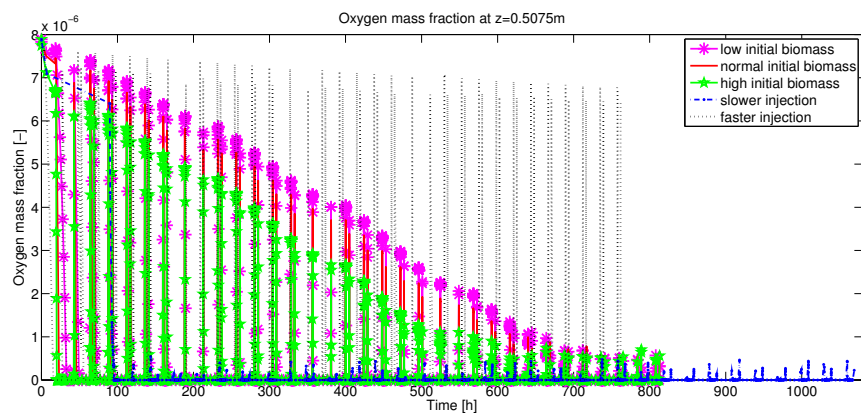


**Figure C.17.:** Oxygen mass fractions for homogeneous initial biomass distributions over time at  $z = 0.5075\text{m}$  distance from the injection for different initial amounts of biomass and injection rates.

## **D. Field scale simulation**

**Table D.1.:** Comparison of the preliminarily estimated parameters as used in *Shigorina* (2014) to the final parameters determined by *Hommel et al.* (2015b). All model parameters, which are not given here, are identical to the parameters in *Hommel et al.* (2015b), see Table 4.6. The scenario setup parameters deviating from those given in Table 4.6 are given in the second part of the table.

Parameter	Unit	<i>Hommel et al.</i> (2015b)	<i>Shigorina</i> (2014)
$\rho_f$	kg/m <sup>3</sup>	6.9	10
$c_{a,1}$	1/s	$8.3753 \cdot 10^{-8}$	$1.5 \cdot 10^{-5}$
$c_{a,2}$	1/s	$8.5114 \cdot 10^{-7}$	$5 \cdot 10^{-6}$
$k_{ub}$	-	$3.81 \cdot 10^{-4}$	0.0014
Assumed angle of injection		360°	only the 22.5° simulation domain
$\phi_0$	-		0.12
$\phi_{crit}$	-		0.10
$p_{w,0}$	Pa		$1.79 \cdot 10^6$
$K_0$	m <sup>2</sup>		$1.0856 \cdot 10^{-14}$
$K_{frac}$	m <sup>2</sup>		$1.645 \cdot 10^{-12}$
$X_{sal}$	kg/m <sup>3</sup>		24
$x_w^{Na} = x_w^{Cl}$	-		0.007
$x_w^{C_{tot}}$	-		$1.79 \cdot 10^{-7}$

This appendix contains the injection strategies considered in the field-scale modeling of MICP in the Tables D.2-D.4. As well as a summary of the differences in the parameters used in the simulations done by *Shigorina* (2014) and those using the “best fit” parameter set from *Hommel et al.* (2015b) in Table D.1. Table D.1 additionally summarizes the setup-specific porous medium properties and the values for boundary and initial conditions used. Figures D.1 and D.2 compare the simulation results for the simulations done by *Shigorina* (2014) and those using the “best fit” parameter set from *Hommel et al.* (2015b).

**Table D.2.:** Injection scheme for the *simple* injection strategy. The injection rate is constant for all injections  $Q = 1.0515 \cdot 10^{-5} \text{m}^3/\text{s}$ .

End time [h]	Injection	End time [h]	Injection
0.7	growth medium	60.4	growth medium
1.4	inoculation	69.4	no flow
9.4	no flow	82.4	calcium rich
21.4	growth medium	84.4	growth medium
34.4	calcium rich	93.4	no flow
36.4	growth medium	106.4	calcium rich
45.4	no flow	108.4	growth medium
58.4	calcium rich	117.4	no flow

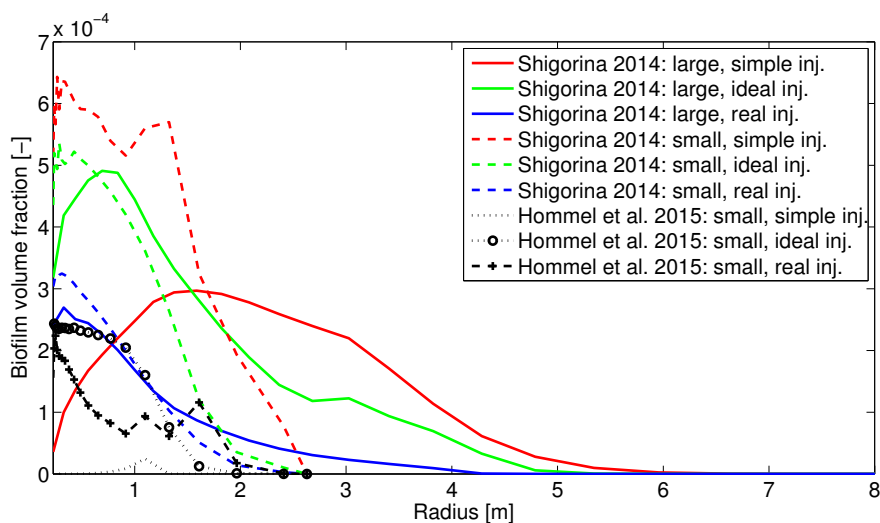


**Figure D.1.:** Biofilm distribution for the simulations done by *Shigorina* (2014) and using the parameter set from *Hommel et al.* (2015b). Note that in *Shigorina* (2014), the injections were erroneously assumed to enter the  $22.5^\circ$  simulation domain completely, leading to an 8-fold increased injection rate and total mass of injected components.

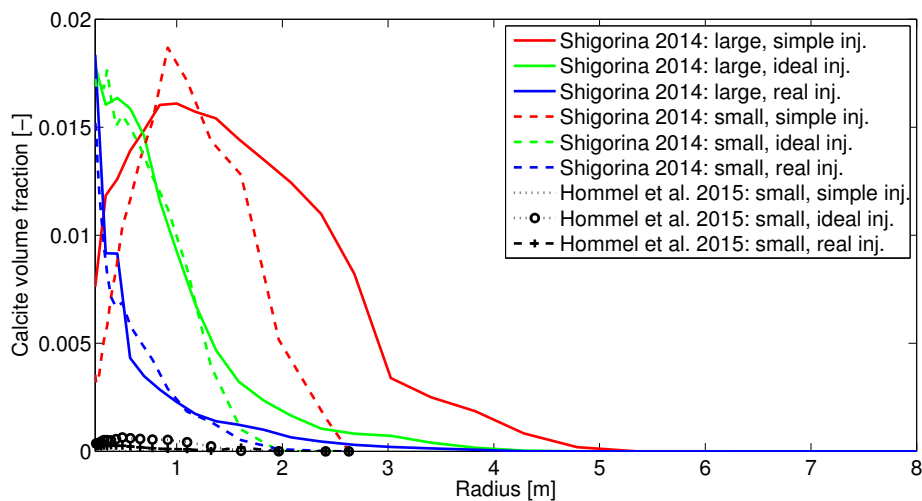


**Figure D.2.:** Precipitated calcite for the simulations done by *Shigorina* (2014) and using the parameter set from *Hommel et al.* (2015b). Note that in *Shigorina* (2014), the injections were erroneously assumed to enter the  $22.5^\circ$  simulation domain completely, leading to an 8-fold increased injection rate and total mass of injected components.

**Table D.3.:** Injection scheme for the *ideal* injection strategy.

End time [h]	Injection	Injection rate [ $\text{m}^3/\text{s}$ ]
1	growth medium	$7.886 \cdot 10^{-6}$
3	inoculation	$9.201 \cdot 10^{-6}$
3.5	no flow	0
4	rinse	$7.886 \cdot 10^{-6}$
4.1667	calcium rich	$5.520 \cdot 10^{-5}$
5	no flow	0
5.167	calcium rich	$5.520 \cdot 10^{-5}$
6	no flow	0
6.167	calcium rich	$5.520 \cdot 10^{-5}$
7	no flow	0
7.167	calcium rich	$5.520 \cdot 10^{-5}$
8	no flow	0
8.167	rinse	$2.366 \cdot 10^{-5}$
9.167	re-inoculation	$9.201 \cdot 10^{-6}$
21.167	no flow	0
21.417	rinse	$2.103 \cdot 10^{-5}$
21.583	calcium rich	$5.520 \cdot 10^{-5}$
22.417	no flow	0
22.583	calcium rich	$5.520 \cdot 10^{-5}$
23.417	no flow	0
23.583	calcium rich	$5.520 \cdot 10^{-5}$
24.417	no flow	0
24.583	calcium rich	$5.520 \cdot 10^{-5}$
26.417	no flow	0
26.667	rinse	$1.577 \cdot 10^{-5}$
26.917	re-inoculation	$3.680 \cdot 10^{-5}$
27.083	calcium rich	$5.520 \cdot 10^{-5}$
27.917	no flow	0
28.083	calcium rich	$5.520 \cdot 10^{-5}$
28.917	no flow	0
29.083	calcium rich	$5.520 \cdot 10^{-5}$
29.917	no flow	0
30.083	calcium rich	$5.520 \cdot 10^{-5}$
30.917	no flow	0

*Continued on next page*

Table D.3 – *Continued from previous page*

End time [h]	Injection	Injection rate $Q$ [ $\text{m}^3/\text{s}$ ]
31.083	calcium rich	$5.520 \cdot 10^{-5}$
31.917	no flow	0
32.083	calcium rich	$5.520 \cdot 10^{-5}$
32.917	no flow	0
33.167	rinse	$1.577 \cdot 10^{-5}$
33.417	re-inoculation	$3.680 \cdot 10^{-5}$
45.417	no flow	0
45.667	rinse	$2.103 \cdot 10^{-5}$
45.833	calcium rich	$5.520 \cdot 10^{-5}$
46.667	no flow	0
46.833	calcium rich	$5.520 \cdot 10^{-5}$
47.667	no flow	0
47.833	calcium rich	$5.520 \cdot 10^{-5}$
48.667	no flow	0
48.833	calcium rich	$5.520 \cdot 10^{-5}$
50.667	no flow	0
50.917	rinse	$1.577 \cdot 10^{-5}$
51.167	re-inoculation	$3.680 \cdot 10^{-5}$
51.333	calcium rich	$5.520 \cdot 10^{-5}$
52.167	no flow	0
52.333	calcium rich	$5.520 \cdot 10^{-5}$
53.167	no flow	0
53.333	calcium rich	$5.520 \cdot 10^{-5}$
54.167	no flow	0
54.333	calcium rich	$5.520 \cdot 10^{-5}$
55.167	no flow	0
55.333	calcium rich	$5.520 \cdot 10^{-5}$
56.167	no flow	0
56.333	calcium rich	$5.520 \cdot 10^{-5}$
57.167	no flow	0
57.417	rinse	$1.577 \cdot 10^{-5}$
57.667	re-inoculation	$3.680 \cdot 10^{-5}$
69.667	no flow	0
69.917	rinse	$2.103 \cdot 10^{-5}$
70.083	calcium rich	$5.520 \cdot 10^{-5}$

*Continued on next page*

Table D.3 – *Continued from previous page*

End time [h]	Injection	Injection rate $Q$ [ $\text{m}^3/\text{s}$ ]
70.917	no flow	0
71.083	calcium rich	$5.520 \cdot 10^{-5}$
71.917	no flow	0
72.083	calcium rich	$5.520 \cdot 10^{-5}$
72.917	no flow	0
73.083	calcium rich	$5.520 \cdot 10^{-5}$
74.917	no flow	0
75.167	rinse	$1.577 \cdot 10^{-5}$
75.417	re-inoculation	$3.680 \cdot 10^{-5}$
75.583	calcium rich	$5.520 \cdot 10^{-5}$
76.417	no flow	0
76.583	calcium rich	$5.520 \cdot 10^{-5}$
77.417	no flow	0
77.583	calcium rich	$5.520 \cdot 10^{-5}$
78.417	no flow	0
78.583	calcium rich	$5.520 \cdot 10^{-5}$
79.417	no flow	0
79.583	calcium rich	$5.520 \cdot 10^{-5}$
80.417	no flow	0
80.583	calcium rich	$5.520 \cdot 10^{-5}$
81.417	no flow	0
93.417	no flow	0

**Table D.4.:** Injection scheme for the *real* injection strategy.

End time [h]	Injection	Injection rate [ $\text{m}^3/\text{s}$ ]	Dilution [-]
0.083	growth medium	$3.15 \cdot 10^{-5}$	0.273
0.25	inoculation	$3.15 \cdot 10^{-5}$	0.273
0.292	no flow	0	
0.333	rinse	$3.15 \cdot 10^{-5}$	0.273
1.167	no flow	0	
1.5	calcium rich	$3.15 \cdot 10^{-5}$	0.273
1.75	no flow	0	
2.083	brine	$3.15 \cdot 10^{-5}$	0.273
2.183	no flow	0	

*Continued on next page*

Table D.4 – *Continued from previous page*

End time [h]	Injection	Injection rate $Q$ [ $\text{m}^3/\text{s}$ ]	Dilution [-]
2.517	calcium rich	$3.15 \cdot 10^{-5}$	0.273
2.85	no flow	0	
3.183	calcium rich	$3.15 \cdot 10^{-5}$	0.273
3.717	no flow	0	
4.05	re-inoculation	$3.15 \cdot 10^{-5}$	0.273
18.8	no flow	0	
18.967	calcium rich	$3.15 \cdot 10^{-5}$	0.429
19.667	no flow	0	
19.9	calcium rich	$3.28 \cdot 10^{-5}$	0.340
20.217	no flow	0	
20.383	calcium rich	$3.15 \cdot 10^{-5}$	0.429
22.233	no flow	0	
22.35	brine	$3.15 \cdot 10^{-5}$	0.517
22.7	no flow	0	
22.933	calcium rich	$3.15 \cdot 10^{-5}$	0.349
23.317	no flow	0	
23.55	calcium rich	$3.15 \cdot 10^{-5}$	0.349
23.8	no flow	0	
24.133	calcium rich	$3.15 \cdot 10^{-5}$	0.185
24.45	no flow	0	
24.783	re-inoculation	$2.84 \cdot 10^{-5}$	0.2
41.233	no flow	0	
41.25	calcium rich	$3.15 \cdot 10^{-5}$	0.24
41.467	calcium rich	$3.15 \cdot 10^{-5}$	0.24
41.767	no flow	0	
42	calcium rich	$3.15 \cdot 10^{-5}$	0.24
42.333	no flow	0	
42.567	calcium rich	$2.84 \cdot 10^{-5}$	0.258
42.85	no flow	0	
43.083	calcium rich	$2.52 \cdot 10^{-5}$	0.279
43.483	no flow	0	
43.65	calcium rich	$3.15 \cdot 10^{-5}$	0.3
43.917	no flow	0	
44.25	calcium rich	$3.15 \cdot 10^{-5}$	0.185
44.6	no flow	0	

*Continued on next page*

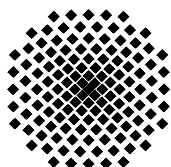
Table D.4 – *Continued from previous page*

End time [h]	Injection	Injection rate $Q$ [ $\text{m}^3/\text{s}$ ]	Dilution [-]
44.9	re-inoculation	$3.15 \cdot 10^{-5}$	0.2
45.133	calcium rich	$3.15 \cdot 10^{-5}$	0.24
45.45	no flow	0	
45.683	calcium rich	$3.15 \cdot 10^{-5}$	0.24
45.917	no flow	0	
46.15	calcium rich	$3.15 \cdot 10^{-5}$	0.24
46.4	no flow	0	
46.633	calcium rich	$3.15 \cdot 10^{-5}$	0.24
46.883	no flow	0	
47.083	calcium rich	$3.15 \cdot 10^{-5}$	0.267
47.35	no flow	0	
47.583	calcium rich	$3.15 \cdot 10^{-5}$	0.24
47.817	no flow	0	
48.15	calcium rich	$3.15 \cdot 10^{-5}$	0.185
48.35	no flow	0	
48.533	re-inoculation	$3.15 \cdot 10^{-5}$	0.282
67.483	no flow	0	
67.675	calcium rich	$8.83 \cdot 10^{-6}$	0.521
67.758	no flow	0	
67.788	calcium rich	$8.83 \cdot 10^{-6}$	0.740
67.871	no flow	0	
67.903	calcium rich	$8.83 \cdot 10^{-6}$	0.735
67.986	no flow	0	
68.015	calcium rich	$8.83 \cdot 10^{-6}$	0.740
68.098	no flow	0	
68.128	calcium rich	$8.83 \cdot 10^{-6}$	0.738
68.212	no flow	0	
68.288	calcium rich	$8.83 \cdot 10^{-6}$	0.659
69.419	no flow	0	
69.469	calcium rich	$8.83 \cdot 10^{-6}$	0.702
69.553	no flow	0	
69.594	calcium rich	$8.83 \cdot 10^{-6}$	0.716
69.678	no flow	0	
69.719	calcium rich	$8.83 \cdot 10^{-6}$	0.716
69.803	no flow	0	

*Continued on next page*

Table D.4 – *Continued from previous page*

End time [h]	Injection	Injection rate $Q$ [ $\text{m}^3/\text{s}$ ]	Dilution [-]
69.844	calcium rich	$8.83 \cdot 10^{-6}$	0.716
69.928	no flow	0	
69.978	calcium rich	$8.83 \cdot 10^{-6}$	0.702
71.061	no flow	0	
71.149	re-inoculation	$8.83 \cdot 10^{-6}$	0.641
71.233	no flow	0	
71.256	re-inoculation	$8.83 \cdot 10^{-6}$	0.751
71.339	no flow	0	
71.363	re-inoculation	$8.83 \cdot 10^{-6}$	0.751
71.446	no flow	0	
71.466	re-inoculation	$8.83 \cdot 10^{-6}$	0.758
71.549	no flow	0	
71.571	re-inoculation	$8.83 \cdot 10^{-6}$	0.754
71.654	no flow	0	
71.67	re-inoculation	$8.83 \cdot 10^{-6}$	0.766
71.753	no flow	0	
71.837	back flow, sampling	$-8.83 \cdot 10^{-6}$	
71.92	no flow	0	
71.943	re-inoculation	$8.83 \cdot 10^{-6}$	0.751
72.027	no flow	0	
72.052	re-inoculation	$8.83 \cdot 10^{-6}$	0.748
73.618	no flow	0	
73.735	calcium rich	$8.83 \cdot 10^{-6}$	0.603
73.818	no flow	0	
73.839	calcium rich	$8.83 \cdot 10^{-6}$	0.756
73.923	no flow	0	
73.945	calcium rich	$8.83 \cdot 10^{-6}$	0.753
74.028	no flow	0	
74.050	calcium rich	$8.83 \cdot 10^{-6}$	0.753
74.134	no flow	0	
74.154	calcium rich	$8.83 \cdot 10^{-6}$	0.756
74.238	no flow	0	
74.26	calcium rich	$8.83 \cdot 10^{-6}$	0.753



## Institut für Wasser- und Umweltsystemmodellierung Universität Stuttgart

Pfaffenwaldring 61  
70569 Stuttgart (Vaihingen)  
Telefon (0711) 685 - 64717/64749/64752/64679  
Telefax (0711) 685 - 67020 o. 64746 o. 64681  
E-Mail: [iws@iws.uni-stuttgart.de](mailto:iws@iws.uni-stuttgart.de)  
<http://www.iws.uni-stuttgart.de>

### Direktoren

Prof. Dr. rer. nat. Dr.-Ing. András Bárdossy  
Prof. Dr.-Ing. Rainer Helmig  
Prof. Dr.-Ing. Silke Wieprecht  
Prof. Dr.-Ing. Wolfgang Nowak

### Vorstand (Stand 1.3.2016)

Prof. Dr. rer. nat. Dr.-Ing. A. Bárdossy  
Prof. Dr.-Ing. R. Helmig  
Prof. Dr.-Ing. S. Wieprecht  
Prof. Dr. J.A. Sander Huisman  
Jürgen Braun, PhD  
apl. Prof. Dr.-Ing. H. Class  
Dr.-Ing. H.-P. Koschitzky  
Dr.-Ing. M. Noack  
Prof. Dr.-Ing. W. Nowak  
Dr. rer. nat. J. Seidel  
Dr.-Ing. K. Terheiden  
Dr.-Ing. habil. Sergey Oladyshkin

### Emeriti

Prof. Dr.-Ing. habil. Dr.-Ing. E.h. Jürgen Giesecke  
Prof. Dr.h.c. Dr.-Ing. E.h. Helmut Kobus, PhD

### Lehrstuhl für Wasserbau und Wassermengenwirtschaft

Leiter: Prof. Dr.-Ing. Silke Wieprecht  
Stellv.: Dr.-Ing. Kristina Terheiden  
**Versuchsanstalt für Wasserbau**  
Leiter: Dr.-Ing. Markus Noack

### Lehrstuhl für Hydromechanik und Hydrosystemmodellierung

Leiter: Prof. Dr.-Ing. Rainer Helmig  
Stellv.: apl. Prof. Dr.-Ing. Holger Class

### Lehrstuhl für Hydrologie und Geohydrologie

Leiter: Prof. Dr. rer. nat. Dr.-Ing. András Bárdossy  
Stellv.: Dr. rer. nat. Jochen Seidel  
**Hydrogeophysik der Vadosen Zone**  
(mit Forschungszentrum Jülich)  
Leiter: Prof. Dr. J.A. Sander Huisman

### Lehrstuhl für Stochastische Simulation und Sicherheitsforschung für Hydrosysteme

Leiter: Prof. Dr.-Ing. Wolfgang Nowak  
Stellv.: Dr.-Ing. habil. Sergey Oladyshkin

### VEGAS, Versuchseinrichtung zur Grundwasser- und Altlastensanierung

Leitung: Jürgen Braun, PhD, AD  
Dr.-Ing. Hans-Peter Koschitzky, AD

## Verzeichnis der Mitteilungshefte

- 1 Röhnisch, Arthur: *Die Bemühungen um eine Wasserbauliche Versuchsanstalt an der Technischen Hochschule Stuttgart*, und Fattah Abouleid, Abdel: *Beitrag zur Berechnung einer in lockeren Sand gerammten, zweifach verankerten Spundwand*, 1963
- 2 Marotz, Günter: *Beitrag zur Frage der Standfestigkeit von dichten Asphaltbelägen im Großwasserbau*, 1964
- 3 Gurr, Siegfried: *Beitrag zur Berechnung zusammengesetzter ebener Flächentragwerke unter besonderer Berücksichtigung ebener Stauwände, mit Hilfe von Randwert- und Lastwertmatrizen*, 1965
- 4 Plica, Peter: *Ein Beitrag zur Anwendung von Schalenkonstruktionen im Stahlwasserbau*, und

- Petrikat, Kurt: *Möglichkeiten und Grenzen des wasserbaulichen Versuchswesens*, 1966
- 5 Plate, Erich: *Beitrag zur Bestimmung der Windgeschwindigkeitsverteilung in der durch eine Wand gestörten bodennahen Luftschicht*, und  
Röhnisch, Arthur; Marotz, Günter: *Neue Baustoffe und Bauausführungen für den Schutz der Böschungen und der Sohle von Kanälen, Flüssen und Häfen; Gesteungskosten und jeweilige Vorteile*, sowie  
Unny, T.E.: *Schwingungsuntersuchungen am Kegelstrahlschieber*, 1967
- 6 Seiler, Erich: *Die Ermittlung des Anlagenwertes der bundeseigenen Binnenschiffahrtsstraßen und Talsperren und des Anteils der Binnenschifffahrt an diesem Wert*, 1967
- 7 *Sonderheft anlässlich des 65. Geburtstages von Prof. Arthur Röhnisch mit Beiträgen von* Benk, Dieter; Breitling, J.; Gurr, Siegfried; Haberhauer, Robert; Honekamp, Hermann; Kuz, Klaus Dieter; Marotz, Günter; Mayer-Vorfelder, Hans-Jörg; Miller, Rudolf; Plate, Erich J.; Radomski, Helge; Schwarz, Helmut; Vollmer, Ernst; Wildenhahn, Eberhard; 1967
- 8 Jumikis, Alfred: *Beitrag zur experimentellen Untersuchung des Wassernachschubs in einem gefrierenden Boden und die Beurteilung der Ergebnisse*, 1968
- 9 Marotz, Günter: *Technische Grundlagen einer Wasserspeicherung im natürlichen Untergrund*, 1968
- 10 Radomski, Helge: *Untersuchungen über den Einfluß der Querschnittsform wellenförmiger Spundwände auf die statischen und rammtechnischen Eigenschaften*, 1968
- 11 Schwarz, Helmut: *Die Grenztragfähigkeit des Baugrundes bei Einwirkung vertikal gezogener Ankerplatten als zweidimensionales Bruchproblem*, 1969
- 12 Erbel, Klaus: *Ein Beitrag zur Untersuchung der Metamorphose von Mittelgebirgsschneedecken unter besonderer Berücksichtigung eines Verfahrens zur Bestimmung der thermischen Schneequalität*, 1969
- 13 Westhaus, Karl-Heinz: *Der Strukturwandel in der Binnenschifffahrt und sein Einfluß auf den Ausbau der Binnenschiffskanäle*, 1969
- 14 Mayer-Vorfelder, Hans-Jörg: *Ein Beitrag zur Berechnung des Erdwiderstandes unter Ansatz der logarithmischen Spirale als Gleitflächenfunktion*, 1970
- 15 Schulz, Manfred: *Berechnung des räumlichen Erddruckes auf die Wandung kreiszylindrischer Körper*, 1970
- 16 Mobasseri, Manoutschehr: *Die Rippenstützmauer. Konstruktion und Grenzen ihrer Standsicherheit*, 1970
- 17 Benk, Dieter: *Ein Beitrag zum Betrieb und zur Bemessung von Hochwasserrück-*

- haltebecken*, 1970
- 18 Gál, Attila: *Bestimmung der mitschwingenden Wassermasse bei überströmten Fischbauchklappen mit kreiszylindrischem Staublech*, 1971, vergriffen
- 19 Kuz, Klaus Dieter: *Ein Beitrag zur Frage des Einsetzens von Kavitationserscheinungen in einer Düsenströmung bei Berücksichtigung der im Wasser gelösten Gase*, 1971, vergriffen
- 20 Schaak, Hartmut: *Verteilleitungen von Wasserkraftanlagen*, 1971
- 21 *Sonderheft zur Eröffnung der neuen Versuchsanstalt des Instituts für Wasserbau der Universität Stuttgart mit Beiträgen von* Brombach, Hansjörg; Dirksen, Wolfram; Gál, Attila; Gerlach, Reinhard; Giesecke, Jürgen; Holthoff, Franz-Josef; Kuz, Klaus Dieter; Marotz, Günter; Minor, Hans-Erwin; Petrikat, Kurt; Röhnisch, Arthur; Rueff, Helge; Schwarz, Helmut; Vollmer, Ernst; Wildenhahn, Eberhard; 1972
- 22 Wang, Chung-su: *Ein Beitrag zur Berechnung der Schwingungen an Kegelstrahlschiebern*, 1972
- 23 Mayer-Vorfelder, Hans-Jörg: *Erdwiderstandsbeiwerte nach dem Ohde-Variationsverfahren*, 1972
- 24 Minor, Hans-Erwin: *Beitrag zur Bestimmung der Schwingungsanfachungsfunktionen überströmter Stauklappen*, 1972, vergriffen
- 25 Brombach, Hansjörg: *Untersuchung strömungsmechanischer Elemente (Fluidik) und die Möglichkeit der Anwendung von Wirbelkammerelementen im Wasserbau*, 1972, vergriffen
- 26 Wildenhahn, Eberhard: *Beitrag zur Berechnung von Horizontalfilterbrunnen*, 1972
- 27 Steinlein, Helmut: *Die Eliminierung der Schwebstoffe aus Flußwasser zum Zweck der unterirdischen Wasserspeicherung, gezeigt am Beispiel der Iller*, 1972
- 28 Holthoff, Franz Josef: *Die Überwindung großer Hubhöhen in der Binnenschifffahrt durch Schwimmerhebwerke*, 1973
- 29 Röder, Karl: *Einwirkungen aus Baugrundbewegungen auf trog- und kastenförmige Konstruktionen des Wasser- und Tunnelbaues*, 1973
- 30 Kretschmer, Heinz: *Die Bemessung von Bogenstaumauern in Abhängigkeit von der Talform*, 1973
- 31 Honekamp, Hermann: *Beitrag zur Berechnung der Montage von Unterwasserpipelines*, 1973
- 32 Giesecke, Jürgen: *Die Wirbelkammertriode als neuartiges Steuerorgan im Wasserbau*, und  
Brombach, Hansjörg: *Entwicklung, Bauformen, Wirkungsweise und Steuereigenschaften von Wirbelkammerverstärkern*, 1974

- 33 Rueff, Helge: *Untersuchung der schwingungserregenden Kräfte an zwei hintereinander angeordneten Tiefschützen unter besonderer Berücksichtigung von Kavitation*, 1974
- 34 Röhnisch, Arthur: *Einpreßversuche mit Zementmörtel für Spannbeton - Vergleich der Ergebnisse von Modellversuchen mit Ausführungen in Hüllwellrohren*, 1975
- 35 *Sonderheft anlässlich des 65. Geburtstages von Prof. Dr.-Ing. Kurt Petrikat mit Beiträgen von:* Brombach, Hansjörg; Erbel, Klaus; Flinspach, Dieter; Fischer jr., Richard; Gàl, Attila; Gerlach, Reinhard; Giesecke, Jürgen; Haberhauer, Robert; Hafner Edzard; Hausenblas, Bernhard; Horlacher, Hans-Burkhard; Hutarew, Andreas; Knoll, Manfred; Krummet, Ralph; Marotz, Günter; Merkle, Theodor; Miller, Christoph; Minor, Hans-Erwin; Neumayer, Hans; Rao, Syamala; Rath, Paul; Rueff, Helge; Ruppert, Jürgen; Schwarz, Wolfgang; Topal-Gökceli, Mehmet; Vollmer, Ernst; Wang, Chung-su; Weber, Hans-Georg; 1975
- 36 Berger, Jochum: *Beitrag zur Berechnung des Spannungszustandes in rotations-symmetrisch belasteten Kugelschalen veränderlicher Wandstärke unter Gas- und Flüssigkeitsdruck durch Integration schwach singulärer Differentialgleichungen*, 1975
- 37 Dirksen, Wolfram: *Berechnung instationärer Abflußvorgänge in gestauten Gerinnen mittels Differenzenverfahren und die Anwendung auf Hochwasserrückhaltebecken*, 1976
- 38 Horlacher, Hans-Burkhard: *Berechnung instationärer Temperatur- und Wärmespannungsfelder in langen mehrschichtigen Hohlzylindern*, 1976
- 39 Hafner, Edzard: *Untersuchung der hydrodynamischen Kräfte auf Baukörper im Tiefwasserbereich des Meeres*, 1977, ISBN 3-921694-39-6
- 40 Ruppert, Jürgen: *Über den Axialwirbelkammverstärker für den Einsatz im Wasserbau*, 1977, ISBN 3-921694-40-X
- 41 Hutarew, Andreas: *Beitrag zur Beeinflußbarkeit des Sauerstoffgehalts in Fließgewässern an Abstürzen und Wehren*, 1977, ISBN 3-921694-41-8, vergriffen
- 42 Miller, Christoph: *Ein Beitrag zur Bestimmung der schwingungserregenden Kräfte an unterströmten Wehren*, 1977, ISBN 3-921694-42-6
- 43 Schwarz, Wolfgang: *Druckstoßberechnung unter Berücksichtigung der Radial- und Längsverschiebungen der Rohrwandung*, 1978, ISBN 3-921694-43-4
- 44 Kinzelbach, Wolfgang: *Numerische Untersuchungen über den optimalen Einsatz variabler Kühlsysteme einer Kraftwerkskette am Beispiel Oberrhein*, 1978, ISBN 3-921694-44-2
- 45 Barczewski, Baldur: *Neue Meßmethoden für Wasser-Luftgemische und deren Anwendung auf zweiphasige Auftriebsstrahlen*, 1979, ISBN 3-921694-45-0

- 46 Neumayer, Hans: *Untersuchung der Strömungsvorgänge in radialen Wirbelkammerverstärkern*, 1979, ISBN 3-921694-46-9
- 47 Elalfy, Youssef-Elhassan: *Untersuchung der Strömungsvorgänge in Wirbelkammerdioden und -drosseln*, 1979, ISBN 3-921694-47-7
- 48 Brombach, Hansjörg: *Automatisierung der Bewirtschaftung von Wasserspeichern*, 1981, ISBN 3-921694-48-5
- 49 Geldner, Peter: *Deterministische und stochastische Methoden zur Bestimmung der Selbstdichtung von Gewässern*, 1981, ISBN 3-921694-49-3, vergriffen
- 50 Mehlhorn, Hans: *Temperaturveränderungen im Grundwasser durch Brauchwasserreinleitungen*, 1982, ISBN 3-921694-50-7, vergriffen
- 51 Hafner, Edzard: *Rohrleitungen und Behälter im Meer*, 1983, ISBN 3-921694-51-5
- 52 Rinnert, Bernd: *Hydrodynamische Dispersion in porösen Medien: Einfluß von Dichteunterschieden auf die Vertikalvermischung in horizontaler Strömung*, 1983, ISBN 3-921694-52-3, vergriffen
- 53 Lindner, Wulf: *Steuerung von Grundwasserentnahmen unter Einhaltung ökologischer Kriterien*, 1983, ISBN 3-921694-53-1, vergriffen
- 54 Herr, Michael; Herzer, Jörg; Kinzelbach, Wolfgang; Kobus, Helmut; Rinnert, Bernd: *Methoden zur rechnerischen Erfassung und hydraulischen Sanierung von Grundwasserkontaminationen*, 1983, ISBN 3-921694-54-X
- 55 Schmitt, Paul: *Wege zur Automatisierung der Niederschlagsermittlung*, 1984, ISBN 3-921694-55-8, vergriffen
- 56 Müller, Peter: *Transport und selektive Sedimentation von Schwebstoffen bei gestautem Abfluß*, 1985, ISBN 3-921694-56-6
- 57 El-Qawasmeh, Fuad: *Möglichkeiten und Grenzen der Tropfbewässerung unter besonderer Berücksichtigung der Verstopfungsanfälligkeit der Tropfelemente*, 1985, ISBN 3-921694-57-4, vergriffen
- 58 Kirchenbaur, Klaus: *Mikroprozessorgesteuerte Erfassung instationärer Druckfelder am Beispiel seegangsbelasteter Baukörper*, 1985, ISBN 3-921694-58-2
- 59 Kobus, Helmut (Hrsg.): *Modellierung des großräumigen Wärme- und Schadstofftransports im Grundwasser*, Tätigkeitsbericht 1984/85 (DFG-Forschergruppe an den Universitäten Hohenheim, Karlsruhe und Stuttgart), 1985, ISBN 3-921694-59-0, vergriffen
- 60 Spitz, Karlheinz: *Dispersion in porösen Medien: Einfluß von Inhomogenitäten und Dichteunterschieden*, 1985, ISBN 3-921694-60-4, vergriffen
- 61 Kobus, Helmut: *An Introduction to Air-Water Flows in Hydraulics*, 1985, ISBN 3-921694-61-2

- 62 Kaleris, Vassilios: *Erfassung des Austausches von Oberflächen- und Grundwasser in horizontalebene Grundwassermodellen*, 1986, ISBN 3-921694-62-0
- 63 Herr, Michael: *Grundlagen der hydraulischen Sanierung verunreinigter Porengrundwasserleiter*, 1987, ISBN 3-921694-63-9
- 64 Marx, Walter: *Berechnung von Temperatur und Spannung in Massenbeton infolge Hydratation*, 1987, ISBN 3-921694-64-7
- 65 Koschitzky, Hans-Peter: *Dimensionierungskonzept für Sohlbelüfter in Schußrinnen zur Vermeidung von Kavitationsschäden*, 1987, ISBN 3-921694-65-5
- 66 Kobus, Helmut (Hrsg.): *Modellierung des großräumigen Wärme- und Schadstofftransports im Grundwasser*, Tätigkeitsbericht 1986/87 (DFG-Forschergruppe an den Universitäten Hohenheim, Karlsruhe und Stuttgart) 1987, ISBN 3-921694-66-3
- 67 Söll, Thomas: *Berechnungsverfahren zur Abschätzung anthropogener Temperaturanomalien im Grundwasser*, 1988, ISBN 3-921694-67-1
- 68 Dittrich, Andreas; Westrich, Bernd: *Bodenseeufererosion, Bestandsaufnahme und Bewertung*, 1988, ISBN 3-921694-68-X, vergriffen
- 69 Huwe, Bernd; van der Ploeg, Rienk R.: *Modelle zur Simulation des Stickstoffhaushaltes von Standorten mit unterschiedlicher landwirtschaftlicher Nutzung*, 1988, ISBN 3-921694-69-8, vergriffen
- 70 Stephan, Karl: *Integration elliptischer Funktionen*, 1988, ISBN 3-921694-70-1
- 71 Kobus, Helmut; Zilliox, Lothaire (Hrsg.): *Nitratbelastung des Grundwassers, Auswirkungen der Landwirtschaft auf die Grundwasser- und Rohwasserbeschaffenheit und Maßnahmen zum Schutz des Grundwassers*. Vorträge des deutsch-französischen Kolloquiums am 6. Oktober 1988, Universitäten Stuttgart und Louis Pasteur Strasbourg (Vorträge in deutsch oder französisch, Kurzfassungen zweisprachig), 1988, ISBN 3-921694-71-X
- 72 Soyeaux, Renald: *Unterströmung von Stauanlagen auf klüftigem Untergrund unter Berücksichtigung laminarer und turbulenter Fließzustände*, 1991, ISBN 3-921694-72-8
- 73 Kohane, Roberto: *Berechnungsmethoden für Hochwasserabfluß in Fließgewässern mit überströmten Vorländern*, 1991, ISBN 3-921694-73-6
- 74 Hassinger, Reinhard: *Beitrag zur Hydraulik und Bemessung von Blocksteinrampen in flexibler Bauweise*, 1991, ISBN 3-921694-74-4, vergriffen
- 75 Schäfer, Gerhard: *Einfluß von Schichtenstrukturen und lokalen Einlagerungen auf die Längsdispersion in Porengrundwasserleitern*, 1991, ISBN 3-921694-75-2
- 76 Giesecke, Jürgen: *Vorträge, Wasserwirtschaft in stark besiedelten Regionen; Umweltforschung mit Schwerpunkt Wasserwirtschaft*, 1991, ISBN 3-921694-76-0

- 77 Huwe, Bernd: *Deterministische und stochastische Ansätze zur Modellierung des Stickstoffhaushalts landwirtschaftlich genutzter Flächen auf unterschiedlichem Skalenniveau*, 1992, ISBN 3-921694-77-9, vergriffen
- 78 Rommel, Michael: *Verwendung von Kluftdaten zur realitätsnahen Generierung von Kluftnetzen mit anschließender laminar-turbulenter Strömungsberechnung*, 1993, ISBN 3-92 1694-78-7
- 79 Marschall, Paul: *Die Ermittlung lokaler Stofffrachten im Grundwasser mit Hilfe von Einbohrloch-Meßverfahren*, 1993, ISBN 3-921694-79-5, vergriffen
- 80 Ptak, Thomas: *Stofftransport in heterogenen Porenaquiferen: Felduntersuchungen und stochastische Modellierung*, 1993, ISBN 3-921694-80-9, vergriffen
- 81 Haakh, Frieder: *Transientes Strömungsverhalten in Wirbelkammern*, 1993, ISBN 3-921694-81-7
- 82 Kobus, Helmut; Cirpka, Olaf; Barczewski, Baldur; Koschitzky, Hans-Peter: *Versucheinrichtung zur Grundwasser und Altlastensanierung VEGAS, Konzeption und Programmrahmen*, 1993, ISBN 3-921694-82-5
- 83 Zang, Weidong: *Optimaler Echtzeit-Betrieb eines Speichers mit aktueller Abflußregenerierung*, 1994, ISBN 3-921694-83-3, vergriffen
- 84 Franke, Hans-Jörg: *Stochastische Modellierung eines flächenhaften Stoffeintrages und Transports in Grundwasser am Beispiel der Pflanzenschutzmittelproblematik*, 1995, ISBN 3-921694-84-1
- 85 Lang, Ulrich: *Simulation regionaler Strömungs- und Transportvorgänge in Karst-aquiferen mit Hilfe des Doppelkontinuum-Ansatzes: Methodenentwicklung und Parameteridentifikation*, 1995, ISBN 3-921694-85-X, vergriffen
- 86 Helmig, Rainer: *Einführung in die Numerischen Methoden der Hydromechanik*, 1996, ISBN 3-921694-86-8, vergriffen
- 87 Cirpka, Olaf: *CONTRACT: A Numerical Tool for Contaminant Transport and Chemical Transformations - Theory and Program Documentation -*, 1996, ISBN 3-921694-87-6
- 88 Haberlandt, Uwe: *Stochastische Synthese und Regionalisierung des Niederschlages für Schmutzfrachtberechnungen*, 1996, ISBN 3-921694-88-4
- 89 Croisé, Jean: *Extraktion von flüchtigen Chemikalien aus natürlichen Lockergesteinen mittels erzwungener Luftströmung*, 1996, ISBN 3-921694-89-2, vergriffen
- 90 Jorde, Klaus: *Ökologisch begründete, dynamische Mindestwasserregelungen bei Ausleitungskraftwerken*, 1997, ISBN 3-921694-90-6, vergriffen
- 91 Helmig, Rainer: *Gekoppelte Strömungs- und Transportprozesse im Untergrund - Ein Beitrag zur Hydrosystemmodellierung-*, 1998, ISBN 3-921694-91-4, vergriffen

- 92 Emmert, Martin: *Numerische Modellierung nichtisothermer Gas-Wasser Systeme in porösen Medien*, 1997, ISBN 3-921694-92-2
- 93 Kern, Ulrich: *Transport von Schweb- und Schadstoffen in staugeregelten Fließgewässern am Beispiel des Neckars*, 1997, ISBN 3-921694-93-0, vergriffen
- 94 Förster, Georg: *Druckstoßdämpfung durch große Luftblasen in Hochpunkten von Rohrleitungen* 1997, ISBN 3-921694-94-9
- 95 Cirpka, Olaf: *Numerische Methoden zur Simulation des reaktiven Mehrkomponententransports im Grundwasser*, 1997, ISBN 3-921694-95-7, vergriffen
- 96 Färber, Arne: *Wärmetransport in der ungesättigten Bodenzone: Entwicklung einer thermischen In-situ-Sanierungstechnologie*, 1997, ISBN 3-921694-96-5
- 97 Betz, Christoph: *Wasserdampfdestillation von Schadstoffen im porösen Medium: Entwicklung einer thermischen In-situ-Sanierungstechnologie*, 1998, ISBN 3-921694-97-3
- 98 Xu, Yichun: *Numerical Modeling of Suspended Sediment Transport in Rivers*, 1998, ISBN 3-921694-98-1, vergriffen
- 99 Wüst, Wolfgang: *Geochemische Untersuchungen zur Sanierung CKW-kontaminierter Aquifere mit Fe(0)-Reaktionswänden*, 2000, ISBN 3-933761-02-2
- 100 Sheta, Hussam: *Simulation von Mehrphasenvorgängen in porösen Medien unter Einbeziehung von Hysterese-Effekten*, 2000, ISBN 3-933761-03-4
- 101 Ayros, Edwin: *Regionalisierung extremer Abflüsse auf der Grundlage statistischer Verfahren*, 2000, ISBN 3-933761-04-2, vergriffen
- 102 Huber, Ralf: *Compositional Multiphase Flow and Transport in Heterogeneous Porous Media*, 2000, ISBN 3-933761-05-0
- 103 Braun, Christopherus: *Ein Upscaling-Verfahren für Mehrphasenströmungen in porösen Medien*, 2000, ISBN 3-933761-06-9
- 104 Hofmann, Bernd: *Entwicklung eines rechnergestützten Managementsystems zur Beurteilung von Grundwasserschadensfällen*, 2000, ISBN 3-933761-07-7
- 105 Class, Holger: *Theorie und numerische Modellierung nichtisothermer Mehrphasenprozesse in NAPL-kontaminierten porösen Medien*, 2001, ISBN 3-933761-08-5
- 106 Schmidt, Reinhard: *Wasserdampf- und Heißluftinjektion zur thermischen Sanierung kontaminierter Standorte*, 2001, ISBN 3-933761-09-3
- 107 Josef, Reinhold.: *Schadstoffextraktion mit hydraulischen Sanierungsverfahren unter Anwendung von grenzflächenaktiven Stoffen*, 2001, ISBN 3-933761-10-7

- 108 Schneider, Matthias: *Habitat- und Abflussmodellierung für Fließgewässer mit unscharfen Berechnungsansätzen*, 2001, ISBN 3-933761-11-5
- 109 Rathgeb, Andreas: *Hydrodynamische Bemessungsgrundlagen für Lockerdeckwerke an überströmbaren Erddämmen*, 2001, ISBN 3-933761-12-3
- 110 Lang, Stefan: *Parallele numerische Simulation instationärer Probleme mit adaptiven Methoden auf unstrukturierten Gittern*, 2001, ISBN 3-933761-13-1
- 111 Appt, Jochen; Stumpp Simone: *Die Bodensee-Messkampagne 2001, IWS/CWR Lake Constance Measurement Program 2001*, 2002, ISBN 3-933761-14-X
- 112 Heimerl, Stephan: *Systematische Beurteilung von Wasserkraftprojekten*, 2002, ISBN 3-933761-15-8, vergriffen
- 113 Iqbal, Amin: *On the Management and Salinity Control of Drip Irrigation*, 2002, ISBN 3-933761-16-6
- 114 Silberhorn-Hemminger, Annette: *Modellierung von Klufftaquifersystemen: Geostatistische Analyse und deterministisch-stochastische Klufftgenerierung*, 2002, ISBN 3-933761-17-4
- 115 Winkler, Angela: *Prozesse des Wärme- und Stofftransports bei der In-situ-Sanierung mit festen Wärmequellen*, 2003, ISBN 3-933761-18-2
- 116 Marx, Walter: *Wasserkraft, Bewässerung, Umwelt - Planungs- und Bewertungsschwerpunkte der Wasserbewirtschaftung*, 2003, ISBN 3-933761-19-0
- 117 Hinkelmann, Reinhard: *Efficient Numerical Methods and Information-Processing Techniques in Environment Water*, 2003, ISBN 3-933761-20-4
- 118 Samaniego-Eguiguren, Luis Eduardo: *Hydrological Consequences of Land Use / Land Cover and Climatic Changes in Mesoscale Catchments*, 2003, ISBN 3-933761-21-2
- 119 Neunhäuserer, Lina: *Diskretisierungsansätze zur Modellierung von Strömungs- und Transportprozessen in geklüftet-porösen Medien*, 2003, ISBN 3-933761-22-0
- 120 Paul, Maren: *Simulation of Two-Phase Flow in Heterogeneous Poros Media with Adaptive Methods*, 2003, ISBN 3-933761-23-9
- 121 Ehret, Uwe: *Rainfall and Flood Nowcasting in Small Catchments using Weather Radar*, 2003, ISBN 3-933761-24-7
- 122 Haag, Ingo: *Der Sauerstoffhaushalt staugeregelter Flüsse am Beispiel des Neckars - Analysen, Experimente, Simulationen -*, 2003, ISBN 3-933761-25-5
- 123 Appt, Jochen: *Analysis of Basin-Scale Internal Waves in Upper Lake Constance*, 2003, ISBN 3-933761-26-3

- 124 Hrsg.: Schrenk, Volker; Batereau, Katrin; Barczewski, Baldur; Weber, Karolin und Koschitzky, Hans-Peter: *Symposium Ressource Fläche und VEGAS - Statuskolloquium 2003, 30. September und 1. Oktober 2003*, 2003, ISBN 3-933761-27-1
- 125 Omar Khalil Ouda: *Optimisation of Agricultural Water Use: A Decision Support System for the Gaza Strip*, 2003, ISBN 3-933761-28-0
- 126 Batereau, Katrin: *Sensorbasierte Bodenluftmessung zur Vor-Ort-Erkundung von Schadensherden im Untergrund*, 2004, ISBN 3-933761-29-8
- 127 Witt, Oliver: *Erosionsstabilität von Gewässersedimenten mit Auswirkung auf den Stofftransport bei Hochwasser am Beispiel ausgewählter Stauhaltungen des Oberrheins*, 2004, ISBN 3-933761-30-1
- 128 Jakobs, Hartmut: *Simulation nicht-isothermer Gas-Wasser-Prozesse in komplexen Kluft-Matrix-Systemen*, 2004, ISBN 3-933761-31-X
- 129 Li, Chen-Chien: *Deterministisch-stochastisches Berechnungskonzept zur Beurteilung der Auswirkungen erosiver Hochwasserereignisse in Flusstauhaltungen*, 2004, ISBN 3-933761-32-8
- 130 Reichenberger, Volker; Helmig, Rainer; Jakobs, Hartmut; Bastian, Peter; Niessner, Jennifer: *Complex Gas-Water Processes in Discrete Fracture-Matrix Systems: Upscaling, Mass-Conservative Discretization and Efficient Multilevel Solution*, 2004, ISBN 3-933761-33-6
- 131 Hrsg.: Barczewski, Baldur; Koschitzky, Hans-Peter; Weber, Karolin; Wege, Ralf: *VEGAS - Statuskolloquium 2004*, Tagungsband zur Veranstaltung am 05. Oktober 2004 an der Universität Stuttgart, Campus Stuttgart-Vaihingen, 2004, ISBN 3-933761-34-4
- 132 Asie, Kemal Jabir: *Finite Volume Models for Multiphase Multicomponent Flow through Porous Media*. 2005, ISBN 3-933761-35-2
- 133 Jacoub, George: *Development of a 2-D Numerical Module for Particulate Contaminant Transport in Flood Retention Reservoirs and Impounded Rivers*, 2004, ISBN 3-933761-36-0
- 134 Nowak, Wolfgang: *Geostatistical Methods for the Identification of Flow and Transport Parameters in the Subsurface*, 2005, ISBN 3-933761-37-9
- 135 Süß, Mia: *Analysis of the influence of structures and boundaries on flow and transport processes in fractured porous media*, 2005, ISBN 3-933761-38-7
- 136 Jose, Surabhin Chackiath: *Experimental Investigations on Longitudinal Dispersive Mixing in Heterogeneous Aquifers*, 2005, ISBN: 3-933761-39-5
- 137 Filiz, Fulya: *Linking Large-Scale Meteorological Conditions to Floods in Mesoscale Catchments*, 2005, ISBN 3-933761-40-9

- 138 Qin, Minghao: *Wirklichkeitsnahe und recheneffiziente Ermittlung von Temperatur und Spannungen bei großen RCC-Staumauern*, 2005, ISBN 3-933761-41-7
- 139 Kobayashi, Kenichiro: *Optimization Methods for Multiphase Systems in the Sub-surface - Application to Methane Migration in Coal Mining Areas*, 2005, ISBN 3-933761-42-5
- 140 Rahman, Md. Arifur: *Experimental Investigations on Transverse Dispersive Mixing in Heterogeneous Porous Media*, 2005, ISBN 3-933761-43-3
- 141 Schrenk, Volker: *Ökobilanzen zur Bewertung von Altlastensanierungsmaßnahmen*, 2005, ISBN 3-933761-44-1
- 142 Hundecha, Hirpa Yeshewatersfa: *Regionalization of Parameters of a Conceptual Rainfall-Runoff Model*, 2005, ISBN: 3-933761-45-X
- 143 Wege, Ralf: *Untersuchungs- und Überwachungsmethoden für die Beurteilung natürlicher Selbstreinigungsprozesse im Grundwasser*, 2005, ISBN 3-933761-46-8
- 144 Breiting, Thomas: *Techniken und Methoden der Hydroinformatik - Modellierung von komplexen Hydrosystemen im Untergrund*, 2006, 3-933761-47-6
- 145 Hrsg.: Braun, Jürgen; Koschitzky, Hans-Peter; Müller, Martin: *Ressource Untergrund: 10 Jahre VEGAS: Forschung und Technologieentwicklung zum Schutz von Grundwasser und Boden*, Tagungsband zur Veranstaltung am 28. und 29. September 2005 an der Universität Stuttgart, Campus Stuttgart-Vaihingen, 2005, ISBN 3-933761-48-4
- 146 Rojanschi, Vlad: *Abflusskonzentration in mesoskaligen Einzugsgebieten unter Berücksichtigung des Sickerraumes*, 2006, ISBN 3-933761-49-2
- 147 Winkler, Nina Simone: *Optimierung der Steuerung von Hochwasserrückhaltebecken-systemen*, 2006, ISBN 3-933761-50-6
- 148 Wolf, Jens: *Räumlich differenzierte Modellierung der Grundwasserströmung alluvialer Aquifere für mesoskalige Einzugsgebiete*, 2006, ISBN: 3-933761-51-4
- 149 Kohler, Beate: *Externe Effekte der Laufwasserkraftnutzung*, 2006, ISBN 3-933761-52-2
- 150 Hrsg.: Braun, Jürgen; Koschitzky, Hans-Peter; Stuhmann, Matthias: *VEGAS-Statuskolloquium 2006*, Tagungsband zur Veranstaltung am 28. September 2006 an der Universität Stuttgart, Campus Stuttgart-Vaihingen, 2006, ISBN 3-933761-53-0
- 151 Niessner, Jennifer: *Multi-Scale Modeling of Multi-Phase - Multi-Component Processes in Heterogeneous Porous Media*, 2006, ISBN 3-933761-54-9
- 152 Fischer, Markus: *Beanspruchung eingeeerdeter Rohrleitungen infolge Austrocknung bindiger Böden*, 2006, ISBN 3-933761-55-7

- 153 Schneck, Alexander: *Optimierung der Grundwasserbewirtschaftung unter Berücksichtigung der Belange der Wasserversorgung, der Landwirtschaft und des Naturschutzes*, 2006, ISBN 3-933761-56-5
- 154 Das, Tapash: *The Impact of Spatial Variability of Precipitation on the Predictive Uncertainty of Hydrological Models*, 2006, ISBN 3-933761-57-3
- 155 Bielinski, Andreas: *Numerical Simulation of CO<sub>2</sub> sequestration in geological formations*, 2007, ISBN 3-933761-58-1
- 156 Mödinger, Jens: *Entwicklung eines Bewertungs- und Entscheidungsunterstützungssystems für eine nachhaltige regionale Grundwasserbewirtschaftung*, 2006, ISBN 3-933761-60-3
- 157 Manthey, Sabine: *Two-phase flow processes with dynamic effects in porous media - parameter estimation and simulation*, 2007, ISBN 3-933761-61-1
- 158 Pozos Estrada, Oscar: *Investigation on the Effects of Entrained Air in Pipelines*, 2007, ISBN 3-933761-62-X
- 159 Ochs, Steffen Oliver: *Steam injection into saturated porous media – process analysis including experimental and numerical investigations*, 2007, ISBN 3-933761-63-8
- 160 Marx, Andreas: *Einsatz gekoppelter Modelle und Wetterradar zur Abschätzung von Niederschlagsintensitäten und zur Abflussvorhersage*, 2007, ISBN 3-933761-64-6
- 161 Hartmann, Gabriele Maria: *Investigation of Evapotranspiration Concepts in Hydrological Modelling for Climate Change Impact Assessment*, 2007, ISBN 3-933761-65-4
- 162 Kebede Gurmessa, Tesfaye: *Numerical Investigation on Flow and Transport Characteristics to Improve Long-Term Simulation of Reservoir Sedimentation*, 2007, ISBN 3-933761-66-2
- 163 Trifković, Aleksandar: *Multi-objective and Risk-based Modelling Methodology for Planning, Design and Operation of Water Supply Systems*, 2007, ISBN 3-933761-67-0
- 164 Götzing, Jens: *Distributed Conceptual Hydrological Modelling - Simulation of Climate, Land Use Change Impact and Uncertainty Analysis*, 2007, ISBN 3-933761-68-9
- 165 Hrsg.: Braun, Jürgen; Koschitzky, Hans-Peter; Stuhmann, Matthias: *VEGAS – Kolloquium 2007*, Tagungsband zur Veranstaltung am 26. September 2007 an der Universität Stuttgart, Campus Stuttgart-Vaihingen, 2007, ISBN 3-933761-69-7
- 166 Freeman, Beau: *Modernization Criteria Assessment for Water Resources Planning; Klamath Irrigation Project, U.S.*, 2008, ISBN 3-933761-70-0

- 167 Dreher, Thomas: *Selektive Sedimentation von Feinstschwebstoffen in Wechselwirkung mit wandnahen turbulenten Strömungsbedingungen*, 2008, ISBN 3-933761-71-9
- 168 Yang, Wei: *Discrete-Continuous Downscaling Model for Generating Daily Precipitation Time Series*, 2008, ISBN 3-933761-72-7
- 169 Kopecki, Ianina: *Calculational Approach to FST-Hemispheres for Multiparametrical Benthos Habitat Modelling*, 2008, ISBN 3-933761-73-5
- 170 Brommundt, Jürgen: *Stochastische Generierung räumlich zusammenhängender Niederschlagszeitreihen*, 2008, ISBN 3-933761-74-3
- 171 Papafotiou, Alexandros: *Numerical Investigations of the Role of Hysteresis in Heterogeneous Two-Phase Flow Systems*, 2008, ISBN 3-933761-75-1
- 172 He, Yi: *Application of a Non-Parametric Classification Scheme to Catchment Hydrology*, 2008, ISBN 978-3-933761-76-7
- 173 Wagner, Sven: *Water Balance in a Poorly Gauged Basin in West Africa Using Atmospheric Modelling and Remote Sensing Information*, 2008, ISBN 978-3-933761-77-4
- 174 Hrsg.: Braun, Jürgen; Koschitzky, Hans-Peter; Stuhmann, Matthias; Schrenk, Volker: *VEGAS-Kolloquium 2008 Ressource Fläche III*, Tagungsband zur Veranstaltung am 01. Oktober 2008 an der Universität Stuttgart, Campus Stuttgart-Vaihingen, 2008, ISBN 978-3-933761-78-1
- 175 Patil, Sachin: *Regionalization of an Event Based Nash Cascade Model for Flood Predictions in Ungauged Basins*, 2008, ISBN 978-3-933761-79-8
- 176 Assteerawatt, Anongnart: *Flow and Transport Modelling of Fractured Aquifers based on a Geostatistical Approach*, 2008, ISBN 978-3-933761-80-4
- 177 Karnahl, Joachim Alexander: *2D numerische Modellierung von multifraktionalem Schwebstoff- und Schadstofftransport in Flüssen*, 2008, ISBN 978-3-933761-81-1
- 178 Hiester, Uwe: *Technologieentwicklung zur In-situ-Sanierung der ungesättigten Bodenzone mit festen Wärmequellen*, 2009, ISBN 978-3-933761-82-8
- 179 Laux, Patrick: *Statistical Modeling of Precipitation for Agricultural Planning in the Volta Basin of West Africa*, 2009, ISBN 978-3-933761-83-5
- 180 Ehsan, Saqib: *Evaluation of Life Safety Risks Related to Severe Flooding*, 2009, ISBN 978-3-933761-84-2
- 181 Prohaska, Sandra: *Development and Application of a 1D Multi-Strip Fine Sediment Transport Model for Regulated Rivers*, 2009, ISBN 978-3-933761-85-9

- 182 Kopp, Andreas: *Evaluation of CO<sub>2</sub> Injection Processes in Geological Formations for Site Screening*, 2009, ISBN 978-3-933761-86-6
- 183 Ebigbo, Anozie: *Modelling of biofilm growth and its influence on CO<sub>2</sub> and water (two-phase) flow in porous media*, 2009, ISBN 978-3-933761-87-3
- 184 Freiboth, Sandra: *A phenomenological model for the numerical simulation of multiphase multicomponent processes considering structural alterations of porous media*, 2009, ISBN 978-3-933761-88-0
- 185 Zöllner, Frank: *Implementierung und Anwendung netzfreier Methoden im Konstruktiven Wasserbau und in der Hydromechanik*, 2009, ISBN 978-3-933761-89-7
- 186 Vasin, Milos: *Influence of the soil structure and property contrast on flow and transport in the unsaturated zone*, 2010, ISBN 978-3-933761-90-3
- 187 Li, Jing: *Application of Copulas as a New Geostatistical Tool*, 2010, ISBN 978-3-933761-91-0
- 188 AghaKouchak, Amir: *Simulation of Remotely Sensed Rainfall Fields Using Copulas*, 2010, ISBN 978-3-933761-92-7
- 189 Thapa, Pawan Kumar: *Physically-based spatially distributed rainfall runoff modeling for soil erosion estimation*, 2010, ISBN 978-3-933761-93-4
- 190 Wurms, Sven: *Numerische Modellierung der Sedimentationsprozesse in Retentionsanlagen zur Steuerung von Stoffströmen bei extremen Hochwasserabflussergebnissen*, 2011, ISBN 978-3-933761-94-1
- 191 Merkel, Uwe: *Unsicherheitsanalyse hydraulischer Einwirkungen auf Hochwasserschutzdeiche und Steigerung der Leistungsfähigkeit durch adaptive Strömungsmodellierung*, 2011, ISBN 978-3-933761-95-8
- 192 Fritz, Jochen: *A Decoupled Model for Compositional Non-Isothermal Multiphase Flow in Porous Media and Multiphysics Approaches for Two-Phase Flow*, 2010, ISBN 978-3-933761-96-5
- 193 Weber, Karolin (Hrsg.): *12. Treffen junger WissenschaftlerInnen an Wasserbauinstituten*, 2010, ISBN 978-3-933761-97-2
- 194 Bliedernicht, Jan-Geert: *Probability Forecasts of Daily Areal Precipitation for Small River Basins*, 2011, ISBN 978-3-933761-98-9
- 195 Hrsg.: Koschitzky, Hans-Peter; Braun, Jürgen: *VEGAS-Kolloquium 2010 In-situ-Sanierung - Stand und Entwicklung Nano und ISCO -*, Tagungsband zur Veranstaltung am 07. Oktober 2010 an der Universität Stuttgart, Campus Stuttgart-Vaihingen, 2010, ISBN 978-3-933761-99-6

- 196 Gafurov, Abror: *Water Balance Modeling Using Remote Sensing Information - Focus on Central Asia*, 2010, ISBN 978-3-942036-00-9
- 197 Mackenberg, Sylvia: *Die Quellstärke in der Sickerwasserprognose: Möglichkeiten und Grenzen von Labor- und Freilanduntersuchungen*, 2010, ISBN 978-3-942036-01-6
- 198 Singh, Shailesh Kumar: *Robust Parameter Estimation in Gauged and Ungauged Basins*, 2010, ISBN 978-3-942036-02-3
- 199 Doğan, Mehmet Onur: *Coupling of porous media flow with pipe flow*, 2011, ISBN 978-3-942036-03-0
- 200 Liu, Min: *Study of Topographic Effects on Hydrological Patterns and the Implication on Hydrological Modeling and Data Interpolation*, 2011, ISBN 978-3-942036-04-7
- 201 Geleta, Habtamu Itefa: *Watershed Sediment Yield Modeling for Data Scarce Areas*, 2011, ISBN 978-3-942036-05-4
- 202 Franke, Jörg: *Einfluss der Überwachung auf die Versagenswahrscheinlichkeit von Staustufen*, 2011, ISBN 978-3-942036-06-1
- 203 Bakimchandra, Oinam: *Integrated Fuzzy-GIS approach for assessing regional soil erosion risks*, 2011, ISBN 978-3-942036-07-8
- 204 Alam, Muhammad Mahboob: *Statistical Downscaling of Extremes of Precipitation in Mesoscale Catchments from Different RCMs and Their Effects on Local Hydrology*, 2011, ISBN 978-3-942036-08-5
- 205 Hrsg.: Koschitzky, Hans-Peter; Braun, Jürgen: *VEGAS-Kolloquium 2011 Flache Geothermie - Perspektiven und Risiken*, Tagungsband zur Veranstaltung am 06. Oktober 2011 an der Universität Stuttgart, Campus Stuttgart-Vaihingen, 2011, ISBN 978-3-933761-09-2
- 206 Haslauer, Claus: *Analysis of Real-World Spatial Dependence of Subsurface Hydraulic Properties Using Copulas with a Focus on Solute Transport Behaviour*, 2011, ISBN 978-3-942036-10-8
- 207 Dung, Nguyen Viet: *Multi-objective automatic calibration of hydrodynamic models – development of the concept and an application in the Mekong Delta*, 2011, ISBN 978-3-942036-11-5
- 208 Hung, Nguyen Nghia: *Sediment dynamics in the floodplain of the Mekong Delta, Vietnam*, 2011, ISBN 978-3-942036-12-2
- 209 Kuhlmann, Anna: *Influence of soil structure and root water uptake on flow in the unsaturated zone*, 2012, ISBN 978-3-942036-13-9

- 210 Tuhtan, Jeffrey Andrew: *Including the Second Law Inequality in Aquatic Ecodynamics: A Modeling Approach for Alpine Rivers Impacted by Hydropeaking*, 2012, ISBN 978-3-942036-14-6
- 211 Tolossa, Habtamu: *Sediment Transport Computation Using a Data-Driven Adaptive Neuro-Fuzzy Modelling Approach*, 2012, ISBN 978-3-942036-15-3
- 212 Tatomir, Alexandru-Bodgan: *From Discrete to Continuum Concepts of Flow in Fractured Porous Media*, 2012, ISBN 978-3-942036-16-0
- 213 Erbertseder, Karin: *A Multi-Scale Model for Describing Cancer-Therapeutic Transport in the Human Lung*, 2012, ISBN 978-3-942036-17-7
- 214 Noack, Markus: *Modelling Approach for Interstitial Sediment Dynamics and Reproduction of Gravel Spawning Fish*, 2012, ISBN 978-3-942036-18-4
- 215 De Boer, Cjstmir Volkert: *Transport of Nano Sized Zero Valent Iron Colloids during Injection into the Subsurface*, 2012, ISBN 978-3-942036-19-1
- 216 Pfaff, Thomas: *Processing and Analysis of Weather Radar Data for Use in Hydrology*, 2013, ISBN 978-3-942036-20-7
- 217 Lebreuz, Hans-Henning: *Addressing the Input Uncertainty for Hydrological Modeling by a New Geostatistical Method*, 2013, ISBN 978-3-942036-21-4
- 218 Darcis, Melanie Yvonne: *Coupling Models of Different Complexity for the Simulation of CO<sub>2</sub> Storage in Deep Saline Aquifers*, 2013, ISBN 978-3-942036-22-1
- 219 Beck, Ferdinand: *Generation of Spatially Correlated Synthetic Rainfall Time Series in High Temporal Resolution - A Data Driven Approach*, 2013, ISBN 978-3-942036-23-8
- 220 Guthke, Philipp: *Non-multi-Gaussian spatial structures: Process-driven natural genesis, manifestation, modeling approaches, and influences on dependent processes*, 2013, ISBN 978-3-942036-24-5
- 221 Walter, Lena: *Uncertainty studies and risk assessment for CO<sub>2</sub> storage in geological formations*, 2013, ISBN 978-3-942036-25-2
- 222 Wolff, Markus: *Multi-scale modeling of two-phase flow in porous media including capillary pressure effects*, 2013, ISBN 978-3-942036-26-9
- 223 Mosthaf, Klaus Roland: *Modeling and analysis of coupled porous-medium and free flow with application to evaporation processes*, 2014, ISBN 978-3-942036-27-6
- 224 Leube, Philipp Christoph: *Methods for Physically-Based Model Reduction in Time: Analysis, Comparison of Methods and Application*, 2013, ISBN 978-3-942036-28-3
- 225 Rodríguez Fernández, Jhan Ignacio: *High Order Interactions among environmental variables: Diagnostics and initial steps towards modeling*, 2013, ISBN 978-3-942036-29-0

- 226 Eder, Maria Magdalena: *Climate Sensitivity of a Large Lake*, 2013, ISBN 978-3-942036-30-6
- 227 Greiner, Philipp: *Alkoholinjektion zur In-situ-Sanierung von CKW Schadensherden in Grundwasserleitern: Charakterisierung der relevanten Prozesse auf unterschiedlichen Skalen*, 2014, ISBN 978-3-942036-31-3
- 228 Lauser, Andreas: *Theory and Numerical Applications of Compositional Multi-Phase Flow in Porous Media*, 2014, ISBN 978-3-942036-32-0
- 229 Enzenhöfer, Rainer: *Risk Quantification and Management in Water Production and Supply Systems*, 2014, ISBN 978-3-942036-33-7
- 230 Faigle, Benjamin: *Adaptive modelling of compositional multi-phase flow with capillary pressure*, 2014, ISBN 978-3-942036-34-4
- 231 Oladyshkin, Sergey: *Efficient modeling of environmental systems in the face of complexity and uncertainty*, 2014, ISBN 978-3-942036-35-1
- 232 Sugimoto, Takayuki: *Copula based Stochastic Analysis of Discharge Time Series*, 2014, ISBN 978-3-942036-36-8
- 233 Koch, Jonas: *Simulation, Identification and Characterization of Contaminant Source Architectures in the Subsurface*, 2014, ISBN 978-3-942036-37-5
- 234 Zhang, Jin: *Investigations on Urban River Regulation and Ecological Rehabilitation Measures, Case of Shenzhen in China*, 2014, ISBN 978-3-942036-38-2
- 235 Siebel, Rüdiger: *Experimentelle Untersuchungen zur hydrodynamischen Belastung und Standsicherheit von Deckwerken an überströmbaren Erddämmen*, 2014, ISBN 978-3-942036-39-9
- 236 Baber, Katherina: *Coupling free flow and flow in porous media in biological and technical applications: From a simple to a complex interface description*, 2014, ISBN 978-3-942036-40-5
- 237 Nuske, Klaus Philipp: *Beyond Local Equilibrium — Relaxing local equilibrium assumptions in multiphase flow in porous media*, 2014, ISBN 978-3-942036-41-2
- 238 Geiges, Andreas: *Efficient concepts for optimal experimental design in nonlinear environmental systems*, 2014, ISBN 978-3-942036-42-9
- 239 Schwenck, Nicolas: *An XFEM-Based Model for Fluid Flow in Fractured Porous Media*, 2014, ISBN 978-3-942036-43-6
- 240 Chamorro Chávez, Alejandro: *Stochastic and hydrological modelling for climate change prediction in the Lima region, Peru*, 2015, ISBN 978-3-942036-44-3
- 241 Yulizar: *Investigation of Changes in Hydro-Meteorological Time Series Using a Depth-Based Approach*, 2015, ISBN 978-3-942036-45-0

- 242 Kretschmer, Nicole: *Impacts of the existing water allocation scheme on the Limarí watershed – Chile, an integrative approach*, 2015, ISBN 978-3-942036-46-7
- 243 Kramer, Matthias: *Luftbedarf von Freistrahlturbinen im Gegendruckbetrieb*, 2015 ISBN 978-3-942036-47-4
- 244 Hommel, Johannes: *Modeling biogeochemical and mass transport processes in the subsurface: Investigation of microbially induced calcite precipitation*, 2016 ISBN 978-3-942036-48-1

Die Mitteilungshefte ab der Nr. 134 (Jg. 2005) stehen als pdf-Datei über die Homepage des Instituts: [www.iws.uni-stuttgart.de](http://www.iws.uni-stuttgart.de) zur Verfügung.